Author:
Boreham, Frances

Title:
Causes and Consequences of Hazardous Lava-Water Interactions, with Particular Focus on Rootless Eruptions

Causes and Consequences of Hazardous Lava–Water Interactions, with Particular Focus on Rootless Eruptions

Frances Boreham

Supervisors: Katharine Cashman & Alison Rust

A dissertation submitted to the University of Bristol in accordance with the requirements for award of the degree of Doctor of Philosophy in the Faculty of Science

School of Earth Sciences

Word Count: 47,659

Abstract

Lava–water interactions (LWI) occur in many different environments, causing secondary hazards, but are not routinely considered in hazard assessments. The variety of deposits from explosive LWI (known as rootless eruptions) reflects the range of eruption dynamics. However, the influences of lava flux, water availability and sediment properties on triggering and sustaining rootless eruptions are poorly understood.

Contemporary accounts of the 1783–1784 Laki fissure eruption highlight the range of hazardous LWI, including lava dams, flooding, disruption of water supplies, and rootless eruptions. The presence of rootless cones around flooded areas shows how lava and water interact to modify the environment, increasing the risk of rootless eruptions in previously dry areas.

A case study of the Younger Laxá Lava in northeast Iceland, which inundated a shallow lake, river gorge and broad glacial valley, shows the relationship between local lava flux, water availability and rootless cone morphology. Areas with abundant water and high local lava flux build large scoriaceous rootless cones. Areas with less water create smaller scoriaceous cones, spatter cones and hornitos. Reduced lava flux, e.g. at flow margins, also results in smaller cones. However, similar analysis of Laki rootless cones shows that the relationship between cone size and environment is not straightforward and depends on the local conditions and sediment properties.

Numerical models show that conduction from a lava flow to a saturated underlying sediment can raise pore pressure enough to trigger a rootless eruption. Sediment permeability controls the rate of pressure build up: coarse, high permeability sediments allow steam to escape as it is generated; high–moderate permeability sediments allow steam to escape as the lava advances, but pressure can rise tens of metres behind the flow front; very low permeability sediments prevent steam escape and drive explosions that disrupt the lava flow advance.

Author's Declaration

I declare that the work in this dissertation was carried out in accordance with the requirements of the University's Regulations and Code of Practice for Research Degree Programmes and that it has not been submitted for any other academic award. Except where indicated by specific reference in the text, the work is the candidate's own work. Work done in collaboration with, or with the assistance of, others, is indicated as such. Any views expressed in the dissertation are those of the author.

.....

Frances Boreham

20^{th} February 2021

Acknowledgments

Firstly, I'd like to thank my supervisors, Kathy Cashman and Alison Rust, for their guidance, feedback and support throughout this project. They have introduced me to the delights of volcanology and helped me develop as a researcher and scientist.

Huge thanks to my husband Christopher, for being my rock. I could not have achieved this without your unwavering support and seemingly-endless faith in me. I love you. Thanks to my mum for encouraging, supporting and advising me. Also to my son Joseph, who brings me endless joy and distraction, reminding me that life is full of wonders, especially when you look away from the computer screen.

Special thanks go to Jen Saxby for being my fieldwork partner and desk buddy over the last five years. I will always have very fond memories of our Iceland trip, especially the hair-raising dirt roads and river fords, terrible weather, cheesy pasta and end-of-the-day beers.

I'd like to thank Tom Richardson for lending me the drone I used for fieldwork, and Matt Watson for teaching me how to fly it. Thanks to Andrey Afanasyev for helping me with the MUFITS modelling, and answering my obscure questions.

Finally, I want to thank all of my friends in the University of Bristol and Earth Sciences communities, for their warm welcome, support and advice, and for keeping me sane. Particular thanks on this front go to Bob Myhill, Nick Hayes, David Edwards and the other denizens of G44.

This work was supported by the Natural Environmental Research Council [grant no: NE/L002434/1], and an AXA Research Fund and Wolfson Merit Award to Kathy Cashman.

Contents

Abstract i

Author's Declaration ii

Acknowledgments iii

Table of Contents iv

List of Figures viii

List of Tables xii

Acronyms and Nomenclature xiv

1 Introduction 1

1.1 Introduction 1

1.2 Background 4

1.2.1 Icelandic Rootless Cones 12

1.2.2 Models of rootless cone formation 15

1.3 Key Questions 19

1.4 Thesis overview 20

1.4.1 Chapter 2: Linking lava flow morphology, water availability and rootless cone formation on the Younger Laxá Lava, NE Iceland 20

1.4.2 Chapter 3: Hazards from lava–river interactions during the 1783–1784 Laki fissure eruption 21

1.4.3 Chapter 4: Numerical modelling of pore fluid evolution in wet sediments heated by lava, with application to triggering rootless eruptions . . . 22
1.4.4 Chapter 5: Conclusion . . . 22

2 Linking lava flow morphology, water availability and rootless cone formation on the Younger Laxá Lava, NE Iceland 23

2.1 Introduction . . . 26
2.2 Background . . . 28
2.2.1 Geological and hydrological setting . . . 28
2.3 Methods . . . 32
2.3.1 Rootless Cone Types . . . 32
2.3.2 Aerial imagery and high-resolution DTMs from drone surveying . . . 34
2.3.3 Cone digitisation, classification, crater size, and nearest neighbour analysis . . . 38
2.3.4 Error analysis . . . 41
2.3.5 Statistical Modelling . . . 42
2.3.6 Flow emplacement temperatures . . . 46
2.4 Results . . . 46
2.4.1 The Younger Laxá Lava and associated rootless cones . . . 48
2.4.2 Rootless cone size and spacing . . . 59
2.5 Discussion . . . 66
2.5.1 What does the morphology of the YLL tell us about how it was emplaced? 66
2.5.2 What does the environment today tell us about water availability? . . . 67
2.5.3 How did the changes in lava and water availability affect LWI? . . . 71
2.6 Summary . . . 77

3 Hazards from lava–river interactions during the 1783–1784 Laki fissure eruption 79

3.1 Introduction . . . 81
3.2 Background . . . 83
3.2.1 1783–1784 Laki fissure eruption . . . 83

3.2.2 Hydrological setting of the 1783–1784 Laki fissure eruption 87
3.3 Methods 92
3.3.1 Analysis of contemporary sources 92
3.3.2 Rootless cone identification, digitisation and statistical modelling . . 93
3.3.3 Electron probe analysis of rootless cone tephra 97
3.4 Results 99
3.4.1 Lava–water interactions in the contemporary accounts 99
3.4.2 Rootless cones 102
3.5 Discussion 114
3.5.1 Lava–river interactions and flooding 115
3.5.2 Explosive lava–water interactions 117
3.5.3 Remote sensing for lava flow assessments 119
3.5.4 Suggestions for future hazard assessments 121
3.6 Concluding remarks 122

4 Numerical modelling of pore fluid evolution in wet sediments heated by lava 124

4.1 Introduction 125
4.2 Modelling heat transfer under lava 127
4.3 Numerical modelling in MUFITS 130
4.3.1 How MUFITS works 130
4.3.2 Setting up the model 132
4.3.3 Modelling strategy and scenarios 141
4.4 Results and analysis 147
4.4.1 General results 147
4.4.2 Specific Scenarios 154
4.5 Discussion 157
4.5.1 Relating our model results to real life 157
4.5.2 Triggering a rootless eruption 158
4.5.3 Effect of sediment saturation 160
4.5.4 Sustaining a rootless eruption 160

4.5.5 Cone spacing and distribution 164
4.6 Summary and suggested further work 164

5 Conclusion **167**
5.1 Research Aims 167
5.2 What is the range of hazardous lava–water interactions? 168
5.3 How are rootless eruptions triggered? 169
5.3.1 Rootless eruptions in different environments 174
5.3.2 Rootless eruptions on 'a'ā lava 176
5.3.3 Non-explosive and 'failed' rootless eruptions 176
5.4 Sustaining rootless eruptions 177
5.4.1 The role of lava volume flux 177
5.4.2 The role of sediment and water distribution 178
5.5 Implications for future hazard assessments 179
5.6 Suggestions for futher research 180

6 References **182**

Appendices **201**

A Supplementary Material for Chapter 2 **203**
A.1 Supplementary Figures 203
A.2 Supplementary Tables 205

B Supplementary Material for Chapter 3 **206**
B.1 Selected passages from contemporary sources 206
B.1.1 Sources 206
B.2 Supplementary Table 220

C Supplementary Material for Chapter 4 **221**
C.1 Example MUFITS input file 221
C.2 Table of published sediment properties 226
C.3 Sediment fluidisation example 229

List of Figures

1.1 Global map of known locations of rootless cones or documented rootless eruptions. 2

1.2 Different types of rootless cones and associated features 7

1.3 Map of rootless cone groups in Iceland. 8

1.4 Rootless cones formed when the Nesjahraun lava entered Lake Thingvallavtn. 9

1.5 Schematic of a cross-section through a scoriaceous rootless cone. 10

1.6 Photograph of an excavated rootless cone from the Rauðhólar group, near Reykjavík, Iceland. 12

1.7 Photograph of rootless cones in Lake Mývatn, NE Iceland. 13

1.8 Photograph of Landbrotshólar rootless cones near Kirkjubæjarkaustur 14

1.9 Photograph of eroded rootless cones in Álftaver, S Iceland. 14

1.10 Photograph of the Hnúta rootless cone group near the Laki crater row, S Iceland. 15

1.11 Conceptual model of conductive heat transfer triggering rootless eruptions. . 16

1.12 Stages of molten fuel–coolant interaction (MFCI). 17

1.13 Conceptual model for triggering mixing between lava and wet sediment through bending and failure of lava basal crust. 18

2.1 View of the Mývatn, Laxárdalur and Aðaldalur region 27

2.2 Map of Mývatn area showing the major landscpe features and hydrology. . . 29

2.3 Overview of Aðaldalur and the surrounding valleys, showing the different rivers in relation to one another and the Younger Laxá lava. Lava entered the southern end of Aðaldalur from Laxárdalur and flowed north towards the Greenland Sea. 31

2.4 Different types of rootless cones and associated features 33

2.5 High resolution DTM of rootless cones in UAS survey area (1) in Aðaldalur. 35

2.6 High resolution DTM of rootless cones and hornitos along the inflation front in Aðaldalur in survey area (2), showing elevation profiles of different cone types. 36
2.7 High resolution DTM of hornitos in UAS survey area (3) in Aðaldalur. . . . 37
2.8 Comparison between lotus-fruit (L) cones and overlapping single-cratered (S) cones on the YLL 39
2.9 Map of Mývatn showing the location of rootless cones, hydrologic features, and elevation 47
2.10 Features of the Younger Laxá Lava on the eastern shore of Mývatn near Höfði 49
2.11 Elevation of the YLL on the east shore of Mývatn 50
2.12 Photographs of Mývatn 50
2.13 Close up views of the Skútustaðir and Vindbelgur cone groups 51
2.14 Comparison of different rootless tephra around Mývatn 52
2.15 Temperature of the YLL with distance from the eruptive vent 53
2.16 Rootless cone groups along Laxárdalur 54
2.17 The Younger Laxá Lava in Aðaldalur and key geographical features 56
2.18 Close-up of key regions of the Younger Laxá Lava 58
2.19 Rootless cones in Aðaldalur shown in Google Earth 59
2.20 Rootless cone properties across the Younger Laxá Lava 63
2.21 Variation in crater size and spacing for Mývatn rootless cones 64
2.22 Variation in cone type with proximity to lake Mývatn 65
2.23 Variation in rootless cone crater radius for cone groups in Aðaldalur 65
2.24 Model for the formation of inflation pits around a pool of water 68
2.25 View of the join between Aðaldalur and Bárðardalur 70

3.1 Overview of the Laki region showing the 1783–1784 lava flow and major landmarks. 84
3.2 Progression of the Laki lava flow throughout the Síða, Landbrot and Meðalland districts in June and July 1783. 86

3.3 Photographs of rootless cones. (A) Rootless cones from the Landbrots group created by the 939–940 AD Eldgjá eruption. (B) View of a partially excavated rootless cone on the Laki lava field (fron group 1 in this study), showing the central crater and a layer of moss-covered spatter on the cone flanks. (C) Close-up of the same rootless cone, showing the layers of ash and lapilli-sized scoria topped with welded spatter, with a trowel for scale. (D) Wider view of the rootless cones in group 1 of this study. 88

3.4 Overview of the Laki lava field showing the eruption fissure and rootless cone groups. 89

3.5 A map of the soils and substrates in the region around the Laki lava flow. . . 90

3.6 Laki rootless cone groups 1–4. 95

3.7 Not rootless cones. 98

3.8 Floods caused by the Laki eruption. 101

3.9 Timeline of the Laki eruption from May–October 1783 102

3.10 View of the western edge of the Laki lava flow. 103

3.11 Laki rootless cone group 5. 105

3.12 Laki rootless cone groups 6–8 106

3.13 Laki rootless cone groups 9–12. 108

3.14 Laki rootless cone groups 13–15. 109

3.15 Plot of SiO_2 against FeO/TiO_2 of matrix glass from the rootless cones in group 8 (black diamonds), vent-proximal Laki lava (black cross) and rootless cones in Landbrotshólar, created by the 940 CE Eldgjá eruption (black square).111

3.16 Approximate extents of possible impounded water in the upper reaches of the Skaftá river 112

3.17 Distribution of Laki rootless cone size (crater radius) by group number . . . 113

4.1 Net for 2^{nd} order upwind scheme. 131

4.2 Diagram of INFTHIN boundary condition in MUFITS. 131

4.3 Corey relative permeability curves for liquid and gas. 137

4.4 Sketch of scenario 0 model setup. 139

4.5 Results of scenario 0 from MUFITS. 140

4.6 Flow diagram of model scenarios and modelling strategy. 142

4.7 Sketch of scenario 1 model setup. 143

4.8 Sketch of scenario 2 model setup. 144

4.9 Sketch of modified Scenario 2 model used to test effect of grid resolution. Subdomains i–iii, separated by grey lines, show the areas of the domain with different cell sizes. Cells in subdomain i are 1 cm, 2.5 cm or 5 cm thick, cells in ii are 5 cm thick and cells in iii are 10 cm thick. All cells are 10 cm wide. 145

4.10 Initial thermal field applied to scenario 3 models. 146

4.11 Sketch of scenario 4 model setup 146

4.12 Cartoon of the general steps of model behaviour. 148

4.13 Variation of pore pressure with time for different sediment permeabilities (scenario 2). 149

4.14 Variation of pore pressure for different sediment porosities. 150

4.15 Pressure and temperature curves for different sediment thermal conductivities (Scenario 2). 151

4.16 Pressure and temperature curves for different heat capacities (scenario 2). . . 152

4.17 Variation in pressure, depth of vapour front, and temperature for different grid resolutions. 153

4.18 Comparison of pressure curves with and without a dry top layer of sediment 154

4.19 Pressure in the top layer of cells (2.5 cm average depth) at different distances behind the lava front. 157

4.20 Excavation potential for different thicknesses of steam layer. 159

4.21 Proposed hybrid model for rootless cone formation. 163

5.1 Flow diagram showing different scenarios for triggering rootless eruptions . . 171

5.2 Schematic illustrating the effects of local lava supply and water distribution on the size and spacing of rootless eruptions. 178

A.1 View of a subset of the rootless cones used for error assessment 204

A.2 Relative (%) error distribution for rootless cone area 204

C.1 Example MUFITS input file (p. 1) 222

C.2 Example MUFITS input file (p. 2) 223

C.3 Example MUFITS input file (p. 3) 224

C.4 Example MUFITS input file (p. 4) 225

List of Tables

2.1 List of statistical models 43

2.2 Size and nearest neighbour distributions for rootless cone groups in Mývatn, Laxárdalur and Aðaldalur 45

2.3 Chemical composition of rootless scoria samples from the Younger Laxá Lava at Mývatn and Aðaldalur. 53

2.4 Expected and observed distributions of different types of rootless cone across the YLL 60

2.5 Correlation coefficients and corresponding p-values and 95 % confidence intervals between cone size and NN distance for different populations of rootless cones on the YLL. 61

2.6 Rootless cone crater radius distributions by type 61

3.1 Likely formation dates and environments of the Laki rootless cone groups. . 96

3.2 Major element composition of matrix glass in tephra samples from Laki and Eldgjá lava flows and rootless cones. 99

3.3 Distribution of rootless cone type and size across the Laki lava field. 114

4.1 Summary table showing the range of published physical properties for different sediment types 134

4.2 Sediment physical properties used in our numerical models 135

4.3 Lava and sediment thermal properties used in this study, compared to values used in other studies of lava–sediment heat conduction. 136

4.4 Estimated failure threshold, P_{max}, through time. 138

4.5 Time-averaged interface temperature between lava and sediment from scenario 0. 140

4.6 Effect of grid resolution and permeability on the initial pressure peak and pressure after two hours 154

4.7 Fluid phases in top cell (1 cm thick) over time, for varying sediment permeability 155
4.8 Fluid phases in top cell (1 cm thick) over time, for varying sediment porosity 155

A.1 Details of DigitalGlobe images used for digitising rootless cones across the YLL. 205
A.2 Flight details for UAS surveys 205

B.1 Table A - Conditions before the eruption 209
B.2 Table B - Lava–river interactions and flooding 217
B.3 Table C - Explosive lava–water interactions 218
B.4 Table D - Weather conditions during the eruption 219
B.5 Details of DigitalGlobe images used for digitising rootless cones across the Laki lava field. 220

C.1 Published sediment properties from various sources. 228

Acronyms and Nomenclature

Acronyms

AIC – Akaike information criterion

ANOVA – analysis of variance

CE – Christian Era

.csv – comma separated variable file type

D – double cones; scoriaceous cones with 2 craters

DTM – digital terrain model

EVZ – Eastern Volcanic Zone

H – hornitos

HRG – Hverfisfljót River Gorge

HSC – High strength concrete

HSD – honest significant difference

In – referring to rootless cones that sit away from the lake shore (in Chapter 2)

Is – referring to rootless cones that sit on islands (in Chapter 2)

L – 'Lotus fruit' cones; scoriaceous cones with >2 inner craters (as defined by Noguchi et al., 2016)

LWI – Lava–water interaction

MFCI – Molten Fuel–Coolant Interaction

MUFITS – Multiphase Filtration Transport Simulator

NE – North-East

NN – nearest neighbour

NVZ – Northern Volcanic Zone

OLL – Older Laxá Lava

P – explosion pits; rootless craters without built-up walls or ramparts

QGIS – Quantum Geographic Information Systems; geospatial analysis software

RM – referring to rootless cones that sit at the mouth of the Laxá river (in Chapter 2)

S – scoriaceous cones with a single inner crater

Sh – referring to rootless cones that sit around the lake shore (in Chapter 2)

SP – rootless spatter cones

SRG – Skaftá River Gorge

U – unclassified rootless cones

UAS – unmanned aerial system

UAV – unmanned aerial vehicle

WVZ – Western Volcanic Zone

yBP – years Before Present (1950)

YLL – Younger Laxá Lava

Nomenclature

C – Courant number

c_p – specific heat capacity [J/kgK]

e – energy per unit area [J/m^2]

g – gravitational acceleration (9.81 m/s^2)

h – enthalpy [J]

k – permeability [mD] or [m^2]

k_r – relative permeability [mD] or [m^2]

m – mass [kg]

P – pressure [Pa]

s – molar entropy [J/K]

T – temperature [^{o}C]

t – time [s]

u – velocity [m/s]

V – volume [m^3]

W – work [J]

$\boldsymbol{w}$ – Darcy velocity [m/s]

x – horizontal distance [m]

z – depth relative to the lava-sediment inerface[m]

α – thermal diffusivity [m^2/s]

γ – ratio of specific heats

μ – viscosity [Pa.s]

ϑ – saturation [%]

$\varkappa$ – thermal conductivity [W/mK]

ϱ – density [kg/m^3]

σ – stress [Pa]

$\boldsymbol{\phi}$ – porosity

χ – molar mass fraction

Subscripts

atm – atmospheric conditions (15 ^{o}C / 0.1 MPa)

crit – critical pressure or temperature of water (374 ^{o}C / 22 MPa)

gas – pertaining to the gaseous phase

mf – minimum fluidising

max - maximum

liq – pertaining to the liquid phase

L – pertaining to the lava

S – pertaining to the sediment

t - total

0 – pertaining to initial conditions

800 – pertaining to the depth of the 800 ^{o}C isotherm

Chapter 1

Introduction

Author Declaration

This thesis includes work from two previously published papers: Boreham et al. (2018) and Boreham et al. (2020). The main body of these papers make up Chapters 2 and 3, but I have edited and combined some of the introductory and background material from these papers and included it in this Introduction to establish the context for my work and how it fits with, and contributes to, knowledge of lava–water interactions. More detailed author declarations are included at the start of Chapters 2 and 3, which describe the contributions from each author to the different papers.

1.1 Introduction

The abundance of both water and effusive volcanism on Earth means that subaerial lava flows and water come into contact in a wide range of environments: coastal, lacustrine, fluvial, wetland and ice. Throughout this thesis, I use 'lava–water interactions' (LWI) as an umbrella term to describe the wide range of outcomes when these two fluids meet: from relatively passive interactions such as lava flows entering water bodies or damming rivers, to steam explosions caused by lava trapping pockets of water or, more commonly, water-laden sediment.

Explosive LWI occur when low viscosity, basaltic lava interacts with surface water and drives steam explosions. They are also known as 'rootless' eruptions because they are not directly connected to a magma source at depth and therefore have no geologic 'roots'. Rootless eruptions occur across the globe in areas with basaltic volcanism and abundant surface

Figure 1.1: Global map of known locations of rootless cones or documented rootless eruptions.

water (Figure 1.1), in a range of environments including lakes (e.g. Thorarinsson, 1953; Einarsson, 1982; Ross et al., 2014; Noguchi et al., 2016), river valleys (Thorarinsson, 1953; Thordarson et al., 1998; Reynolds et al., 2015), wetlands (e.g. Hamilton et al., 2010a), coastal settings (e.g. Jurado-Chichay et al., 1996; Mattox and Mangan, 1997) and on ice and snowpacks (Edwards et al., 2012; Edwards et al., 2015; Andronico et al., 2018). Over the last two decades they have been of particular interest to planetary geologists, following their identification in imagery of Mars (e.g. Jaeger et al., 2007; Keszthelyi et al., 2010; Hamilton et al., 2011; Noguchi and Kurita, 2015).

LWI fall into the broader category of hydrovolcanism, which generally describes any interaction between volcanic processes or products and the hydrosphere or cryosphere. Phreatomagmatism, where magma interacts explosively with external water as it ascends, is also a form of hydrovolcanism. Phreatomagmatic eruptions can build maar-diatreme structures and tuff rings (e.g. Lorenz and Kurszlaukis, 2007; White and Ross, 2011; Valentine et al., 2014; Valentine and White, 2012; Agustín-Flores et al., 2015; Liu et al., 2017), and also occur when magma erupts through a glacier (e.g. Graettingar et al., 2013). LWI are distinct from phreatomagmatism: during a LWI the interaction with water occurs away from the main vent, after the lava has erupted, as opposed to during magma ascent. Additionally,

LWI are not always explosive, whereas phreatomagmatism is.

LWI, including rootless eruptions, are generally overlooked in lava flow hazard assessments despite the broad range of secondary hazards they can create (Deligne, 2012). This is exacerbated by their association with otherwise relatively 'safe', slow-moving lava flows (e.g. Mattox, 1993). For example, a group of tourists and a BBC film crew were injured by a rootless eruption from lava flowing over snow on Mt Etna in 2016 (Andronico et al., 2018).

It is likely that LWI and rootless eruptions are more common than the geologic record suggests. Recent witnessed rootless eruptions during the Fimmvörðuháls eruption in 2010 (Edwards et al., 2012), Tolbachick in 2012–2013 (Edwards et al., 2015) and at Mt Etna in 2016 (Andronico et al., 2018) left no lasting deposits. Additionally, they are easily buried by later lava flows or eroded by water (e.g. floods or wave action in coastal or lake settings). Similarly, while some passive LWI create lava-dammed lakes that persist for thousands of years (e.g. Orem, 2010; Deligne et al., 2017), they may also be very short-lived and leave no deposits preserved in the geological record (e.g. lakes formed during the 1783–1784 Laki fissure eruption, as described in Chapter 3). This makes it even more crucial to study the existing deposits and eyewitness accounts of LWI and understand where and how they occur, and the hazards that arise from them.

Icelandic rootless cones have been studied as an analogue for their Martian counterparts. These studies have often focused on cone morphology and spatial distribution, which can be directly related to satellite images and digital terrain models (DTMs) of Mars (e.g. Greeley and Fagents, 2001; Fagents et al., 2002; Fagents and Thordarson, 2007; Noguchi and Kurita; 2015). Numerical models have been used to compare the ballistics of ejecta from rootless eruptions (Fagents et al., 2002) and feasible trigger mechanisms in an environment where surface water is scarce or completely absent (Dundas and Keszthelyi, 2013), as expected for Mars.

Rootless eruptions are also of interest because they provide a bridge between laboratory experiments of melt–water interactions and large-scale hydrovolcanism (Fitch et al., 2017). This has motivated recent detailed stratigraphic and componentry studies of individual rootless cones (Fitch et al., 2017; Hamilton et al., 2017). Comparison of ash and scoria from rootless eruptions, phreatomagmatic eruptions, and experiments shows that there are common heat transfer and fragmentation mechanisms in all three cases (Fitch et al, 2017).

1.2 Background

To put the work in this thesis into context, in this section I briefly outline and review the existing knowledge of LWI, their deposits and the different locations in which they occur.

Ocean entries

Many volcanic islands around the world are built by lava deltas, which form where a lava flow enters a large body of water, e.g. sea, ocean or lake. When the lava contacts the relatively cold water, it quenches and fragments, building up steeply dipping foreset beds of glassy, clastic rubble (hyaloclastite). As subaerial lava later advances over these deposits, it creates new land (e.g. Skilling, 2002; Umino et al., 2006). Lava deltas are often unstable, however, and prone to subsidence or collapse under their own weight (Kauahikaua et al., 1993). When deltas collapse, lava tubes feeding the flow front may be severed, exposing the hot interior lava directly to water, which can cause explosive tephra blasts, lava fountaining and bubble bursts driven by steam (Mattox and Mangan, 1997).

Some lava flows remain coherent as they enter water, producing the subaqueous lava flows that are common at ocean ridges, seamounts and in coastal waters and lakes. Subaqueous lava flows display a range of surface morphologies, including rubbly, lobate and pillowed, or channelized forms (e.g. Moore et al., 1973; Moore, 1975; Tribble, 1991; Gregg and Smith, 2003). Where trapped steam passively degasses through thick inflated flows or ponded lava, it solidifies the surrounding lava, leaving behind hollow pillars (Gregg and Chadwick, 1996). These are most common in submarine settings but have also been recorded in subaerial lava flows in Iceland (Gregg and Christle 2013; Boreham et al., 2018).

Lava–river interactions

Lava–river interactions are widely recognized as modifying river drainages and affecting landscape evolution. Notable and well-studied examples in the USA include the Columbia River and its tributaries (e.g. O'Connor et al., 2009; Ely et al., 2012; Deligne et al., 2017; Jensen and Donnelly-Nolan, 2017; and references therein), and the Colorado River in the Grand Canyon (e.g. Crow et al., 2008; Fenton et al., 2004; 2006).

Where a lava flow enters a canyon, gorge or valley, the style of LWI varies depending on the geometry of the interaction. Where lava meets a river on low-relief topography, the river

can divert around the lava flow rather than be dammed by it. For example, when the 2014 Holuhraun lava flow from Bárðarbunga entered the channel of the Jökulsá á Fjöllum river, lava–river interactions were limited to passive steaming with only a few steam explosions (Pedersen et al., 2017). Here, lava displaced the water from the riverbed but the coarse, gravelly sediments were permeable enough to allow the water to escape passively from the lava.

Where a lava flow enters and blocks a steep river canyon, the river cannot go around the flow and is therefore dammed. On the upstream side, the dam comprises dipping foreset beds of pillow lavas and hyaloclastite debris where the lava interacted with river water, covered by a topset bed of coherent, subaerially emplaced lava that generally exhibits columnar jointing (e.g. Crow et al., 2008; Ely et al., 2012) These features are sometimes repeated in vertical cross section, indicating persistent LWI with rising water levels behind the dam (Crow et al., 2008). The downstream side of the dam is characterized by gently sloping subaerial lava flows, which may run for great distances along the dried-up riverbed (Crow et al., 2008)

Lava dams impound water, creating upstream lakes and wetlands that may persist for tens of thousands of years. For example, the West Crater lava dam on the Owyhee River created an upstream lake at least 29 km long that persisted for ∼24 ka (Orem, 2010). The Lava Butte flow dammed the Deschutes River in Oregon creating Lake Benham, which persisted from ∼7 ky to ∼1.95 ky, extending >22 km upstream and covering ∼48 km^2 (Deligne et al., 2017). Damming of the McKenzie River in Oregon by the Clear Lake South lava ∼3 ky created Clear Lake, which is still present today (Deligne, 2012).

Lava dams may vary substantially in permeability, from impermeable dams that create large, long-lived upstream lakes to more permeable dams where water exploits cracks, lava tubes and pore space in tephra and cinder deposits inside or underneath the dam (Crow et al., 2008). Springs at the base of the downstream side of lava dams are common, even where impounded water is still present (e.g. Clear Lake; Deligne, 2012). Similar springs at the base of Benham Falls and Dillon Falls, Oregon show that the lava dam that created Lake Benham was also leaky (Deligne et al., 2017). Failure of lava dams have been variously interpreted from downstream deposits as the consequence of sudden, catastrophic outburst flooding (Fenton et al., 2006) or gradual overtopping and erosion (Crow et al., 2008).

Lava dam formation and failure has been studied by geomorphologists to understand the evolution of drainage systems, with little attention paid to the potential resulting hazards. Impounded water upstream of a lava dam has been recognized as a hazard (Scott et al., 1999), but disruption to water supplies downstream is not considered in volcanic hazard

assessments, despite the risk to agriculture, industry, hydroelectric power generation and drinking water (Deligne, 2012; Deligne et al., 2016).

Cooling effects of water on lava

Where the Holuhraun lava entered the Jökulsá á Fjöllum river, the cooling effect of the river water slowed the advance of the lava front by an order of magnitude, causing the lava to over-thicken at the flow front and eventually causing the main lava channel to overflow in several places (Pedersen et al., 2017). Similar overthickening is found where the Clear Lake East lava flow entered Clear Lake, creating a 25-m-thick flow-front that stops abruptly on a steep slope (Deligne, 2012).

Water cooling has been used to deliberately quench active lava flow fronts for the purpose of stalling and diverting lava flows, most notably during the 1973 eruption of Eldfell on Heimaey, Vestmannaeyjar, Iceland (Williams and Moore, 1983; Williams, 1997; Morgan, 2000). From February to July 1973, $\sim$56 km^3 of seawater was sprayed onto the lava front to try to save an important harbor, which housed Iceland's largest fishing fleet (Williams and Moore, 1983). Similar methods have since been attempted to divert lava flows from Mauna Loa and Kīlauea on Big Island, Hawai'i, but were unsuccessful (Williams, 1997).

Rootless Eruptions

Rootless eruptions are the result of explosive LWI. Deposits range from large scoriaceous cones of ash and lapilli, hundreds of metres in diameter with single or multiple central craters (Figure 1.2a; e.g. Thorarinsson, 1953; Fagents and Thordsarson, 2007; Hamilton et al., 2010a; Noguchi et al., 2016), to hornitos and small spatter cones, only a few metres wide (Figure 1.2d; Gao et al., 2013a and b). The majority of rootless eruptions happen on pāhoehoe lava flows in inland settings (lakes, rivers, wetlands), but they also occur in coastal settings on both pāhoehoe and 'a'ā lava flows, where the deposits are known as littoral cones (Moore and Ault, 1965; Fisher, 1968; Jurado-Chichaey et al., 1996; Mattox and Mangan, 1997).

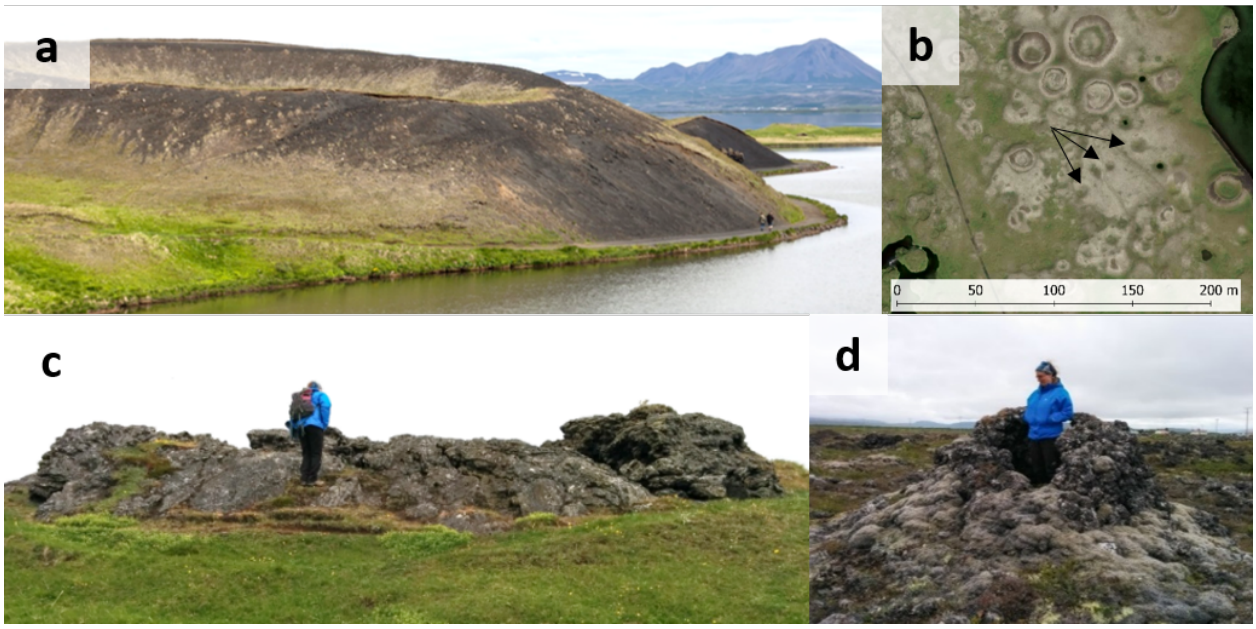

Figure 1.2: Different types of rootless cone and associated features. a) Scoriaceous rootless cone at Skútustaðir, Mývatn. Cone base is ∼100 m diameter. b) Explosion pits (marked with arrows) surrounding a scoriaceous rootless cone near Mývatn. c) Spatter cone at Mývatn. d) Hornito in Aðaldalur, NE Iceland. Map imagery on b ©2017 DigitalGlobe, Google

Previous studies have linked cone morphology and pyroclast type (ash, scoria or spatter) to the conditions of cones formation. In Iceland, the ratio between crater radius and outer flank radius of larger cones resemble tuff rings, whereas smaller cones are steeper and similar to cinder cones, suggesting a link between morphology and formation conditions (Greeley and Fagents, 2001; Fagents et al., 2002). Fagents et al. (2002) compared the morphology and grain size of different cone groups in Iceland and found that larger cones tended to be made of vesicular, angular lapilli, whereas smaller cones tended to be more spatter-rich, implying weaker fragmentation. Similarly, studies of littoral cones show that cones on flows fed by high lava fluxes tend to be larger and finer-grained than those where lava flux is lower. For example, littoral cones formed by high-flux 'a'ā flows can reach 450 m diameter and are typically composed of both coarse and fine ash (Moore and Ault, 1965; Fisher, 1968), whereas littoral cones on lower-flux pāhoehoe flows tend to be smaller (30–300 m diameter) and composed of lapilli and spatter clasts (Jurado-Chichay et al., 1996; Mattox and Mangan, 1997). The same dependence on flow rate is observed on the Nesjahraun lava flow at Thingvallavatn, a large lake in southwest Iceland (Figure 1.3). As the lava entered the lake it produced two rootless cones: Eldborg formed on a pāhoehoe lobe, is 150 m in diameter and constructed of layers of scoria with a 3 m cap of spatter; Grámelur, a pair of half-cones on an 'a'ā flow lobe, is 400 m long and made of coarse ash and angular lapilli

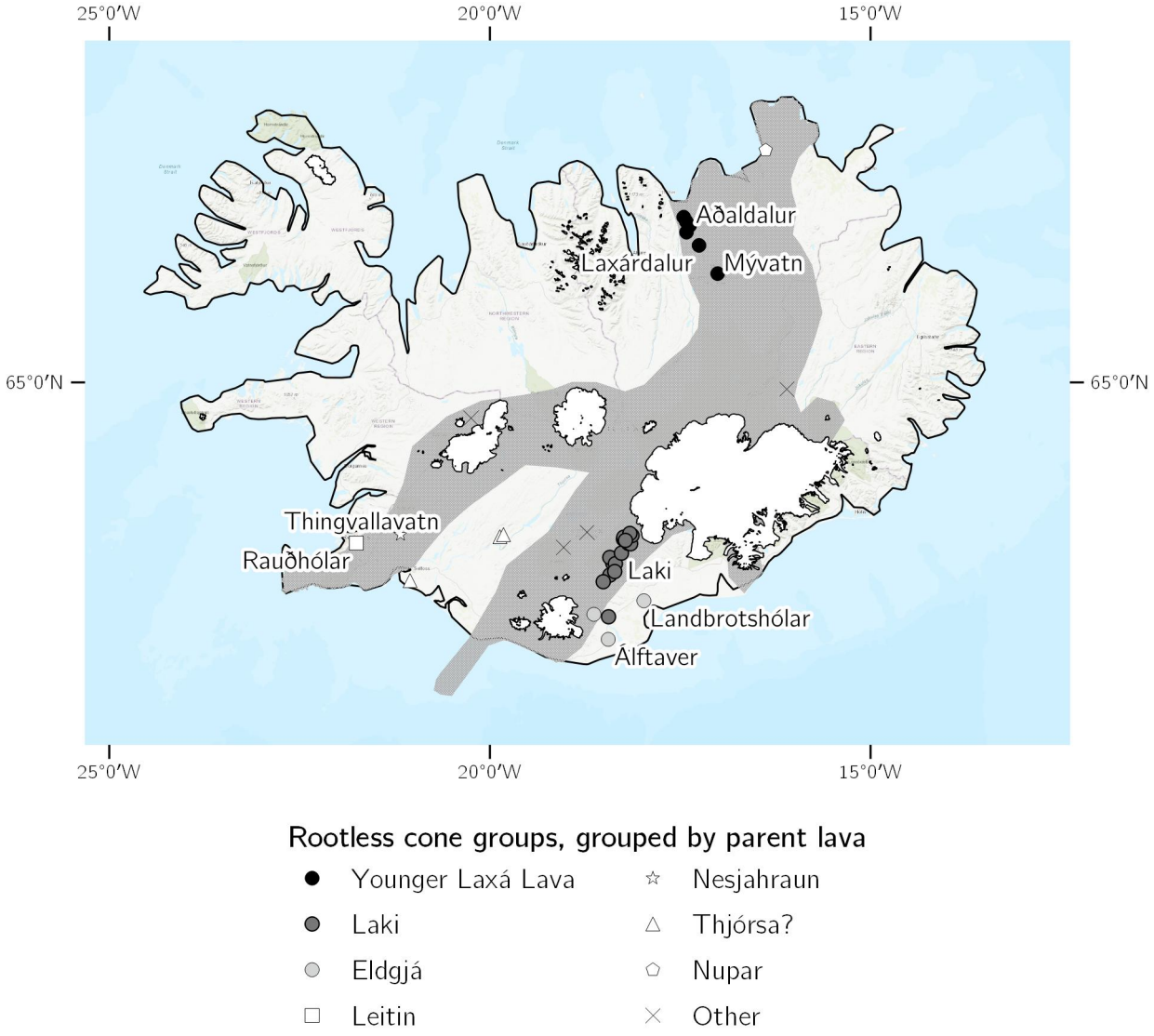

Figure 1.3: Map of rootless cone groups in Iceland. Hashed grey regions show Iceland's volcanic zones. White areas show icecaps and glaciers.

(Stevenson et al., 2012; Figure 1.4).

The morphology and spatial distribution of the cones is also affected by the mode of lava supply, with lava tubes, sheets and channels producing distinct patterns. For example, lava tubes and channels build cones (or half-cones) that follow the path of the tube or channel (Hamilton et al., 2010a). In contrast, rootless cones formed on sheet lobes tend to cluster into groups that may exhibit regular spacing (Bruno et al., 2004). This 'self-organization' can be explained by competition between neighboring cones for water supplies trapped in the underlying sediment (Hamilton et al., 2010b).

Rootless cone cross-sections reveal that deposits are often inversely graded with a cap of

Figure 1.4: Rootless cones formed when the Nesjahraun lava entered Lake Thingvallavatn. (1) Gramelur: a pair of half-cones formed on an 'a'ā portion of the lava flow, max. diameter 730m. (2) Eldborg: a scoriaceous rootless cone formed on the pāhoehoe part of the flow, max. diameter 155 m. Imagery from `https://map.is`, © Loftmyndir ehf. 2019.

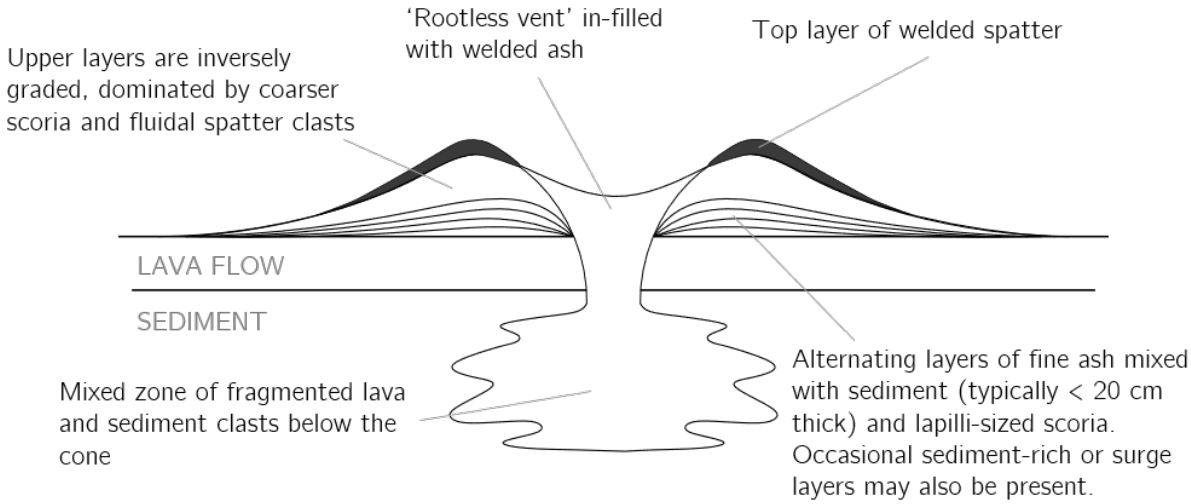

Figure 1.5: Schematic of a cross-section through a scoriaceous rootless cone. Cones are typically tens to hundreds of metres in diameter.

welded spatter (Thorarinsson, 1953; Fagents and Thordarson, 2007; Figure 1.5). They often contain layers, showing that large rootless edifices are built up over a series of repeated explosions at a single site, requiring a plentiful and continuous or pulsed supply of both lava and water to the eruption site (Hamilton et al., 2017; Fitch et al., 2017). The size and shape of pyroclasts depends on the fragmentation energy: small grain sizes require higher explosive energy than larger clasts and spatter (Sheridan and Wohletz, 1983; Zimanowski et al., 1997a; White and Valentine, 2016; Sumner et al., 2005). Therefore, the range in pyroclast types and sizes at rootless eruption sites, from very fine ash to welded spatter, shows that the dynamics of LWI can vary considerably. The presence of armoured bombs (tephra covered in outer layers of lava) in rootless cones also demonstrates that cones are formed over a series of discrete explosions (Reynolds et al., 2015; Noguchi et al., 2016). Some rootless cones also have multiple inner craters, interpreted to have formed during a separate, later phase of cone building driven by a recharge in water supply (Noguchi et al., 2016). Here, the outer flanks are made of loose scoria and ash, with slopes limited by the angle of repose ($\sim 33^{o}$). In contrast, the inner cones often have a higher proportion of welded material and steeper slopes. Noguchi et al. (2016) also found that smaller scoriaceous cones with caps of welded spatter had higher slope angles at the summit than lower down the flanks, as spatter is not limited by angle of repose. These outer layers of welded spatter are common and have been linked to waning energy in the final stages of rootless eruptions as the availability of either lava or water dwindles (e.g. Fagents and Thordarson, 2007).

The approximately symmetric shape and often sizeable edifices of surviving rootless cones show that they form on lava flows with a solid top crust capable of supporting tephra deposits, as tephra falling on a moving flow would be swept away rather than building up a cone (e.g. Fagents and Thordarson, 2007). However, the weight of the resulting edifice can be enough to deform and crack crusts, leaving cones on tilted platforms (Jaeger et al., 2010; Keszthelyi et al., 2010). The substantially-crusted lava confines any water trapped below it in pools or sediment which aids the build-up of pressure as it is heated by the lava (Fagents et al., 2002).

These previous studies show that cone morphology and grain size distribution are affected by a range of factors. The grain size distribution is controlled by the fragmentation energy, which depends on the interacting ratio of lava and water, and the degree of mingling. The size and shape of the edifice will ultimately be controlled by the supplies of lava and water that sustain the eruption and build up the cone in layers. However, while past studies have looked at cone morphology, they have often been focused on single sites; there has been no systematic quantitative comparisons of rootless cones across different sites to examine the effect of lava and water supply rates on cone size, morphology and LWI dynamics.

Rootless eruptions on snow and ice

While there are no surviving examples of rootless cones formed on snow or ice, rootless eruptions in these environments have been recorded on recent lava flows. Lava flows from the 2012–2013 eruption of Tolbachik interacted extensively with the underlying and surrounding snow and ice, depending on the flow rate and emplacement style: 'a'ā lava sat on top of the snow and pāhoehoe lava tended to flow in lobes under the snow (Edwards et al., 2015). While steam generation was generally limited, observation pits dug in front of the advancing flow showed that the snow ahead of the lava was saturated with flowing melt-water. Comparison of the calculated melt rate and Darcy flow of water through snow show that they are of the same order of magnitude, suggesting that the melt-water was able to move through the snowpack away from the lava as fast as it was generated (Edwards et al., 2015). However, there were sporadic rootless eruptions from this lava flow, all occurring on the 'a'ā parts of the flow. Edwards et al. (2015) speculated that these were caused by pockets of melt-water gathering in local depressions at the base of snowpack. As the overlying lava thickened, the weakened snowpack collapsed into slush, allowing direct contact between the hot fluid lava and meltwater, and generating steam. This is similar to littoral explosions triggered by the collapse of a lava bench, allowing hot lava to mix with sea water (Mattox and Mangan, 1997).

Figure 1.6: Photograph of an excavated rootless cone from the Rauðhólar group, near Reykjavík, Iceland. Different layers within the cone are denoted with dashed lines. Pen for scale.

While ash and lapilli were deposited around the Tolbachik eruption site, photographs of the plumes from these rootless eruptions show that they had a very high proportion of steam (see Figure 9 in Edwards et al., 2015). Similar rootless eruptions casued by lava interacting with snow were observed during the Fimmvörðuháls eruption in 2010 (Edwards et al., 2012) and on Mt Etna in March 2016 (Andronico et al., 2018).

1.2.1 Icelandic Rootless Cones

Rootless cones are particularly common in Iceland, forming on at least 8 different lava flows over the last 8500 years, due to the frequency of basaltic effusive eruptions and the wet environment (Figure 1.3; Fagents and Thordarson, 2007). One of the oldest exposed cone groups in Iceland is Rauðhólar, formed on the shore of Lake Elliðavatn near Reykjavík ∼4600 yBP (Thorarinsson, 1953; Fagents and Thordarson, 2007). These cones have been extensively quarried for building material, exposing the inner structure and allowing for detailed stratigraphic and morphometric studies (Figure 1.6; Hamilton et al., 2017; Fitch et al., 2017).

The most famous, and probably the most studied rootless cones, are around Lake Mývatn

Figure 1.7: Photograph of rootless cones in Lake Mývatn, NE Iceland. The hyaloclastite mountain Vindbelgjarfjall is visible in the background. For scale, the rootless cone in the centre of the photo has a basal diameter of ∼85 m.

in northeast Iceland (Figure 1.7; e.g. Thorarinsson, 1953; Einarsson, 1982; Noguchi et al., 2016). Thorarinsson (1953) was the first to establish that they were caused by LWI and were not primary craters. They formed when the Younger Laxá Lava inundated a large, shallow lake ∼2200 yBP (Höskuldsson et al., 2010). The same lava flow also created rootless cones as it flowed down the Laxárdalur gorge and out into the broad glacial valley of Aðaldalur (Thorarinsson, 1953). Despite their proximity to Mývatn, these cones have received far less attention. In total, the Younger Laxá Lava created >6600 rootless cones and hornitos, covering ∼38 km^2. Chapter 2 is a detailed case study of these cones and their formation.

More recently, the 939–940 AD Eldgjá fissure eruption created at least three groups of rootless cones in southern Iceland (Figure 1.3; Thorarinsson, 1953; Greeley and Fagents, 2001; Fagents and Thordarson, 2007). The largest group, Landbrotshólar, formed on a glacial outwash plain and consists of >4200 rootless cones spread across ∼50 km^2 (Figure 1.8). The nearby Álftaver group also formed on a glacial plain and have been heavily eroded by subsequent glacial floods (>540 cones over 3.8 km^2; Figure 1.9; Greeley and Fagents, 2001).

The 1783–1784 Laki fissure eruption created >2900 rootless cones, spread across 15 groups, predominantly in the boggy highlands near the fissure (Figures 1.3 and 1.10; Thordarson and

Figure 1.8: Photograph of Landbrotshólar rootless cones near Kirkjubæjarkaustur

Figure 1.9: Photograph of eroded rootless cones in Álftaver, S Iceland.

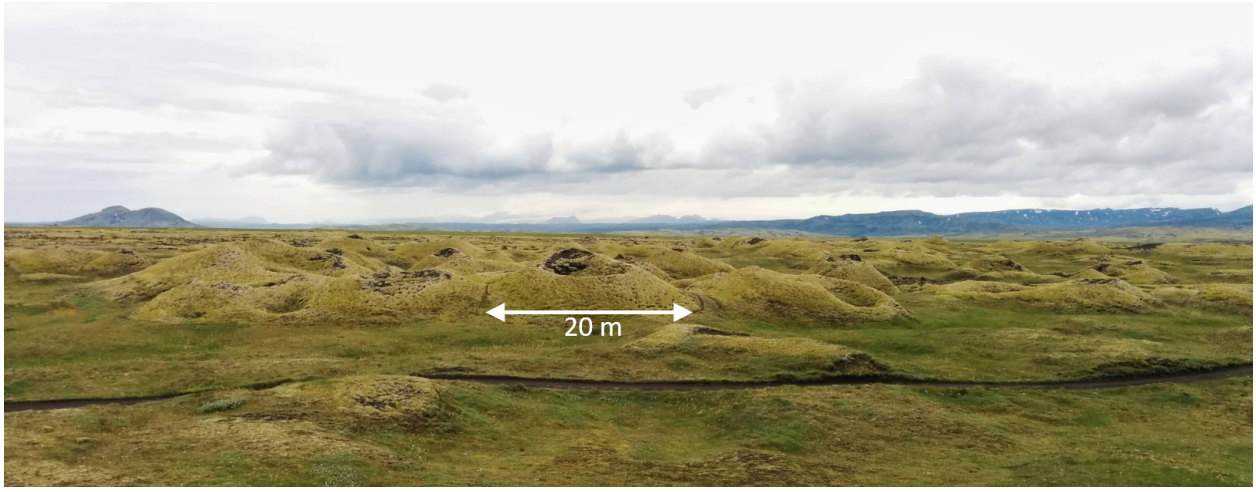

Figure 1.10: Photograph of the Hnúta rootless cone group near the Laki crater row, S Iceland.

Self, 1993; Thordarson et al., 1998; Thordarson et al., 2003; Guilbaud et al., 2005; Hamilton et al., 2010a and b). Of these groups, 13 had been identified in previous studies, but only three groups had been mapped or studied in detail (Thordarson et al., 1998; Bruno et al., 2004; Hamilton et al., 2010a and 2010b). I map and discuss the formation of all the Laki cone groups in Chapter 3.

There are numerous other groups of rootless cones around Iceland, mostly within Iceland's volcanic zones (Figure 1.3; Fagents and Thordarson, 2007), that have had little or no study, possibly because of difficulties with access or because the age of the cones means that they have been heavily eroded.

1.2.2 Models of rootless cone formation

Conceptual models of rootless cone formation have evolved as studies of rootless cones and associated deposits have improved our understanding of their physical properties. From his observations of rootless cones on the Younger Laxá Lava, Thorarinsson (1953) suggested that they were created by pockets of water trapped in cracks in the underlying Older Laxá Lava, which boiled and triggered explosions. After similar cone features were identified on Mars (e.g. Keszthelyi et al., 2010), Icelandic rootless cones were used as an analogue to understand more about LWI on Mars, where the thin atmosphere makes it difficult for liquid water to survive at the surface and most water is held in ice in the regolith (Greeley and Fagents, 2001; Fagents et al., 2002; Dundas and Keszthelyi, 2013).

Greeley and Fagents (2001) proposed a static heat transfer model, where an advancing lava

flow heats the substrate by conduction, boiling the liquid water or ice in the pore space (Figure 1.11i). The resulting vapour builds up until the pore pressure is greater than the weight of the overlying lava flow, at which point a rootless eruption occurs (Figure 1.11ii). Lava then fills in the crater, sealing it off, and pressure starts to build again Figure 1.11iii). Repeated cycles of pressure build-up, explosions, and crater-filling deposit debris on the lava flow surface, building a rootless cone. However, this conceptual model fails to explain some key physical aspects of excavated rootless cone deposits, including the presence of very fine ash that indicates high energy fragmentation, and the observed inverse grading within some cones from fine ash and lapilli to larger scoria, spatter and agglutinates (Fagents and Thordarson, 2007).

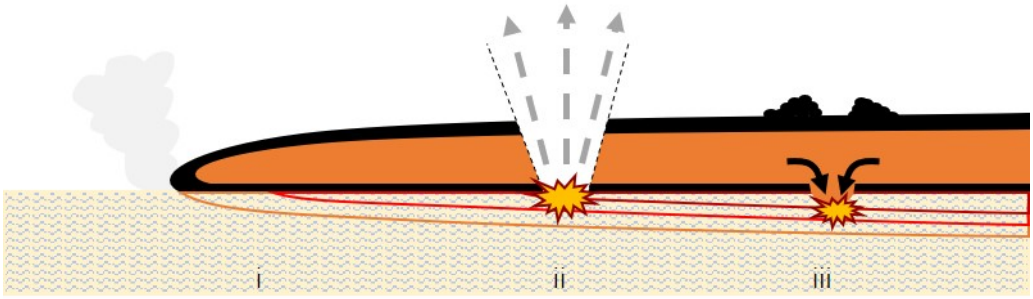

Figure 1.11: Conceptual model of conductive heat transfer triggering rootless eruption (after Fagents et al., 2002) i. Lava advances over a wet or frozen substrate, boiling the water in the pore space. ii. When the pore pressure exceeds the confining pressure of the lava flow, it triggers a rootless eruption that breaks through the lava flow. iii. Lava fills in the excavated hold in the sediment, creating more steam and allowing the pressure to rise. Repeating cycles of steam generation and explosion deposit debris on the lava flow surface and build a rootless cone.

The finest ash in scoriaceous rootless cones (3.5–4 ϕ; 88–62 µm) is commonly attributed to a highly explosive form of steam eruption known as a molten fuel–coolant interaction (MFCI; Zimanowski et al., 1997b; Fagents and Thordarson, 2007; Hamilton et al., 2017; Fitch et al., 2017;). In MFCI, intimate mingling between water (or wet sediment) and melt creates a very high contact surface area (Figure 1.12i). Trapped pockets of water first experience stable film boiling; the vapour film insulates the liquid water from the melt, known as the Leidenfrost effect. If the vapour film breaks down, generally due to an outside shock, the rate of heat transfer increases dramatically, quenching and fracturing the melt surface (Figure 1.12ii) and creating supercritical steam, which expands (Figure 1.12iii). Melt fragmentation further increases the surface area of the melt-water interface, increasing the heat transfer rate and causing further fragmentation and expansion. This sets up a self-sustaining explosive cycle that continues until either the water or melt runs out. MFCI is assumed to be the explosive mechanism in larger scale hydrovolcanism (e.g. Wohletz et al., 2013). The grain size

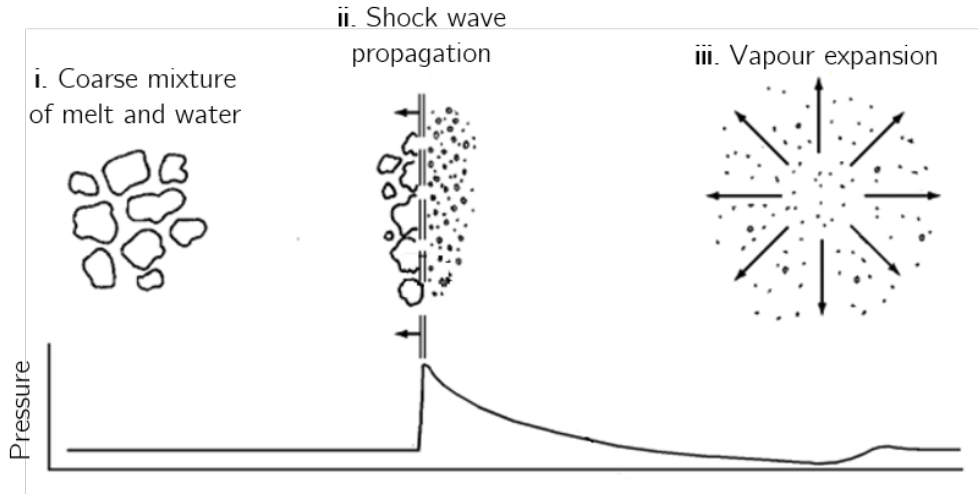

Figure 1.12: Stages of molten fuel–coolant interaction (MFCI). Adapted from Wohletz et al. (2013).

distribution is controlled by the kinetic energy release, which is controlled by the mass ratio of interacting lava and water (Sheridan and Wohletz, 1983). This depends on the contact surface area between lava and water over which heat transfer takes place, and a degree of pre-explosion mingling between the two fluids is generally required to reach sufficient heat transfer rates to initiate an explosion. It is important to note that the interacting lava–water mass ratio may be different from the total ratio of lava and water in the wider environment, and explosions can occur in apparently sub-optimal conditions (White and Valentine, 2016).

MFCI is the basis for a proposed a dynamic heat transfer model of rootless cone formation, where hot, fluid lava mingles with wet sediment to create the required pre-mix (Fagents and Thordarson, 2007). Fagents and Thordarson (2007) proposed that gravity-driven mixing of fluid lava and sediment could create the necessary pre-mix for MFCI. Specifically, they suggest that a lava flow could sink into soft, wet sediment, bending and cracking the brittle basal crust of the flow, and allowing the hot, fluid lava from the flow interior to mingle with the sediment below (Figure 1.13). The resulting explosion both generates the fine ash seen in rootless cones and fragments the surrounding lava to form coarser ash and lapilli, all of which are deposited around the eruption site. The bulk of the mass of rootless scoria cones is built of lava that is not active in MFCI (Hamilton et al., 2017; Fitch et al, 2017). While only the finest particles are created at the 'active' lava-water interface in a MFCI, the energy released by the explosion will also affect the fragmentation of other lava it passes through, thereby indirectly controlling the grain size distribution of the rest of the deposit. Rootless tephra exhibit a mix of fluidal, blocky and 'mossy' (highly irregular surfaces made of a fine network of deformed void walls and protrusions, as defined by Fitch et al., 2017)

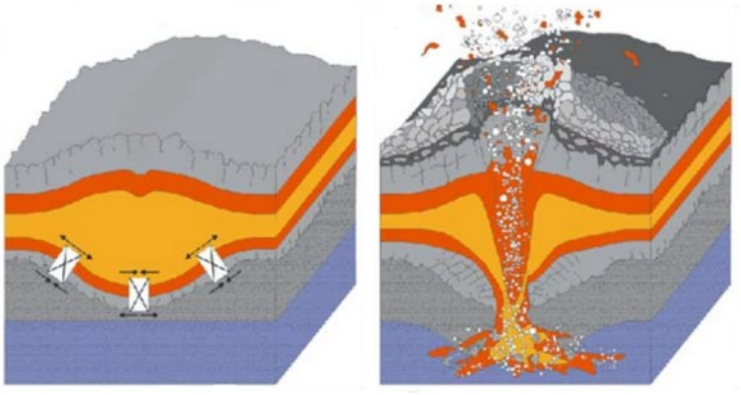

Figure 1.13: Conceptual model for triggering mixing between lava and wet sediment through bending and failure of lava basal crust. From Hamilton et al. (2010a)

morphologies that are comparable to those in Hawai'ian or Strombolian scoria cones (Walker and Croasdale, 1971, Hamilton et al., 2017). Repeated cycles of MFCI, separated by periods of ground-water recharge, explain the presence of very fine ash and inversely graded layers within rootless cones (Hamilton et al., 2017). Later stages of cone building are attributed to fire-fountaining and lower energy explosions as the water in the sediment is depleted, explaining the upper layers of fluidal spatter and agglutinate (Hamilton et al., 2017).

However, to sustain the necessary heat transfer rates to initiate an explosion, MFCI requires a significant starting contact surface area between the melt and the water, and creation of new contact area at a rate of $\sim$1 $m^2/m^3/s$ of melt and water (Austin-Erickson et al., 2008). Mingling may be hydrodynamic, or driven by brittle fragmentation (Austin-Erickson et al., 2008; Wohletz et al., 2013; White and Valentine, 2016), and laboratory experiments have successfully recreated MFCI and fine ash comparable to deposits from phreatomagmatic and rootless cone deposits (Büttner et al., 1999; Büttner et al., 2002; Büttner et al., 2006; Fitch et al., 2017), though these do no account for the role of bubbles in melt fragmentation (Liu et al., 2017). These experiments that inject water into melt have used an external trigger (such as a hammer blow or impact from a falling object) to initiate an explosion, though some explosions happen spontaneously. Additionally, analogue experiments that mix fluids with density and viscosity ratios similar to melt and water or water-sediment slurries have shown that hydrodynamic mingling is only effective at high relative flows rates (>10 m/s); experiments with silicate melt showed no significant mixing at injection rates of $\sim$4 m/s (Zimanowski et al., 1997; Zimanowski and Büttner, 2002). These experiments also used melts with viscosities three to four orders of magnitude lower than erupted basaltic lavas.

In natural settings, hydrodynamic mingling between melt and wet sediment is identified in the distinctive textures of peperites, which can form at the interface between an intruded

magma body or lava flow and a wet unconsolidated sediment (e.g. Zimanowski and Büttner, 2002; Skilling et al., 2002). Juvenile clasts in peperites exhibit a range of textures from blocky to fluidal, depending on the relative flow rates, density contrast, degree of sediment fluidization, autobrecciation, melt quenching, and steam explosions that occur at the interface (Skilling et al., 2002). The role of sediment in this process is important, as water is both less dense and less viscous than lava, so free-flowing water and lava do not readily mingle. Liquified sediment slurries are much closer in density and viscosity to lava, which may allow them to mingle more readily with silicic melts (White, 1996). However, no modelling has been carried out to assess whether gravity-driven mingling would create the relative flow rates or surface area between the two fluids required for efficient mixing. The mechanism for creating a viable pre-explosion mixture of lava and wet sediment in a natural setting remains unclear. Similarly, while the effects of sediment permeability and porosity are well documented for perperite formation (e.g. Skilling et al., 2002), they have not been considered in the context of rootless cone formation.

Importantly, the recent focus on MCFI has meant that the static heat transfer model has been discounted as a mechanism for sustaining rootless eruptions and building rootless cones, primarily because it does not explain the very fine ash fraction, inverse grading, or internal layering seen in some rootless cones (e.g. Fagents and Thordarson, 2007). However, the dynamic model is also unable to explain the full range of rootless eruption deposits. Hornitos and spatter cones have no fine ash or internal layering, being constructed entirely from welded spatter, suggesting that MFCI is not involved in their formation. Observations from Hawai'ian lava flows show that rootless features formed predominantly or entirely of spatter (spatter cones and hornitos) are built through low-energy bubble bursts or the escape of pressurised lava and gas from a lava tube (Mattox and Mangan, 1997; Kauahikaua et al., 2003).

1.3 Key Questions

Broad questions remain about the secondary hazards created by LWI, and the conditions under which they occur. Understanding whether an eruption will lead to passive or explosive LWI, and where and how rootless eruptions are triggered, is crucial for assessing the hazards posed by LWI in future eruptions. The key questions that I address in this thesis are:

1. What is the range of hazardous LWI that should be considered for future eruptions, and under what circumstances are they most likely to occur?

2. What is the role of lava flow emplacement style and local lava flux in triggering rootless eruptions and controlling the eruption style?

3. How does local environment (sediment type, topography, hydrology) affect the likelihood and dynamics of rootless eruptions?

1.4 Thesis overview

This thesis consists of two published papers and an unpublished chapter, followed by a synthesis and outline of further work. Below are brief descriptions of each chapter and how they fit with the key themes/questions noted above.

1.4.1 Chapter 2: Linking lava flow morphology, water availability and rootless cone formation on the Younger Laxá Lava, NE Iceland

This chapter is a case study of rootless cones on the Younger Laxá Lava (YLL) in NE Iceland, published in the Journal of Volcanology and Geothermal Research (Boreham et al., 2018). It describes and assesses the >6,500 rootless cones formed when a single lava flow inundated a large, shallow lake (Mývatn), dammed and flowed down a narrow river valley (Laxárdalur), and then spread across a broad glacial valley containing rivers and wetlands (Aðaldalur). I combine field observations of these different environments and their associated rootless cones with morphological analysis of high resolution digital terrain models (DTMs) and satellite photographs, to categorise, map and measure all of the rootless cones on the YLL. I then use these data to assess how rootless cone type and size are affected by the environment in which they formed and the local lava flux.

I find that the type and size of rootless cones formed reflects the availability of water and the local lava flux. The large, multi-cratered scoriaceous rootless cones around Mývatn are the product of large, high-energy rootless eruptions driven by the high availability of water in the diatomaceous lake sediments and relatively high, continuous lava supply from the nearby fissure. The extent of rootless cones around the present-day Mývatn reflects the extent of the pre-YLL lake, with smaller rootless cones formed around the lake edges where there was less water available. In contrast, I found that in Laxárdalur, where the YLL had dammed and completely dried up the river Laxá, rootless cones were limited to areas where small

tributaries carried melt-water and precipitation off the surrounding highlands. Cones were widespread across Aðaldalur in areas where there is evidence for small lakes and ponds, and where the YLL dammed and impounded water from the Reykjadalsá river. However, these cones were significantly smaller than those around Mývatn, reflecting the lower water availability. Cones around the edges of the lava flow and along a preserved inflation front were also significantly smaller due to the lower local lava flux. Beyond the inflation front, I mapped an extensive area containing several thousand hornitos, and suggest that they formed by low energy bubble-burst type events caused by volatiles boiling and escaping from the underlying wetland sediment.

1.4.2 Chapter 3: Hazards from lava–river interactions during the 1783–1784 Laki fissure eruption

This chapter examines LWI during the 1783–1784 Laki fissure eruption in southern Iceland, the only historically documented eruption to form abundant, surviving rootless cones. It is published in GSA Bulletin (Boreham et al., 2020). I analyse contemporary eyewitness accounts of the eruption to assess how the lava interacted with the local topography and hydrology. Alongside this, I used the morphological and spatial analysis techniques developed in Chapter 2 to map, measure and assess the numerous Laki rootless cone groups. I combine these two datasets to build a timeline of LWI during the eruption and the hazards it created for local residents. I find that the lava dammed two large rivers and numerous smaller tributaries, impounding water that flooded farms and impeded travel in the region. Lava inundating wetlands and interacting with impounded water created at least 2979 rootless cones across the lava field. Using major element geochemistry, we show that a group of rootless cones previously attributed to the 939–940 Edlgjá eruption was actually built by the Laki eruption. My findings demonstrate the broad range of secondary hazards that can be caused by LWI. Based on these findings, I make recommendations for assessing LWI hazard in future eruptions and using remote sensing techniques to facilitate these assessments and identify LWI deposits in past lava flows.

1.4.3 Chapter 4: Numerical modelling of pore fluid evolution in wet sediments heated by lava, with application to triggering rootless eruptions

This chapter focuses on the role of wet sediment in triggering, and potentially sustaining, rootless eruptions. I use numerical modelling to assess the effects of sediment physical and thermal properties on heat transfer, steam generation and pressure build up in saturated sediment underneath a lava flow. From these models, I find that heat conduction from a lava flow to a saturated moderate-to-high permeability sediment (e.g. sand, peat, loam, sandy clay) could create pore pressures high enough overcome the confining weight of the overlying lava flow and strength of the lava flow crust, triggering a rootless eruptions metres to tens of metres behind the lava flow front. I find that pressure builds up faster in lower permeability sediments, where fluid flow, and therefore steam escape, are much slower. In low and very low permeability sediments (e.g. silt, clay, ooze), pore pressure in the subsurface builds up fast enough to drive steam explosions at the lava front, likely disrupting the advance of the lava flow. Higher porosity increases pressure build-up, as there is more water per unit volume of sediment, and therefore a greater volume of steam is generated. However, the energy released by these initial steam explosions is relatively low, and perhaps insufficient to excavate the entire thickness of the overlying lava flow. I suggest a hybrid conceptual model of rootless cone formation for moderate-to-high permeability sediments: pore pressure build-up triggers an initial steam explosion, which injects wet sediment into the hot, fluid interior of the lava flow, creating the pre-mix of lava and wet sediment necessary to initiate a more energetic rootless eruption and sustained rootless cone building. In contrast, I suggest that small, spatter-dominated rootless eruption deposits, such as hornitos and rootless spatter cones, could be the product of repeated cycles of pore pressure build-up and steam escape, without triggering a MFCI.

1.4.4 Chapter 5: Conclusion

The concluding chapter brings together the findings from the three core chapters to address the questions set out in this Introduction. It examines the range of environments in which LWIs occur and the resulting deposits, relating them to the roles of sediment and lava flux in rootless eruption dynamics. Based on this, I comment on the implications for future hazard assessments. I also discuss remaining open questions about rootless cone formation, and suggested areas for further investigation.

Chapter 2

Linking lava flow morphology, water availability and rootless cone formation on the Younger Laxá Lava, NE Iceland

Author contributions and declaration: This chapter is based on a paper that has been published in the Journal of Volcanology and Geothermal Research: Boreham, F., Cashman, K.V., Rust, A. and Höskuldsson, Á, 2018. Linking lava flow morphology, water availability and rootless cone formation on the Younger Laxá Lava, NE Iceland, *Journal of Volcanology and Geothermal Research*, 364, pp. 1–19. The paper has been edited to make it flow better as part of a single thesis. Some of the Background sections of the paper have been moved to the thesis Introduction. Additionally, some of the supplementary material and figures from the original paper have been incorporated into this chapter. Initial field investigations were carried out by Frances Boreham, Kathy Cashman, Alison Rust and Ármann Höskuldsson in July 2015, including collecting samples, and photographing and locating different rootless cone types. Frances Boreham did follow-up fieldwork in July 2016, collecting further samples and conducting unmanned aerial system (UAS) surveys of selected rootless cone groups, helped by Jennifer Saxby. Tom Richardson of the University of Bristol School of Engineering provided the UAS used in this study. Frances Boreham created high resolution digital terrain models of the selected rootless cones from the drone survey data. Other digital terrain models were provided by the Polar Geospatial Center under NSF OPP awards 1043681, 1559691 and 1542736. All digitising, measuring and categorising of rootless cones in this

study was done by Frances Boreham. Spatial and statistical analysis of the cones and lava flow morphology was done by Frances Boreham, with statistics advice from Bob Myhill and Isabel Wilson. Hannah Buckland measured the major element composition of the tephra samples, which Frances Boreham used to calculate the lava flow emplacement temperatures. Frances Boreham wrote the manuscript, incorporating comments and feedback from Kathy Cashman, Alison Rust and Ármann Höskuldsson. Christopher Hamilton and one anonymous reviewer provided thorough and constructive comments that greatly improved the paper.

Supplementary figures and tables for this chapter are included in Appendix A. Additional supplementary data and files can be found in the University of Bristol data repository at: `https://data.bris.ac.uk/data/dataset/ojcw17r060lu21o7lbjeoftbf`.

Abstract

It is well established that rootless cones and associated deposits are the result of explosive interactions between lava flows and environmental water, but there is substantial uncertainty about the dynamics of rootless eruptions, particularly the relative importance of lava supply, water availability and the conditions under which they meet. Here we present a case study of the Younger Laxá Lava in NE Iceland, and the >6500 rootless cones that it created. Critically, this long (63 km) lava flow interacted with water along its length, from flow through/around a large lake (Mývatn), down a narrow river gorge (Laxárdalur) and across a broad glacial valley with wetlands and rivers (Aðaldalur). Using high-resolution digital terrain models and aerial photographs, we map the flow surface morphology, and classify, measure and analyse the rootless cone type, size and spatial distribution in the context of both lava and water availability. We find that rootless cone size is controlled by the combined availability of lava and water: large rootless cones require sustained, high volumes of lava (related to proximity to vent) and water (e.g., Lake Mývatn), whereas limited supplies of lava with distance (from the vent and from the centre of the flow) and water (particularly in dammed river valleys) build smaller cones. Where we infer that water was distributed in sediment, the lava–water interaction style changed to low-energy and distributed bubble bursts that created >3000 hornitos in the lower reaches of Aðaldalur. The distribution of rootless cones around Mývatn also defines the pre-eruption extent of the lake and suggests substantial lake level changes during the course of the eruption. By looking at the variation in rootless cone type and size in the context of the parent lava flow and the local environment, we explain how the availability of water and local mass flow rate of lava affect the dynamics of rootless eruptions.

Highlights:

- Environmental conditions and lava supply affect the type and size of rootless cones formed
- Rootless cone distribution reflects the available water at the time of lava emplacement
- Large cones require sustained supplies of lava and water e.g. near Lake Mývatn
- Limited lava and water supplies build smaller cones e.g. on flow margins
- Reduced supply of lava and water leads to low-energy bubble bursts, creating hornitos
- Cones show pre-eruption extent of Mývatn and imply syn-eruptive lake level change

2.1 Introduction

The dynamics of lava–water interactions (LWI) and the type of deposits they produce are affected by the lava flow properties, available water and the degree of mingling between the two (e.g. Fagents and Thordarson, 2007). However, there is still substantial uncertainty around the role of each variable and how it affects the morphology, deposit type (dominantly ash, scoria or spatter) and spacing of rootless cones. In this chapter we examine the morphology of the Younger Laxá Lava (YLL) in NE Iceland and the thousands of rootless cones it created as it flowed from its source east of Lake Mývatn, through the Laxárdalur gorge and into the glacial U-shaped valley of Aðaldalur (Figure 2.1). We also present a detailed description and analysis of the cones in Laxárdalur and Aðaldalur. The YLL is a particularly good case study because it created a variety of rootless eruption features (scoria cones, spatter cones and hornitos) as it interacted with different water sources (lakes rivers, wetlands). Our goal is to link the lava emplacement style, its response to, and modification of, the local environment and available water, and the variation in size and type of rootless cone. This will allow us to better understand the factors that control rootless cone formation, interpret deposits on Earth and Mars, and inform hazard assessments for future lava flows in water-rich environments.

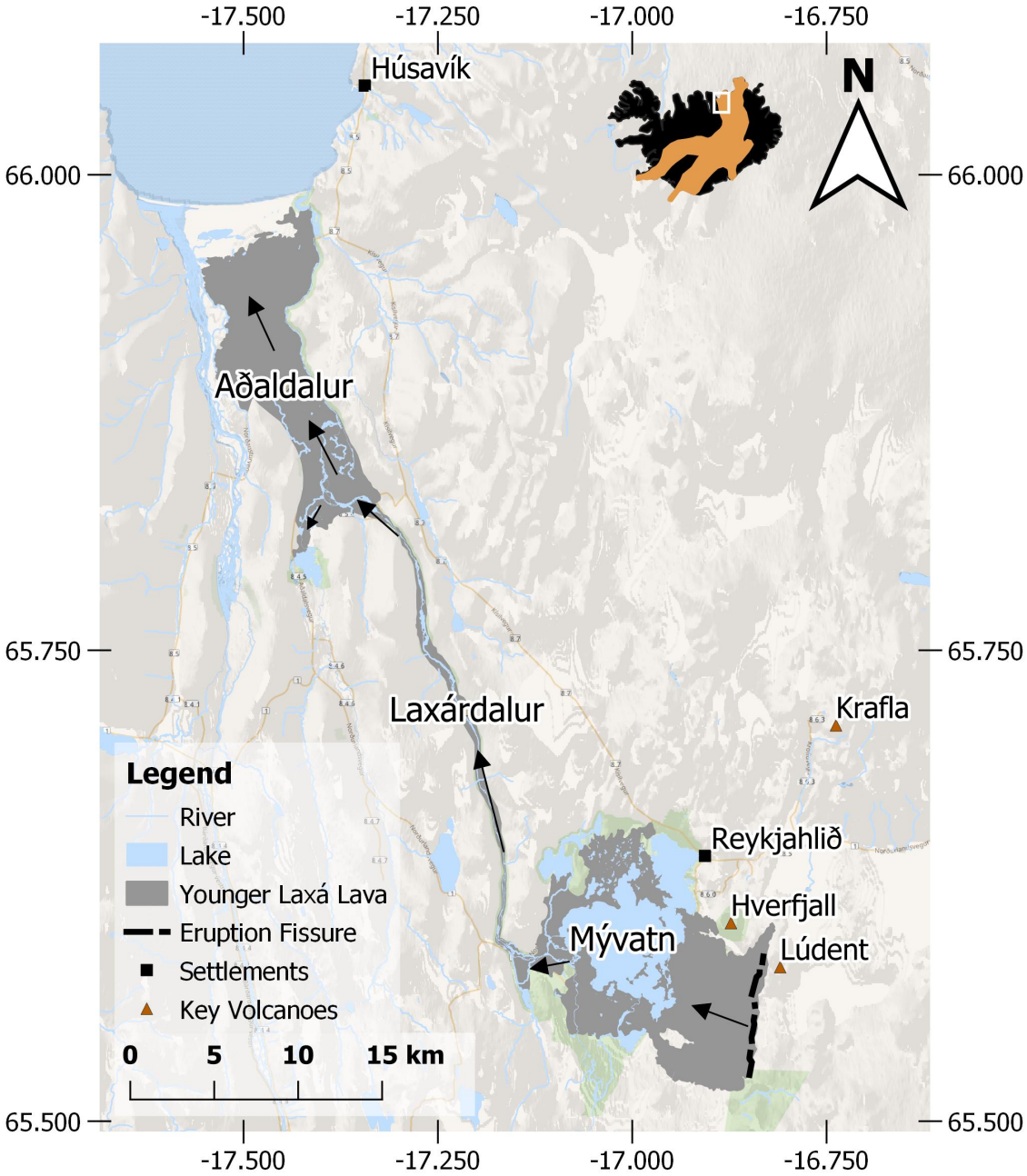

Figure 2.1: View of the Mývatn, Laxárdalur and Aðaldalur region. The extent of the Younger Laxá Lava is shown in grey. Lakes, rivers and the Greenland sea are shown in blue. Key local volcanic centres are shown by orange triangles. Nearby settlements are shown with black squares. Green areas represent conservation areas or national parks. Black arrows show the direction of lava flow from vent to lava flow front. Inset: The island of Iceland. Volcanic zones are shown in orange. The extent of the main map is shown with a white box.

2.2 Background

2.2.1 Geological and hydrological setting

Lake Mývatn lies in Iceland's Northern Volcanic Zone ∼50 km east of Akureyri, the largest city in northern Iceland, and (Figure 2.1). It is a shallow eutrophic lake and Iceland's fourth-largest lake, ∼10 km long and 7.5 km wide, covering an area of 37 km^2 (Einarsson et al., 2004). The surface elevation of the lake is 277 m asl. The northern edge of the lake, near the village of Reykjahlið, is marked by the end of the lava flow from the 1724–1729 eruption of Krafla, known as the Mývatn Fires (Einarsson, 1982). The landscape to the east of Mývatn is dominated by a phreatomagmatic tuff cone, Hverfjall, and associated deposits (Figures 2.1 and 2.2), formed by the Hverfjall Fires eruptive episode ∼2500 yBP when a propagating dike encountered the active ground water system (Mattsson and Höskuldsson, 2011; Liu et al., 2017). The basin of the pre-YLL lake Mývatn was formed by the Older Laxá Lava (OLL), which erupted ∼3800 yBP from a shield volcano 25 km south of Mývatn (Einarsson, 1982). This lava flow underlies the YLL at Mývatn and throughout the Laxá gorge; drilling during the construction of a hydro-electric power station at the end of the gorge showed that the OLL was ∼20 m thick, ∼600 m from the start of Aðaldalur (Thorarinsson, 1951). There are no known outcrops of the OLL in Aðaldalur.

The YLL erupted 2180 ±34 yBP from the Threngslaborgir–Lúdentsborgir crater row, which lies 5 km to the east of present-day Mývatn (Figures 2.1 and 2.2; Höskuldsson et al., 2010). The vast majority of the YLL flowed west towards Mývatn, and created a complex of lava pillars, collapse slabs and lava tubes known as Dimmuborgir (meaning 'dark castles'), which has been interpreted as the remains of shield complex that formed when the YLL stalled, ponded and then drained in stages into the lake (Skelton et al., 2016; Figure 2.2). As Dimmuborgir drained and the eruption continued, the YLL inundated and interacted explosively with a pre-existing lake to create the famous Mývatn rootless cones (Thorarinsson, 1953). Skelton et al. (2016) estimated that lava discharge rates of 0.7–7 m^3/s from Dimmuborgir that were sustained over days to weeks through a network of drainage channels, providing a continuous supply of lava to the eastern shore of Mývatn.

After inundanting the lake and surrounding areas, the YLL followed the pre-existing course of the River Laxá through the narrow Laxárdalur gorge (Figure 2.1) and created several small groups of rootless cones. After ∼30 km, Laxárdalur opens into a flat plain called Aðaldalur, where it merges with the Reykjadalur valley to the west (Figure 2.3). The YLL spread out across the full width of Aðaldalur backed up ∼2 km into the Reykjadalur, creating

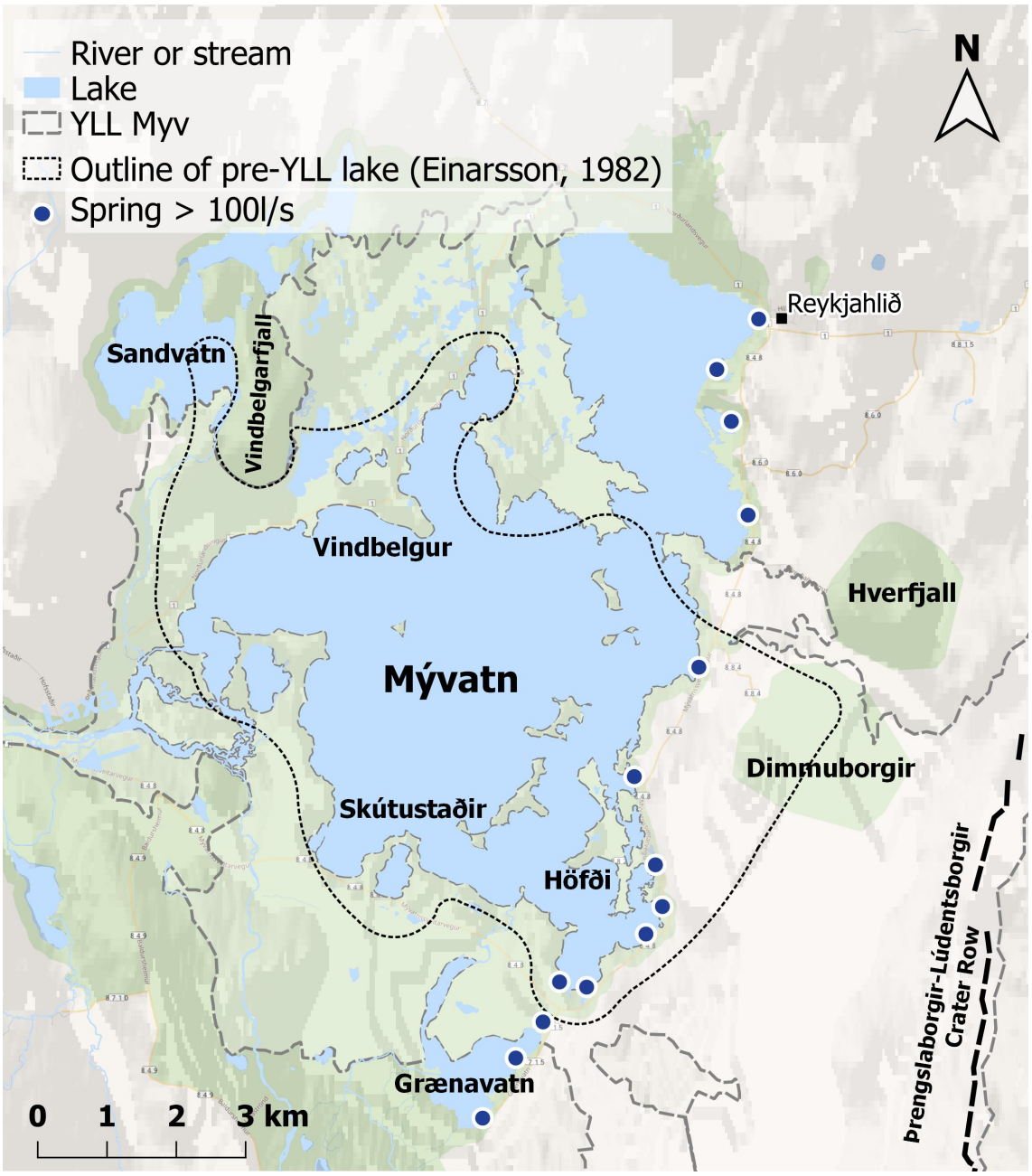

Figure 2.2: Map of Mývatn area showing the major landscape features and hydrology. The extent of the YLL is shown by a dashed grey line. The eruption fissure is marked with a black dashed line. The outline of the pre-existing lake, as drawn by Einarsson (1982) is shown with a dotted black line. Green areas represent conservation areas or national parks. Blue circles indicate the position of springs feeding the lake.

more rootless cone groups across the valley. Early studies attributed the rootless cones in Aðaldalur to the OLL (Jakobsson, 1963), but they were later shown to be from the YLL (Thorarinsson, 1979; Sæmundsson et al., 2012). The lava flow then progressed a further 18 km north down the valley, towards the Greenland Sea, but did not reach the coastline.

In total, the eruption produced 3.7 km^3 of lava with an average thickness of ∼17 m and covered an area of 220 km^2, travelling 63 km from the fissure (Höskuldsson et al., 2010). To put it into perspective, this makes the YLL an order of magnitude larger than the 1984 Mauna Loa eruption in Hawai'i, and over twice the volume and nearly three times the area of the 2014 Holuhraun eruption from Barðabunga in Iceland (Cashman and Mangan, 2014; Pedersen et al., 2017).

The YLL modified the extent and depth of lake Mývatn and forms the basin of the present-day lake. Analysis of the diatom layers shows that the lake took up to 700 years to recover and stabilise (Einarsson et al., 1988). Preserved diatoms in rootless cone tephra from around the lake show that it was originally larger and deeper than present day (Einrarsson, 1982). Based on these diatoms and the rootless cone distribution, Einarsson (1982) proposed a minimum extent of the original lake that, in places, extends >1 km inland from the current lake shore (Figure 2.2). The ground around the cones and away from the lake is water-logged, with numerous small ponds, streams and wetland areas that make the region one of the Europe's largest breeding sites for water birds.

Today, the hydrological system in the region is dominated by Mývatn and the Laxá river, with smaller inputs from other rivers and streams. The cold and warm springs on the eastern shore of Mývatn provide a plentiful and steady supply of water to the lake at 32–33 m^3/s in total, 44 % of which comes from the springs near Höfði (Einarsson et al., 2004; Figure 2.2). This inflow is balanced by outflow to the Laxá, which drains from the south-west corner of the lake and then flows north through the narrow Laxá gorge (Laxárdalur) and the glacial U-shaped valley of Aðaldalur (Figure 2.3) before draining into the Greenland Sea. As it flows through Laxárdalur, the Laxá is fed by small drainage streams off the surrounding highlands, which fluctuate seasonally with snowmelt.

The Reykjadalsá river, which flows through Reykjadalur and then merges with the Laxá in Aðaldalur, is substantially smaller than the Laxá because it drains the highlands west of Mývatn where there is a lower groundwater flow (Figure 2.3; Einarsson et al., 2004). Just before it joins the Laxá, the Reykjadalsá moves through an area of small lakes and wetlands. Similar but smaller ponds, providing contained but limited sources of water, are found throughout Aðaldalur. Half-way down, Aðaldalur merges with the adjacent valley of

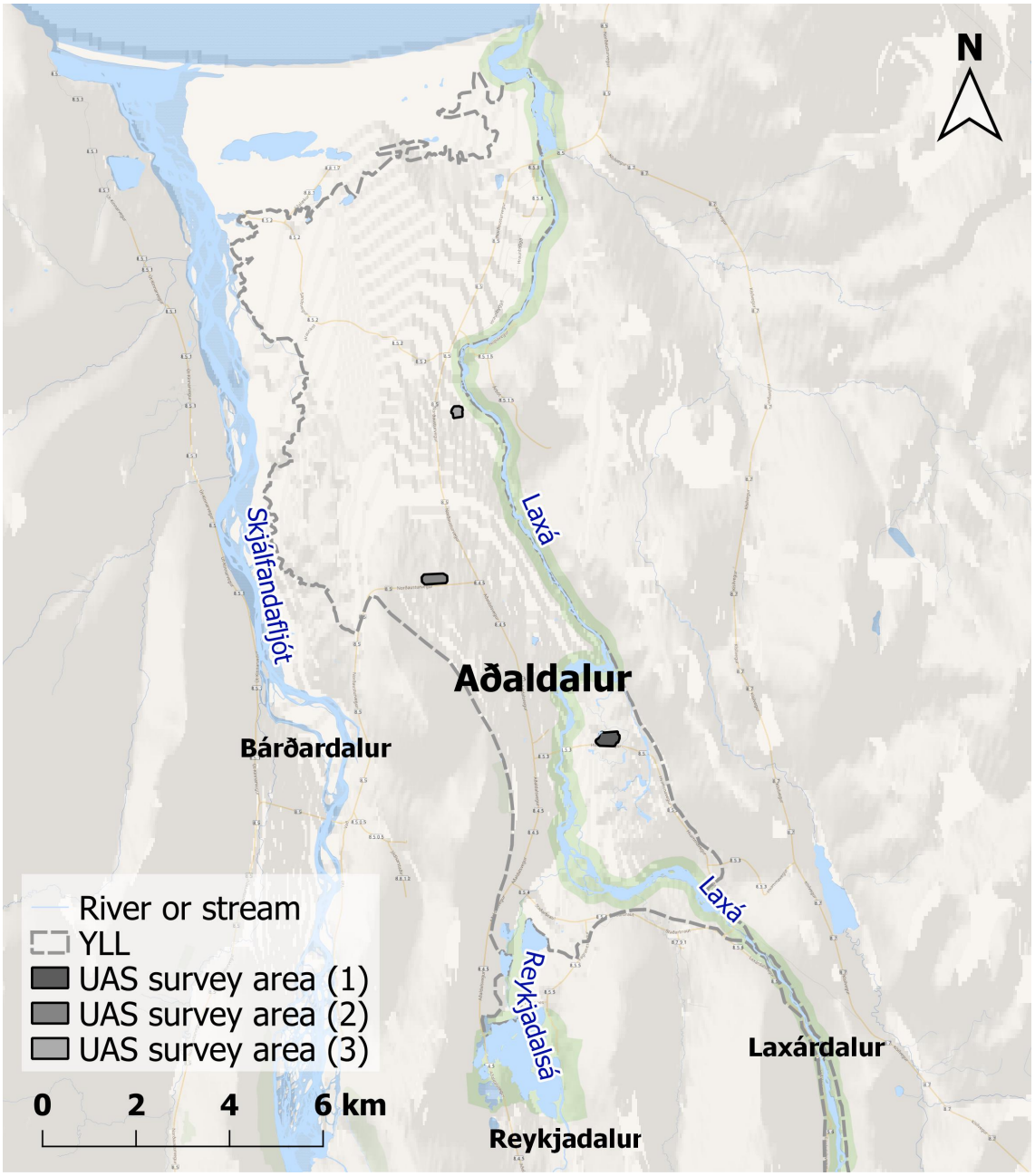

Figure 2.3: Overview of Aðaldalur and the surrounding valleys, showing the different rivers in relation to one another and the Younger Laxá lava. Lava entered the southern end of Aðaldalur from Laxárdalur and flowed north towards the Greenland Sea.

Bárðardalur, to the west (Figure 2.3). The river Skjálfandafljót, fed through Bárðardalur and travelling along the western side of Aðaldalur, is a shallow braided river with numerous banks and islands, and a bed >800 m wide. In contrast, the Laxá is confined to the eastern edge of the valley by the YLL and is deeper and narrower (<100 m wide) than the Skjálfandafljót, confined to a single channel with only a few small islands. The northern end of the valley is covered by the YLL, where the lava surface is broken and heavily vegetated.

Lake Mývatn, the groundwater system feeding it and the Laxá and Reykjadalsá rivers all pre-date the YLL. The remains of birch trees immediately under the YLL in Aðaldalur and in the northern basin of Mývatn suggests that the climate at the time of the eruption was comparable to present-day (Hauptfleisch and Einarsson, 2012). The similar hydrology and climate mean that the range of environments and water sources in the region today are likely to be very similar to those encountered by the YLL.

2.3 Methods

2.3.1 Rootless Cone Types

We have divided the rootless cones in the study area into seven classes based on size, shape and pyroclast type (i.e. ash, scoria or spatter): single-cratered scoriaceous rootless cones (S; Figure 2.4a), double-cratered scoriaceous cones (D), multi-cratered or 'lotus-fruit' cones (L), spatter cones (SP; Figure 2.4c), hornitos (H; Figure 2.4d) and explosion pits (P; Figure 2.4b). These classifications are consistent with previous studies of rootless deposits. Any cones we were not able to categorise with certainty are referred to as 'unclassified' (U).

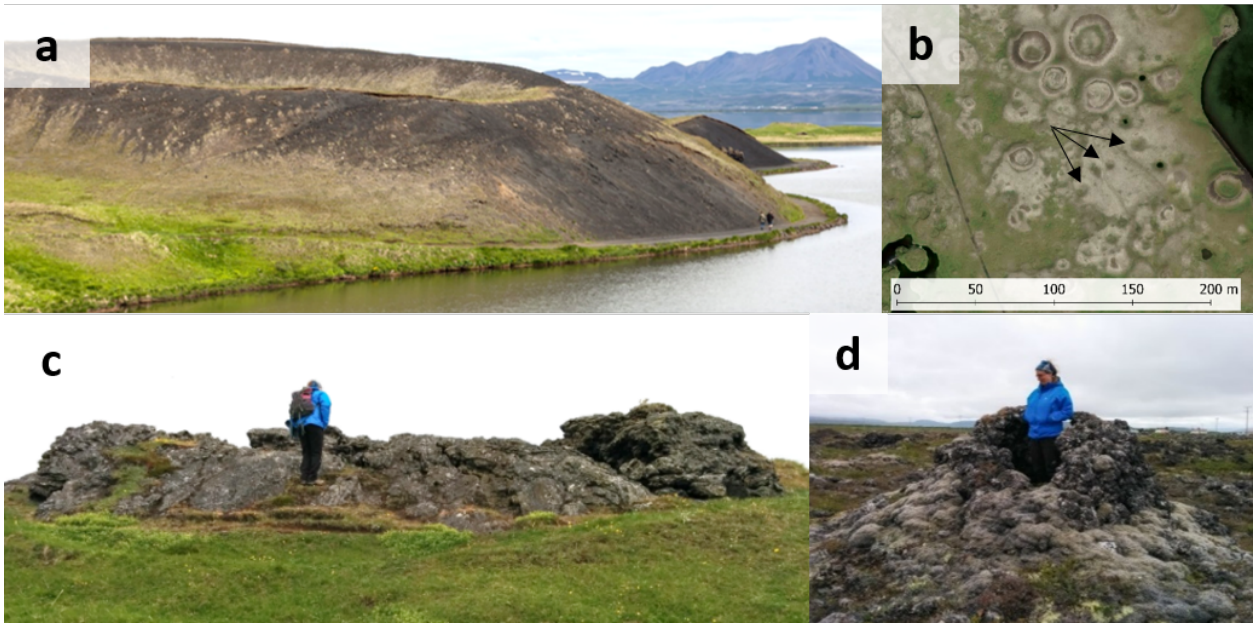

Figure 2.4: Different types of rootless cone and associated features. a) Scoriaceous rootless cone at Skútustaðir, Mývatn. Cone base is ∼100 m diameter. b) Explosion pits (marked with arrows) surrounding a scoriaceous rootless cone near Mývatn. c) Spatter cone at Mývatn. d) Hornito in Aðaldalur, NE Iceland. Map imagery on b ©2017 DigitalGlobe, Google

Scoriaceous rootless cones are the most common and widely distributed cone type and include three different classes based on the number of summit craters (inner cones) present. The classic rootless cone is a low-profile single-cratered (S) cone composed of scoria and ash, often with a layer of welded spatter covering the top surface (Thorarinsson, 1953; Fagents and Thordarson, 2007). Rootless cones may have multiple craters at their centre, positioned above a 'rootless conduit' filled with denser, welded material. Cones with two craters (i.e. an inner cone inside an outer cone), often concentric, are referred to as double cones (D). Outer cones with more than one inner cone have been called 'lotus-fruit' scoriaceous cones (L; Noguchi et al., 2016). The basal diameters of scoriaceous rootless cones found in this study range from metres to hundreds of metres, with the largest single cones ∼200 m diameter, and multi-cratered cones up to 350 m diameter.

Spatter cones were first described by Thorarinsson (1953) as *schweiss-schlacken* cones, meaning 'welding slag'. They are made entirely from agglutinated spatter, with no ash or loose scoria (Figure 2.4c). The spatter cones in this study are hollow with sloping walls and have basal diameters of 5–50 m. Spatter cones tend to have steeper slopes than scoriaceous cones, as their construction is not limited by angles of repose and they are more resistant to erosion (Thorarinsson, 1953).

Hornitos, meaning 'little ovens', are stacks of welded spatter a few metres in diameter and height, and are often hollow (Figure 2.4d). We distinguish hornitos from spatter cones by size and aspect ratio: they have diameters ≤5 m and a height comparable to or greater than the diameter. Large fields of hornitos have been reported where lava flows encountered a shallow lake in Wudalianchi National Park, China (Gao et al., 2013), and they are seen in close association with rootless cones in Aðaldalur. However, hornitos are not always a result of LWI and are often found above skylights in lava tubes where internal pressure causes lava to spatter and build up ramparts (Kauahikaua et al., 2003).

Explosion pits are rootless craters that have no built-up walls or ramparts (Figure 2.4b). They are generally found clustered around a larger scoriaceous rootless cone and were probably sites of smaller or shorter-lived rootless eruptions whose cone walls have been buried by scoria from larger nearby rootless vents.

2.3.2 Aerial imagery and high-resolution DTMs from drone surveying

We use a combination of satellite and aerial photographs and digital terrain models (DTMs) derived from them. We primarily use Google Earth images from the DigitalGlobe image library, which have spatial resolutions of 0.35–0.58 m/pixel (see Table A.1 for further details). Where the resolution of the Google Earth images was poor or where features were indistinct we referred to higher resolution Loftmyndir ehf. imagery available on `http://map.is/base/m`, which has a spatial resolution of 0.15–1 m/pixel (Loftmyndir, 2014; Noguchi et al., 2016).

We supplemented these with high-resolution DTMs that we created using a small unmanned aerial system (UAS). We surveyed three rootless cone groups (Figure 2.3): (1) part of the first group of scoriaceous rootless cones in Aðaldalur (Figure 2.5); (2) the transition from scoriaceous rootless cones to hornitos approximately half way down Aðaldalur (Figure 2.6); and (3) an area of hornitos at the northern end of the valley (Figure 2.7). We did not survey any areas around Mývatn because of the high density of nesting water birds.

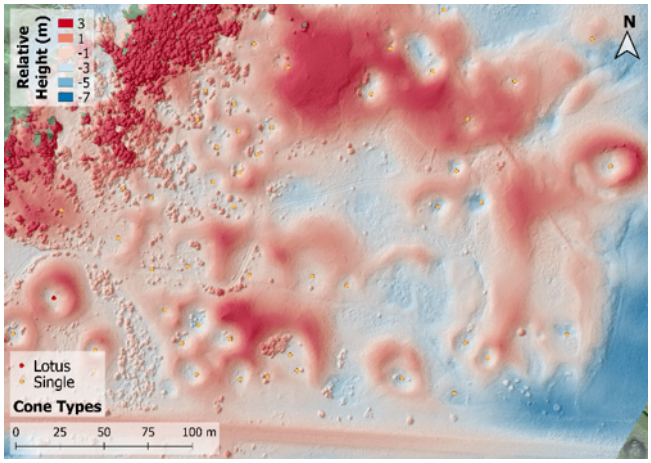

Figure 2.5: High resolution DTM of rootless cones in UAS survey area (1) in Aðaldalur. The heights given are all relative to the average of the DTM itself, as the DTMs created by drone survey are not georeferenced for elevation.

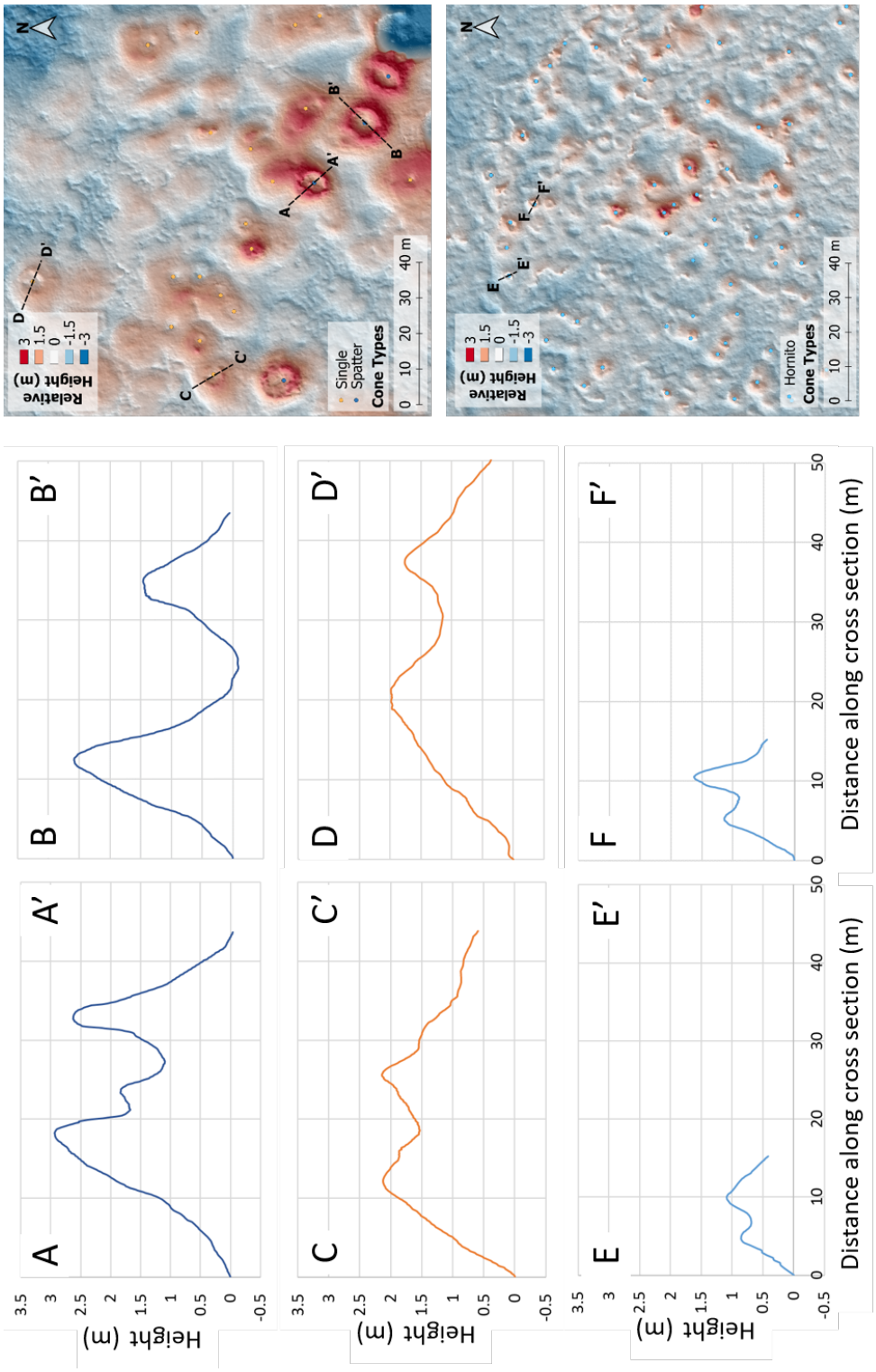

Figure 2.6: High resolution DTM of rootless cones and hornitos along the inflation front in Aðaldalur in survey area (2), showing elevation profiles of different cone types. The heights given are all relative to the average of the DTM itself, as the DTMs created by drone survey are not georeferenced for elevation. The lines on the DTMs show the position of the profiles. Profiles A and B are of spatter cones, C and D are single-cratered scoriaceous cones, and E and F are hornitos. The profiles show that the spatter cones and hornitos have significantly steeper slopes than the scoriaceous cones, which helps distinguish between the cone types.

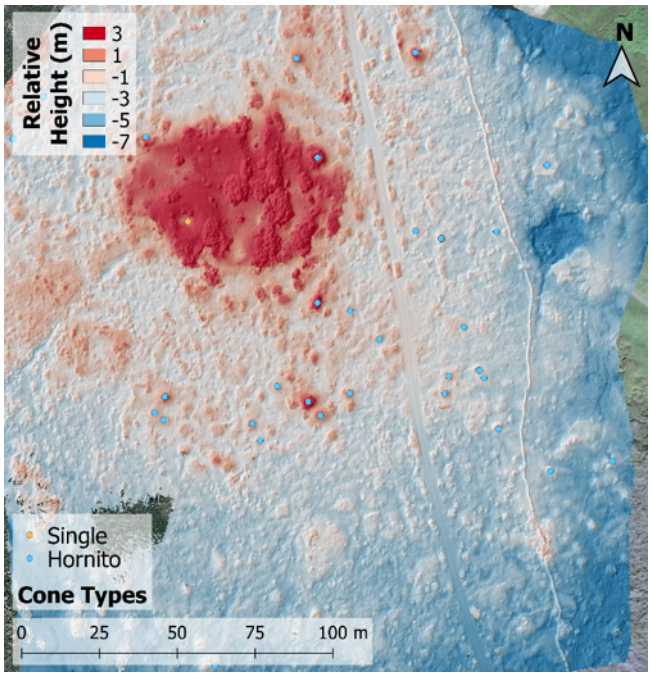

Figure 2.7: High resolution DTM of hornitos in UAS survey area (3) in Aðaldalur. The heights given are all relative to the average of the DTM itself, as the DTMs created by drone survey are not georeferenced for elevation.

To create our high-resolution DTMs, we used a DJI Phantom 2 Vision+ quadcopter, which has an integrated camera. The battery life of quadcopters limits flight to approximately 15 minutes, enough to survey ~0.12 km^2. This limit made it unfeasible to cover entire cone groups, so we selected representative accessible areas within each group, or regions that contained features of particular interest. Flights were made in a regular grid pattern, controlled using the DJI Vision smartphone app. The grid spacing and altitude were chosen to give an overlap of >70 % between adjacent passes and a spatial resolution of ≤10.5 cm/pixel (details flight time, altitude, grid spacing and spatial resolution of captured images of each flight are available in Table A.2).

The on-board camera captured video at 1080p and 29 frames per second (fps) with a 110° field of view, which was split into full size (1920 × 1080 pixel) JPEG images at a rate of 1 fps. This gave a minimum overlap of 80 % between images in the direction of travel, ensuring good coverage when constructing a 3D model of the site. The images were processed and stitched together using Agisoft Photoscan, a commercial structure-from-motion software package. Because we chose to capture video, no GPS data were saved from the UAS, so we georeferenced our models in the Geographic Information Systems (GIS) package QGIS to features visible in the Google Earth base map. With these control points, we optimised and georeferenced the 3D models in Photoscan to produce fully georeferenced DTMs (see Table

A.2 for RMS errors on georeferencing). All elevations in the DTMs are relative to the DTM average and do not correspond to the altitude above sea level. The DTMs were exported from Photoscan as .tiff files (available in Supplementary Material), which were then imported into QGIS for further analysis.

To investigate the lava flow morphology, we also used the ArcticDEM dataset produced by the Polar Geospatial Center (available from the ArcticDEM webtool at: `https://livingatlas2.arcgis.com/arcticdemexplorer/`), which provides 2 m/pixel DTMs across the arctic circle. DTMs are built from data gathered from WorldView-1, WorldView-2 and WorldView-3 satellites and processed according to Noh and Howat (2015). A the time that this work was done, data were provided in swathes, which did not always overlap and sometimes had a vertical offset relative to adjacent swathes. Elevation is also provided as ellipsoidal height rather than orthometric height (m a.s.l.), so these factors were corrected before using the data. The difference between orthometric and ellipsoidal height at a given point is displayed in the ArctiDEM wetbtool. The ArcticDEM coverage of both Mývatn and Aðaldalur are slightly patchy and there are some holes in the DTM.

Mývatn was covered by two different swathes of data, separated by a gap, but no vertical offset. Using QGIS, we applied a -66.25 m correction to the Mývatn DTM to convert from ellipsoidal height to orthometric height. Aðaldalur also lay on the boundary between two overlapping swathes, which had a slight vertical offset from one another. We applied a vertical transform of +2.4 m to the western segment to bring it in line with the eastern segment and merged the two parts into a single DTM. A further correction of -68.4 m was applied to the merged dataset to convert the elevation to orthometric height. Finally, we cropped the DTM in Aðaldalur to the extent of the YLL, based on a geological map of the area (Sæmundsson et al., 2012).

2.3.3 Cone digitisation, classification, crater size, and nearest neighbour analysis

To explore their distribution, we digitised rootless cones using QGIS, with Google Earth imagery as a base map. We digitised each cone as a point at the centre of the crater, or the inferred centre if the cone was incomplete, using the highest resolution image available for the area. Each cone was given a unique identifier combining its locality (Mývatn, Laxárdalur or Aðaldalur), a number and, in some cases, a sub-group number (e.g. *Ada2_1* for cone 1 in sub-group 2 in Aðaldalur). In this chapter, sub-groups are numbered in the order in which they were mapped, and numbers generally progress clockwise around the lake edge, then

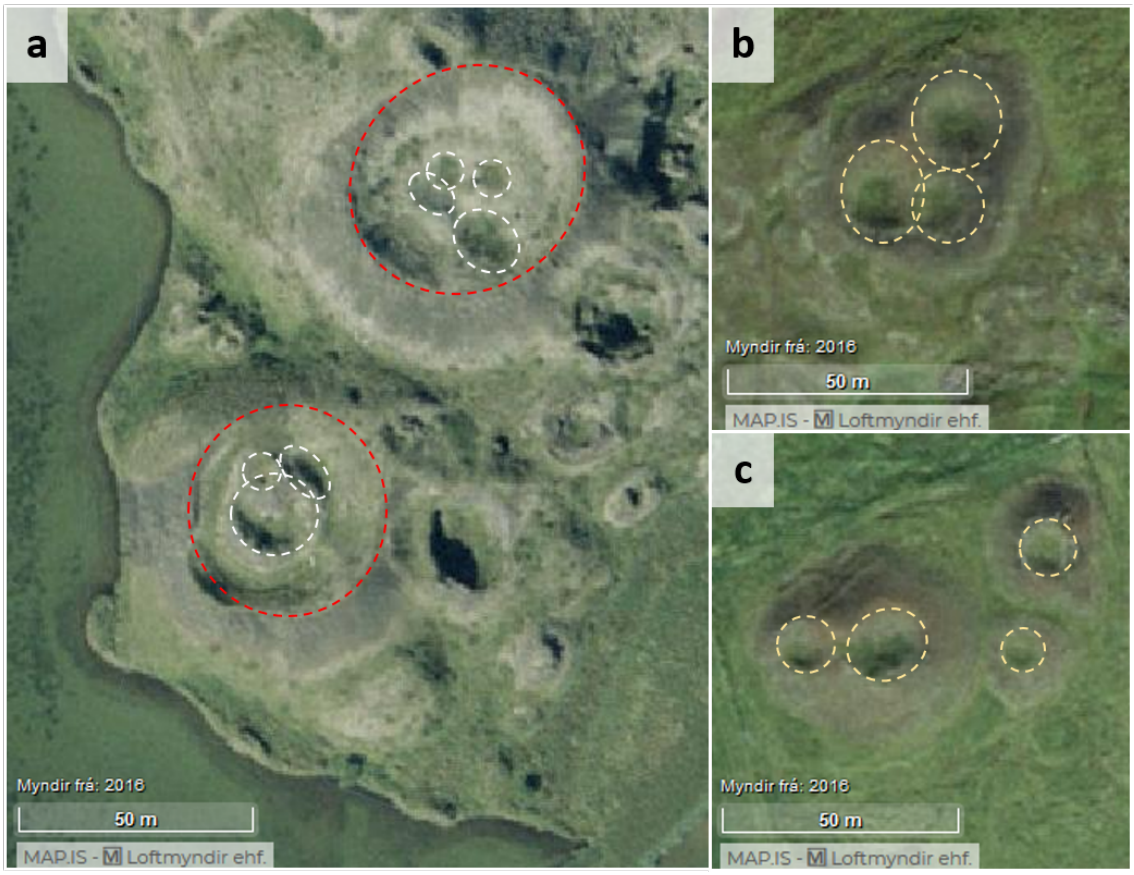

Figure 2.8: Comparison between lotus-fruit (L) cones and overlapping single-cratered (S) cones on the YLL. a) The outer craters of two L cones are picked out in a red dashed line, while the inner craters and picked out in white dashed lines. b) and c) show examples of overlapping S cones, with the craters picked out in dashed yellow lines. All images from Loftmyndir ehf. (available on http://map.is)

inland from the lake for Mývatn, and then south to north for Laxárdalur and Aðaldalur. Sub-group numbers do not necessarily correlate to formation order or any other physical parameters or features.

Based on the images and field observations, we grouped the cones into previously listed categories (L, D, S, SP, H, P and U). Where adjacent cones overlap, we counted each crater as an S cone if the cone flanks were distinct. Multi-cratered cones (L and D) are distinguished from overlapping S cones by the presence of a single continuous, smooth exterior wall, although complex cone morphologies can make this distinction difficult (see Figure 2.8 for example).

To improve cone classification, we compared field notes and photographs to the appearance of the different cone types in aerial photographs and the maximum slope angles in the high resolution DTMs. Among the Aðaldalur cones, S cones had slope angles of $<20^{o}$. In contrast,

SP cones had maximum slope angles >25°, and were especially steep around the crater rim as a result of their hollow structure (Figure 2.6). The steep crater edges help to identify SP cones in aerial photographs, especially in strong sunlight, as they cast a darker, sharper shadow than the gentler crater rims of S cones. Field observations and high-resolution slope maps show that hornitos also have high (>30°) maximum slope angles (Figure 2.6). Two other differences between S and SP cones are that: (1) all of the S cones in Aðaldalur showed some degree of oxidisation, giving the cones a reddish appearance in contrast to the grey SP cones; (2) many of the S rootless cones are vegetated, whereas the SP cones and hornitos host much less vegetation on their flanks. These qualitative data helped to distinguish between S and SP cones in the less accessible areas of the valley.

Not all of the digitised rootless cones have been classified because the aerial imagery was insufficient to distinguish cone type without additional field observations. The unclassified cones are all either small S cones or large SP cones because these two types are particularly difficult to distinguish. They make up 5.7 % of the total possible population of S and SP cones, and 2.0 % of all rootless cones.

To investigate variations in cone size, we digitised the craters of the rootless cones around Mývatn, in Laxárdalur and in Aðaldalur, using the Google Earth base-map, our high-resolution DTMs and the 2 m/pixel ArcticDEM data. Since hornito craters are too small to see in Google Earth images, we only digitised the craters of two groups of covered by our high-resolution DTMs. We used the radius of the crater rather than the whole cone as a measure of cone size because many cones have gentle slopes that overlap with adjacent cones, making it difficult to determine their extent. We approximated craters as ellipsoids in QGIS and calculated their areas using the QGIS field calculator.

We also categorised rootless cones based on their locality. Cone groups around Mývatn were initially given one of four classifications according to their proximity to the lake edge: islands (Is); lake shore (Sh); inland (In); at the mouth of the Laxá river (RM). The Laxárdalur cones form discrete groups, which we numbered 1–4 (Figure 2.16). The cones in Aðaldalur were classified as: Reykjadalur (group A); ropy pāhoehoe (groups B1 and B2); inflated pāhoehoe (groups C1 and C2); the western edge of Aðaldalur (group D); along the inflation front (group F); and hornitos (groups H1 and H2; Figure 2.17b).

We exported the locality, type, crater area, group and unique ID for each cone as a comma separated variable (.csv) file for further spatial analysis in statistical software package *R* (script available in Supplementary Material). To assess their spatial distribution, we used the *geosphere* package in *R* to calculate the distance in metres between each cone and the

closest adjacent cone (i.e. the nearest neighbour distance / NN distance). Since the craters are ellipsoids, we calculated the radius of the circle of equivalent area for each crater to give a measure of cone size.

The number of digitised cones is a minimum estimate, as some rootless cones across the YLL have been quarried or demolished, and others may not be identifiable in existing aerial photographs (particularly small hornitos). The land around Mývatn and between the rootless cone groups has been farmed since the area was settled in the 10^{th} Century AD. The cones at Mývatn are now protected, but we cannot rule out destruction by human activity in the past. The Rauðhólar cone group in Laxárdalur has been partially quarried. Some cones in Aðaldalur have clearly been demolished to make space for roads and buildings or excavated to improve farmland, and it is possible that more cones have been removed as a result of farming or development. Historical satellite images in Google Earth do not date back far enough to see the area before it was ploughed, but vegetation patterns in some fields hint at possible additional rootless cone sites.

2.3.4 Error analysis

Digitising cones and craters from aerial photographs introduces unavoidable uncertainty to the data set, as it requires judgement of the positions of the cone centre and crater edge. These errors are exacerbated by approximating the craters as ellipses. To assess the accuracy of our measurements of cone area and NN distance, we selected a sample of 315 cones in Aðaldalur and independently digitised the craters and cone centres four times (Figure A.1). We measured the crater area and NN distance for each repeat and amalgamated the datasets so that each cone had four associated values of area and NN distance. We then calculated the mean values for each cone, and the difference between the mean and each measurement to give a distribution of the absolute errors associated with crater area and NN distance. From the absolute errors and the mean, we calculated the relative errors and fit these to two Gaussian distributions in *R* (script in Supplementary Material; Figure A.2). We took the standard deviation of the fitted distributions as the standard errors for our area and NN measurements. We then converted the standard error of the area to an error for equivalent crater radius, to fit with our statistical modelling. We calculated a standard error of ±26.2 % on crater area, corresponding to +12.3 % / -14.1 % error in equivalent radius, and a ±5.0 % error on NN distance. This error is small enough that it does not affect the outcomes of the statistical modelling of different cone populations.

2.3.5 Statistical Modelling

To explore the relationship between the size, type and NN spacing of the rootless cones, we carried out Analysis of Variance (ANOVA) tests on the different rootless cone populations using the statistical package *R*. A base 10 logarithmic transform was applied to the radius and NN data to make the distribution appropriate for statistical modelling. All models were validated in *R* by checking that the assumptions of normally-distributed variables and heteroscedasticity were true, and that the model was not influenced by outliers. Each cone appears only once in the dataset, so there is no auto-correlation. A list of the ANOVA models and the dependent and independent variables for each is given in Table 2.1. Tukey Honest Significant Difference (HSD) tests were used to compare the means and give the significance between each explanatory factor (full table is available in the University of Bristol data repository at `https://data.bris.ac.uk/data/dataset/ojcw17r060lu21o7lbjeoftbf`). In line with standard practice, we took $p < 0.05$ as the threshold for determining statistical significance. The p-values are reported in Table 2.1 alongside the degrees of freedom and F-statistic, which gives a measure of the variability between groups compared to the variability within each group, for each model. We used the Akaike information criterion (AIC) to compare the quality of fit of the different models to the data; a lower AIC value indicates a better model fit.

	Model Name	Dependent Variable	Independent Variables	Results (X^2,F, p)	Adjusted R^2	AIC	Data
X^2	-	Type	Location[a]	X^2=3795.4*, p <0.001	N/A	N/A	All YLL features
ANOVA	AllModel1	Log_{10}(radius)	Location	F(2, 2866) = 114.8, p <0.001	0.07	2202	All YLL cones
	AllModel2	Log_{10}(radius)	Type[b]	F(2, 2866) = 114.8, p <0.001	0.44	726	All YLL cones
	AllModel3	Log_{10}(radius)	Location + Type	F(8, 2860) = 317.8, p <0.001	0.47	610	All YLL cones
	MyvModel1	Log_{10}(radius)	Category[c] + Type	F(8, 1460) = 100.0, p <0.001	0.38	407	All Mývatn cones
	MyvModel2	Log_{10}(radius)	Modified category[d] + Type	F(8, 1465) = 108, p <0.001	0.40	330	All Mývatn cones
	LxModel1	Log_{10}(radius)	Group	F(3, 106) = 2.2, p <0.094	0.032	-87.9	All Laxárdalur cones
	AdaModel1	Log_{10}(radius)	Category[e]	F(9, 240.9) = 240.9, p <0.001	0.63	-113	All Aðaldalur cones
	AdaModel2	Log_{10}(radius)	Type	F(5, 1260) = 286.5, p <0.001	0.53	187	All Aðaldalur cones
	AdaModel3	Log_{10}(radius)	Category[e]	F(6, 989) = 73.1, p <0.001	0.30	-125	S cones in Aðaldalur
Linear Model	AllModel5	Log_{10}(radius)	Log_{10}(NN) + Location + Type	F(9, 2859) = 411, p <0.001	0.56	55	All YLL cones

[a] Mývatn, Laxárdalur and Aðaldalur
[b] L, D, S, SP, H, P, U
[c] proximity to current lake edge
[d] proximity to estimated original lake edge
[e] position on the YLL

Table 2.1: List of statistical models used in this study

We assessed the correlation between the size (crater radius) and NN distribution using a simple linear regression. We calculated the correlation coefficient (r) and corresponding p-value for the entire population, and for each locality (Mývatn, Laxárdalur and Aðaldalur) and type separately (Table 2.5). We then assessed difference in the size distributions of the different cone types (L, D, S, SP, H and P) across the whole YLL. We controlled for cone type in all subsequent models, unless otherwise stated. The quartiles, mean and standard deviation of NN distances for each group are given in Table 2.2.

We used a chi-squared test to compare the proportion of different cone types between the three sites: Mývatn, Laxárdalur and Aðaldalur. For this comparison, we used the whole population of hornitos in Aðaldalur, not just those with digitized areas. Because the number of cones at each locality varies by more than an order of magnitude, and not all cone types appear at each locality, p-values for the chi-squared test were calculated using a Monte Carlo test with 2000 replications to account for the fact that the count data for each type was not normally distributed.

We tested the relationship between cone size and proximity to the lake edge for the Mývatn cones using two different models: one where the cones were categorised based on their proximity to the current lake edge and one based on the proximity to the estimated edge of the lake before the YLL. We also tested to see whether there were any significant differences in cone size between the different Laxárdalur groups.

The distribution of rootless cones across Aðaldalur means that some groups contain only one type of cone, which violates the assumption of no collinearity in the independent variables necessary for ANOVA. To avoid this problem, we tested the relationships between cone size and type, and cone size and group, separately. We then tested the relationship between cone size and group for the S cones only. While this reduces the data available for analysis, S cones are the most numerous type across different lava flow textures in Aðaldalur and are also present at Mývatn and Laxárdalur, allowing comparison between the three localities. Hornitos are the most numerous cones by type in Aðaldalur, but we have size data for them in only two parts of the valley. Because the size of rootless cones is correlated to the NN distance, we did not model the NN distributions in terms of type and group separately.

				Crater Radius [m]							Nearest Neighbour Distance [m]						
	Group	Cat A	Cat B	n	Min	Q1	Median	Mean	Q3	Std Dev	Min	Q1	Median	Mean	Q3	Std Dev		
Mývatn	1	Sh	Sh	8	5.5	6.2	10.9	13.9	19.9	28.4	9.1	21.39	93.66	130.9	143.1	163.4	357.1	108.8
	2	Is	Is	128	0.9	4.2	6.8	9.5	12.3	44.6	7.4	4.8	19.1	27.0	29.7	38.7	97.4	14.5
	3	Is	Is	29	2.0	3.6	7.1	9.8	14.1	31.1	7.6	8.4	36.6.	41.2	53.0	60.0	215.2	46.3
	4	Is	Is	35	1.4	3.0	5.2	9.4	10.7	41.6	10.4	5.0	13.6	34.8	54.9	75.8	385.1	69.2
	5	Sh	Sh	35	2.5	8.2	12.4	12.1	21.7	38.5	10.1	19.4	46.3	54.3	73.6	81.8	288.6	60.4
	6	Sh	Sh	39	1.6	4.3	6.9	12.2	17.9	39.0	10.6	15.8	313.6	46.1	69.6	91.4	361.7	66.2
	7	Sh/In	Sh/In-1	88	1.1	3.3	5.3	7.0	9.5	30.2	5.5	9.6	20.5	28.9	33.4	43.5	103.8	18.0
	8	Sh	Sh	10	3.2	6.1	12.4	20.1	19.1	64.4	21.0	21.7	35.4	41.4	50.0	64.8	100.0	24.9
	9	In	In-1	22	1.2	3.1	5.6	6.7	8.0	19.6	5.0	29.9	46.6	66.3	76.5	109.1	164.2	40.2
	10	Sh	Sh	218	1.1	3.1	6.1	8.6	13.0	36.3	7.2	3.3	16.5	26.0	3.5	37.5	141.3	22.4
	11	Sh	Sh	36	1.4	3.2	6.8	8.2	10.4	28.6	6.9	8.2	24.3	37.8	40.8	52.5	89.3	32.7
	12	Sh	Sh	18	1.9	4.7	8.7	11.1	13.0	32.3	8.8	19.4	42.7	60.0	64.3	88.1	112.3	32.0
	13	Sh	Sh	71	1.3	4.0	7.4	12.0	13.0	62.3	13.5	16.3	27.1	40.7	81.0	77.5	721.8	128.6
	14	In	In-1	12	3.9	5.3	11.4	12.1	15.7	28.5	7.9	21.9	32.0	37.3	58.6	66.1	250.7	62.8
	15	In	In-1	109	1.3	3.5	6.1	7.0	6.6	20.2	4.2	5.4	12.9	27.1	34.1	47.8	207.1	30.7
	16	In	In-1	49	1.8	2.7	3.6	4.2	4.7	13.8	2.5	8.2	12.0	14.1	16.8	17.7	42.1	7.8
	17	In	In-2	32	1.9	4.0	5.8	7.5	10.3	22.5	4.7	11.3	19.6	25.7	31.0	35.3	102.3	19.5
	18	In	In-2	155	1.1	2.7	3.7	4.1	4.8	18.6	2.3	3.3	8.4	11.4	14.9	17.1	94.0	11.9
	19	Is	Is	26	4.2	6.2	7.8	8.6	10.0	22.2	3.7	13.5	18.9	24.5	24.2	29.5	34.4	6.5
	20	RM	RM	363	0.9	2.1	3.4	4.7	6.0	38.5	3.9	4.3	10.3	19.7	23.7	30.0	182.3	18.5
	21	In	N/A	10	9.5	17.6	19.3	19.6	23.5	28.8	5.7	37.8	38.9	44.5	105.0	53.1	604.9	176.5
Laxárdalur	Lx1			27	1.8	2.7	3.3	3.6	4.0	7.7	1.5	6.5	9.2	13.6	15.4	15.8	43.5	10.3
	Lx2			7	1.8	2.6	3.0	2.9	3.4	3.6	0.7	15.4	21.4	27.5	32.3	34.4	71.4	19.0
	Lx3			33	1.1	2.4	3.1	3.1	3.4	9.5	1.4	6.5	11.3	14.5	23.2	19.8	175.2	30.4
	Lx4			43	1.6	2.6	3.4	3.8	4.8	7.3	1.4	5.4	8.2	13.9	18.1	20.7	64.5	14.2
Aðaldalur	A			225	1.3	2.9	4.0	4.6	5.8	23.9	2.8	5.5	15.3	22.7	28.4	33.2	187.2	22.9
	B1			308	1.4	3.7	5.7	6.3	8.5	19.1	3.2	6.1	13.4	17.9	22.4	23.4	200.8	18.9
	B2			64	2.0	4.8	6.1	7.7	7.9	33.9	5.8	7.6	13.4	22.2	37.6	38.2	264.7	49.7
	C1			74	2.6	6.5	8.8	9.8	12.6	30.2	4.9	9.1	18.3	23.7	32.6	44.7	100.5	20.7
	C2			114	1.1	2.8	4.9	6.1	7.5	23.2	4.8	5.3	17.0	23.7	36.6	39.3	263.5	42.6
	D			29	1.3	2.2	2.5	2.4	2.7	3.8	0.6	5.5	9.0	10.6	14.0	18.0	45.4	8.6
	F			224	0.8	1.9	2.8	3.1	4.0	9.6	1.5	5.2	10.4	14.4	18.3	20.3	175.4	17.8
	Sp			56	0.9	1.6	2.3	2.8	3.5	6.4	1.4	6.4	12.1	16.8	23.0	23.2	166.3	23.5
	H1			134	0.2	0.5	0.7	0.8	1.1	2.3	0.4	3.7	5.9	7.9	10.0	10.1	100.3	10.4
	H2			29	0.3	0.5	0.6	0.8	1.0	3.0	0.5	2.8	5,9	10.9	13.6	17.8	54.3	11.5

Table 2.2: Size and nearest neighbour distributions for rootless cone groups in Mývatn, Laxárdalur and Aðaldalur

2.3.6 Flow emplacement temperatures

To determine the change in lava temperature along the length of the YLL, we measured the glass composition of scoria samples from Mývatn and Aðaldalur . The Mývatn scoria clast was collected from the surface of one of the rootless cones at Skútustaðir (group 6 in Figure 2.9a; sample location: 65.57011, -17.03132). The Aðaldalur sample came from an excavated rootless cone along the inflation front (65.88592, -17.45599). Both samples were selected in the field for their high glass content. We have assumed that glassy material from rootless cone scoria records the temperature of the lava as it interacted with water, while recognising that this is a simplifying assumption and that lava flows are not homogenous in temperature.

We analysed thin sections of both samples on a JEOL JXA8530F Hyperprobe at the University of Bristol (20 keV accelerating voltage, 10 µm beam diameter, 5 nA current). We measured ten points per sample and normalised the proportion of each element or oxide based on the totals for each point. We took the mean value of the ten points to give the average glass composition for each sample. We then calculated the temperature of the melts when they were quenched from the weight % MgO, following the method of Putirka (2008).

2.4 Results

In this section we follow the path of the YLL from its eruptive vent near Lake Mývatn, through the Laxárdalur gorge and then along the length of the broad Aðaldalur valley, describing the changes in flow morphology and the rootless cones from our analysis of aerial photographs, the ArcticDEM and our own high resolution DTMs. We then examine the relationship between the size, type and spacing of the YLL rootless cones, and the systematic variation of cone size across the lava flow.

Figure 2.9: a) Map of Mývatn showing the locations of rootless cones and extent of the Younger Laxá Lava, as mapped by Sæmundsson et al (2012). Cone groups are outlined and numbered in a white broken line. Arrows show direction of lava flow and are sized to represent the volume of lava flowing in that area. Scoriaceous cones are marked as circles, spatter cones by triangles and unclassified cones as diamonds. b) ArcticDEM showing the elevation of the area around Mývatn (in m above seal level), including the Younger Laxá Lava and surrounding countryside. Note that the colour ramp is scaled to highlight the area with an elevation of 279 m ± 1 m. The lake surface has an elevation of 277 m asl. The eruptive fissure is marked by the dashed black line, and arrows show the direction of the lava flow. Proposed outlines for the original lake are shown by a dotted black line (Einarsson, 1982) and solid black lined (this study). DEM created by the Polar Geospatial Center from DigitalGlobe, Inc. imagery. Map imagery ©2017 DigitalGlobe, CNES/Airbus. Map data ©2017 Google

2.4.1 The Younger Laxá Lava and associated rootless cones

Mývatn

On the eastern edge of the Dimmuborgir complex is a cluster of nine single-cratered scoriaceous (S) cones (group 21 on Figure 2.9a). These cones have a mean basal elevation of 303.2 m a.s.l., making them the highest group of cones on the YLL, 27 m higher than current lake level. Einarsson (1982) found buried rootless cones between Dimmuborgir and Mývatn and showed that vesicles in these cones contain diatoms from the pre-existing lake.

South of Dimmuborgir, the surface of the YLL is dominated by pressure ridges showing that the lava flowed towards the lake, draining through channels (Figure 2.10a; Figure 2.11). This region begins as a single, coherent flow ∼800 m wide, before splitting into two separate flow lobes: the larger (northern) lobe fans out to 1.4 km wide; the smaller lobe turns to the southwest and is ∼250 m wide where it meets the current edge of the lake. Where these two lava lobes meet the present-day lake near Höfði, there are lava structures with bathtub rings and lava pillars (Figures 2.10b, 2.10c) that suggest ponding and LWI, respectively (e.g. Gregg et al. 2000; Gregg and Christle, 2013; Skelton et al., 2016). Curiously, there are very few rootless cones in this region (an exception is group 1 in Figure 2.9a).

The land around Mývatn and the central lake basin is blanketed by tephra from the rootless cones, which obscures the lava flow surface. Around and between the rootless cone groups, the lake edges comprise black beaches of coarse scoria (Figure 2.12a). Aerial photographs show that the shores of the islands are the same and reveal the remains of islands, and possibly rootless cones, that have been eroded to black sandbanks in the lake (Figure 2.12b-c).

The islands in eastern Mývatn are covered in scoriaceous rootless cones (groups 2–4), with 149 cones on the largest island alone. Most are S cones, although there are numerous double-cratered (D) and lotus-fruit (L) cones. There are also a few explosion pits (P) close to or surrounding the larger cones. We have not found any spatter (SP) cones or hornitos on the islands.

The rootless cones around the southern and western shores of Mývatn are also a mix of S, L and D cones (groups 5–8, 11–13). The Skútustaðir cones (group 6) are the most accessible and are a popular tourist attraction. A radial transect through this group shows that the cones become smaller with distance from the current lake edge, decreasing in crater radius from 39.0 m to 1.6 m over ∼500 m (Figure 2.13a). The largest rootless cones around Mývatn

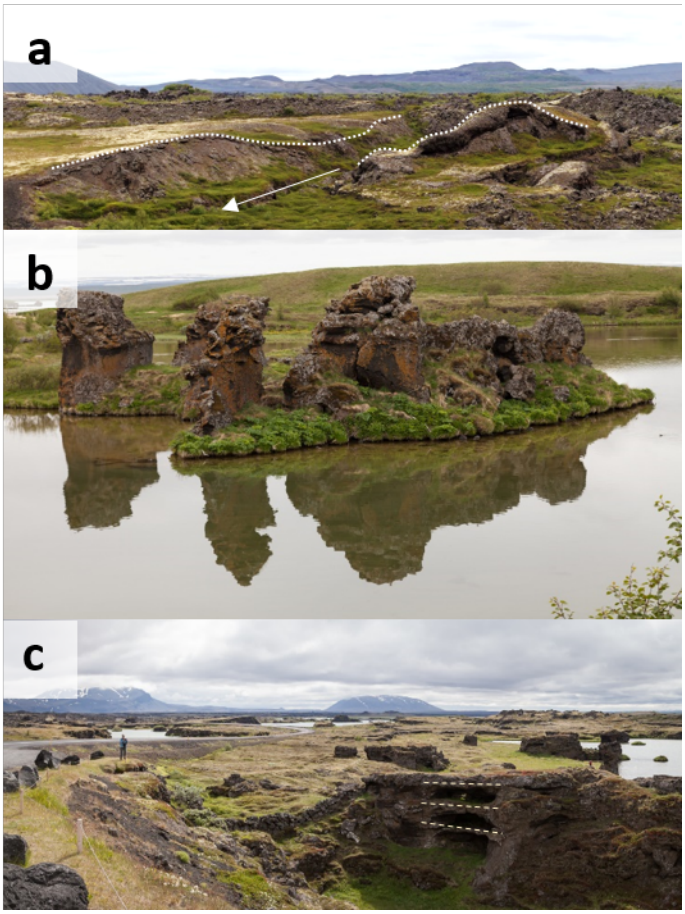

Figure 2.10: Features of the Younger Laxá Lava on the eastern shore of Mývatn near Höfði. a) Levees of a lava channel entering Mývatn, shown by white dotted lines. The channel is approx. 10 m wide. Arrow shows direction of lava drainage. b) Lava pillars, formed by passive steam escape through ponded lava. For scale, the island with the pillars is approx. 20 m long. c) View towards the lake from the road, showing stacked lava pond surfaces (dashed lines, approx. 10 m long), caused by drainage of ponded lava in several stages. More lava pillars are visible in the background.

are the Vindbelgur cones (group 13), with crater radii ≤62.8 m. As with the Skútustaðir group, the largest of these are L and D cones that sit on a peninsula jutting into Mývatn and get smaller as they move inland (Figure 2.13b).

There are also numerous rootless cone groups inland of the present-day lake, among smaller pools of water and wetlands (groups 9, 14–18), and on an island in Sandvatn (group 19). Because of nesting birds, most of these cones are inaccessible during the summer months, so we mapped them based on aerial photographs. The most northerly cones (group 18) lie at the furthest edge of the YLL and >1 km from the shore of the present-day lake. These S cones form a densely packed, elongate group and sit on either side of the modern ring-road around the lake. The scoria in the visible outer layers of these cones appears larger and denser than the scoria that makes up the Skútustaðir cones (Figure 2.14). Finally, there is a concentration of rootless cones where the lake drains into the Laxá river (Figure 2.9a). We have split the cones here into two groups. Those at the mouth of the Laxá (group 20) are predominantly SP cones and are the smallest around Mývatn. Those closer to the lake (group 10) are larger and are a mixture of L, D, S, SP and P cones.

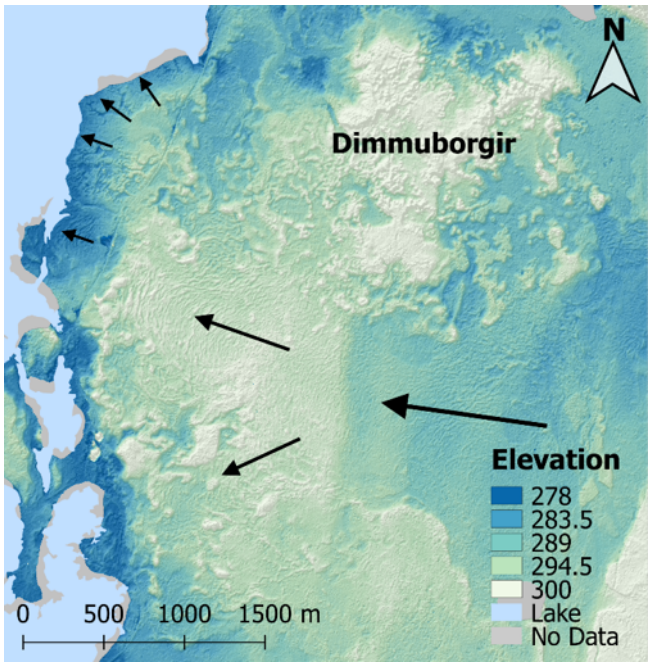

Figure 2.11: Elevation of the YLL on the east shore of Mývatn. The rootless shield complex of Dimmuborgir and lava channels with pressure ridges are visible. Direction of lava flow into the lake is indicated by arrows. DEM created by the Polar Geospatial Center from DigitalGlobe, Inc. imagery.

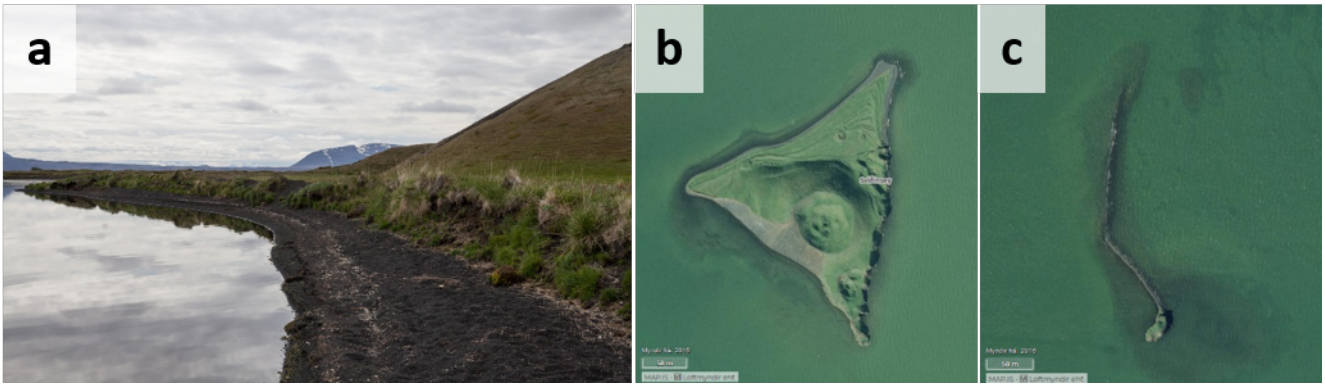

Figure 2.12: a) A beach near Skútustaðir made up of black rootless tephra. b) Sviðinsey island in Mývatn. Erosion of the island and main rootless cone show that they are both constructed entirely of black rootless scoria. c) Sandbank of rootless tephra in Mývatn. A thin spine projects out of the lake, but the extent of the bank can be seen through the shallow water. Images in b) and c) are from map.is / Loftmyndir ehf. ©2017 Notkunarskitmálar.

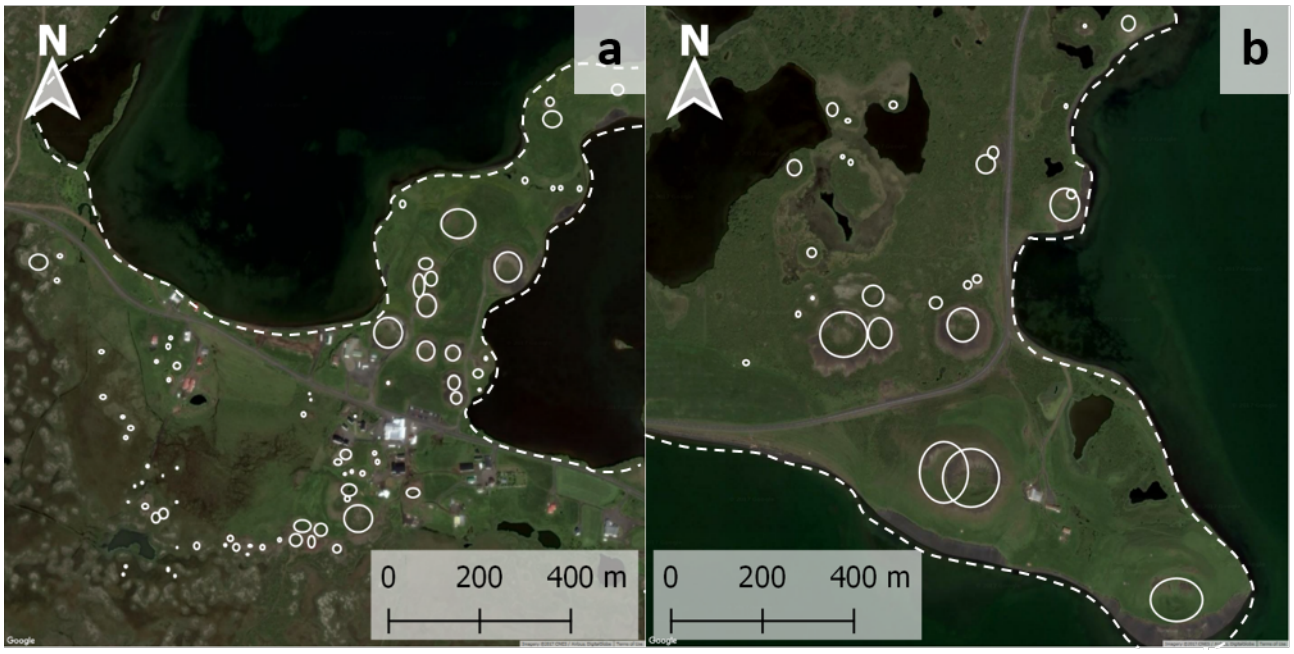

Figure 2.13: Close up views of the Skútustaðir (a) and Vindbelgur (b) cone groups. Craters are outlined in white, showing how craters become smaller away from the lake edge (shown by white dashed line). Map imagery ©2017 DigitalGlobe, CNES/Airbus. Map data ©2017 Google.

Laxárdalur

After leaving Mývatn, the YLL followed the course of the Laxá. Our glass geochemistry data show that the lava cooled very little as it progressed through Laxárdalur, dropping only 10 ^{o}C over 45 km: from 1175.0 ±3.1 ^{o}C at the southern shore of Mývatn to 1165.0 ± 1.7 ^{o}C at the inflation front mid-way down Aðaldalur (see Table 2.3, Figure 2.15), in agreement with a previous study (Aebischer, 2018).

The YLL created four distinct rootless cones groups in Laxárdalur (Figure 2.16). The first group (L1) lies 12 km down the valley and contains at least 27 cones clustered along the eastern edge of the lava flow and river. We have provisionally identified these as S cones, but the group may also contain some SP cones. The second group is 16 km down Laxárdalur and comprises 7 cones in the middle of the lava flow on the western side of the river (L2). The third group, comprising 33 cones in the middle of the lava flow, lies 21.5 km down Laxárdalur where the valley temporarily widens from ∼0.5 km to ∼1 km (L3). The final, and largest, rootless cone group lies 24 km from Mývatn and is made up of at least 43 S cones (L4). It is known locally as Rauðhólar, meaning 'red hills', due to the orange-red colour of the weathered scoria. There is no apparent size difference between cones in the Laxárdalur groups, although the number of cones in each group is too small for robust statistical analysis.

Figure 2.14: Comparison of different rootless tephra around Mývatn. a) Typical clast from the surface of a scoriaceous cone at Skútustaðir (group 6). Note that the tephra is black, shiny and contains lots of small vesicles and no sign of oxidation. b) Typical tephra from the surface of a scoriaceous cone north of Mývatn (group 18). Note that the outsides of the clasts are generally oxidised to red-orange, and lumps of paler sediment can be seen clinging to the outside of the central clast. Tephra often has fluidal outer surfaces. c) Cross section of the outer layer of a recycled bomb (missing core) from group 18. The inner surface is oxidised and the clast has fewer small vesicles but numerous large vesicles, compared to the Skútustaðir tephra in part a.

	Mývatn		Aðaldalur	
	Mean	Std Dev	Mean	Std Dev
SiO_2	49.95	0.17	50.06	0.22
CaCO	12.36	0.16	11.92	0.21
TiO_2	1.89	0.02	2.03	0.04
Al_2O_3	13.23	0.11	13.04	0.11
Na_2O	2.27	0.08	2.33	0.12
MgO	6.87	0.12	6.48	0.07
K_2O	0.21	0.01	0.22	0.01
FeO	12.75	0.12	13.46	0.08
Cl	0.01	0.00	0.01	0.01
MnO	0.22	0.02	0.23	0.01
P_2O_5	0.18	0.02	0.20	0.02
F	0.06	0.07	0.01	0.10
Temp (°C)	1175.0	3.11	1165.0	1.72

Table 2.3: Chemical composition (%) of rootless scoria samples from the Younger Laxá Lava at Mývatn and Aðaldalur. The Mývatn sample was taken from the surface of a rootless cone at Skútustaðir. The Aðaldalur sample was taken from a rootless cone along the inflation front half way down the valley. Temperature in °C at each location was calculated based on the MgO content after Putirka (2008). The mean and standard deviation were calculated based on 10 data points.

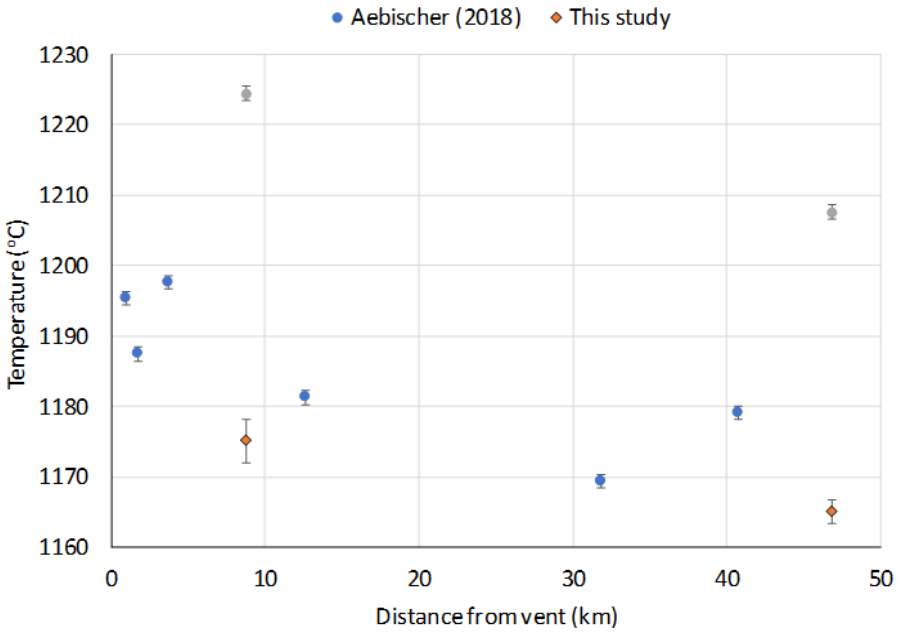

Figure 2.15: Temperature of the YLL with distance from the eruptive vent, calculated from MgO content of glassy samples. Data from this study is shown by orange diamonds with black outlines. Data from Aebischer (2018) is shown in blue circles for comparison. Outliers from the Aebischer dataset, where the temperature shown is higher than eruption temperature, are kept for completeness but shaded in grey.

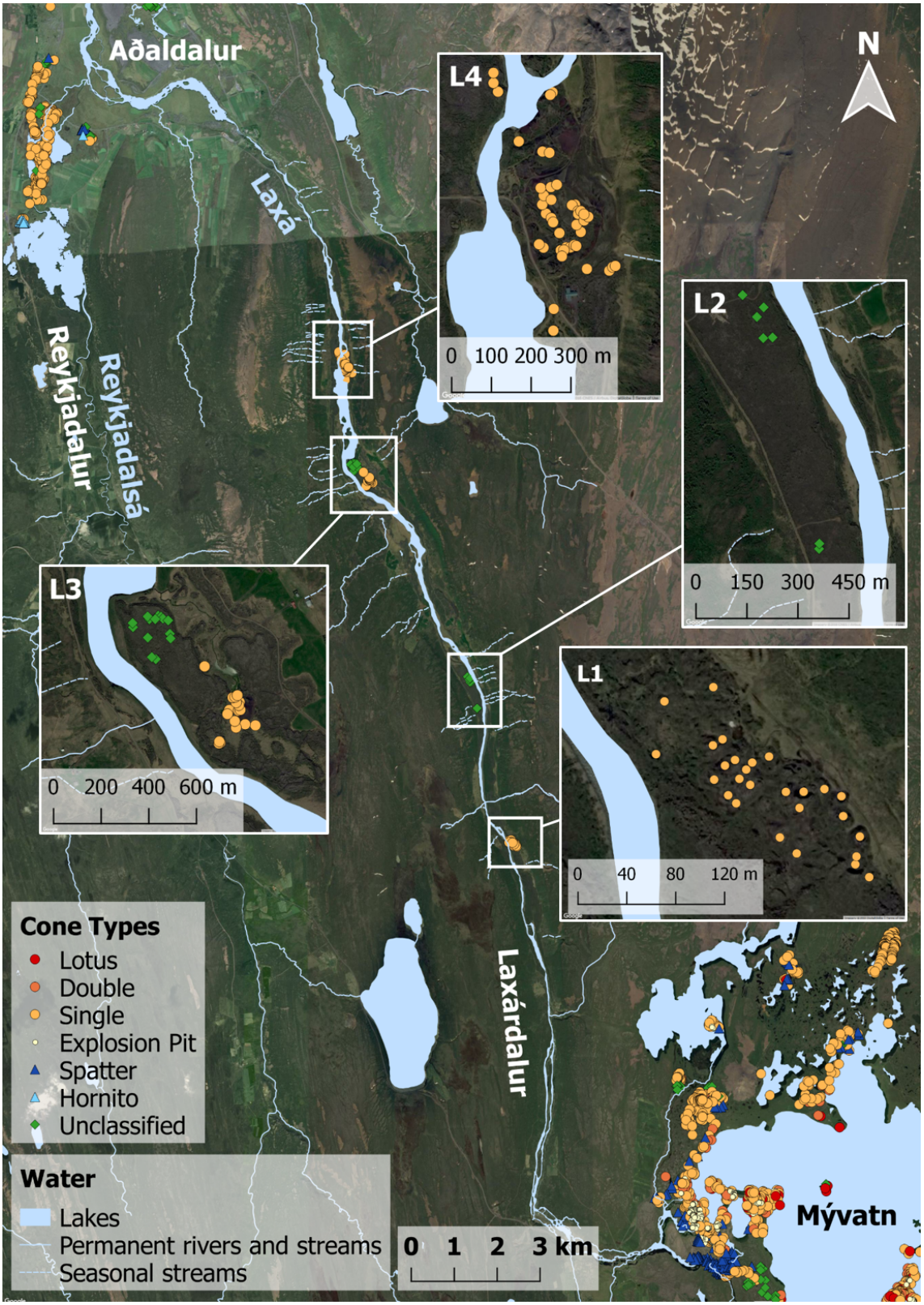

Figure 2.16: Rootless cone groups along Laxárdalur, with inset close-up views of each group. Map imagery ©2017 DigitalGlobe, CNES/Airbus. Map data ©2017 Google

Aðaldalur

As the YLL left the confines of Laxárdalur it spread out, filling the 3.7 km width of Aðaldalur and backing up into the adjacent Reykjadalur, initially covering the entire width of the valley but narrowing to the south (up the valley; Figure 2.17). Approximately 250 rootless cones are spread along the lava flow in Reykjadalur, with crater radii of 1.3–23.9 m, terminating in a group of ∼34 hornitos at the end of the lava flow (Figure 2.18i). These cones are currently surrounded by wetlands and small lakes.

In Aðaldalur proper, the first few kilometres of the lava flow have a ropy surface texture, with metre-scale folds visible in both the ArcticDEM and aerial photographs (Figure 2.18ii). Individual folds can often be traced for hundreds of metres and outline several broad lobes in the flow as it spread across the valley. There are no cones in this part of the flow. The first rootless cones (group B1 in Figure 2.17b; Figure 2.18ii) lie in a topographic depression on the eastern margin where the lava flow has no visible surface texture. Most of these cones form a single compact group (group B1.1), bordered by streams and a small lake (Figure 2.19). They are predominantly S cones with crater radii ranging from 1.7 m–19.1 m. They are closely spaced for their size and many of the cones overlap with their neighbours. The remaining cones in group B1 are smaller and more widely spread. The land around the central cone group is covered with ploughed fields, and the main road cuts straight through the central cone group. Therefore, it is possible that the central group and the outer cones were once part of a single continuous group.

A second group of cones, on the western side of the ropy pāhoehoe flow (group B2, Figure 2.17b), comprises several smaller sub-groups, the smallest being an isolated pair of cones. Cones are closely spaced within each sub-group, and the outer walls of adjacent cones often overlap. These cones are also located in a low-lying part of the lava flow amongst pools of standing water. A chain of S and SP cones and hornitos is spread over 2 km along the western margin of the YLL next to Fljótsheiði (group D in Figure 2.17b; Figure 2.18iv). Going north down the valley, the cones in this group change from predominantly S to a mix of S and SP cones. At the northern end, hornitos appear and eventually join up with groups C2 and H1 (Figure 2.18iii). The surface of the YLL in this region is featureless, both in the ArcticDEM and aerial photographs.

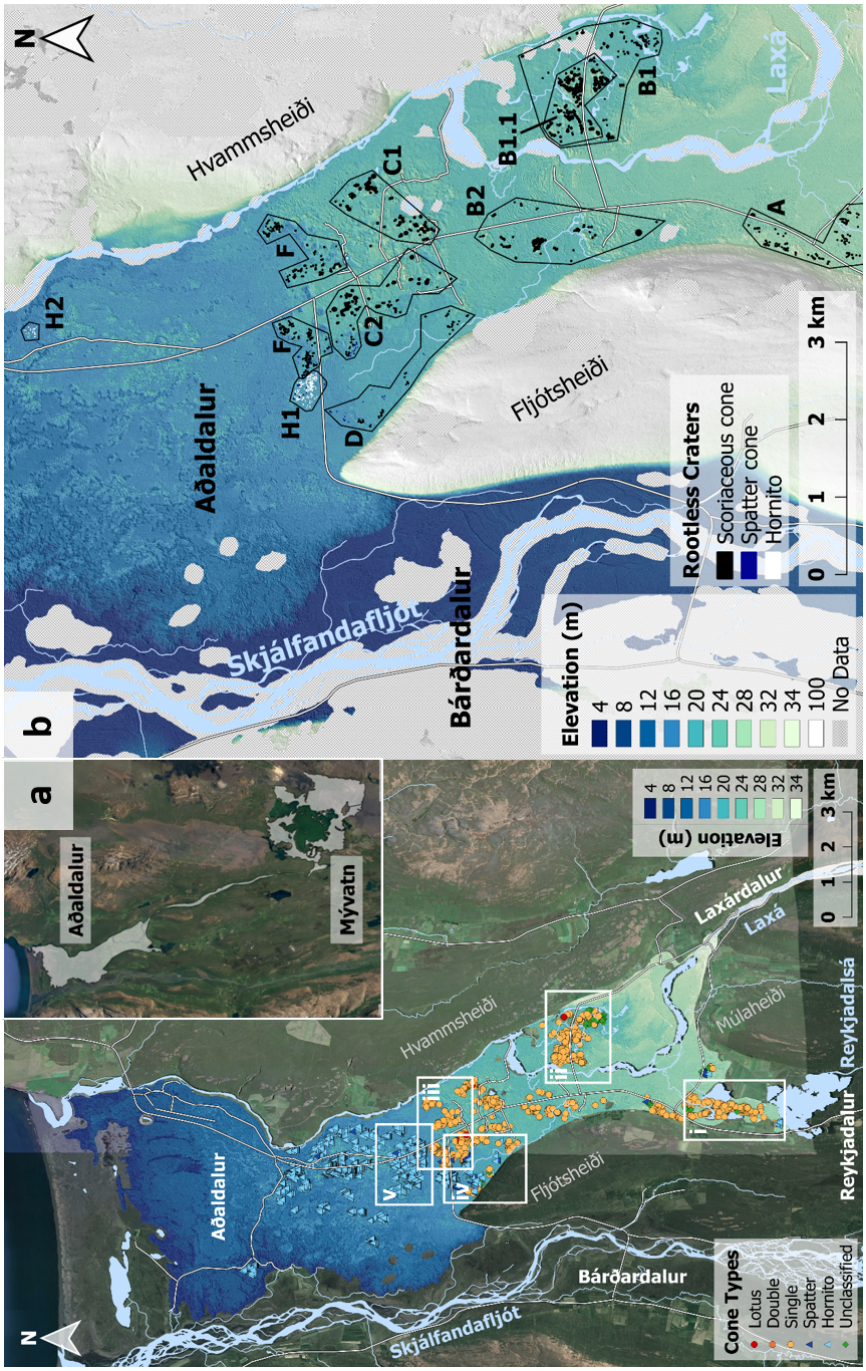

Figure 2.17: The Younger Laxá Lava in Aðaldalur and key geographical features. Elevation data are from the 2 m resolution ArcticDEM dataset, clipped to the extent of the YLL in Aðaldalur. Principal rivers in the area are shown by pale blue lines and labelled in blue text. Valleys are labelled in black text and mountains and hills between valleys are labelled in grey. a) View of Aðaldalur showing the elevation of the lava flow and the location of rootless cones and hornitos. Scoriaceous cones are represented by circles, spatter cones and hornitos by triangles. White boxes i–v correspond to the areas shown in Figure 2.18. b) The join between Aðaldalur and Bárðardalur, coloured by elevation. Cones have been grouped by their location on the lava flow and correspond to the groups described in Results. Note that the holes and gaps in the DEM are gaps in the ArcticDEM dataset and are cross-hatched in grey. DEM created by the Polar Geospatial Center from DigitalGlobe, Inc. imagery. Map imagery ©2017 DigitalGlobe, CNES/Airbus. Map data ©2017 Google

Approximately 6.5 km down Aðaldalur, the YLL morphology changes abruptly from ropy pāhoehoe to a flow surface marked by depressions several metres deep and wide, which is characteristic of inflated lava flows (Figure 2.18iii). We interpret the depressions as inflation pits, formed when the lava flowed around an obstacle and then inflated, leaving behind a pit in the surface of the flow (Hon et al., 1994; Self et al., 1998). The scoriaceous cones on this part of the YLL are among the largest in the valley; they are more widely separated than those further up the flow and do not form discrete clusters (groups C1 and C2 in Figure 2.17b).

The inflated region of the YLL terminates in a 4–6 m step down in the flow surface height, level with the northern end of the Fljótsheiði mountain (Figure 2.17b, Figure 2.18iii). Numerous small S cones are distributed along the up-flow (southern) side of this step (group F), bordered by clusters of SP cones that transition abruptly to hornitos on the down-flow side. The SP cones are similar in size to the small S cones along the step and are larger than the nearest hornitos (group H1). Notably, SP cones are almost entirely limited to this transitional region with the exception of a few isolated SP cones in group D and a cluster of eight SP cones at the edge of group A.

The YLL hosts ∼3800 hornitos, separated into several large groups. The hornitos are too small to see in the ArcticDEM but our high-resolution DTM of the transition region confirms that all of the hornitos fall on the down-flow side of the step, which is located where Aðaldalur joins the adjacent valley, Bárðardalur (Figure 2.17). The largest group contains 1422 hornitos and covers ∼1.18 km^2 (Figure 2.18v), almost twice the area of the largest group of scoriaceous cones in Aðaldalur (group B1; ∼0.66 km^2, 308 cones). This part of the flow also has a pitted texture, though much of the region is vegetated, obscuring the surface of the lava. Both aerial photographs and the ArcticDEM show a dried-up river bed (likely the former course of the Skjálfandafljót) that flowed up to and along the margin of the YLL. Small streams are still present around the edge of the lava flow. The surface of the lava in this region is broken up by pits and cracks (Figure 2.18v).

The YLL stopped approximately 18 km down the valley. There are no obvious changes in the surface morphology between the inflation front at the end of the lava flow, and the edge of the lava flow does not correspond to any features in the landscape that might mark an older coast. From this evidence, the lava does not appear to have reached the sea during the eruption.

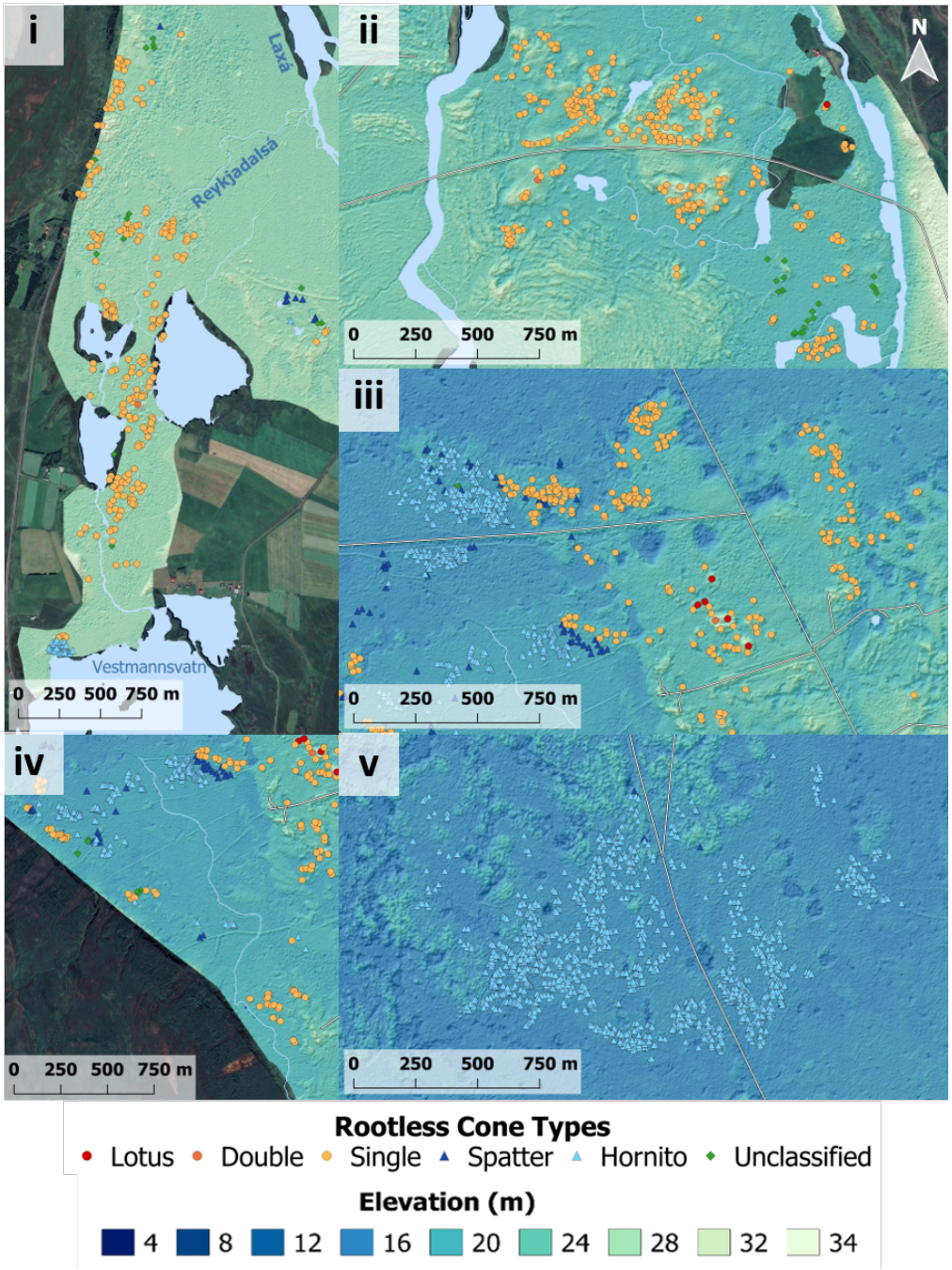

Figure 2.18: Close-up of key regions of the Younger Laxá Lava, corresponding to areas i–v in Figure 2.17. i) Scoriaceous cones and hornitos formed when the YLL backed up into Reykjadalur and dammed the Reykjadalsá river. ii) Scoriaceous rootless cones formed in a depression in the lava flow. The folds and wrinkles of ropey pahoehoe lava are visible in to the West of the cones. iii) Preserved inflation front marked with inflation pits. Scoriaceous cones are found along the front, with spatter cones and hornitos downstream of the front. iv) Scoriaceous and spatter cones and hornitos along the western edge of the YLL. v) Hornitos further down Aðaldalur. Inflation pits are visible, though the lava flow morphology is partially masked by vegetation. DEM created by the Polar Geospatial Center from DigitalGlobe, Inc. imagery. Map imagery ©2017 CNES/Airbus, DigitalGlobe, Landsat/Copernicus. Map data ©2017 Google

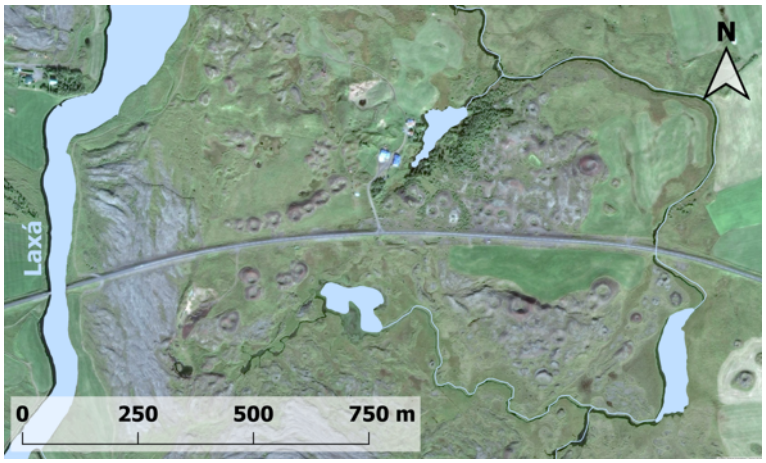

Figure 2.19: Rootless cones in Aðaldalur shown in Google Earth. The area shown is a closer view of that shown in Figure 2.18ii. Areas of standing water can be seen around the rootless cone group, connected by streams. Map imagery ©2017 DigitalGlobe, CNES/Airbus. Map data ©2017 Google.

2.4.2 Rootless cone size and spacing

Our statistical analysis is used to assess the variation in cone type, size and spacing within and between the different rootless cone sites across the YLL. From our analysis of the lava flow morphology and water availability in the environment today, we link this variation to the inferred lava supply and water availability at the time of the eruption and variations in the LWI dynamics.

The different cone types are not equally distributed across the three localities (Table 2.4, Figure 2.20a). Mývatn is dominated by scoriaceous cones with a high proportion of L and D cones (9.8 %) but no hornitos. In contrast, Aðaldalur hosts ∼3900 hornitos but far fewer L and D cones (0.22 %). Cones in Laxárdalur show little variation and are all either S or unclassified (i.e. S or SP). Regardless of cone type, there is a moderate positive correlation ($r = 0.56$, $p < 2.2e\text{-}16$) between log crater radius and log NN distance (Figures 2.20b), i.e. larger rootless cones tend to be further from their neighbours than smaller cones. Breaking the data down by locality shows that this correlation exists and is significant at both Mývatn ($r = 0.60$, $p < 2.2e\text{-}16$) and Aðaldalur ($r = 0.48$, $p < 2.2e\text{-}16$) but not in Laxárdalur ($r = 0.14$, $p = 0.16$; Table 2.5). There is a significant correlation between crater radius and NN distance for all cone types except hornitos ($r_H = 0.14$, $p = 0.074$), ranging from weak to moderately-strong ($r_L = 0.38$, $r_D = 0.50$, $r_S = 0.45$, $r_{SP} = 0.40$, $r_P = 0.60$, $r_U = 0.49$; $p < 0.005$ for all these types; subscripts denote cone type; see Table 2.5 for 95 % confidence intervals).

	Mývatn		Laxárdalur		Aðaldalur	
	Expected	Observed	Expected	Observed	Expected	Observed
Lotus	13.01	50	0.96	0	43.95	8
Double	22.56	97	1.66	0	75.78	3
Single	441.20	870	32.51	89	1482.29	997
Spatter	47.73	151	3.49	0	159.14	59
Pit	57.07	253	4.20	0	191.73	0
Hornito	881.95	0	65.00	0	2963.07	3910
Unclassified	29.77	72	2.19	21	100.3	39
Total		1493		110		5016

Table 2.4: Expected and observed distributions of different types of rootless cone across the YLL based on X^2 distribution modelling

Cone population	Population size (n)	Correlation coefficient (r)	p-value	95 % Confidence interval on r	
				Lower	Upper
All cones	2869	0.56	p <2.2e-16	0.54	0.59
All Mývatn cones	1493	0.60	p <2.2e-16	0.57	0.63
All Laxárdalur cones	110	0.14	p = 0.16		Not significant
All Aðaldalur cones	1266	0.48	p <2.2e-16	0.43	0.52
All lotus cones (L)	58	0.38	p = 0.0029	0.14	0.59
All double cones (D)	100	0.50	p = 1.1e-7	0.34	0.64
All single cones (S)	1956	0.45	p <2.2e-16	0.41	0.48
All spatter cones (SP)	208	0.40	p = 1.5e-9	0.28	0.51
All explosion pits (P)	253	0.60	p <2.2e-16	0.51	0.67
All measured hornitos (H)	162	0.14	p = 0.074		Not significant
All unclassified cones (U)	132	0.49	p = 2.1e-9	0.35	0.61

Table 2.5: Correlation coefficients and corresponding p-values and 95 % confidence intervals between cone size and NN distance for different populations of rootless cones on the YLL. We use the standard threshold of p <0.05 to assess significance

	Min	Q1	Median	Mean	Q3	Max	Std Dev	Mean +12.3%	Mean -14.1%
Lotus	4.85	13.51	20.34	22.28	28.52	64.38	12.47	25.02	19.10
Double	2.60	10.07	14.34	17.41	21.66	62.34	11.13	19.55	15.00
Single	0.78	3.08	4.70	6.18	7.62	41.59	4.73	6.97	5.30
Spatter	0.87	2.39	3.68	4.57	5.67	17.16	3.02	5.13	3.93
Pit	0.89	1.72	2.42	3.28	4.01	5.96	2.39	3.63	2.82
Hornito	0.23	0.48	0.64	0.79	1.01	3.00	0.44	0.89	0.68
Unclassified	1.14	2.44	3.39	4.66	5.22	19.35	3.63	5.23	4.00

Table 2.6: Rootless cone crater radius distributions by type (all dimensions in metres

The size (crater radius) of rootless cones on the YLL varies with cone type, although not all cone types are distinct (Table 2.6; Figure 2.20c). Specifically, there is no significant difference between the L and D cones. All other rootless cone types are significantly different in size from one another. L and D cones are on average larger than S cones (M_L = 22 m, M_D = 17 m, M_S = 6 m; M = mean, subscripts denote cone type), which in turn are larger than SP cones (M_{SP} = 5 m). Explosion pits are the next-smallest (M_P = 3 m), and hornitos are the smallest (M_H = 1 m). When comparing cones across all sites, unclassified cones and spatter cones are statistically indistinguishable (M_U = 5 m).

Rootless cone size varies with locality for all cone types (i.e. L, D, S and SP; Figure 2.20d–f; full table is available in the University of Bristol data repository at `https://data.bris.ac.uk/data/dataset/ojcw17r060lu21o7lbjeoftbf`). The crater radius of cones around Mývatn is, on average, larger than cones in Aðaldalur. There is no significant difference between the size of equivalent cones in Aðaldalur and Laxárdalur, but there are too few cones in Laxárdalur for a robust statistical test.

Rootless cones around Mývatn decrease in size with distance from the lake edge (Figure 2.21a). There is no significant size difference between cones on islands and those around the lake shore, although cones inland of the current lake shore are significantly smaller. The cones around the mouth of the Laxá river are the smallest. We note, however, that the extent of Mývatn was modified by the YLL, changing the distance between the cones and the lake. We divided the inland cones into two groups based on their proximity to the predicted lake before the eruption: groups 7, 9, 14–16 fall within the predicted lake (inland-1), and groups 17–18 fall on the predicted lake shore (inland-2). Comparing the crater radii of these two groups shows that they have statistically different size distributions. The inland-1 cone groups are similar to the shore and island cone groups (Figure 2.21b). The inland-2 cones are smaller and closer in size to those at the river mouth, although the types of cones that make up the river mouth and inland-2 groups are very different: inland-2 is over 90% S cones, whereas the river mouth group has a more even mix of S, SP and P cones (Figure 2.22).

In Aðaldalur, the crater size is affected by location on the lava flow (e.g. middle, margin or inflation front), both when considering all cone types, and when considering S cones only (Figure 2.23). Cones formed in the middle of the lava flow (groups B1, B2, C1 and C2) are larger than those at the margins of the flow or along the inflation front part-way down the valley (groups D and F). The cones in Reykjadalur (group A) fall between the size ranges of the ropy and inflated groups (B1, B2, C1, C2), and those on the flow margins (D and F).

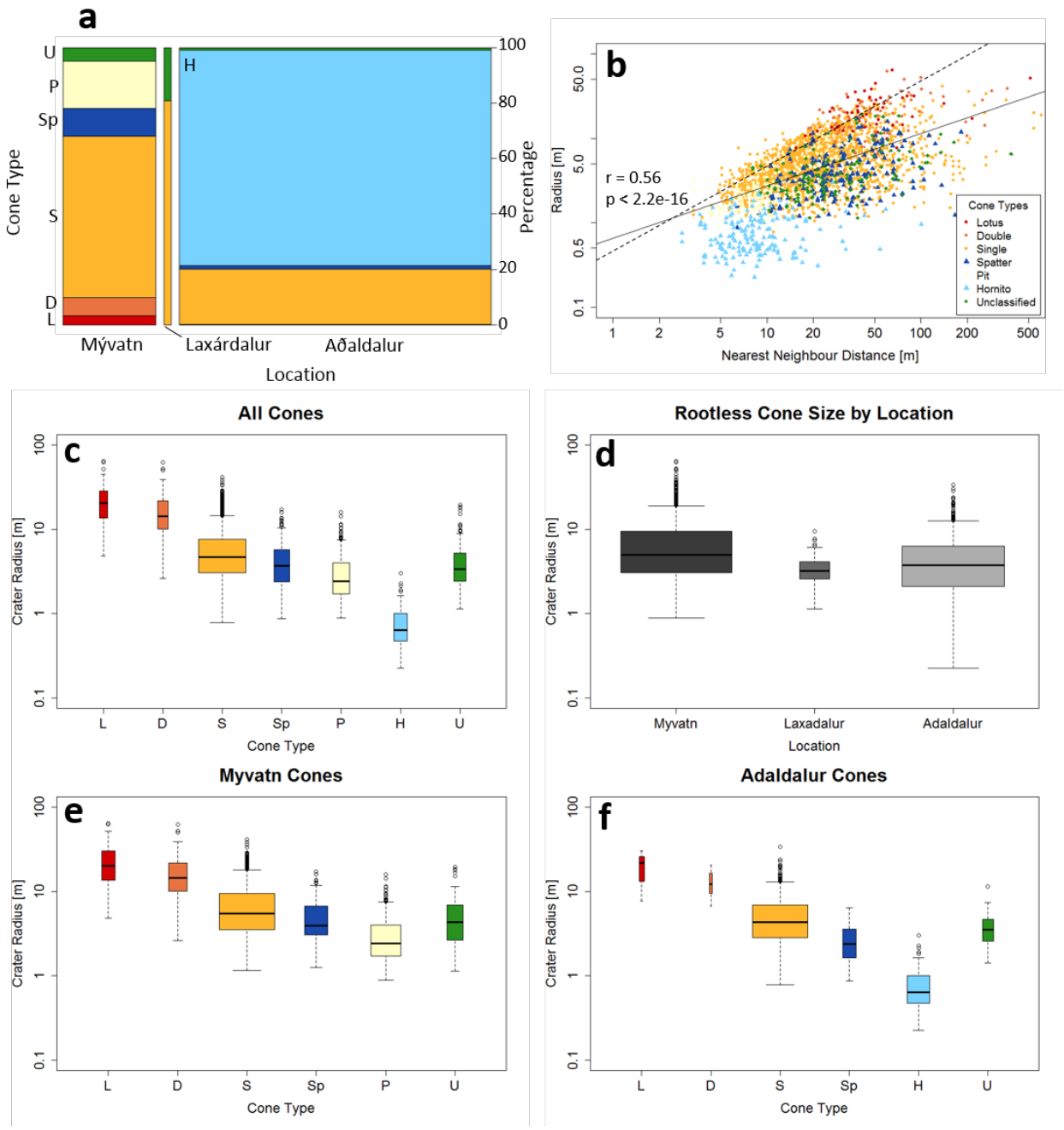

Figure 2.20: Rootless cone properties across the Younger Laxá Lava, coloured by cone type. a) Scatter plot of crater radius and nearest neighbour distance for all YLL cones. Solid line shows the correlation between cone size and NN distance, with correlation coefficient (r) and p-value quoted. Dashed line shows the relationship y = (x/2) i.e. the NN distance is half the crater radius (i.e. points above this line represent overlapping cones). b) Distribution of the different types of rootless cones in Mývatn, Laxárdalur and Aðaldalur. Cones are coloured using the same scheme as other Figures. Bar width is proportional to the number of cones in the sample. c–f) Variation in rootless cone crater size across the YLL, Mývatn, Laxárdalur and Aðaldalur respectively. Black circles represent data points that lie more than 1.5 times the inter-quartile range away from the median (outliers). Cones are coloured by type, consistent with the colour scheme used throughout this paper. Bar width is proportional to the number of cones in each sample.

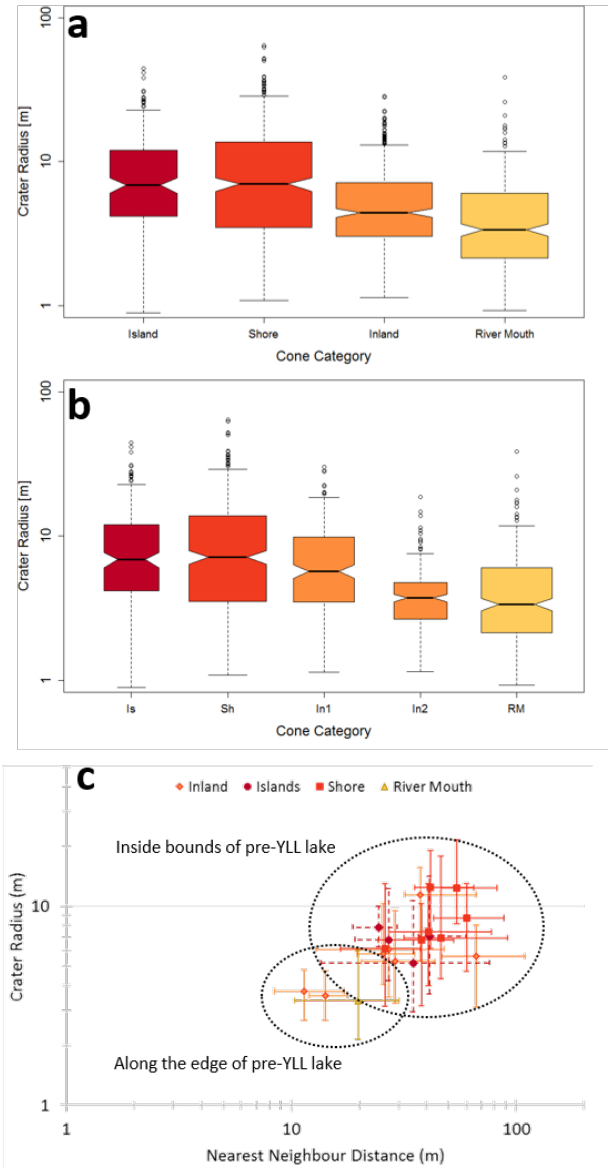

Figure 2.21: 8 Variation in crater size and spacing for Mývatn rootless cones, grouped by proximity to the lake shore lake (i.e. island, shore, inland or river mouth). a) Groups based on the proximity to the present-day lake. b) Modified groupings, with the inland cones split into those thought to be inside the bounds of the original lake (In1) and those thought to have been formed on the lake shore (In2). Box width is proportional to the number of cones in the group. c) Relationship between crater size and nearest neighbour distance for rootless cones at Mývatn. Each data point represents the median of a group of cones, and the error bars show the 1st and 3rd quartiles of that group. Data points are coloured by the proximity of the group to the current lake.

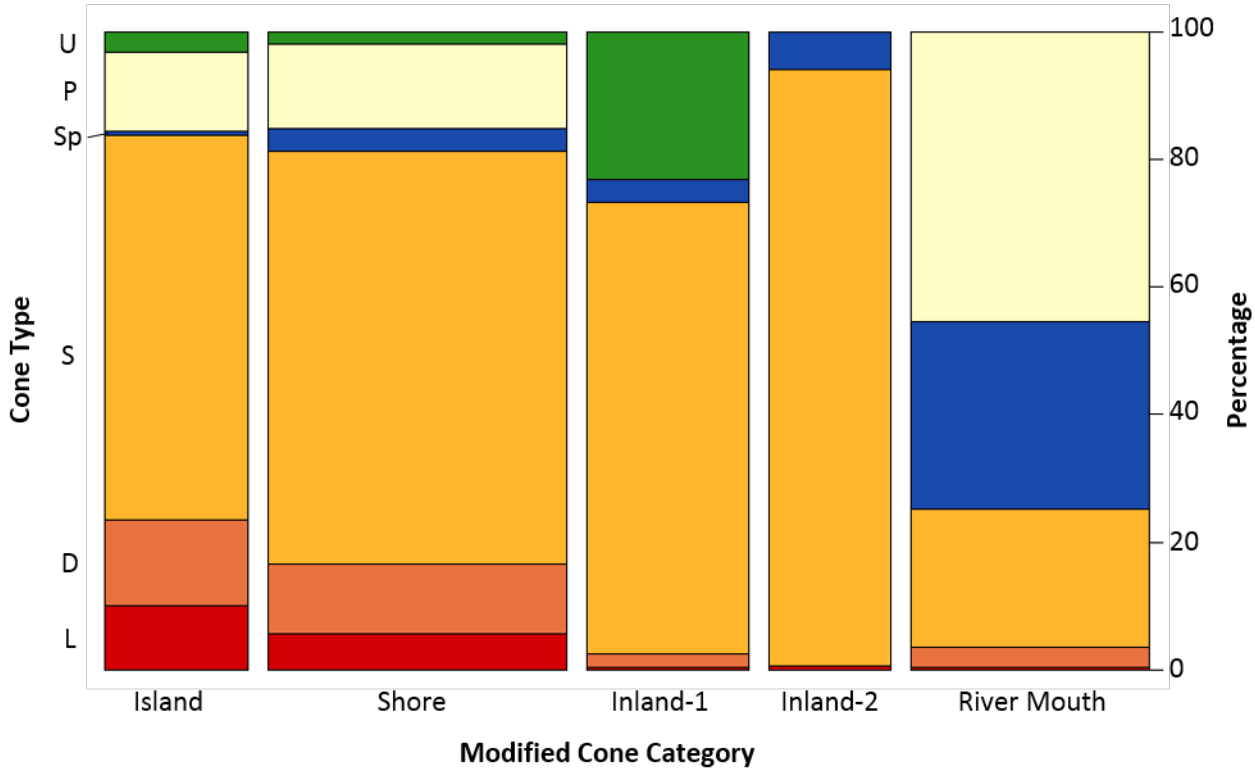

Figure 2.22: Variation in cone type with proximity to lake Mývatn; island (Is), shore (Sh), inland-1 (In1), inland-2 (In2) and river mouth (RM). Lotus cones (L) are shown in red, double-cratered cones (D) in orange, single cratered scoriaceous cones (S) in gold, spatter cones (SP) are in dark blue, explosion pits (P) in pale yellow and unclassified cones (U) in dark green.

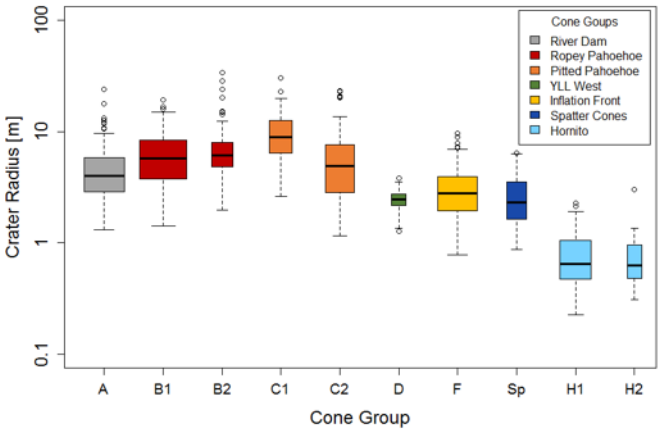

Figure 2.23: Variation in rootless cone crater radius for cone groups in Aðaldalur. Cones have been groups based on their location on the YLL, and group outlines are shown in Fig. 5.

Hornitos are the smallest rootless features in Aðaldalur and show very little variation in size across the valley (Figure 2.23). The two groups measured (H1 and H2) have almost identical size distributions and though this represents only a small sample of the hornitos in Aðaldalur, it matches our observations from the field. However, the spacing between the hornitos does change between the groups: those towards the end of the YLL (H2) are more widely spaced than those further up the valley (H1).

2.5 Discussion

The variation in types and sizes of rootless cones along the Younger Laxá Lava (YLL), from large multi-cratered scoriaceous cones to small spatter-rich hornitos, shows that there were considerable changes in the lava–water interaction (LWI) dynamics. Here, we explore how these changes relate to the environment in which the rootless cones formed, particularly the availability of lava and water. Our goal is to assess how the YLL was emplaced, what sources of water it encountered, how it affected these water sources, and finally how changes in lava flow and water availability affected the LWI dynamics and rootless cones formations.

The landscape and environment of the region today, along with studies of the area's post-glacial history, give an insight into the likely availability of water at the time of the eruption. We use the morphology and surface features of the YLL to assess flow development as it progressed from the eruptive vent, around lake Mývatn and through both the narrow Laxárdalur and wide Aðaldalur valleys. This provides context for our assessment of cone size, type, location and LWI dynamics.

2.5.1 What does the morphology of the YLL tell us about how it was emplaced?

Surface textures and features on the YLL show that the emplacement style varied substantially between the source vent near lake Mývatn and the flow terminus in Aðaldalur. We use these changes to examine how the lava flow responded to the environment. Lake Mývatn is close to the eruptive fissure, which supplied abundant lava from east the lake, as indicated by the broad flow lobes, lava channels and ponding at Dimmuborgir. The lava pillars, bathtub rings and other drainage features around Höfði show that the lava also ponded in this region. The extent of the YLL around the lake and the accompanying tephra blanket provide additional evidence for a high lava flux.

In Laxárdalur, much of the YLL surface has been obscured or eroded by the Laxá river, which has now reclaimed the gorge. However, the inferred 10 °C temperature drop over the 45 km (Figure 2.15) shows that the flow must have formed an insulating lava tube through the valley. The narrow width of the Laxádalur gorge (0.5–1 km) would have aided tube formation and efficient transport of lava to Aðaldalur.

The variety of surface morphologies on the YLL in Aðaldalur shows that the emplacement style changed as the flow progressed. The pressure ridges and flow lobes in the upper part of the valley imply that it was emplaced as a broad sheet, with a mass flow rate low enough to form a stable top crust but high enough to deform the crust as the lava advanced (Walker, 1971; Fink and Griffiths, 1992; Kerr et al., 2006). In contrast, the numerous pits on the flow surface further down the valley indicate inflation, possibly because of a reduction in flow advance rate because of the decreasing slope of the valley floor (e.g. Hon et al., 1994). The inflation pits must have formed as the lava diverted around obstacles in its path (Hon et al., 1994; Self et al., 1998). We propose that these pits were formed where a slowly-advancing lava front was quenched by pools of water, causing the flow to divert and inflate around the pool (Figure 2.24). Contact with the lava could cause the water to boil away, in which case the pool may be filled in by the advancing lava flow. However, a pit would still remain because of the inflation on either side of the pool. Some of larger pits are >9 m deep and still hold water, suggesting that they were not filled in with lava and the flow diverted around them. The rootless cones around these pits may be the result of faster-moving parts of the lava flow filling in pools and driving rootless eruptions from the saturated sediments underneath (group C cones).

2.5.2 What does the environment today tell us about water availability?

Einarsson (1982) showed that a larger and deeper lake existed at Mývatn before it was inundated by the YLL. He found that the lake bed was thickly coated with diatomaceous sediments, similar to those present in the lake today. Because diatoms have hollow silicate shells filled predominantly water, these sediments can hold a much more water than sediments limited by particle packing fraction (77–78% water, rising to 98% water in the top 60 cm; Einarsson et al., 1988). The water in these sediments would have been heated by contact with the YLL and released steam, driving rootless eruptions, as shown by the presence of sediments inside vesicles in rootless tephra (Einarsson, 1982).

The distribution of rootless cones around Mývatn allows us to reconstruct the outline of the

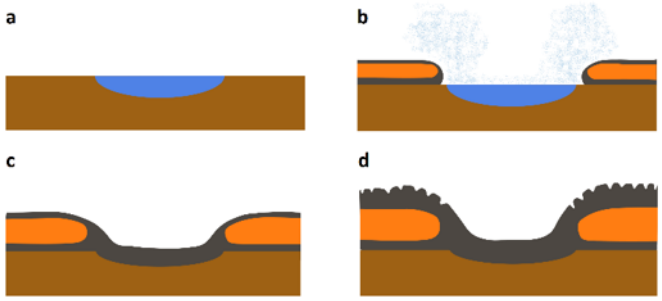

Figure 2.24: Model for the formation of inflation pits around a pool of water. a) Lava flow advances towards a pool of water (blue). b) Where the lava flow meets the water, the flow is quenched and stops advancing. The lava flow splits into lobes that flow either side of the pool. The pool is gradually boiled away or displaced by the lava flow c) The lobes on either side of the pool inflate as more lava is injected and the crust thickens with cooling. The pool is gradually covered over but because the water quenched the flow around the pool, it does not inflate. Eventually all of the water in the pool is boiled away or displaced. d) The lobes on either side of the pool continue to advance and inflate, joining up at the far side of the pool, leaving a pit in the surface of the lava flow.

original lake and extend Einarsson's (1982) original estimate (Figure 2.9b). The ArcticDEM shows that all but one of the cone groups around the lake have the same basal elevation of 279 m (Figure 2.9b), which indicates that the top surface of the YLL around Mývatn was remarkably level with constant thickness (∼10 m). Given the lava thickness and the presence of lake diatoms inside vesicles in rootles cones (Einarsson, 1982), the constant basal elevation of the cones suggests that they were all formed by lava interacting with the lake and lake sediments. This implies that the lake was not only larger than present, but probably linked with the smaller lake Sandvatn to the north. A more extensive lake and adjacent wetlands than at present explains the numerous scoriaceous rootless cones along the western shore and inland towards Sandvatn.

The group of cones near Dimmuborgir (group 21; 2.9a) has a mean basal elevation of 303.2 m (i.e. 24 m higher than the other groups and 27 m above the current lake level) but still includes diatoms consistent with the pre-existing lake (Einarsson, 1982), showing that the lake must have extended further east than at present. The difference in basal elevation is likely because the YLL is thicker in this area. No rootless cones are visible on the surface of the YLL between Dimmuborgir and the eastern edge of Mývatn, but construction of the road to Dimmuborgir revealed rootless cones buried under lava, confirming that there was sufficient water in this region to drive rootless eruptions. Given the presence of lake-dwelling diatoms in the Dimmuborgir cones (Einarsson, 1982), the edge of the pre-existing lake may have been the barrier that caused the lava flow to pond and create Dimmuborgir in the first place, rather than a water-filled fault as suggested by Skelton et al. (2016).

When the YLL reached the southwest corner of the lake, it would have blocked the flow of water into the Laxá. Comparable damming of rivers by lava was recorded during the 1783–84 Laki fissure eruption. Rev. Jón Steingrímsson, who witnessed and recorded the eruption, described how a "*cloud of smoke and steam moved along the gorge of the river Hverfisfljót*" and that "*in some channels, the water seethed with heat*" (Kunz, 1998), prior to the river level dropping and then drying up completely. It is reasonable to assume that a similar situation occurred as the YLL first heated the water in Mývatn and then dammed the Laxá, cutting off the main source of water in the gorge and leaving behind only small ponds and feeder streams from the surrounding highlands. In fact, all four cone groups in Laxárdalur coincide with the location of one of these feeder streams, although not all streams have associated rootless cones (Figure 2.16). The streams would also have built deltas of wet sediment, that could have held water and contributed to rootless cone formation.

Unlike the Laxá, the source of the Reykjadalsá was unaffected by the YLL, and provided a steady, if somewhat smaller, supply of water to the top of Aðaldalur. The easiest path for the YLL to follow into Reykjadalur was along the existing river channel. Damming the river would have caused localised flooding, similar to during the Laki fissure eruption. We suggest that the lakes at the mouth of Reykjadalur (Figure 2.18i are the remnants of flooding caused by the YLL damming the Reykjadalsá. These lakes would have provided a continuous supply of water to drive rootless cones along the edge of the lava flow.

Damming the two rivers cut off the supply of water to the southern part of Aðaldalur, leaving only the water contained in pools and dispersed in sediments in wetland areas. The numerous inflation pits with standing water may be the remains of some of these ponds. At the northern end of the Fljóstheiði mountain, Aðaldalur joins the adjacent Bárðardalur valley, which hosts the braided river Skjálfandafljót (Figure 2.17b). We found rounded pebbles consistent with a riverine environment embedded in a rootless cone in this part of the valley. We do not know the original position of the river, but the presence of river channels at the edge of the YLL (several hundred metres from the current path of the river; Figure 2.25) suggests that the river could have been a source of water for the northern part of Aðaldalur. The inflation front that lies level with the Aðaldalur–Bárðardalur valley confluence may reflect the lava flow encountering an area of increased water in the underlying sediment, most likely from a wetlands environment similar to that beyond the YLL today.

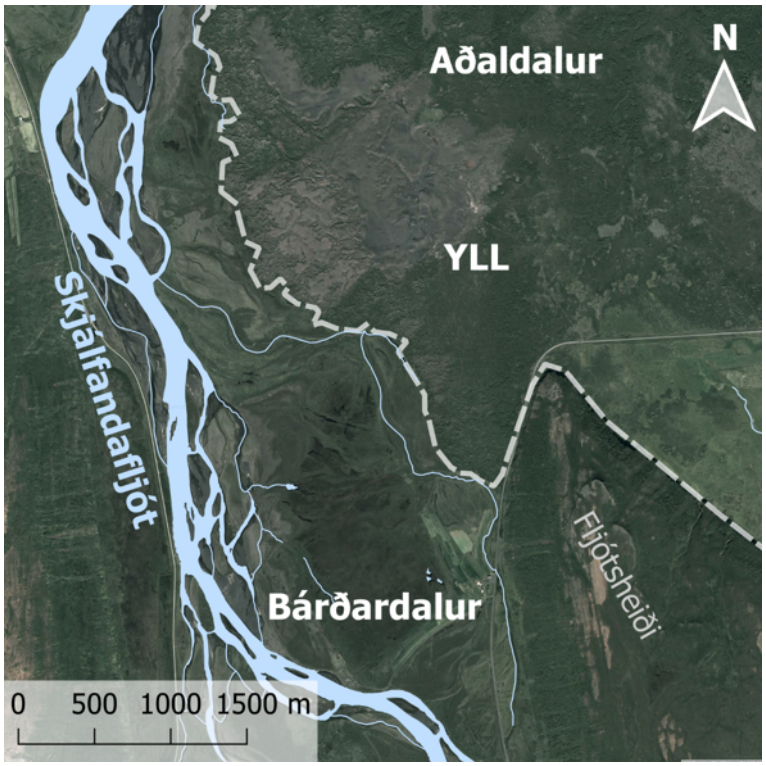

Figure 2.25: View of the join between Aðaldalur and Bárðardalur. The outline of the YLL in Aðaldalur is shown by the grey dashed line. The mountain between Aðaldalur and Bárðardalur is labelled in grey. The current path of the river Skjálfandafljót is shown with a solid blue line. Old riverbeds around the YLL are shown by dotted blue lines. Map imagery ©2017 DigitalGlobe, CNES/Airbus. Map data ©2017 Google.

2.5.3 How did the changes in lava and water availability affect LWI?

From the distribution of rootless cones across the YLL and the trends in cone type and size, we can draw links between the supplies of lava and water across Mývatn, Laxárdalur and Aðaldalur and the resulting rootless eruptions. It is reasonable to assume that cone location must reflect the water availability, since rootless eruptions require water. Similarly, we can relate cone size to the supply rates of lava and water: continuous or pulsed high volume-flux supplies of lava and water will be able to sustain long-duration rootless eruptions, building up large rootless cone edifices. More limited supplies of lava or water will produce shorter eruptions and smaller cones. Since rootless cones require a stable lava flow surface to support the edifice, this implies that the lava flow is relatively well established and lava supply rate will be controlled by the thickness of the molten flow core and the internal flow velocity (we note that LWI may take place before the flow is well established but not produce surviving deposits). Pyroclast type (ash, lapilli or spatter) is controlled by the intensity of the LWI (i.e. the rate of heat transfer from lava to water and the resulting rate of steam generation).

The largest cones are found around Mývatn, which is close to the eruptive vent and provided a sufficiently large and continuous supply of water to drive long duration LWI and build large cones. While the total available volumes of lava and water do not directly control the rates of heat transfer and steam generation, the high proportion of scoriaceous (L, D, S and P) cones around Mývatn shows that there must have been intense, explosive LWIs (Figure 2.20a). It is possible that the fine saturated lake sediments promoted this, and their presence inside vesicles in rootless cones suggests that they contributed to the rootless eruptions. Firstly, these sediments can retain a large volume of water (Einarsson et al., 1988) so would have increased the total available water. Secondly, their low permeability would speed the increase in pore pressure as the sediments were heated by lava. Finally, the lower density and viscosity contrasts between the lava and water-sediment mix could allow coarse mingling between the two, ultimately promoting FCI (White, 1996).

In contrast, in Aðaldalur the rootless cones are smaller, reflecting the more limited supply of water after the two rivers feeding the valley were dammed by the YLL. The shallow ($\sim 1^{o}$) slope of Aðaldalur fed by numerous rivers means that it has coarser sandy sediments and peat-like soils in wetland areas. Coarser sediments generally have higher permeability, reducing the pressure build-up as lava heats the interstitial water. In Laxárdalur, which dried up after the Laxá was dammed, sedimentary deltas from small streams probably provided water to drive rootless eruptions.

The down-flow change into spatter features (SP and H) suggests a shift to lower energy LWI. This change occurs where we believe the available water changed from isolated pools to a wetland environment. The lack of any scoria or ash deposits at SP and hornitos implies that the conditions were not right for explosive FCI, either because there was insufficient lava or water, or because the necessary high contact area between lava and water was not achieved. These SP cones are similar in size and texture to the deposits formed by bubble bursts in littoral settings (Mattox and Mangan, 1997), suggesting a similar mechanism. Since hornitos (and spatter cones) are built by successive layers of welded spatter, their width must be controlled ballistically by the kinetic energy of steam expansion that controls the spatter trajectories, whereas their height reflects the LWI duration. This suggests that wider features form from higher energy bubble bursts, and tall features form by longer duration events (e.g. longer series of bubble bursts).

In the following sections, we illustrate specific LWI scenarios using case studies across the YLL to show how the lava flux and water availability affected the LWI dynamics and the resulting rootless cones. Examples include the change in cone size around Mývatn, the link between cone size and lava flow morphology in Aðaldalur, and the transition from scoriaceous cones to hornitos in Aðaldalur. We then briefly discuss the effect of lava and water availability on NN distribution.

Changes in LWI around Mývatn

Our proposed new extent of pre-YLL Mývatn (Figure 2.9b) not only fits with the distribution of rootless cones around the lake, but also explains the observed variation in cone size. The inferred extent of the pre-YLL lake means that all of the rootless cones on the islands (Is), lake shore (Sh) and most of the inland groups (those categorised as In-1) would have formed within the lake and adjacent wetlands, which would have supplied these rootless eruption sites with a large and effectively continuous supply of lake water, and a high volumetric flux of lava from the nearby eruptive vent. This explains both the presence of large scoriaceous cones and the statistical similarity in size between these three cone groups (Figure 2.21). In contrast, the rootless cone groups that lie near the proposed edge of the lake and along the margins of the YLL (groups 17 and 18) would have had a lower supply of both lava and water. They are predominantly S cones (Figure 2.22), and their small size compared to the other Mývatn cones suggests shorter duration LWI, fitting with the reduced supplies of lava and water.

The high proportion of SP cones at the river mouth (group 20; Figure 2.22) suggests lower

intensity LWI. Comparing these cones with those nearby (group 20), we can see a marked transition in cone type: all of the cones in the interior of the lake are scoriaceous, with a high proportion of L and D cones, whereas those along the edges and the Laxá river channel are predominantly SP cones (Figure 2.9a). The reduction in intensity may reflect the reduced supply of water as the lava dammed the Laxá.

There is also evidence for passive (non-explosive) LWI around Mývatn, in the form of lava pillars at the south-east corner of the lake. Bathtub rings indicate that the lava ponded here and then drained in stages, similar to Dimmuborgir (Figure 2.10c). The lava pillars resemble those described by Gregg and Christle (2013) and Skelton et al. (2016), interpreted to have formed by steam escaping passively through ponded lava, freezing the surrounding lava (Figure 2.10b). The pillars at Mývatn may have been formed by the eastern edge of the lake or by feeder springs (Figure 2.9b); a steady supply of water from springs under deep, ponded lava may have been enough to establish permanent outlets for steam through the lava, preventing the steam pressure from building up to explosive levels.

The buried cones on the road towards Dimmuborgir show that the scarcity of rootless cones along the eastern shore of the lake is not because there was no LWI, but because any rootless cones formed were buried by later lava flows. Buried rootless cones are also found in the Columbia River Flood Basalts (Reynolds et al., 2015). These examples suggest that rootless eruptions are more common than surviving deposits suggest.

Aðaldalur: the effect of local water and lava availability

The range of cone sizes and types across Aðaldalur show that the LWI dynamics varied throughout the valley. By looking at the different groups in detail, their position on the lava flow and the sources of environmental water, we can infer the effect of lava and water availability on rootless eruptions.

In the main part of Aðaldalur, rootless cone size varies with position on the lava flow. S cones make up the vast majority (98.9%) of the scoriaceous cones in this region, so to simplify the statistical modelling we consider only S cones. Cones that formed in the middle of the YLL, both on ropy and inflated pāhoehoe, are, on average, 2–3 times larger than those formed at the edge of the flow and along the inflation front (Figure 2.23). This difference could reflect changes in the local lava mass flow rate, the availability of water, or both.

The location of group B1 in a topographic depression and the close NN spacing suggests that here the YLL flowed into a low-lying area of the valley with a contained supply of water.

Figure 2.19 shows that the group are surrounded by water, which may be the remnants of a pre-existing small lake. We propose that the YLL overwhelmed this lake and that water trapped in the basin and sediment drove intense rootless eruptions (group B1.1). The smaller cones in the rest of B1 were formed by more distributed water in a wetland-type environment around the central lake. The ropy, sheet-flow morphology of the YLL in this area suggests there was a continuous supply of lava, implying that the LWI was not lava-limited. Therefore, the size of the rootless cones was probably controlled by the limited availability of water in the lake and sediment.

The largest rootless cones in Aðaldalur formed on the inflated region of the YLL (Figure 2.23). The inflated flow morphology shows that the bulk advection rate of the lava flow had slowed. This slower emplacement would allow the lava front to be quenched and diverted by small pools of water, further slowing its advance and creating numerous inflation pits (Figure 2.24). The diversion of flow around pools would have concentrated the lava into lobes, rather than a broad sheet, although there are no sinuous ridges or tumuli to indicate a long-lived tube system. The rootless cones do not fall into well-defined groups (C1 and C2 in Figure 2.17b), but the numbers of both inflation pits and cones suggest that there was plenty of standing water, probably from wetlands and scattered pools. The similarity in cone size and types between the ropy (groups B1 and B2) and inflated (groups C1 and C2) regions suggests that the dynamics of the LWI were not significantly affected by the concentration of lava into lobes, which could have compensated for the reduced bulk flow rate (Figure 2.23). The rootless cones in this region probably formed on pockets of water that were too small to quench the lava but sufficiently large to fuel rootless eruptions.

In contrast, rootless cones on the western margin of Aðaldalur and along the inflation front (groups D and F) are significantly smaller than those in the middle of the YLL (Figure 2.23). This could record a reduction in either the local lava mass flow rate, or the availability of water, or both. Group D cones record the presence of some water along the western edge of Aðaldalur, most likely the remains of the Reykjadalsá after it was dammed by the YLL. However, the sparseness and small size of these cones, as well as their position along the edge of the lava flow, suggest that neither water nor lava was plentiful. Therefore, we cannot separate the effects of water and lava on cone size for this group.

The hundreds of small rootless cones along the inflation front, in contrast, suggest a plentiful and widely distributed source of water in the area, probably distributed in the underlying sediment rather than contained within discrete pools, and an evenly distributed supply of lava along the inflation front. We suggest that this combination of a lower, more distributed supply of both lava and water drove numerous, short-lived rootless eruptions along the

inflation front, creating the smaller, more closely spaced rootless cones in this region.

In summary, although we cannot completely distinguish the individual effects of lava and water availability on LWI, placing the trends in cone size and spacing found in our statistical analysis in the context of the lava flow morphology and available water helps interpret the variation in the deposits.

The change from scoriaceous cones to hornitos

The trends discussed above relate to the variation in S cones, but the lower part of Aðaldalur is covered almost exclusively in hornitos. The abrupt change from predominantly scoriaceous cones to hornitos marks a step-change in the dynamics of LWI in the valley and coincides with the position of the YLL inflation front. Moreover, almost all of the SP cones in Aðaldalur are found along this boundary (Figure 2.18c). Their location and intermediate size between small S cones and hornitos suggests that SP cones are transitional features, produced as the rootless eruptions changed from explosions capable of producing ash and scoria to milder eruptions, generating only spatter. The stalling of the lava flow and the concentration of rootless cones along the inflation front suggest the presence of widespread water at or near the surface (i.e. an increase in saturation of the underlying sediment). Therefore, it is likely that the shift in LWI style that formed the hornitos is also linked to this change.

The hornitos in Aðaldalur are widespread, covering an estimated 2.5 km^2. UAS surveys near the inflation front and at the far end of the YLL, and broader field observations, indicate that there is very little variation in hornito size across the valley. The two sample groups (H1, H2) are statistically indistinguishable and have the lowest variation in crater size of any rootless cone type (Figure 2.23). This lack of variation implies that there was little change in either the supply of lava or availability of water across this part of the flow. Hornitos on top of lava tubes are formed by low energy degassing and spattering, and it is likely that the hornitos in Aðaldalur were formed in a similar way. In the case of Aðaldalur hornitos, however, the driving force was steam escaping from a widely distributed water source under the lava flow, probably underlying saturated sediments. Another lava flow with large numbers of hornitos is in the Wudalianchi National Park in China, where lava flowed over a shallow lake (Gao et al., 2013).

The change in dynamics of the LWI from explosive to bubble-burst eruptions, and the implied reduction in LWI intensity, suggests that the rate of heat transfer between lava and water, and therefore the rate of steam generation, decreased significantly beyond the inflation front. We cannot be certain why the intensity dropped, but we suggest three factors that would have a

strong influence. Firstly, the widespread formation of hornitos required a widely distributed water source, most likely saturated sediment. Where lava interacts with contained water (e.g. a lake or pool), most of heat transferred from the lava will generate steam. The presence of sediment, however, would act as a contaminant that reduces the heat transfer rate between the lava and water by absorbing some of the heat itself (White, 1996). Secondly, hornitos are >50 km from the eruptive fissure. On its journey through Laxárdalur, the YLL was well insulated by a lava tube formed in a narrow valley. However, as the lava spread out across Aðaldalur, the surface area to volume ratio increased, increasing the cooling rate of the lava. This is reflected in the change in flow morphology from an insulated tube to a broad sheet flow and then to an inflated flow. Thirdly, the type of sediment in the valley may have contributed to hornito formation. Wetland environments in Iceland today have peaty soils that hold lower volumes of water than lake sediments. Peaty soils would not readily mingle with lava, hindering FCI. However, if the YLL caused an underlying peat bog to burn, it would release CO_2 and methane. Because peat burns slowly, these volatiles would build up until they could overcome the confining pressure of the lava flow as bubble bursts and building up hornitos. The lava flow is a few metres thinner downstream of the inflation front, indicating a diminished lava supply and therefore lower confining pressure on the underlying sediment. The low energy release of these hot gasses may have generated spatter and contributed to hornito formation. It is possible that the combination of a lower supply rate, cooler lava and slow rates of water release would lead to passive steam escape through the YLL in bubble-bursts, creating spatter cones and hornitos instead of scoriaceous rootless cones.

The relationship between cone size and spacing

The analysis and discussion so far have considered rootless cones forming in isolation, but many cones form in close proximity to their neighbours, often overlapping. This raises the possibility of adjacent cones interacting with one another during formation. The correlation between crater size and NN distance suggests that cone spacing is also controlled by the supply of water and lava to the rootless eruption sites (Figure 2.20b).

We use the heuristic model that adjacent rootless cones compete for a limited supply of water (Hamilton et al., 2010b) to consider the effect of NN interaction on cone size. In this model, the size of an active rootless cone would be limited by the proximity of its neighbours, which would 'compete' for resources (i.e. lava and water). If active cones are close together, there will be less water and lava available for each rootless eruption site, limiting the duration of

the LWI, and therefore cone size. This explains the correlation between cone size and NN distance found in this study for all cones except hornitos.

Hornitos have the lowest size variability of any type of rootless cone, and their size does not correlate with NN distance. This fits with our suggestion that the dynamics of LWI creating hornitos are substantially different to other rootless cones. Hornitos sit at the lowest energy end of the LWI spectrum, formed by spattering more akin to bubble bursts than explosions. The low energy of this interaction is more likely to limit their size than competition from nearby hornitos.

2.6 Summary

The YLL and its associated rootless cones provide an excellent case study for understanding the dynamics of LWI during lava flow emplacement. Comparing the rootless cones in Mývatn, Laxárdalur and Aðaldalur shows the effect of the supply of water and lava on the type and size of the cones formed. The cone distribution around Mývatn reveals the extent of the pre-existing lake, showing how it was modified by the YLL. Rootless cone size is related to proximity to the original lake, with larger cones found nearer the middle of the lake, and smaller cones around the edges, reflecting the availability of water. Damming of the river Laxá at the outlet from Mývatn explains the relative scarcity and small size of cones in Laxárdalur, as well as their location where smaller streams and channels drain the surrounding hills. Laxárdalur's narrow aspect, together with upstream damming, permitted thermally efficient transport of lava through the valley, probably via an insulating lava tube. The different cone groups in Aðaldalur reflect the different water sources that the YLL encountered and how it interacted with them: damming and flooding a river flowing in from the adjacent valley, inundating small lakes and pools, or bypassing and inflating around them. The smaller rootless cones found along the edges of the lava flow and along the inflation front demonstrate the effect of a lower local mass flow rate of lava compared to the middle of the lava flow. The abrupt change from scoriaceous cones to spatter cones and hornitos in Aðaldalur, coincident with a preserved inflation front, suggests a change in LWI dynamic, probably a response to the substrate changing to a wetland environment with abundant water distributed throughout the sediment rather than in discrete pools. Stalling and inflation of the YLL reflect this change in substrate; water-logged sediment would increase the cooling at the base of the flow and drive the formation of rootless cones seen all along the inflation front.

From our observations, we predict the types rootless cones that would be expected for given lava and water supplies. Environments with abundant water and lava (e.g. a large lake close to the eruptive vent) create larger rootless cones and a higher proportion of multi-cratered cones. In contrast, areas where there is less available water, such as (temporarily dammed) river valleys, smaller lakes or wetlands, produce fewer and smaller rootless cones. Similarly, rootless cones along inflation fronts and the edges of lava flows are smaller because of the reduced local mass flow rate of lava. The size of the rootless cones also correlates with the distance to their NN and may be the result of adjacent cones 'competing' for finite amounts water and lava, reducing the duration of the LWI and limiting the size of the resulting cones. The spacing of the cones will also depend on the distribution of water: concentrated and plentiful water supplies will produce discrete clusters rather than widely distributed rootless cones. With decreasing intensity of LWI comes a change in rootless eruption dynamics, from cones of scoria and ash to spatter cones and hornitos suggestive of littoral bubble bursts (Mattox and Mangan, 1997). At the lowest energy end of the LWI spectrum, large fields of hornitos can be created, most likely as a result of steam escaping through a lava flow from a saturated substrate.

Using case studies like the YLL to link rootless cone type and size to lava supply and water availability gives us insight into how these factors affect rootless eruption dynamics. Understanding the type of cones likely to form in different conditions can inform hazard assessments for future lava flows interacting with water and helps us interpret existing deposits on Earth and Mars.

Chapter 3

Hazards from lava–river interactions during the 1783–1784 Laki fissure eruption

Author contributions and declaration: This chapter is based on a paper published in the Geological Society of America Bulletin: Boreham, F., Cashman, K.V., and Rust, A., 2020, Hazards from lava–river interactions during the 1783–1784 Laki fissure eruption, *Geological Society of America Bulletin*, 132, pp. 2651–2668. The paper has been edited to make it flow better as part of a thesis. Some of the Background sections of the paper have been moved to the thesis Introduction. Additionally, some of the supplementary material and figures from the original paper have been incorporated into this chapter.

Frances Boreham read, analysed and compiled references to lava–water interactions in contemporary sources. All digitising and measuring of rootless cones, statistical modelling, and morphological analysis of the lava flow was also done by Frances Boreham. Digital terrain models of Iceland were provided by the Polar Geospatial Center under NSF OPP awards 1043681, 1559691 and 1542736. Samples from the Laki lava flow and Landbrots cones were collected by Frances Boreham in July 2016, with help from Jennifer Saxby. Alison Rust collected samples from the group 8 Laki rootless cones in July 2018. Sample preparation and electron probe microanalysis was done by Frances Boreham, with help from Stuart Kearns. Frances Boreham prepared the bulk of the manuscript, incorporating comments and feedback from Kathy Cashman and Alison Rust. The paper was also greatly improved by reviews from Marie-Noelle Guilbaud, Ryan Crow, Stephen Self, Michael Ort, and one anonymous reviewer. Please note that spelling in this chapter uses American English, as it was published

in an American journal.

Supplementary figures and tables for this chapter are included in Appendix B. Additional supplementary data and files are available through the University of Bristol Data Repository at: `https://data.bris.ac.uk/data/dataset/ch1ck57uyjms2m9c7pb7svuke`.

Abstract

Interactions between lava flows and surface water are not always considered in hazard assessments, despite abundant historical and geological evidence that they can create significant secondary hazards (e.g. floods, steam explosions). We combine contemporary accounts of the 1783–1784 Laki fissure eruption in southern Iceland with morphological analysis of the geological deposits to reconstruct the lava–water interactions and their impact on residents. We find that lava disrupted the local river systems, impounded water that flooded farms and impeded travel, and drove steam explosions that created at least 2979 rootless cones on the lava flow.

Using aerial photographs and satellite-derived digital terrain models, we mapped and measured 12 of the 15 rootless cone groups on the Laki lava field. We have identified one new rootless cone group and provide data that suggest another cone group previously attributed to the 939–940 AD Eldgjá eruption was created by the Laki eruption. We then use contemporary accounts to estimate formation dates and environments for each cone group, which formed in wetland/lake areas, on riverbeds and near areas of impounded water. Furthermore, comparison with previous field studies shows that assessments using remote sensing can be used to identify and map meter-scale and larger features on a lava flow, although remote mapping lacks the detail of field observations.

Our findings highlight the different ways in which lava can interact with surface water, threatening people, property, water supplies, and infrastructure. For these reasons, anticipation of such interactions is important in lava flow hazard assessment in regions with abundant surface water; we further demonstrate that remote sensing can be an effective tool for identifying lava–water interactions in past lava flows.

3.1 Introduction

Interactions between lava flows and surface water or ice are common and are responsible for a wide range of deposits and hazards (e.g. Fagents and Thordarson, 2007). While most of these interactions occur in coastal settings, there is also abundant geological evidence for lava flows interacting with and disrupting river systems (e.g. Fenton et al., 2004; Crow et al., 2008; O'Connor and Burns, 2009; Ely et al., 2012; Deligne, 2012). However, most studies of lava–river interactions focus on river and landscape evolution, and they are rarely considered for lava flow hazard assessments (Deligne et al., 2016).

The 1783–1784 Laki fissure eruption in southern Iceland presents an excellent case study of the interactions between a large lava flow and the surrounding hydrology. The eruption

occurred in a particularly wet part of Iceland and disrupted two major river systems, as recorded by contemporary observers of the eruption, especially the Rev. Jón Steingrímsson (1728–1791; Björnsson, 1783; Steingrímsson 1783a and b; Steingrímsson et al., 1783; Jónsson, 1784; Pálsson, 1784; Stephensen, 1785; Einarsson et al., 1984; Kunz, 1998; Fell, 2002). These accounts have allowed volcanologists to reconstruct the evolution of the eruption in great detail, from the dates when each individual fissure segment opened and the progression of the lava flow to the immediate and long-term effects on the local communities (e.g. Thordarson and Self, 1993; Thordarson, 2003; Thordarson et al., 2003). However, less attention has been paid to the parts of these eyewitness accounts related to the interaction of lava flows with surface water.

Because so much is known about the Laki eruption, both from analysis of historical accounts (e.g. Kunz, 1998; Thordarson et al., 2003) and from recent detailed field studies (Thordarson and Self, 1993; Thordarson et al., 1996; Thordarson et al., 1998; Bruno et al., 2004; Guilbaud et al., 2005; Hamilton et al., 2010a; b), it also presents an opportunity to test the use of remote sensing as a tool for broad-scale assessments of lava flows and morphological evidence for their interaction with water. Remote sensing through satellite-derived data, particularly with the advent of high-resolution digital terrain models such as the 2 m/pixel ArcticDEM, offers an efficient method for assessing entire lava fields. It allows volcanologists, geomorphologists and hazard assessors to take a whole-flow view and can help identify features that may not be obvious on the ground. It also opens areas that may be otherwise inaccessible and can strip away the masking effects of vegetation. Remote sensing, however, has its limitations: spatial resolution is often poor compared to ground-based techniques, and field studies are vital for ground-truthing interpretations. Here we examine the Laki lava flow field using both satellite images and the high-resolution ArcticDEM, and compare the results with the findings of previous field-based studies. Our aim is to show the capabilities and limitations of remote sensing for hazard mapping. Toward this end, we also use contemporary accounts of the Laki eruption to constrain the spatial locations of the observed interactions between the lava flow and the local hydrologic system. We highlight not only the range of hazards caused by lava–water interactions during the eruption, but also their effect on the local population. We also review and assess the deposits of explosive lava–water interactions (rootless cones) across the Laki lava field, and compare the data that can be obtained through remote sensing with previous ground-based studies. Finally, we take a broad view and discuss the hazards posed by lava–water interactions in future eruptions, the implications for hazard assessments and planning scenarios, and how remote sensing can be best used in these situations to help emergency planners.

3.2 Background

3.2.1 1783–1784 Laki fissure eruption

The Laki fissure eruption took place in the Síða highlands, ∼50 km inland from Iceland's south coast. The fissure lies in Iceland's Eastern Volcanic Zone, an embryonic rift system on the spreading center between the North American and European tectonic plates (Thordarson and Höskuldsson, 2008). It is part of the Grímsvötn Volcanic System, which stretches ∼70 km from Laki in the southwest to the Grímsvötn caldera under the Vatnajökull icecap in the northeast (Figure 3.1A; e.g. Sigmarsson et al., 1991; Thordarson and Larsen, 2007). The eruption was named after Mt Laki, a pre-existing mountain that is cut by the fissure (Thordarson et al., 2003). It is also referred to as the Skaftár Fires, because the lava occupied the gorge of the river Skaftá. The crater row is known as Lakagígar.

Numerous parallel fissures of Plio-Pleistocene and Holocene age record the long history of volcano-tectonic activity in the region (Thordarson and Larsen, 2007). One of these parallel fissures is from the 939–940 CE Eldgjá eruption fed by Katla volcano, which erupted 19.7 km^3 of lava and 1.3 km^3 of tephra, and partly underlies the Laki lava field (Figure 3.1A; Moreland et al., 2019). The Eldgjá lava created an extensive group of >4000 rootless cones covering ∼50 km^2 in the Landbrot district (Figure 3.1A; Thorarinsson, 1953), some of which have been buried by the Laki lava (Guilbaud et al., 2005).

The Laki fissure eruption lasted from June 1783 to February 1784 (Thordarson and Self, 1993). Over that period, 14.7 km^3 (dense rock equivalent) of lava and tephra as erupted, along with 122 Tg of SO_2 (Thordarson et al., 1996). The resulting cooling contributed to crop failure across Europe and North America (Schmidt et al., 2011 and 2012) and has been linked to excess mortality across Europe (e.g. Grattan et al., 2003; Witham and Oppenheimer, 2004). Locally, famine killed >20% of Iceland's inhabitants (Thordarson et al., 2003). Previous studies (Thordarson and Self, 1993; Thordarson, 2003; Thordarson et al., 2003) have established a detailed chronology of the eruption from physical volcanological evidence and analysis of contemporary reports, which we briefly summarize here.

The eruption started on 8^{th} June 1783 after 3 weeks of felt seismic unrest, with the opening of the first of ten fissure segments (Thordarson and Self, 1993; Thordarson et al., 2003). Over the following 8 months, the fissure propagated from south-west to north-east. Throughout June and July, fissure segments 1-5 opened on the south-west side of Mt Laki. Lava was channeled through the Úlfarsdalur and Varmárdalur valleys into the deep and narrow Skaftá

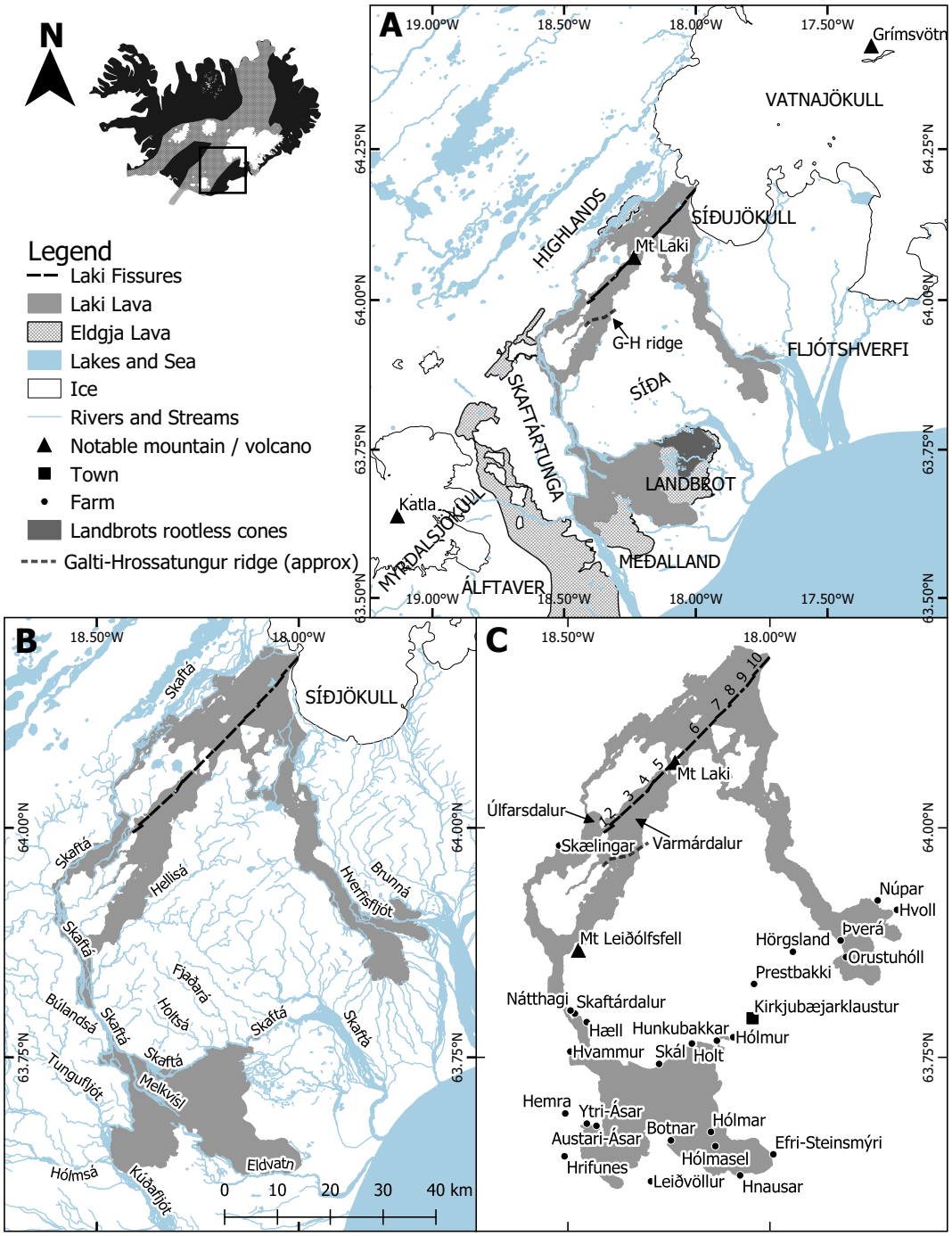

Figure 3.1: Overview of the Laki region showing the extent of the 1783-1784 lava flow (grey) and major landmarks. (A) Laki lava field in relation to the different regions affected by the eruption, the underlying Eldgjá lava field (hatched light grey, based on Thordarson et al., 2001), and the Katla and Grímsvötn volcanic centers (black triangles). (B) Hydrological map of the region surrounding the Laki lava field, noting the key rivers that interacted with the lava. (C) Key locations across the Laki region. Farms are marked by small black circles, and the local town of Kirkjubæjarklaustur is shown with a black square. Key mountains are marked by black triangles. The individual vents of the Laki fissure are shown by the black line and numbered in the order in which they opened. **Inset**: Iceland and its volcanic zones. Box shows the region covered by main figure. Map data ©OpenStreetMap contributors and available from `https://www.openstreetmap.org`.

gorge and towards the districts of Álftaver, Landbrot, Meðalland, Síða and Skaftártunga, collectively known as the Fire Districts (Figure 3.1).

On 29th of July 1783, fissure segment 6 opened on the north-east side of Mt Laki (Thordarson and Self, 1993). Topographically constrained by the highlands and Mt Laki, subsequent lava flows were channeled into the Hverfisfljót gorge or north towards the upper reaches of the Skaftá river (Figure 3.1). The lava that flowed south through the Hverfisfljót gorge spread across Fljótshverfi and the eastern edge of the Landbrot district (Figure 3.1A). Fissure segments 7–10 continued in a northeast trend towards Grímsvötn, sending more lava flows down the Hverfisfljót gorge. Eruptive activity at the fissure ceased in Feb 1784, although earthquakes and eruption columns from Grímsvötn were recorded in April 1784 and May 1785 (Thordarson and Self, 1993; Thordarson et al., 2003).

Thordarson and Self (1993) used tephrostratigraphy alongside accounts of seismicity and ash fall to determine opening dates for each of the fissure segments. At two of the fissure segments (4 and 6), rising magma interacted with groundwater and constructed phreatomagmatic tuff cones (Thordarson et al., 2003).

The progression of the lava front has been established through analysis of contemporary accounts, first by Thordarson and Self (1993), and then in more detail by Thordarson et al. (2003; Figure 3.2). A morphological analysis of the Laki lava field was conducted by Guilbaud et al., (2005), using field observations and high-resolution aerial photographs. They concluded that most of the flow was emplaced as inflating pāhoehoe sheets but identified areas where the top crust was disturbed and broken into plates that rafted on the lava and piled up down-flow, creating rubbly surface textures. Guilbaud et al. (2005) also noted the widespread presence of hummocky regions around the flow margins and determined these to be outbreaks from the front of the advancing lava flow that failed to coalesce into a single coherent sheet flow.

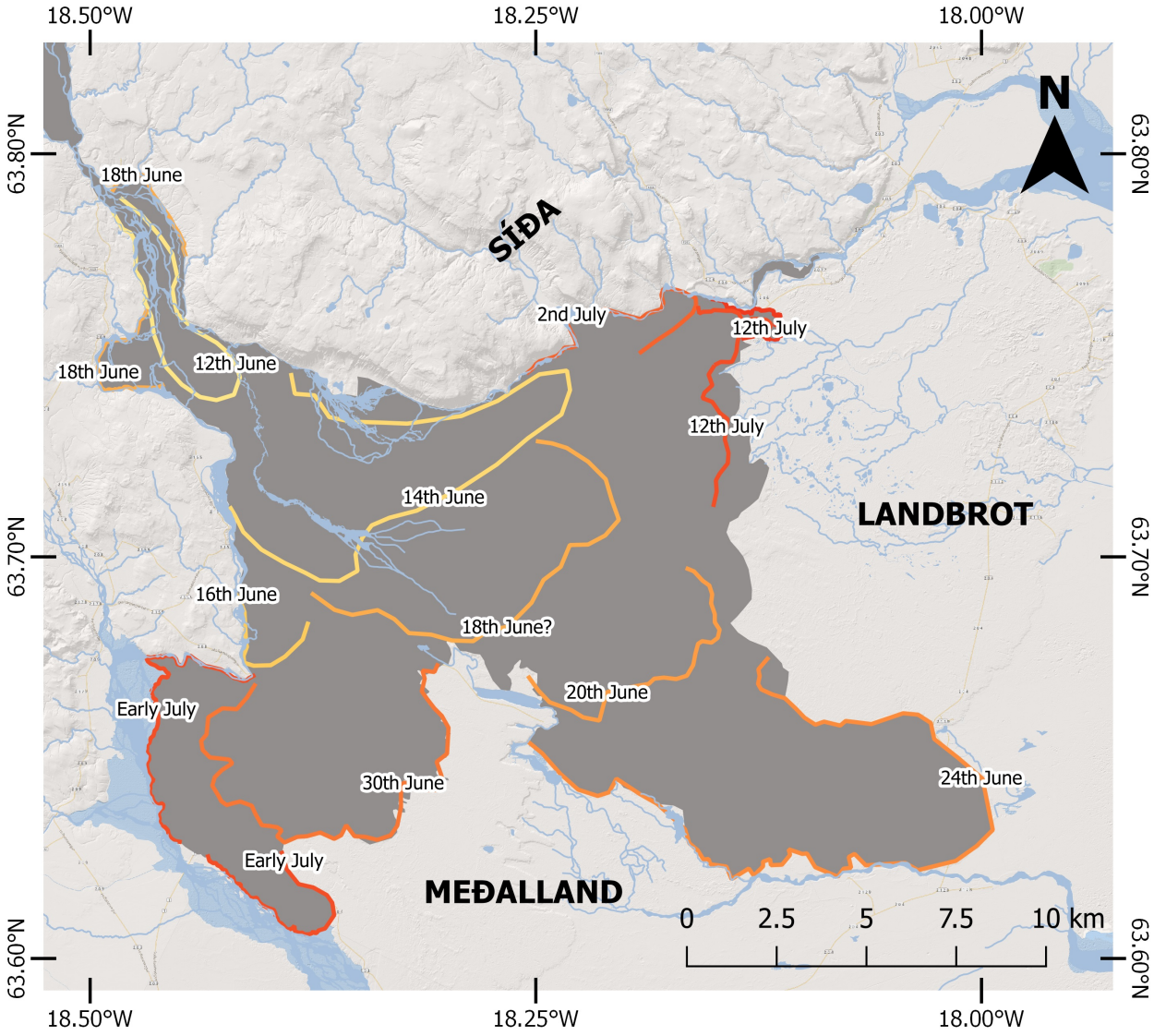

Figure 3.2: Progression of the Laki lava flow throughout the Síða, Landbrot and Meðalland districts in June and July 1783 (based on Thordarson et al., 2003). Rivers are shown in light blue. The final exent of the Laki lava is shown in grey. Approximate position of the lava flow front at different dates are shown with coloured lines.

Individual rootless cones were first mapped by Thordarson et al. (1998), focusing on the rootless cones near Mt Leiðólfsfell (group 6 in this study; Figure 3.1C; Figure 3.4). They found that these cones formed when the lava interacted with the waterlogged bed of the Hellisá river and dated them to the 17th of June based on tephra stratigraphy and contemporary accounts. Bruno et al. (2004) mapped the large group of cones near fissure segment 1 from aerial photographs (group 1 in this study; Figure 3.3D; Figure 3.4). Hamilton et al. (2010a, 2010b) mapped the same group in much more detail using a Differential Global Position System (DGPS) survey. This study also established that the group 1 cones formed

during the opening days of the eruption, fueled by lava from fissure segment 1. From tephra stratigraphy and the high-resolution digital terrain model (DTM) from their DGPS study, they concluded that the group was formed in six discrete phases as lava was directed around existing topographical features, with each phase lasting a few days.

In summary, despite the detailed analysis of the lava flow and reconstruction of its emplacement from contemporary records, and the recognition that the lava flow dammed several rivers (Thordarson et al., 2003), previous studies include very little on the wider effects of LWI and the resulting hazards. Additionally, although rootless cones have long been recognized on the Laki lava field, and previous studies have identified 13 different cone groups (groups 1–3, 5, 6, 9–15 in this study; Thorarinsson, 1968; Thordarson and Self, 1993; Thordarson et al., 2003; Bruno et al., 2004; Guilbaud et al., 2005), there has been no comprehensive review of these cone groups and their relationship to the lava flow and water sources, and only two of these groups have been mapped in detail (groups 1 and 6).

3.2.2 Hydrological setting of the 1783–1784 Laki fissure eruption

We give a brief description of the present-day hydrology and environment around the Laki fissure and the Fire Districts to put the contemporary accounts (Appendix B) and results of this paper into context (Figures 3.1B, 3.5). Most important are the two major rivers that flow through the region: the Skaftá and the Hverfisfljót. Prior to the eruption, both the Skaftá and Hverfisfljót river gorges were deeper: up to 74 m and 28 m respectively (Thordarson and Self, 1993). Both rivers were displaced from their pre-eruption paths as the gorges filled with lava, as was the Hellisá river near Mt Leiðólfsfell (Thordarson et al., 1998).

The Skaftá river drains ∼3640 km^2 and has an average discharge of 115 m^3/s, measured at the Skaftárdalur farmstead (`http://www.katlageopark.com/geosites/skafta/`), though discharge is higher at the height of summer. The river now flows along the northern and western boundaries of the Laki lava field. Its source is meltwater from the Skaftárjökull glacier, an outlet of the Vatnajökull icecap. It is also fed by tributaries carrying precipitation and spring-water off the highlands. It flows southwest from the icecap as a braided river, parallel to the Laki fissure. The river comes together as it enters Úlfarsdalur, then turns south as it passes into the Skaftá gorge. Along the gorge, the Skaftá river is joined by the Hellisá river and other small tributaries. Where the gorge opens out into the lowlands, the river splits into three branches. The most westerly branch flows south around the western margin of the Laki lava field and merges with the Tungufljót and Hólmsá rivers to become

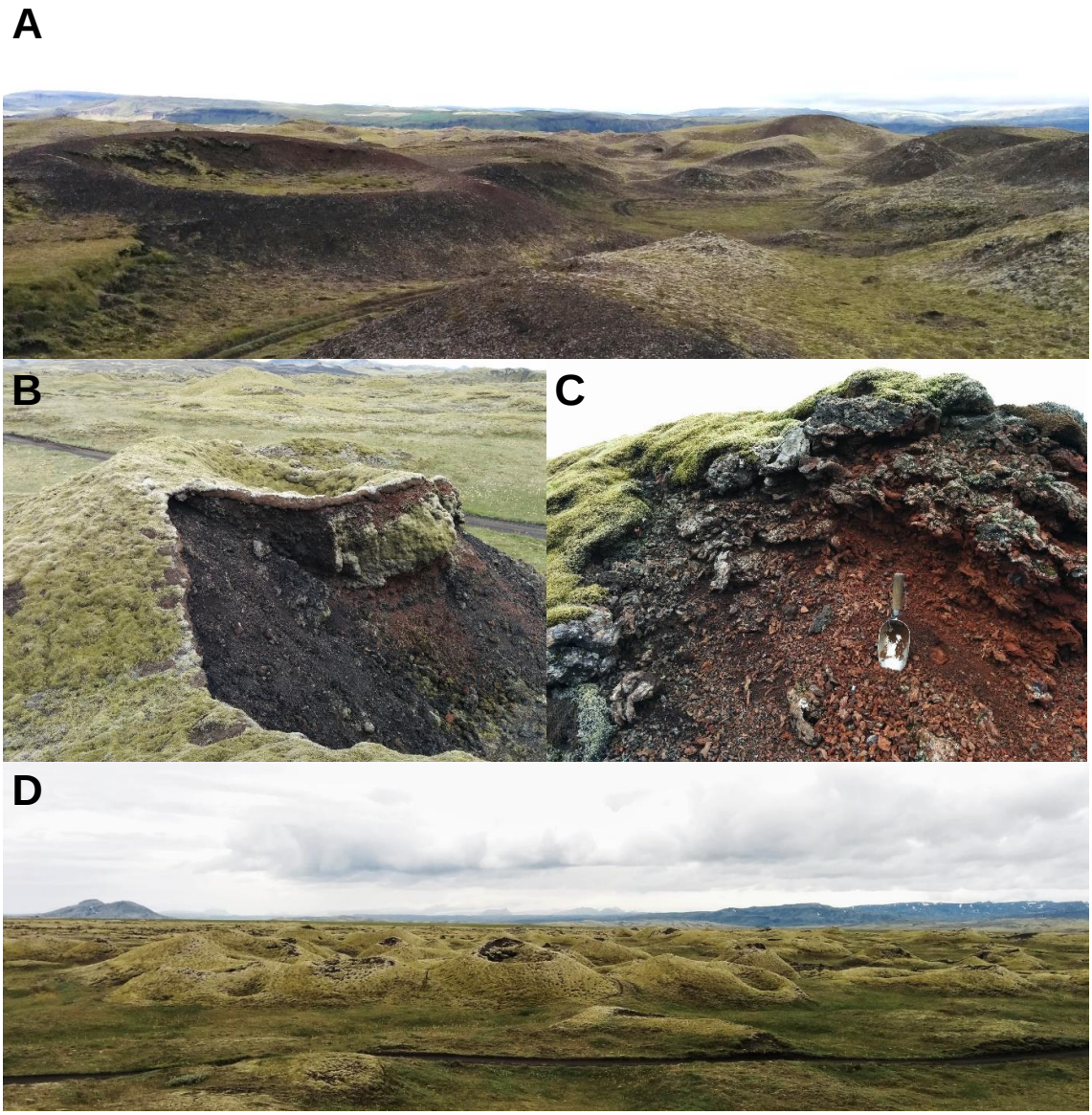

Figure 3.3: Photographs of rootless cones. (A) Rootless cones from the Landbrots group created by the 939–940 AD Eldgjá eruption. (B) View of a partially excavated rootless cone on the Laki lava field (fron group 1 in this study), showing the central crater and a layer of moss-covered spatter on the cone flanks. (C) Close-up of the same rootless cone, showing the layers of ash and lapilli-sized scoria topped with welded spatter, with a trowel for scale. (D) Wider view of the rootless cones in group 1 of this study.

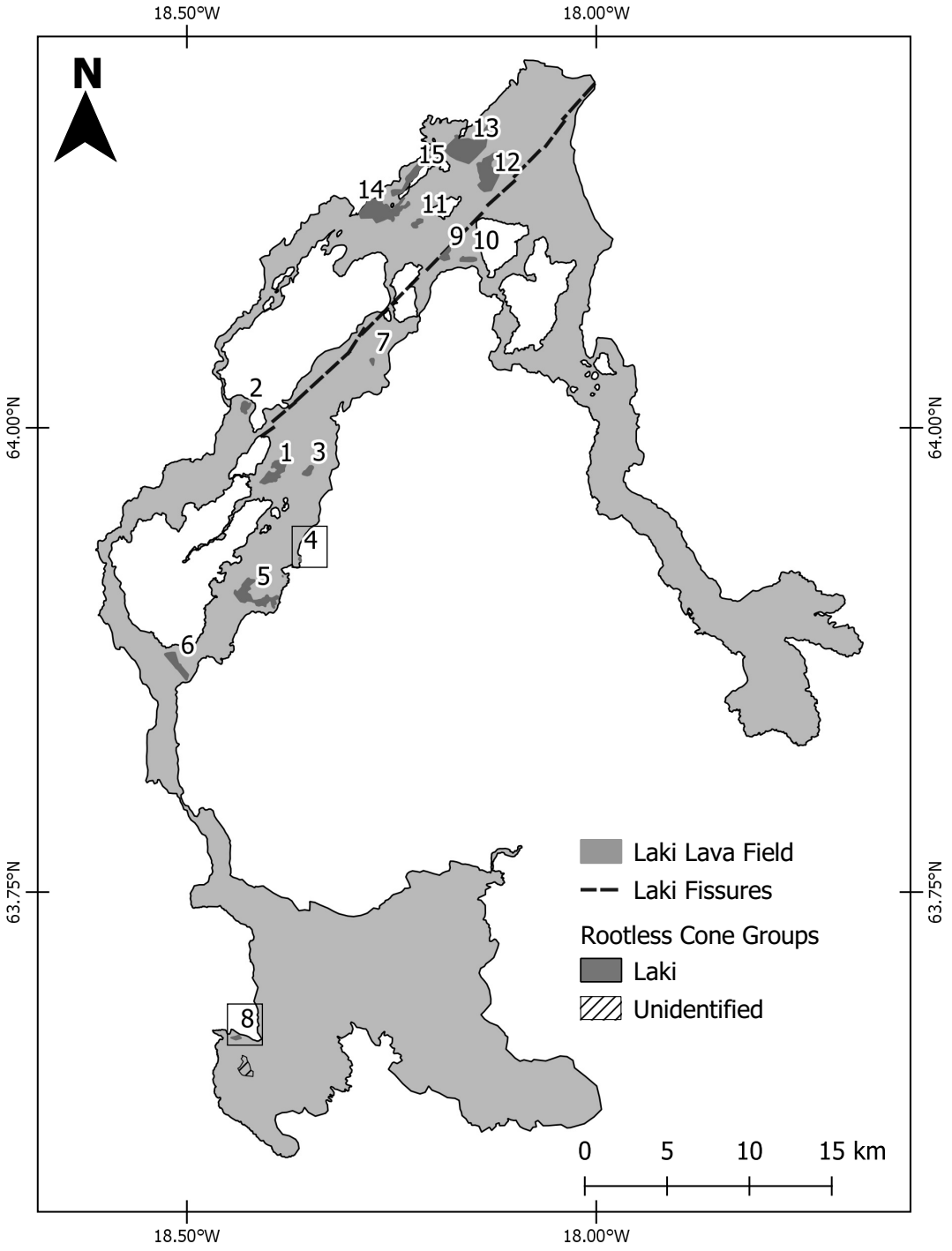

Figure 3.4: Overview of the Laki lava field showing the eruption fissure (dashed black line) and rootless cone groups (dark grey areas). Rootless cone groups that are new to this study are surrounded by a black box.

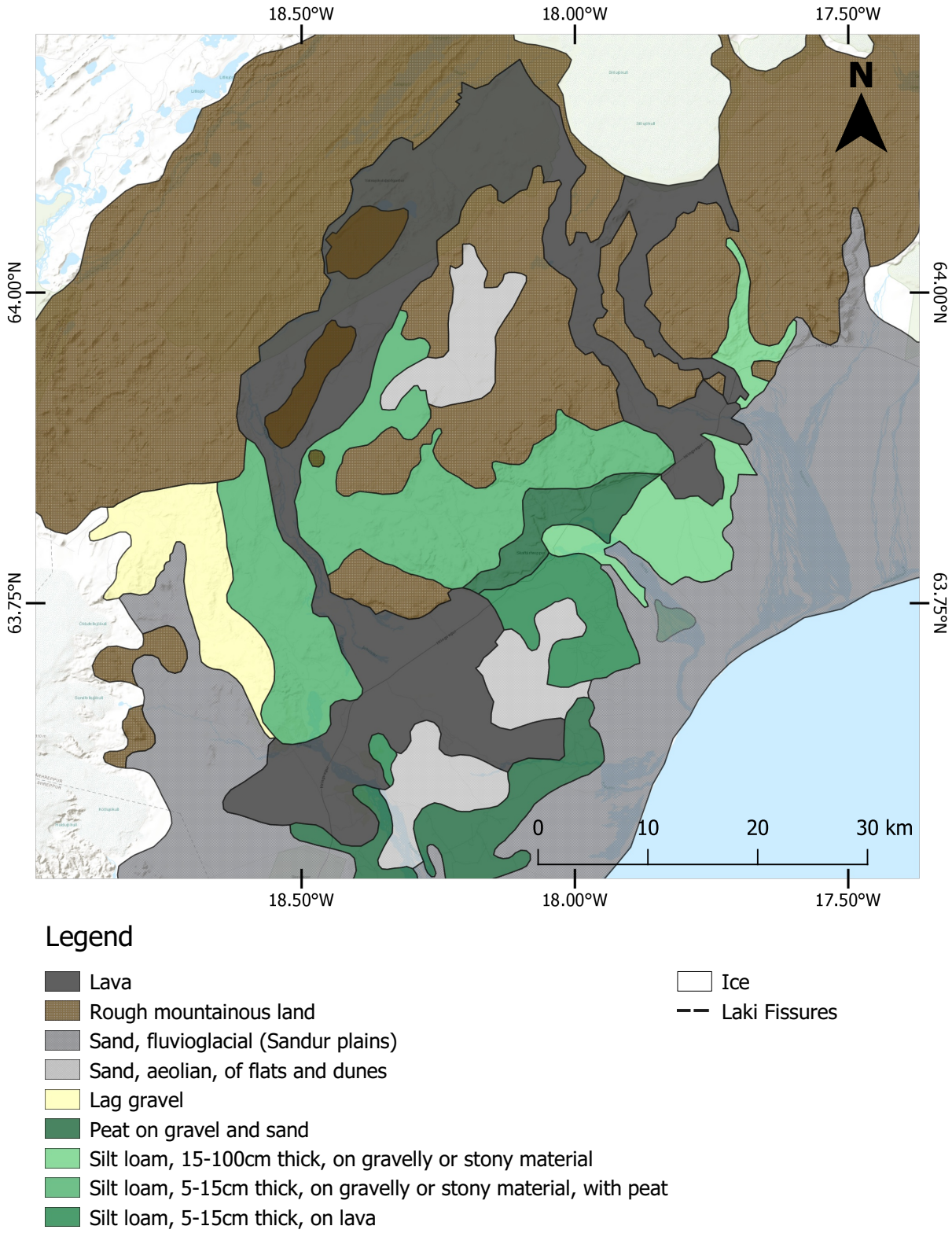

Figure 3.5: A map of the soils and substrates in the region around the Laki lava flow (based on Nygard, 1959).

the Kúðafljót. The central, and smallest, branch is called Árkvíslar and flows south-east into the center of the Laki lava field, where it dries up as the water permeates into cracks in the lava flow. It follows the approximate course of the pre-eruption river Melkvísl, which is referred to in contemporary accounts but was buried by lava. The third branch runs east-northeast towards Kirkjubæjarklaustur between the scarp of the Síða highlands and the edge of the lava field. It is fed by several tributaries, including the Holtsá and Fjaðará rivers, before turning south-east and draining into the North Atlantic Ocean.

The Hverfisfljót is fed by meltwater from the Síðujökull glacier (part of the Vatnajökull icecap), and discharge varies significantly with season: 50–150 m^3/s in summer, dropping to 5–30 m^3/s in winter (`https://www.nat.is/hverfisfljot-river/`). The Laki lava filled in the Hverfisfljót gorge proper, displacing the river to the east. In the highlands, the river now flows along the eastern edge of the Laki lava field for ∼10 km before diverting around a mountain. South of the mountain, it follows the eastern margin of the Laki lava for a further 14 km. As it emerges onto the plains, the Hverfisfljót follows the northeast margin of the Laki lava and merges with other rivers, including the Núpsvötn and Brunná, before flowing south-southeast into the North Atlantic Ocean. However, prior to the eruption the river spread from Hvoll in the east to Orustahóll in the west, ∼8.4 km wide (`https://www.nat.is/hverfisfljot-river/`; Figure 3.1C).

Prior to the Laki eruption, the site of the Laki fissures, the Varmárdalur valley, was enclosed at the southern end by the 40–50–m–high Galti-Hrossatungur ridge (Figure 3.1A; Hamilton et al., 2010a). The valley was described as one of the 'boggiest dells' in the highlands (Thordarson et al., 2003; A2 in Appendix B.1.1) and would have drained through a narrow valley north of the Hrossatungur mountain, which is now filled with Laki lava. By contrast, the lowland Fire Districts had been rich agricultural land, used for livestock grazing and cultivating crops such as hay (on silt or loam soils) and lyme grass (on sandy soils; see A3–A11 in Appendix B.1.1). The substrates in the Fire Districts today fall into five major categories: bare or moss-covered lava, aeolian sands covering lavas, fluvio-glacial sands (sandur plains, primarily on the coast), silt loams and peats (Figure 3.5; Nygard, 1959), with the latter hosting most of the farming areas. Although the Laki lava now covers part of the land, it is likely that the exposed sediments are similar today to those at the time of the eruption.

3.3 Methods

3.3.1 Analysis of contemporary sources

Contemporary accounts of the eruptive activity and its impacts on the local and national population are a valuable source of data for understanding how the eruption progressed, and how the lava interacted with the landscape. The most detailed accounts, which are the source of most of our data, were written by Rev. Jón Steingrímsson (1728–1791), pastor to the affected Síða district during the eruption and based at Prestbakki (Figure 3.1C). He chronicled events in the Fire Districts throughout the eruption, including observations of ash clouds at the fissure, ash fall throughout the districts, the progress of the lava flows, the behavior of the local rivers, and the effect of the eruption on the residents and their livestock (Steingrímsson 1783a, b; Steingrímsson and Ólafsson, 1783; Kunz, 1998). Other contemporary accounts were collected into a single volume alongside modern research (Einarsson et al., 1984), including statements from the local people and accounts from local prefects (Stephensen, 1785), pastors from neighboring parishes (Björnsson, 1783) and a medical student at a local hospital (Pálsson, 1784). This collection is published in Icelandic, but Thordarson et al. (2003) published English translations of selected passages in their study of contemporary accounts of the Laki fissure eruption. Where these passages refer to the lava flow and its interaction with lakes, rivers or other water, we have used Thordarson et al.'s (2003) translations to corroborate Kunz's (1998) translation of Steingrímsson's accounts.

We reviewed these accounts and collated passages that describe interactions between the lava and water, flooding, and explosive LWI. We also noted descriptions of the pre-eruptive environment (land use, locations of lakes etc.) and weather conditions (e.g. heavy rain or snow) that might affect the rivers or lava flow. These passages allowed us to construct a timeline of the lava–river interactions and fit it alongside the existing eruption chronology from Thordarson et al. (2003), including dates of lava surges, fissure migration and lava production rate. These passages are presented in tables in Appendix B.1.1, grouped by theme, and cross-referenced throughout the Results and Discussion. They are organized chronologically, with the passage of interest (in English), the date, and the source text. Each passage has a unique reference number given by a combination of the table number and row number, e.g. A1 refers to row 1 in Table A. From the timeline of events, we attribute likely formation dates to previously undated rootless cone groups.

We mapped the locations of these events (e.g. floods, destroyed farms, other LWI) using the Quantum Geographic Information System (QGIS) software package. It is impossible to

accurately map the extent of each area covered by water, so we estimate the flooding extents using named locations and qualitative descriptions in the primary sources. Where sources do describe the extent of floods, we have estimated the flooded area in QGIS by measuring the area from the edge of the lava flow to the flooded locations, following topographic features. We also combined mapped descriptions of land use with a regional soil map (Nygard, 1959) to understand the type of substrate that the lava flowed over (Figure 3.5).

In their analysis of contemporary accounts of the Laki fissure eruption, Thordarson et al. (2003) established that the directions quoted differ from the true directions. This is because contemporary writers used a prominent scarp running from the end of the Skaftá gorge to Kirkjubæjarklaustur (an old sea-cliff) as the basis for local navigation. They assumed that the scarp ran East-West, but it actually runs 15°–25° anti-clockwise of E–W, hence the error in the quoted directions. We accounted for this in our analysis of the texts and, where possible, used existing place names and a modern high-resolution map of Iceland (http://map.is).

3.3.2 Rootless cone identification, digitisation and statistical modelling

We mapped the location of individual cones in all cone groups previously identified in the Laki lava field. In addition, we have identified two new groups of rootless cones that appear related to the Laki eruption and have expanded the extent of one of the already-identified cone group. Where the resolution of our data allowed, we have also measured the crater area of individual cones.

We used a combination of aerial photographs and high resolution (2 m/pixel) DTMs available through the ArcticDEM project. These DTMs are derived from images gathered by instruments on-board the WorldView 1, 2 and 3 satellites, and provided in tiles, (data available online at `https://livingatlas2.arcgis.com/arcticdemexplorer/`) that we stitched together to cover the full extent of the Laki lava field. Aerial photographs came from Google Earth and Loftmyndir ehf. (available through `http://map.is`). The Loftmyndir ehf. images have a spatial resolution of 0.15–1 m/pixel (Loftmyndir, 2014; Noguchi et al., 2016). The resolution of images in Google Earth varies across the Laki lava field. The best resolved areas are those covered by WorldView 2 images, including the Skaftá river gorge, eastern part of the Fire Districts, and Hverfisfljót river gorge, and have a maximum resolution of 0.5 m/pixel (image references and capture dates in Supplementary Table 1). The remaining area, which includes most of the fissure and highlands, is covered

by CNES/Airbus images, for which Google Earth does not provide metadata, but are considerably lower resolution. The contrast between the two sets of images can be seen side by side in panel 4 of Figure 3.6, which covers the boundary between the WorldView and CNES/Airbus images. In these lower resolution areas we relied heavily on the ArcticDEM and reference to the Loftmyndir ehf. images. We digitized the cones in QGIS using the images and DTMs as a base map, according to the method of Boreham et al. (2018), which is based on extensive comparison between field observations, aerial photographs and DTMs of rootless cone groups on the Younger Laxá Lava in northern Iceland. We digitized cones as a single point at the center, or inferred center for incomplete cones, of the crater, and used ellipsoids to approximate the craters. We calculated the radius of a circle of equal area as a measure for cone size, using the built-in field calculator in QGIS. We then gave each cone a unique identified (e.g. *Lk2_1* for cone 1 in group 2). Cone groups in this chapter are numbered for the order in which they formed during the eruption. We attempted to classify each cone group as either 'river/flood' or 'wetlands/lake', according to our best guess of their formation environment, based on the cone location on the lava flow, the local topography and hydrology, and contemporary descriptions (Table 3.1). We recognize that these classifications are far from perfect, as the topography and hydrology were significantly altered by the Laki eruption and we lack sediment samples from each location to confirm the pre-eruptive conditions.

We exported the digitized cone data as a comma separated variable file for analysis. We used a simple linear model to test the relation between crater radius and formation environment, using the statistical software package *R*. We also compared the distribution of Laki cone sizes to rootless cones on the Younger Laxá Lava in northeast Iceland (data from Boreham et al., 2018). The scripts, raw, and processed data files are all available in Supplementary Material.

We recognize that the number of rootless cones identified is a minimum estimate, as some are too small to identify from aerial images or the ArcticDEM, and some may have been eroded or covered by later lava. To assess the limits of our method, we then compared our results with those of Hamilton et al. (2010a; 2010b), who provide detailed maps of the Hnúta and Hrossatungur rootless cones (group 1 in this study).

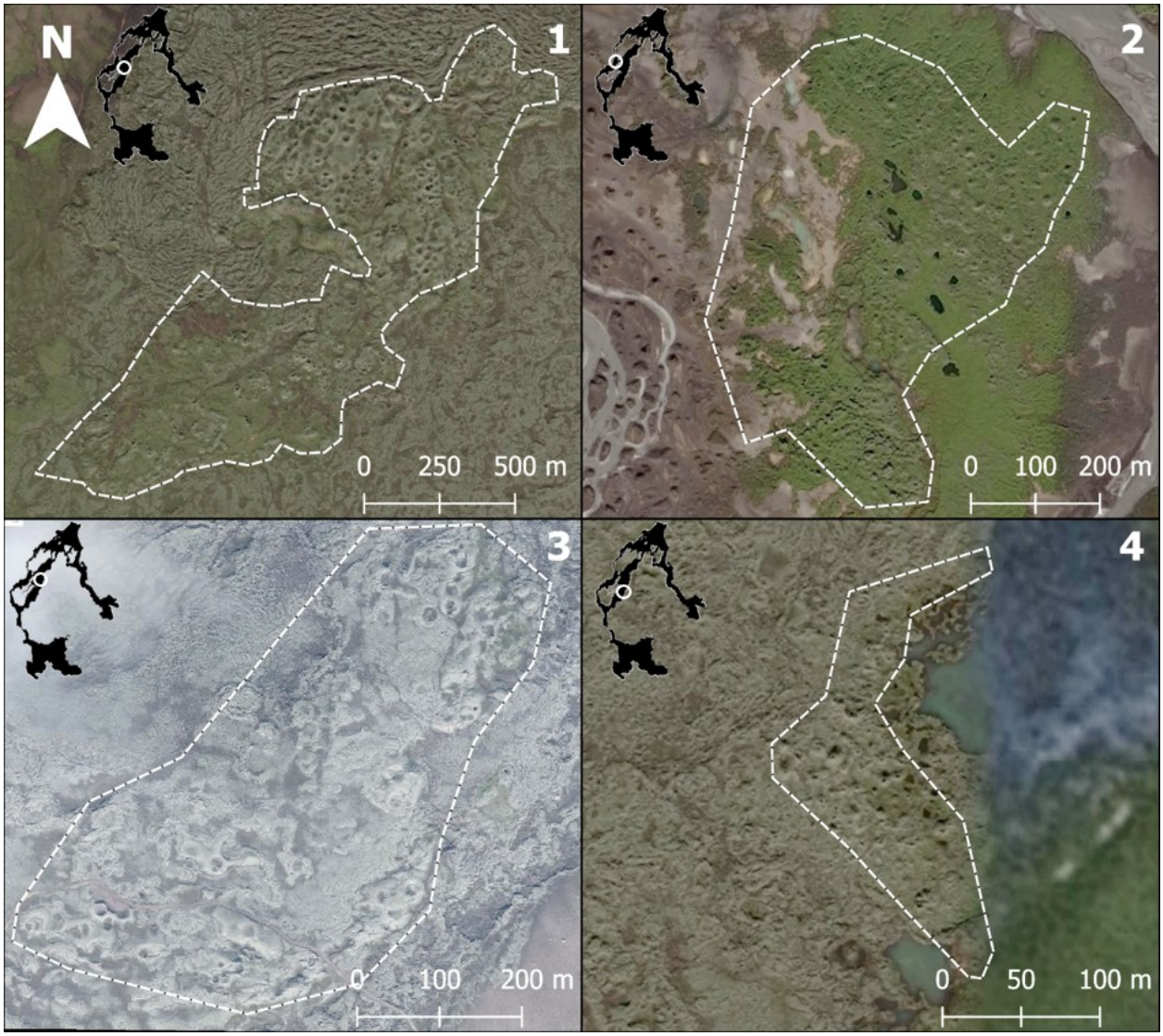

Figure 3.6: Laki rootless cone groups 1–4. The outline of each group is shown with a dashed white line. Images are from Google Earth, ©2020 DigitalGlobe, CNES/Airbus, Map data ©2020 Google (groups 1, 2, 4) and Loftmyndir ehf. (group 3; `http://map.is`

Group	Date	Location and probable formation environment	First identified in...	Date based on...
1	8^{th}–15^{th} June	Wetland or shallow lake near FS1	Thorarinsson (1968)	Hamilton et al. (2010a)
2	9^{th}–10^{th} June	Skaftá riverbed in Úlfarsdalur	Thorarinsson (1968)	Drying up of the Skaftá
3	13^{th}–14^{th} June	Wetland or shallow lake east of group 1	Thordarson and Self (1993)	Opening of FS3 + lava travel time
4	14^{th}–15^{th} June	Eastern margin of the lava flow near Grenbotar	This study	Opening of FS3 + lava travel time
5	15^{th}–16^{th} June	Spread across width of lava flow north of Eyrarhólmur, likely formed in wetlands given broad extent of group	Thordarson and Self (1993)	Opening of FS3 + lava travel time
6	17^{th} June	Old Hellisá riverbed where it joins the Skaftá river gorge	Thordarson and Self (1993)	Thordarson et al. (1998)
7	23^{rd} June	Wetland or lake near FS4	Thordarson and Self (1993)	Opening of FS4
8	$\sim 30^{th}$ June	Near Ytri-Ásar farm, possibly from impounded water from the Tungufljót and Hólmsá rivers	This study – attributed to Eldgjá eruption by Guilbaud et al. (2005)	Steingrímsson's account (D8, D9)
9	29^{th} July	Wetland or lake (?) near FS7	Thordarson et al. (2003)	Opening of FS6
10	29^{th} July	Wetland or lake (?) east of FS7	Guilbaud et al. (2005)	Opening of FS6
11	20^{th}–30^{th} July	Wetland or small lake (?) north of FS6	Thordarson et al. (2003)	Opening of FS7 + lava travel time
12	23^{rd} August	Wetland (?) near the upper reaches of the Skaftá river bed	Thordarson et al. (2003)	Opening of FS 7 + lava travel time
13	Late August	Upper reaches of the Skaftá river bed	Guilbaud et al. (2005) – area extended by this study	Opening of FS7 + lava travel time
14	Late August	Upper reaches of the Skaftá river bed	Thordarson et al. (2003)	Opening of FS7 + lava travel time
15	Late August	Upper reaches of the Skaftá river bed	Thordarson et al. (2003)	Opening of FS7 + lava travel time

Table 3.1: Likely formation dates of the Laki rootless cone groups, the environments they formed in, and the dating evidence.

Not rootless cones

There are 8 areas of the Laki lava field where previous studies had indicated rootless cone or possible rootless cone groups, but where were could not find any evidence of rootless cones (Figure 3.7A). However, we did find features that resembled inflation or collapse pits, based on the presence of cracks around the perimeter of the pits and into the surface of the surrounding lava (Figure 3.7B). We also found features that looked like rootless cones but are covered by later stages of the lava flow (Figure 3.7C). We have not included any of these areas in our count of rootless cone groups on the Laki lava field. Some of these areas may have been misidentified as rootless cones in previous studies; some may have rootless cone groups that we missed or are all too small to resolve from aerial photographs or the ArcticDEM.

3.3.3 Electron probe analysis of rootless cone tephra

There is one group of rootless cones on the Laki lava field that was previously attributed to the Eldgjá lava flow (Group 8 on Fig. 2; Guilbaud et al., 2005). However, the prominence of the cones above the Laki lava in an area where contemporary accounts show that there was a large body of impounded water led us to question this attribution. We analyzed tephra samples from two rootless cones in this group (collected by Alison Rust in summer 2018; see Table 3.2 for sample co-ordinates) and measured the major element composition of the matrix glass using a Cameca SX100 electron microprobe at the University of Bristol with a 20 keV beam, current of 10nA and spot size of 10µm. We checked the beam calibration against the Kakanui hornblende (Carpenter and Vicenzi, 2012) and Columbia River basaltic glass secondary standards before and after analysis of our samples. We analyzed seven points per sample and calculated their mean. We also analyzed samples of fissure-proximal Laki lava and scoria from a rootless cone in the Landbrotshólar group, created by the Eldgjá eruption. The full set of collected data, standard deviations on the measurements, detection limits, and calibration against secondary standards can be found in Supplementary Materials (`https://data.bris.ac.uk/data/dataset/ch1ck57uyjms2m9c7pb7svuke`).

The Katla (Eldgjá) and Grímsvötn (Laki) volcanic systems can be distinguished by the FeO/TiO_2 ratio of their products (Larsen 1981; Óladóttir et al., 2008). We compared our data to published compositions of matrix glass in tephra and lava samples from the Eldgjá and Laki eruptions, and the Grímsvötn and Kalta volcanic systems (Thordarson et al., 1996; Thordarson et al., 2001; Guilbaud et al., 2007; Óladóttir et al., 2008) to determine the parent

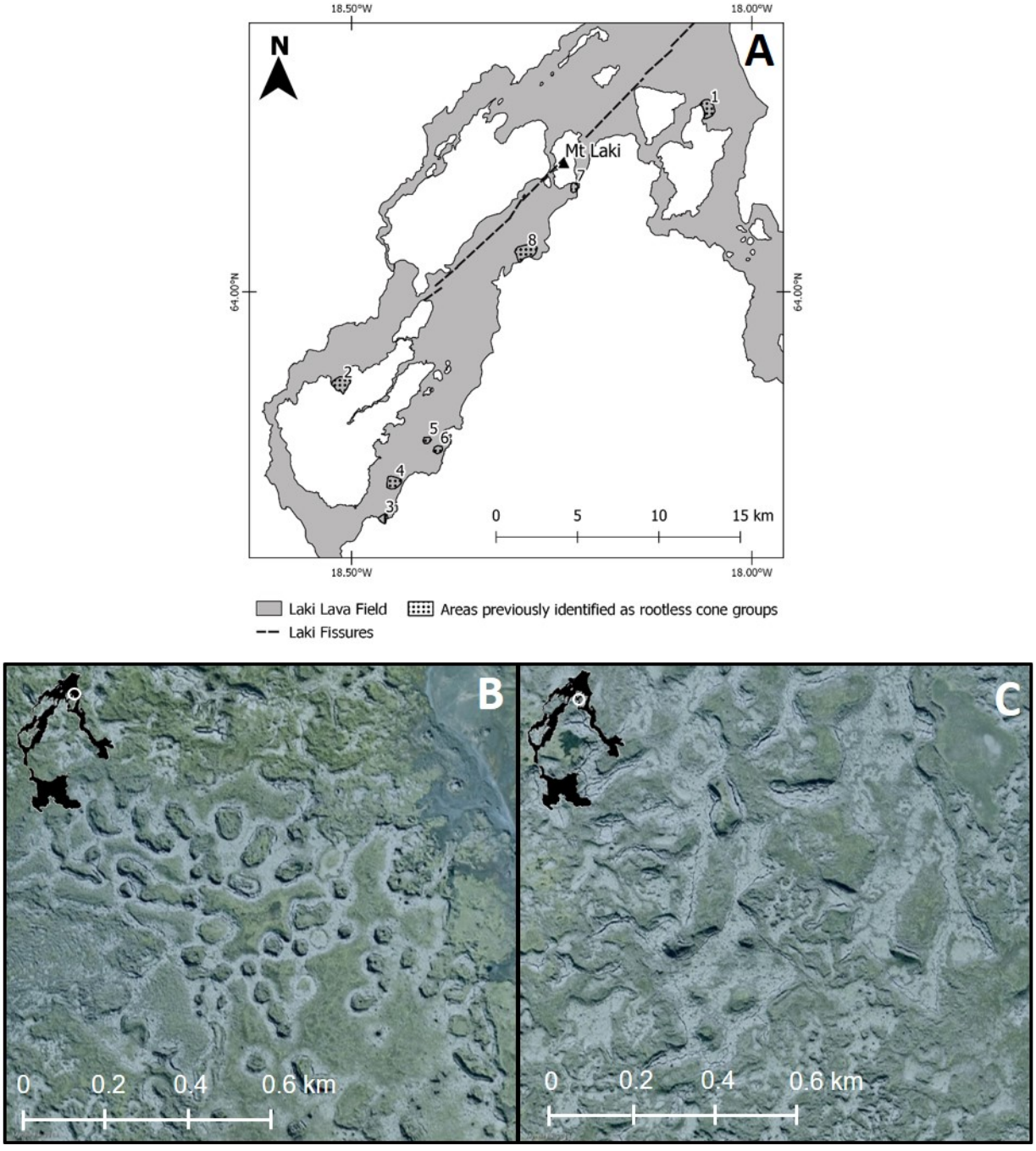

Figure 3.7: A) Map of the areas on the Laki lava field where previous studies had marked rootless cone groups, but where we could not find any rootless cones. B) Collapse puts resembling rootless cones. Note the continuous cracks running around the perimeter of the pits, hiwhc are not presernt on rootless cones, and the very sharp crater edges. These pits correspond on group 1 on panel A. C) Possible buried rootless cones. There are continuous cracks around the perimeter of the pits, but the slope of the craters is much shallower, suggesting that there my be underlying structure. Images are from Loftmyndir ehf. (available on `http://map.is`).

Sample	1	2	3	4
Location	(-18.4369, 63.6722)		(-17.9803, 63.7614)	(-18.3046, 64.0357)
SiO_2	49.76 (0.36)	49.98 (0.36)	48.46 (0.35)	50.06 (0.36)
TiO_2	3.70 (0.07)	3.71 (0.07)	5.03 (0.08)	3.29 (0.07)
Al_2O_3	11.63 (0.20)	11.70 (0.02)	11.40 (0.19)	12.54 (0.20)
FeO	16.22 (0.47)	16.27 (0.32)	17.36 (0.35)	15.64 (0.31)
MnO	0.30 (0.08)	0.27 (0.08)	0.23 (0.08)	0.26 (0.08)
MgO	4.69 (0.16)	4.68 (0.16)	4.16 (0.15)	5.12 (0.17)
CaO	9.44 (0.21)	9.41 (0.21)	7.22 (0.17)	9.74 (0.22)
Na_2O	2.74 (0.18)	2.80 (0.19)	2.48 (0.18)	2.15 (0.16)
K_2O	0.55 (0.05)	0.56 (0.05)	1.52 (0.08)	0.46 (0.05)
P_2O_5	0.42 (0.03)	0.42 (0.03)	0.81 (0.04)	0.36 (0.03)
Total	99.46	99.79	98.76	99.56
FeO/TiO_2	4.39 (0.21)	4.39 (0.17)	3.45 (0.13)	4.74 (0.19)

Table 3.2: Major element composition of matrix glass in tephra samples from rootless cone group 8 (samples [1] and [2]), rootless cones from the Landbrots cone group (Eldgjá eruption; sample [3]) and Laki lava from fissure segment 3 (sample [4]). Major element composition is given as the mean weight percentage of seven points per sample. Standard deviation for each element is given in parentheses. Co-ordinates given in decimal degrees (WGS84)

lava flow for the rootless cone group of uncertain origin (Group 8). As a note, one reviewer suggested that the Hálsagígar/Botnar lava flow could also be the parent lava. We were unable to find any published glass chemistry data for this lava flow, so have used the whole rock composition to give a first-order comparison to our data (Jakobsson, 1979).

3.4 Results

Contemporary accounts of the eruption describe the interactions between the Laki lava and local rivers, and the resulting impacts, which we summarize in chronological order and cross-reference to the relevant passages in contemporary accounts (see Appendix B: letters and numbers are keyed to the appendix tables, so C1 refers to table C, passage 1). We then describe the different rootless cone groups across the Laki lava field.

3.4.1 Lava–water interactions in the contemporary accounts

As lava entered the Skaftá river gorge, it quickly dammed the river, as evidenced by the reduced flow at the southern end of the gorge on the 9th of June; the river had almost completely dried up by the 10th, fed only by inputs from local tributaries (see passages B1–B5 in Appendix B.1.1; Thordarson et al., 2003). Large steam clouds were seen above the

gorge on the 11th (B6). The first surge of lava exited the Skaftá gorge into the Síða district on the 12th of June (Thordarson and Self, 1993; Thordarson et al., 2003). Steingrímsson described what appear to be rootless eruptions as the lava advanced, noting that *"when the molten lava ran into wet-lands or streams of water, the explosions were as loud as if many cannon had fired"* (C1). This first surge followed the course of the river and covered an area of the older Eldgjá lava field that had been used for forestry and grazing (A6, B8–B10). The continued supply of lava gradually filled the Skaftá gorge, damming its tributaries and impounding water. On the 18th of June, another surge of lava dammed the Búlandsá river (Figures 3.8, 3.9), causing the water level to rise and flood the nearby farm (B11).

As the lava spread into the lowland districts it split into three branches, channeled by the (now mostly dry) rivers in the area, before spreading laterally to cover the land in between (B13). The middle branch followed the course of the (now buried) Melkvísl river, destroying several properties in its path, including farmland and pastures, and displaced the river water, causing flooding (B12, B13, B15, B16, B18, B19, B28, B29; Figure 3.8). The most westerly branch of the lava entered the Kúðafljót river and followed it south (B22). As the flow spread, it dammed the river near Hrífunes. Since the Kúðafljót's two main tributaries (the Tungufljót and Hólmsá rivers) were still flowing, this created a temporary lava-dammed lake that flooded nearby farms (B23). Based on descriptions of the flood extent (from Hrífunes in the south to the ford at Hemruvað in the north), we estimate the area inundated with water covered at least 10.9 km^2 (Figures 3.8, 3.10). The third lava branch followed the Skaftá river east along the edge of the Síða scarp and dammed two tributaries, the Holtsá and Fjaðará rivers, flooding several farms and pastures (B17, B24–B27; Figure 3.8). Between the 2nd and 20th of July, the impounded rivers rose and eventually *"came flooding down upon the heaped-up lava, and violently quenched it"* (B30, B31). Throughout this period, the Fire Districts experienced frequent heavy rain and occasional snow (Table D), which exacerbated the flooding (D7).

As the fissure propagated northeast, lava was channeled towards the Hverfisfljót gorge, rather than towards the Skaftá river. On the 31st of July, the water in the Hverfisfljót river became hot and steamy (B32). The river level began to drop on the 1st of August and by the 4th of August it had completely dried up. The first lava exited the gorge on the 7th of August (B33–B35). This lava dammed tributaries to the Hverfisfljót river, causing flooding and hindering travel across the region (B36–B38; Figure 3.8). By the 21st of September, the Skaftá and Hverfisfljót rivers were both flowing (B41), although the Hverfisfljót river dried up again on the 29th (B42). Lava continued to flow down the Hverfisfljót gorge throughout autumn and winter 1783. The fissure eruption continued until February of 1784.

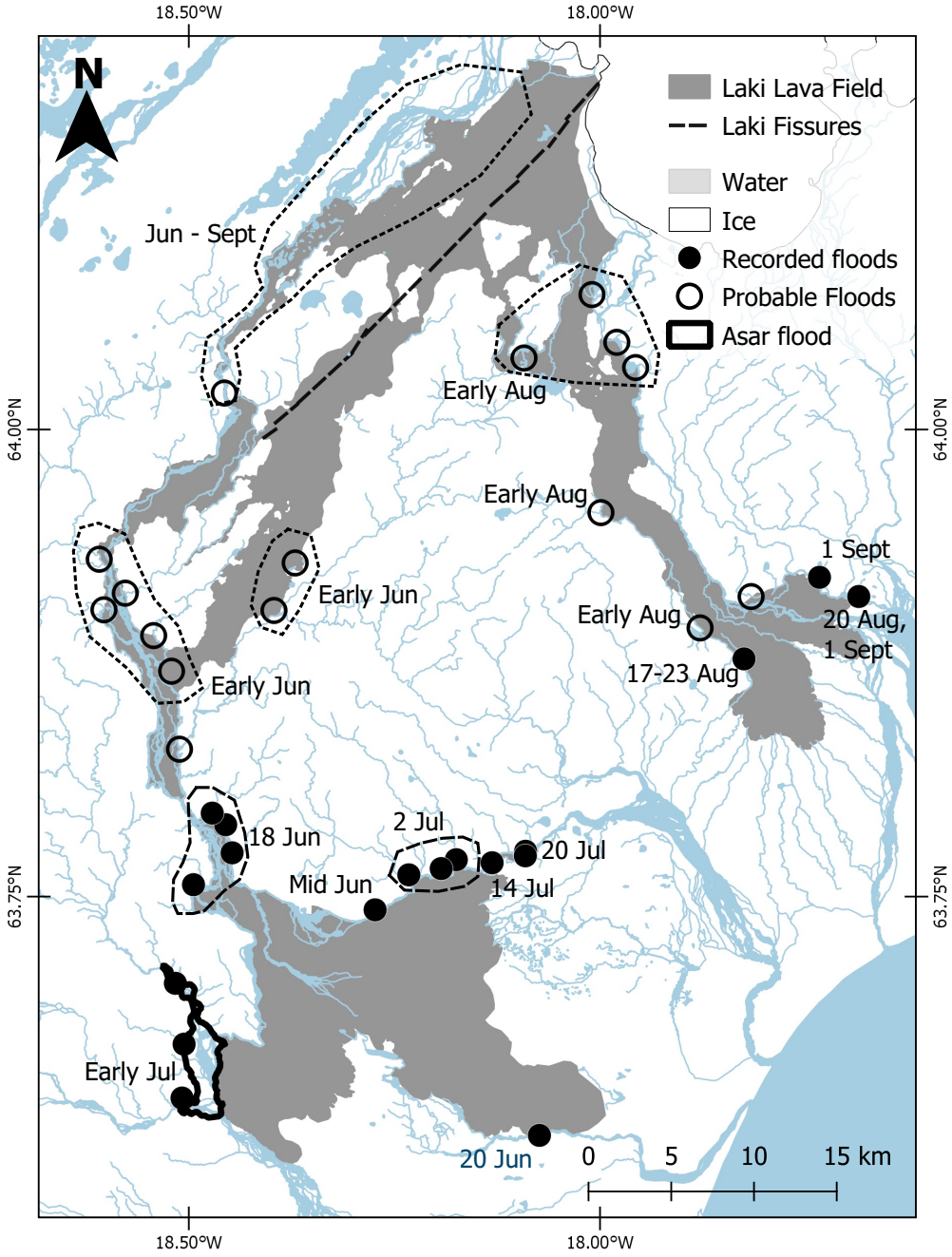

Figure 3.8: Floods caused by the Laki eruption. Flooded locations named in eyewitness accounts are shown as solid dark circles. Likely flooding locations where there were not eyewitness accounts are shown by light circles. The estimated extent of a temporary lava-dammed lake is outlined in black. Dates, or probable dates, are given for each event. Locations that flooded on the same date are grouped by dashed lines.

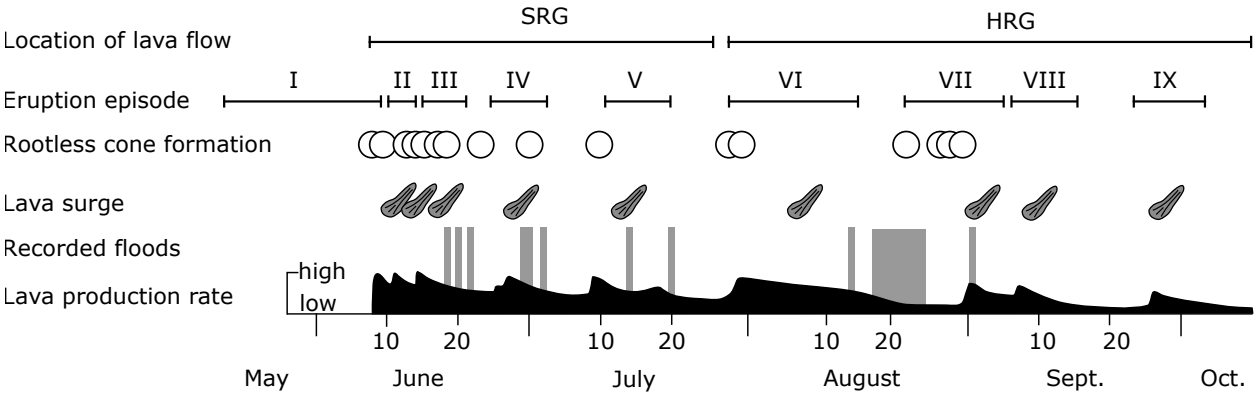

Figure 3.9: Timeline of the Laki eruption from May–October 1783, showing the active fissure segment (eruption episode), formation of rootless cones, lava surges, recorded floods, lava production rate, and whether the lava was flowing down the Skaftá river gorge (SRG) or Hverfisfljót river gorge (HRG). Modified from Thordarson et al. (2003).

3.4.2 Rootless cones

We have identified two new groups of rootless cones on the Laki lava field, in addition to those identified by previous studies (Figure 3.4). Mapping the location of all the individual cones visible in remote sensing datasets, we count 2979 cones spread across at least 15 groups, ranging from fissure-proximal to ∼47 km from the fissure. Based on their locations and the published lava flow chronology, we determined the likely timing of each group's formation, although there is still considerable uncertainty in many of these dates (Table 3.1). We now briefly describe each cone group.

Lava from the opening phase of the eruption at fissure segment 1 flowed south and formed a large group of rootless cones where it encountered a wetland or shallow lake, ∼2.5 km south of the fissure (group 1; Figure 3.6; Hamilton et al., 2010a). These cones were formed in six distinct phases, starting on the 8$^{\text{th}}$ of June and continuing until at least the 15$^{\text{th}}$ (Hamilton et al., 2010a). Here, we mapped 910 cones, whereas Hamilton et al. (2010a) identified ∼930 cones with 2216 explosion sites using a DGPS study where they walked the boundaries of each geological feature (lava flow margins, kipuka, cones, craters rims and floors, explosion sites). This comparison shows that remote sensing does a good job of identifying individual cones but lacks the resolution for individual crater mapping at this location.

On the northern side of fissure segment 1, the lava entered Úlfarsdalur and dammed the Skaftá river. Just upstream of where the lava first enters the gorge is a group of small rootless cones (group 2; Figure 3.6). The current Skaftá river flows along the western edge of this (group 2). Additionally, numerous 10–30-m-diameter mounds are located in the course of the current river; these may be the eroded remains of more cones. The timing

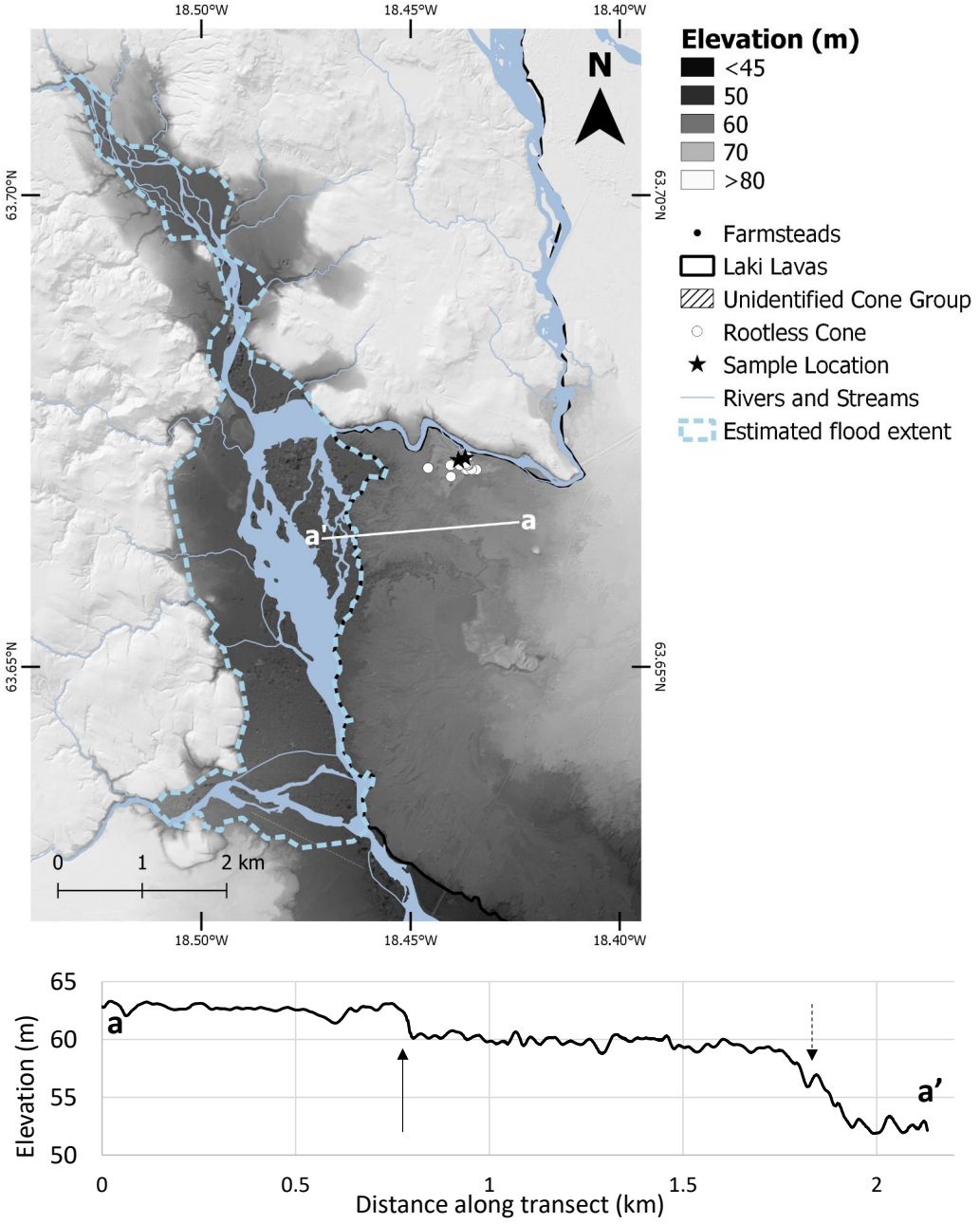

Figure 3.10: View of the western edge of the lava flow where it met the Kúðafljót river. The estimated extent of the temporary lava-dammed lake created is indicated by a dashed black line. Rootless cones on the Laki lava flow are shown as white circles. Black stars indicate sample locations. Profile a–a' shows the elevation of the lava flow surface, highlighting a preserved inflation front (marked by a black arrow), the downstream hummocky margin, and the edge of the lava flow (black arrow, dashed line). The morphology and elevation of the lava surface is from the ArcticDEM (created by the Polar Geospatial Center from DigitalGlobe, Inc. imagery.)

of the formation of this group is ambiguous. When lava first entered the gorge, it would have encountered the saturated sediments of the Skaftá riverbed and may have formed these rootless cones. However, the lava in this part of the gorge is >70 m thick (Thordarson and Self, 1993) and any deposits from the early stages of the eruption could well be buried. If the cones formed later in the eruption, then the source of water (or water-saturated sediments) is unclear. One possibility is that the cones formed early in the eruption on top of a stable crust, which was then uplifted as the underlying lava flow inflated.

East of group 1 is a similar but smaller group of cones (group 3; Figure 3.6) that may have formed in a similar environment. The group itself sits on the northern side of the Galti-Hrossatungur ridge, a 40-50 m high antiform that separated Varmárdalur from the next valley and was buried by the Laki lava (Hamilton et al., 2010a).

There are three groups of cones in the valley between the Galti-Hrossatungur ridge and Mt Leiðólfsfell (groups 4-6). Group 4 (Figure 3.6) has not been identified in previous studies and comprises a cluster of small cones near the eastern edge of the flow, next to a small lava-dammed pond. This pond probably formed during or after the eruption, when lava flow blocked a small river carrying precipitation and seasonal meltwater off the nearby mountains. In contrast, the cones in group 5 (Figure 3.11) are spread across the breadth of the valley and the group is cut by subsequent lava channels. The valley-filling spread of this group suggests that it may have formed in a wetland environment. Group 6 lies across the mouth of the valley where the Hellisá river joins the Skaftá gorge, near Mt Leiðólfsfell (Figure 3.12). The group 6 cones were mapped by Thordarson et al. (1998), who linked them to a contemporary account of explosions where the lava dammed the Hellisá river on the 17th of June 1783 (see C2 and C3 in Appendix B.1.1). Later surges of lava have partially covered this group, but cones are still visible on both sides of a central lava channel. The time between fissure segment 3 opening and the creation of the Leiðólfsfell cones (4 days), indicates that the lava advanced by 5-6 km per day (Thordarson et al., 1998), allowing us to estimate the first possible formation dates of the groups 3–6 (Table 3.2).

Group 7 is a cluster of small rootless cones, isolated in the middle of the lava flow at the north end of Varmárdalur (Figure 3.12). The resolution of the Google Earth images in this part of the valley is too low to accurately map these cones and they are too small to resolve through the ArcticDEM, though they are clearly visible in Loftmyndir ehf. images. An anonymous reviewer has suggested that these cones pre-date the Laki eruption and sit on a kipuka in the lava flow. However, previous studies linked them to the Laki eruption (Thordarson and Self, 1993; Thordarson et al. 2003; Guilbaud et al., 2005) and we have no evidence that contradicts these studies.

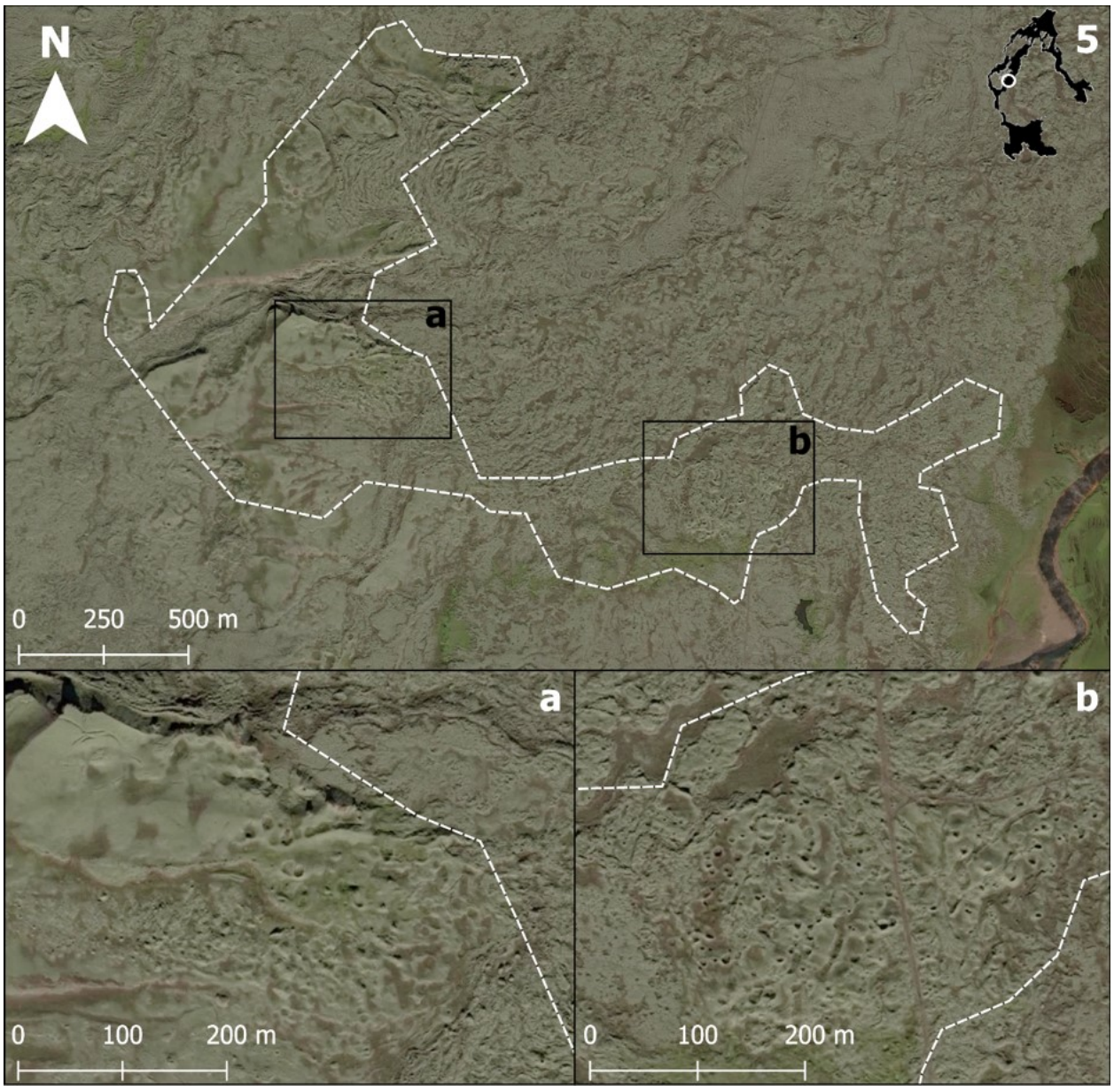

Figure 3.11: Laki rootless cone group 5. The group outline is shown with a white dashed line. Panels a and b show close-up views of two parts of the group, indicated by boxes a and b in the top panel. Images are from Google Earth, ©2020 DigitalGlobe, CNES/Airbus, Map data ©2020 Google

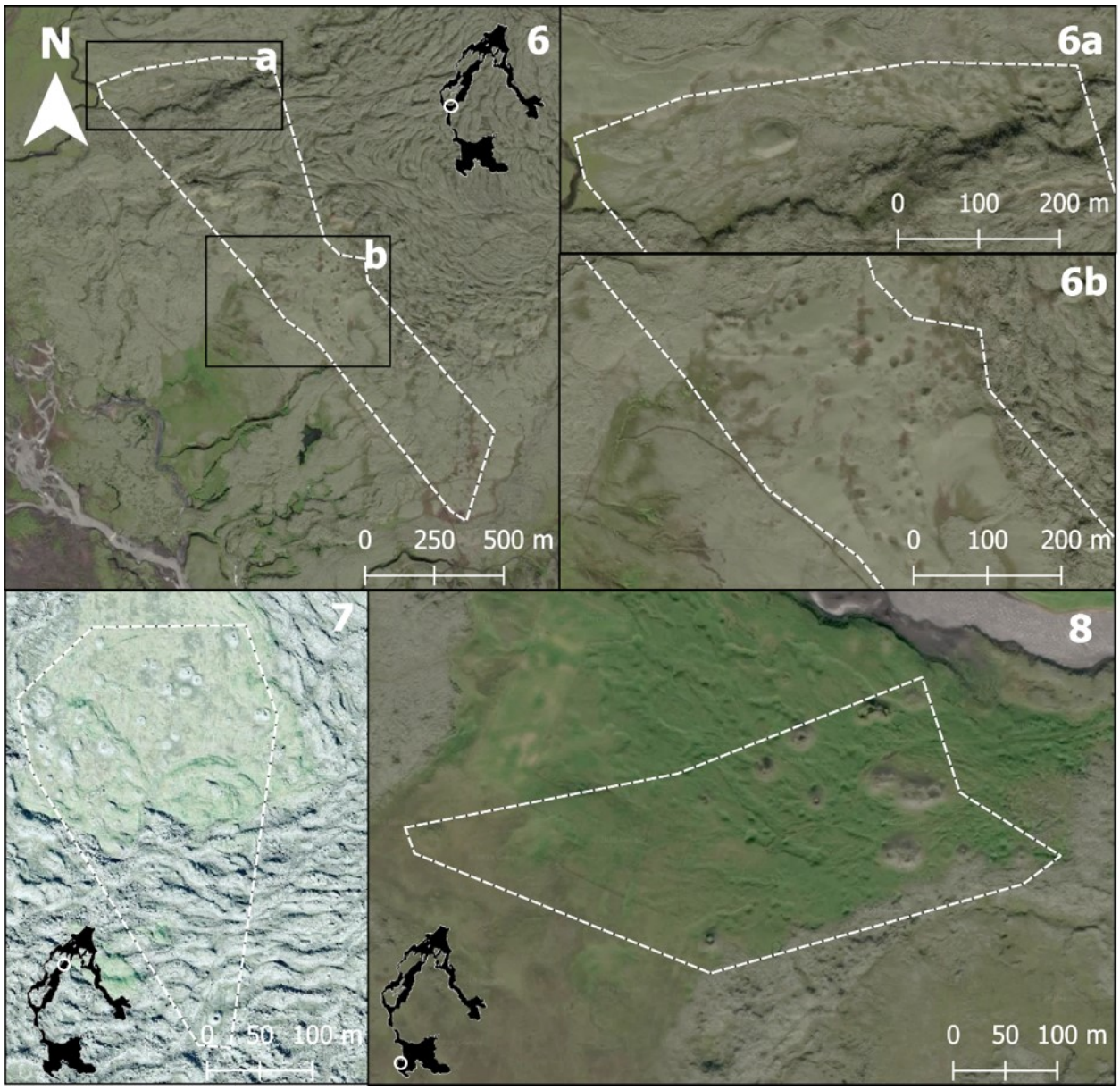

Figure 3.12: Laki rootless cone groups 6–8. The group outlines are shown with a white dashed line. Panels 6a and 6b show close-up views of the two parts of group 6, indicated by boxes a and b in panel 6. Images are from Google Earth, ©2020 DigitalGlobe, CNES/Airbus, Map data ©2020 Google (groups 6 and 8) and Loftmyndir ehf. (group 7; available on `http://map.is`.

Group 8 lies on the lowland plain near the farm Ytri-Ásar (Figures 3.10, 3.12). Guilbaud et al. (2005) originally identified these cones as belonging to the earlier Eldgjá lava flow, which underlies the Laki lava field throughout the region. Major-element analysis of groundmass glass in tephra samples from two of these cones, however, show that they are tholeiitic basalt and do not match the composition of the Eldgjá eruption (Table 3.2, Figure 3.15). The composition is very similar to that of samples from lava selvages and other rootless cones on the Laki lava field (comparison data from Thordarson et al., 1996 and Guilbaud et al., 2007). We also tested the reviewer hypothesis that they may have been formed by the c. 6000 BP Hálsargígar eruption, also a tholeiitic basalt. Whole-rock data (Jakobsson, 1979) show that the Hálsargígar lava is 2.25 wt.% lower in SiO_2 and has a higher FeO/TiO_2 ratio than the reported Laki whole-rock composition. For these reasons, we suggest that neither the Eldgjá nor Hálsagígar eruptions are a good geochemical match for the Ásar (group 8) rootless cones, and that they were probably formed by the Laki eruption. Steingrímsson described an extensive lava-dammed lake near the Ásar cones (B23) as the lava dammed the nearby rivers. It is possible these cones formed in waterlogged sediments on the edge of this temporary lake, but there may have been another pre-existing body of water in the area. Another group of rootless cones lies approx. 2 km south of the Ásar group, which have also been attributed to the Eldgjá eruption (Guilbaud et al., 2005). Since we did not analyze samples from these cones, we cannot comment on their provenance.

The remainder of the Laki rootless cone groups lie in the highlands near the fissure, and there are no descriptions of their formation. We can, however, infer their order of formation from the eruption sequence. The opening of fissure segment 6 on the north side of Mt Laki on 29th July created a phreatomagmatic tuff ring and clusters of rootless cones on the south side of the fissure segment (groups 9 and 10; Figure 3.13; Thordarson and Self, 1993). Lava from fissure segment 6 also flowed north toward the upper reaches of the Skaftá river, creating rootless cones ∼2 km from the fissure segment (group 11). Lava from fissure segment 7, which opened on the 23rd of August, created four separate groups of rootless cones, probably in late August or early September (groups 12–15; Figures 3.13, 3.14). The cones closest to the fissure segment (group 12) form a cluster of large single-cratered and multi-cratered cones, probably in a wetland or shallow lake area. The remaining three groups formed where the lava flow approaches the current braided channel of the Skaftá river. The more northern and middle groups (13, 15) have been eroded by subsequent flooding, but the southern group (14) is intact and contains numerous small, closely spaced scoriaceous cones. We have also extended the boundaries of group 13 compared to Bruno et al. (2004), who first identified cones in this area. These cones groups probably formed either on the waterlogged sediments of the Skaftá riverbed or surrounding wetlands.

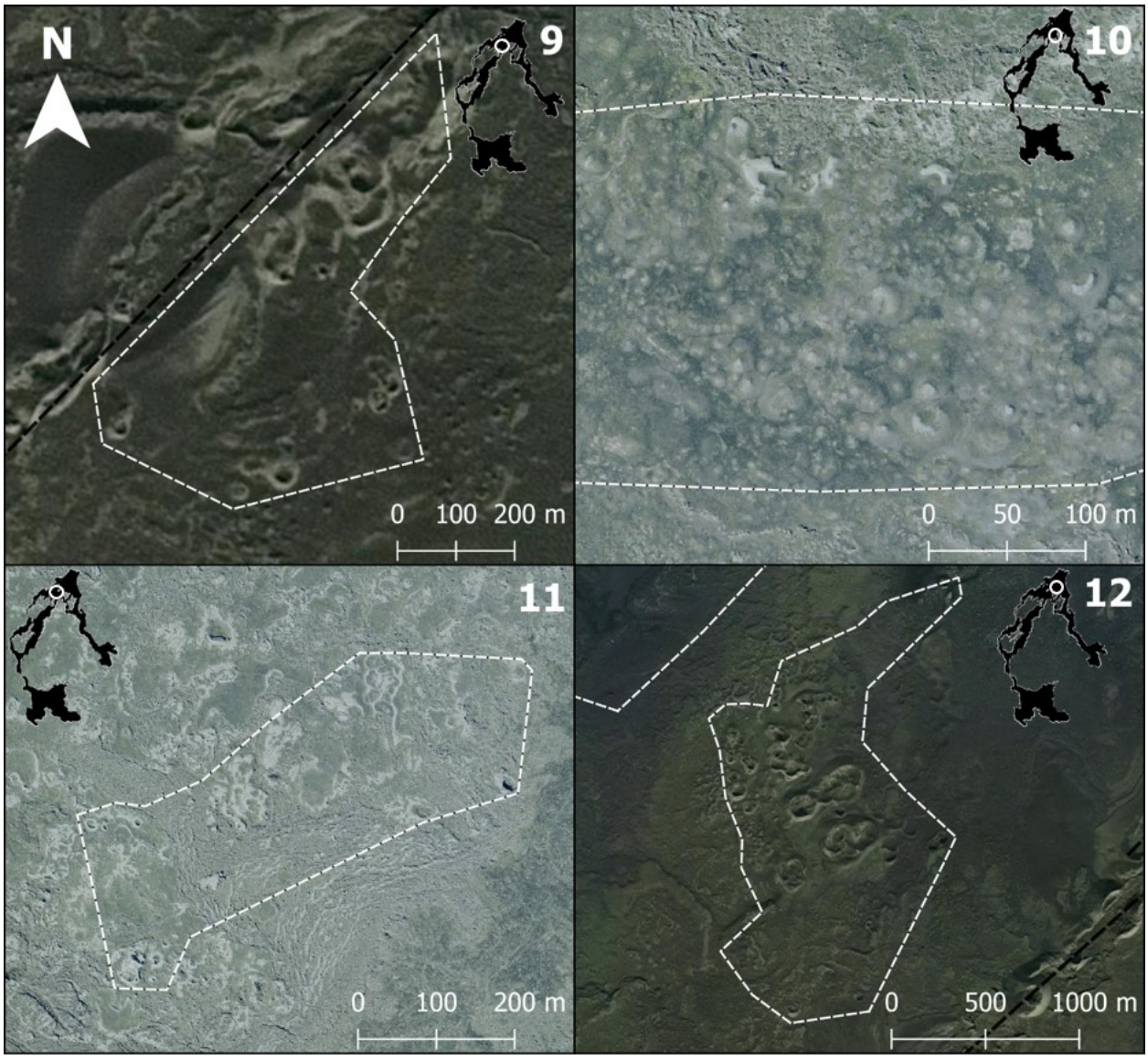

Figure 3.13: Laki rootless cone groups 9–12. The group outlines are shown with a white dashed line. Images are from Google Earth, ©2020 DigitalGlobe, CNES/Airbus, Map data ©2020 Google (groups 9 and 12) and Loftmyndir ehf. (groups 10 and 11; available on `http://map.is`.

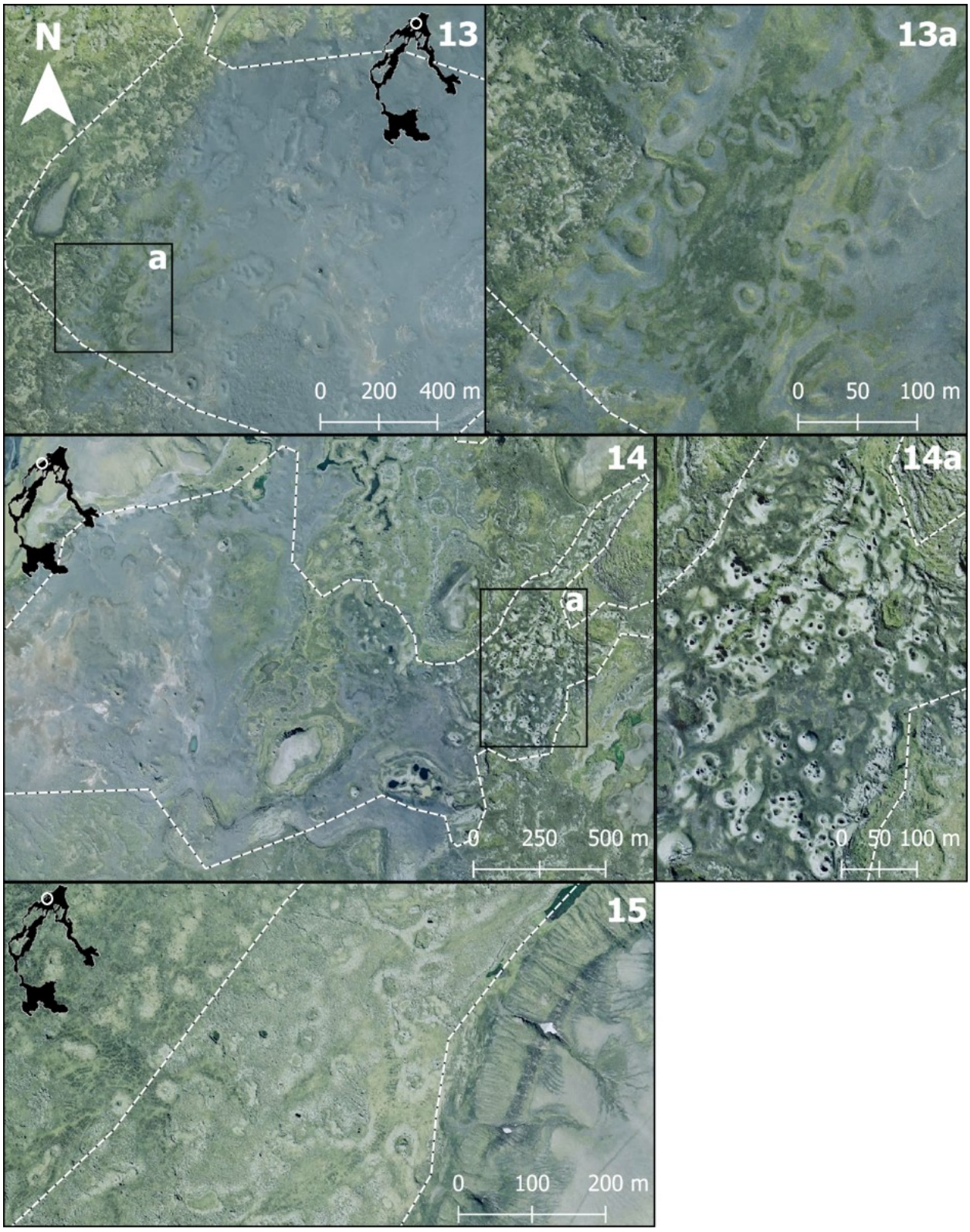

Figure 3.14: Laki rootless cone groups 13–15. The group outlines are shown with a white dashed line. Panels 13a and 14a show close-up views of rootless cones in groups 13 and 14, and the extense are indicated by boxes in the main panels for each group. Images are from Loftmyndir ehf. (available on `http://map.is`.

By the time the lava reached this area, the Skaftá river had been dammed downstream for almost two months, meaning that water would have backed up in the river channel. While we do not know the extent or depth of the impounded water, we can make an approximation using the discharge of the Skaftá river and the valley dimensions. Thordarson and Self (1993) estimated that the lava in this part of the flow is ∼15 m thick. By measuring the area of the Skaftá river channel behind the lava dam and multiplying by this depth, we can estimate the total volume of water needed to flood the river channel back to the location of the rootless cone groups (Figure 3.16). Measurements from the lava dam to rootless cone groups 14 (minimum extent) and 13 (maximum extent) give areas of 20 km^2 (0.303 km^3 to 15 m depth) and 42 km^2 (0.633 km^3 to 15 m depth) respectively. The current average discharge of the Skaftá river is 115 m^3/s. This includes contributions from the Hellisá river and other tributaries, so is likely to be higher than the discharge in the upper reaches of the river. However, Steingrímsson records that the pre-eruption river levels were unusually high and that there was heavy rain throughout, which would have increased the river discharge. For the purposes of this estimation, and without a way to quantify either effect, we will assume that these two factors cancel each other out and use the quoted current average discharge. Based on these assumptions, it would take ∼30 days for water to back up to group 14, and ∼64 days to reach group 13. Given that the Skaftá river was dammed on the 9^{th} of June, and that both rootless cone groups formed in late August, it is plausible that these areas were flooded when the rootless cones formed.

Cone sizes

We were able to map and measure cone sizes in 12 of the 15 identified rootless cone groups. The cones in groups 4, 7 and 10 were too small to see in the ArcticDEM, the Google Earth image resolution in these areas is poor, and the Loftmyndir ehf. were not sufficient for mapping these groups. Cones in the other groups across the lava field have cone sizes (crater radius) ranging from 0.5–89.8 m. However, most of the cones measured (88.2 %) have a crater radius <10 m, and 56.9 % are <4 m radius (3.3). This distribution is similar to that found at the Younger Laxá Lava in northeast Iceland (83.3 % < 10 m; 44.4 % < 4 m), excluding the large expanse of hornitos on the latter flow, which have a different formation mechanism (Figure 3.17; Boreham et al., 2018). Spacing between cones correlates with crater radius ($r = 0.51$, $p < 0.005$), as observed on the Younger Laxá Lava. We found no statistically significant relation between cone size and estimated formation environment (adjusted $r^2 = 0.007$, $p < 0.005$).

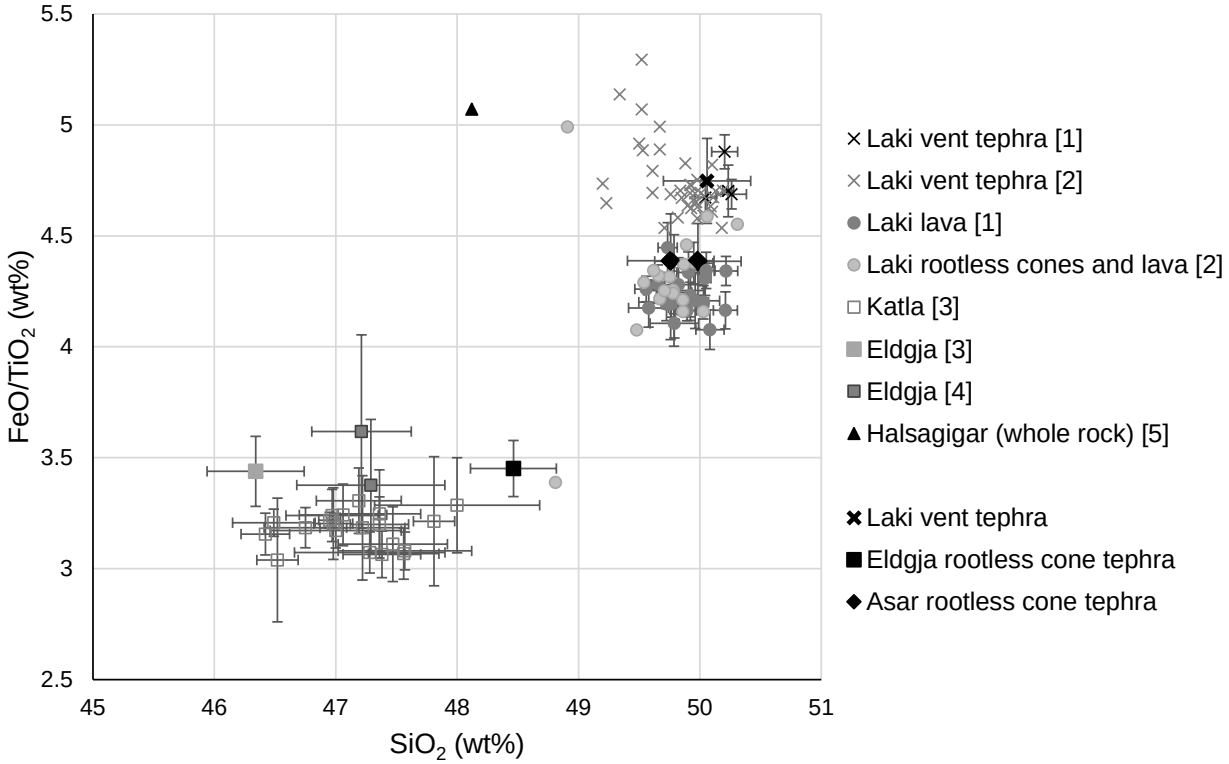

Figure 3.15: Plot of SiO_2 against FeO/TiO_2 of matrix glass from the rootless cones in group 8 (black diamonds), vent-proximal Laki lava (black cross) and rootless cones in Landbrotshólar, created by the 940 CE Eldgjá eruption (black square). These are overlaid on previously published compositions from the Laki eruption, Katla volcanic system and Hálsagígar eruption: [1] Guilbaud et al., 2007; [2] Thordarson et al., 1996; [3] Óladóttir et al., 2008; [4] Thordarson et al., 2001; [5] Jakobsson, 1979.

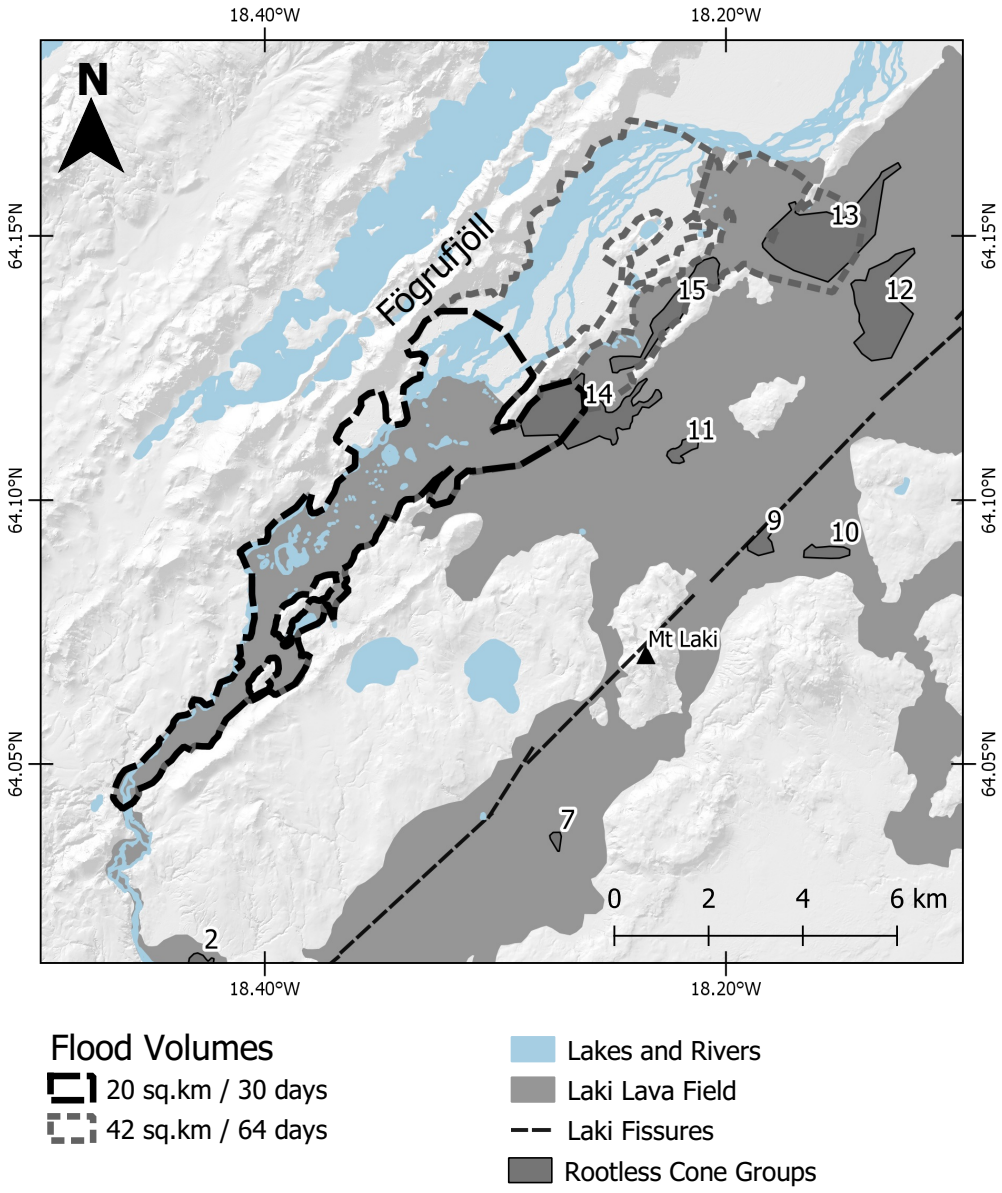

Figure 3.16: Approximate extents of possible impounded water in the upper reaches of the Skaftá river 30 and 64 days after the river was dammed. Flood extents are shown as speckled areas. Rootless cone groups are shaded in dark grey.

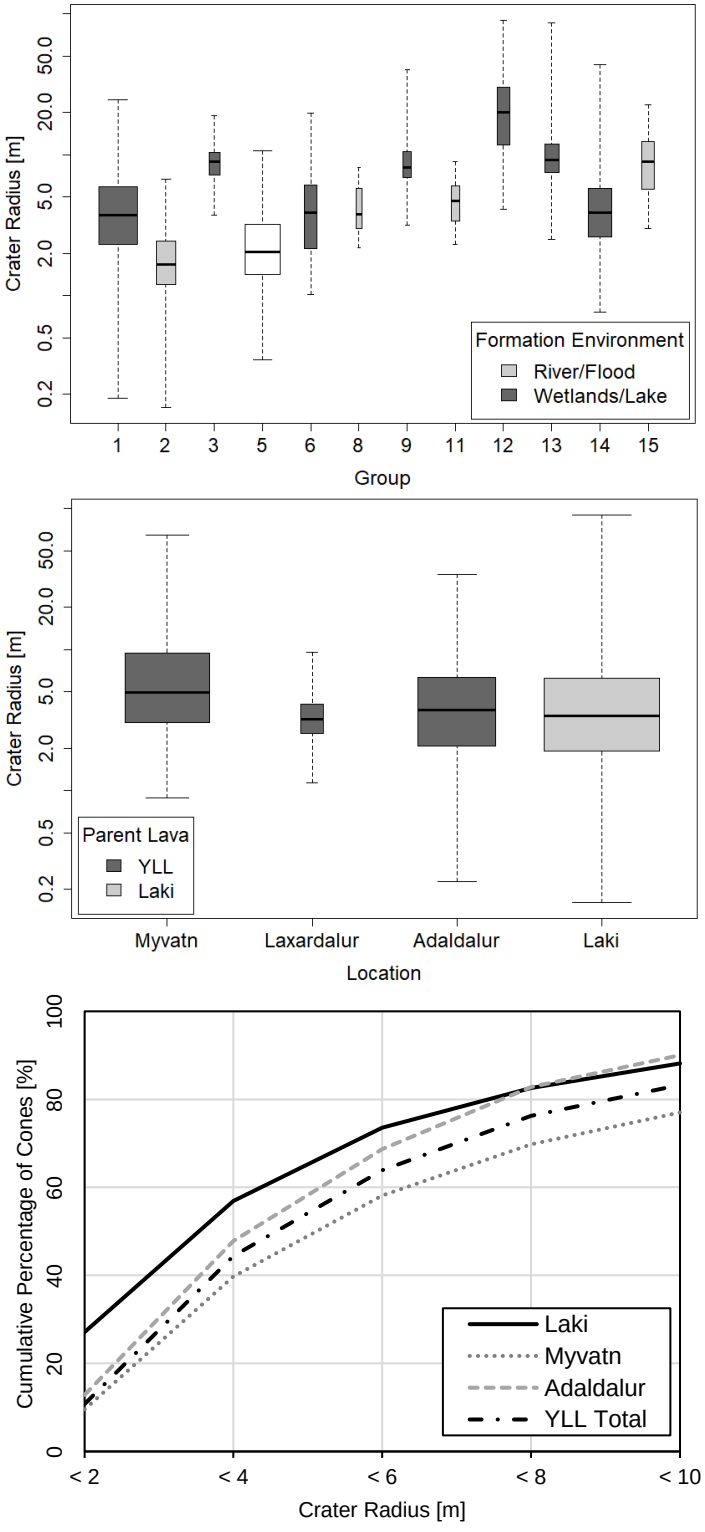

Figure 3.17: Distribution of Laki rootless cone size (crater radius) by group number, colored by environment (white group are unclassified). Middle: Comparison between the total cone size distribution at Laki and on the Younger Laxá Lava, with cones colored by parent lava flow. Bottom: Comparison of the cumulative percentage of small cones (<10 m crater radius) on the Laki and Younger Laxá Lava.

Group	Distance from vent [km]	No. of cones	Crater radius [m]						
			Min	Q1	Median	Mean	Q3	Max	Std Dev
1	2.6	910	0.5[a]	2.3	3.7	4.9	5.9	24.6	3.8
2	3.8	282	0.6[a]	1.2	1.7	1.9	2.4	6.7	1.1
3	3.9	70	3.7	7.2	9.0	9.0	10.3	18.8	2.8
4[b]	8.9	51	Not measured						
5	11.7	776	0.5[a]	1.4	2.0	2.6	3.2	10.6	1.6
6	17.8	1.0	2.2	3.9	4.4	6.1	19.8	2.8	
7[b]	1.6	34	Not measured						
8	47.1	20	2.2	3.0	3.8	4.5	5.7	8.1	1.7
9	0.1	44	3.2	6.9	8.2	10.4	10.5	40.3	7.1
10[b]	1.5	?	Not measured						
11	2.5	44	2.3	3.4	4.7	4.9	5.9	8.9	1.8
12	1.7	88	4.1	44.7	19.8	23.3	30.1	89.8	16.5
13	3.7	120	2.5	7.5	9.2	11.6	12.0	85.7	9.7
14	7.8	342	0.8	2.7	3.9	5.5	5.7	43.6	5.3
15	11.3	100	3.0	5.7	9.0	9.7	12.3	22.5	4.7
All	n/a	2979	0.5[a]	1.9	3.4	5.3	6.2	89.8	6.3

Table 3.3: Distribution of rootless cone type and size across the Laki lava field. [a]Minimum crater radius in these groups is limited by the resolution of available aerial photographs. Cones with smaller craters were identified but not measured. [b]Crater radii of rootless cones in these groups were not measured because they were too small to be discerned with the available aerial photographs.

As noted above, the resolution of our data is insufficient to map individual explosion craters. For example, Hamilton et al (2010a) identified a total of 2038 eruption craters, the smallest of which had a crater radius of 0.4 m; the smallest crater we could identify is >0.5 m radius. Our ability to identify cones from satellite images and DTMs is based on the visible contrast between the crater and the cone walls, which depends on the image processing, the angle and strength of the sun in photographs, and the height and slope difference between cone and crater. For smaller features, this contrast is lower, making it hard to pick out individual cones and craters. Similarly, overlapping craters in a single cone can be very hard to distinguish unless their crater rims are meters apart and cast distinct shadows. Our success in identifying cones, however, is demonstrated by the comparison between ∼930 cones reported by Hamilton et al., (2010a; 680 in the northern half of the group, and 250 in the southern half) without our count of 910 for the same region.

3.5 Discussion

The Laki eruption highlights the hazards posed by lava–water interactions (LWI), particularly lava–river interactions, which are not often included in lava flow models and hazard assessments (Deligne, 2012; Deligne et al., 2016). Not only does it demonstrate the

wide range of hazards, but it also allows reconstructions based on eyewitness accounts and knowledge of the eruption progression from field studies. This makes Laki a good case study to test the use of remote sensing for whole lava field assessments, particularly to determine the circumstances in which different hazards arise and how they develop. In this section, we discuss the major hazards of LWI as illustrated by both the Laki eruption and other examples, the value of remote sensing tools in assessing past LWI deposits, and the hazard implications for similar future eruptions.

3.5.1 Lava–river interactions and flooding

The Laki lava dammed or affected the course of at least 10 rivers across the Fire Districts: the Skaftá, Hellisá, Búlandsá, Holtsá, Fjaðará, Tungufljót, Hólmsá, Kúðafljót, Hverfisfljót and Brunná (Figure 3.8), and possibly many more small tributaries in the highlands. The Skaftá river dammed quickly in Úlfarsdalur due to the combination of high lava effusion rate and the deep, narrow geometry of the gorge. Impounded water above the lava dam would have been further constrained by the Fögrufjöll ridge to the northwest and the Laki lava to the southeast (Figure 3.16). Along the length of the Skaftá gorge, the lava flow blocked smaller tributaries, causing water to back up in steep-sided valleys. There is evidence of passive LWI in Skælingar in the highlands, where the Laki lava dammed two tributaries of the Skaftá river (Figure 3.1C; Gregg and Christle, 2013). In other areas, there are accounts of impounded water flooding farms. In some cases, valley-confined water bodies overtopped the dams. In contrast, where the lava dammed the larger Tungufljót, Hólmsá and Kúðafljót rivers on the plains, the impounded lake covered a large area (10.9 km^2). However, it was only temporary as the rivers diverted around the lava and across soil banks near Hrífunes. From this we can see that steep topography favors dams and impounded water, while in areas of lower relief, rivers are diverted, and water impoundment is less likely.

More generally, during the Laki eruption, lava-induced flooding was short-lived: ∼3 weeks passed between lava damming the Holtsá and Fjaðará rivers (2nd July and 13th July; B12, B13) and impounded water overtopping the dam (20th July; B17, B18), though contemporary accounts do not record how long the dam persisted and upstream flooding lasted. Upstream impoundment of the larger Skaftá river lasted at least a few months (from the 9th of June until ∼21st of September 1783; B1, B41). Blockage of the Hverfisfljót river was episodic, linked to activity at the fissure. The first blockage lasted from the 3rd of August until ∼21st of September (fissure segments 6–8); the river then dried up again when fissure segment 9 opened on the 29th of September, indicating the formation of a fresh dam (B42). The

fact that no lava-dammed lakes from the Laki eruption persist today, even in areas of steep topography, is probably a consequence of both the leakiness of the dams and the permeability of underlying bedrock. The Laki lava primarily lies on top of older lava flows, including the 939–940 AD Eldgjá lava, which contain cracks and vesicles that give the lavas a high permeability. Leakage of water through both dams and young lava flows is seen, for example, at Benham Falls, Sahalie Falls and Koosah Falls in Oregon, USA (Deligne et al., 2017). In contrast, the long-lived lava-dammed lakes in the Grand Canyon, AZ, USA and on the Owyhee River, OR, USA formed on low permeability sedimentary rocks, meaning that water had to either erode the dam or incise a new path around it (Crow et al., 2008; Ely et al., 2012). This slower process created upstream lakes that persisted for up to tens of thousands of years (e.g. Orem, 2010).

Steingrímsson also describes the impact of outburst flooding from lava dams on the eastern margin of the lava flow near Kirkjubæjarklaustur. Most famous is what later became known as the 'Fire Sermon', which Steingrímsson thought would be the last sermon in his church as it was threatened by the encroaching lava. When he and the congregation "*went out to see how the fire had advanced, it turned out that it had not come a foot nearer than before. During the time which had elapsed, it had collected and piled up in the same place, layer upon layer [...]. The rivers Holtsá and Fjaðará poured over the dams which the new lava had made them, and with great torrents and splashing smothered the fire*" (Kunz, 1998; B30, B31). Although it is possible that the flow was reaching its natural end (Thordarson and Self, 1993), Steingrímsson's account makes an interesting case for the role of water in at least slowing, if not stopping, the flow advance. For example, the Clear Lake East lava flow stalled and thickened as it entered Clear Lake, Oregon, USA (Deligne, 2012). Similarly, a preserved inflation front at the distal end of the Younger Laxá Lava in northeast Iceland is flanked by rootless cones, suggesting that the inflation occurred when the lava stalled as it interacted with water. There is a similar preserved inflation front near rootless cone group 8 on the Laki lava field (Figure 3.10). Thus, although individual lava lobes can stall for a variety of reasons (e.g. a reduction in effusion rate or redirection of lava supply to another flow lobe; e.g. Dietterich and Cashman, 2014), cooling by water is an effective way to stall lava advance, as most famously demonstrated during the 1973 Heimaey eruption in Iceland (e.g. Williams and Moore, 1983).

The Laki eruption shows that even temporary flooding and disruption of river flows can cause significant problems. Impounded or displaced water from dammed rivers devastated at least 9 farms that had escaped direct damage from the lava flow (B11, B16, B17, B21, B23, B25, B27, B28, B29, B37, B39). Moreover, contact with the lava made the water

boil and steam (B11), and adversely affected the water quality. Additionally, the extent of flooding was exacerbated by the unusually high river levels before the eruption (A1) and heavy rainfall throughout (D1–D14), a common occurrence in southern Iceland. As well as damaging property and farmland, flooding temporarily cut off access to some farms, and turned previously passable areas into quicksand, making travel across the region difficult and hindering attempts to get aid to isolated dwellings (B36, B38). While current roads and other infrastructure are more robust than they were in the 1780s, in large part because of responses to frequent jökulhlaups (glacial outburst floods), flooding from future eruptions has the potential to wash out roads and bridges, delaying evacuations or the delivery of aid to affected areas. These events demonstrate how the risk to property and infrastructure extends beyond the edge of the lava flow and how areas away from the path of the flow can still be adversely affected.

More generally, lava–river interactions are problematic for downstream communities that rely on rivers for industry, irrigation and other daily water requirements. Indeed, contemporary accounts describe how pollution of the rivers by the eruption cause livestock to sicken and stop producing milk (Kunz, 1998). This forced locals to drink water instead of milk, which also made them sick (B32, B33). Where lava–river interaction is widespread, disruption to water supplies has the potential to impact communities hundreds of kilometers from the vent, and to affect industry, agriculture and hydroelectricity generation in addition to drinking water (Deligne, 2012).

Finally, large fissure eruptions in Iceland are often associated with accompanying activity or unrest in nearby subglacial volcanic systems, e.g. Eldgjá (940 CE) with Katla Volcanic System, Laki with Grímsvötn, and Holuhraun (2014) with Bárðarbunga caldera (Thordarson et al., 2001; Thordarson and Self, 1993; Pedersen et al., 2017). Ash clouds from Grímsvötn were witnessed throughout, and for over a year after, the Laki fissure eruption, with accompanying jökulhlaups recorded in April 1784 and November 1785 (Thordarson and Self, 1993). Jökulhlaups accompanying eruptive activity represent additional hazards to travel and infrastructure.

3.5.2 Explosive lava–water interactions

The widespread rootless cone groups across the Laki lava field show that explosive LWI occurred throughout the Laki eruption. Steingrímsson described the explosions caused as the first surge of lava poured down the Skaftá gorge across the wet sediments of the riverbed (D1). Morphologic evidence for explosive LWI includes rootless cone groups that are found

both in wetland/shallow lake environments (e.g. group 1) and on saturated riverbeds (e.g. group 6). There are also cone groups close to where the lava entered areas of impounded water. This mirrors events during the Younger Laxá Lava eruption in north-east Iceland, which created rootless cones around the shore of a large lake, then in numerous groups across three river valleys where lava met wetlands and dammed rivers (Boreham et al., 2018).

While we do not know for certain what the pre-eruption conditions were, cones in group 8 and groups 13–15 all formed on relatively flat topography upstream of earlier lava dams, where contemporary accounts described impounded water or where we expect water to have accumulated. This would have created large areas of saturated sediment, capable of driving rootless eruptions when covered by lava from later stages of the eruption.

However, rootless cones did not form at all lava–river interaction sites during the Laki eruption. Notably, there are no rootless cones near Kirkjubæjarklaustur where the lava dammed the Holtsá and Fjaðará rivers, nor where the lava dammed tributaries in the Skaftá and Hverfisfljót gorges. In these cases, all of the lava was confined to the downstream side of the dam, so the dams acted as a barrier between the saturated riverbed sediments and the hot, fluid interior of the lava flow, and thus prevented rootless eruptions. Where water built up and overtopped the lava dams, e.g. near Kirkjubæjarklaustur, the lava flow was rapidly quenched, again preventing rootless eruptions (B17, B18).

Similarly, there are no rootless cones on the southern flow margin in the Meðalland and Landbrot districts, despite accounts of flooding and the presence of >4000 cones created by the 939–940 CE Eldgjá lava when it covered glacial outwash plains in this region. The ArcticDEM shows that the Eldgjá lava field is 5–10 m thick at the margins in this area, similar to the Laki lava field. Therefore, the most likely explanation for the lack of rootless cones is a change in the available water. Contemporary accounts show that at the time of the Laki eruption farms in this area grew lyme grass (A9, D8), which prefers porous, sandy soils. Indeed, modern soil maps show that adjacent areas (not covered by Laki lava) are aeolian sand deposits lying on top of the Eldgjá lava. It seems likely that these highly permeable sediments, as well as the inherent permeability of the Eldgjá lava, would have enabled sufficient steam escape to prevent rootless eruptions. Importantly, these sediments provide a stark contrast to the low-permeability, peaty sediments underlying the Laki rootless cone groups in the highlands.

These examples demonstrate how the hydrology, constraining topography and lava flow behavior combine to determine whether explosive LWI occurs. In all cases, the physical properties of the underlying sediments probably control the nature of LWI, with fine-grained,

low permeability sediments most conducive to rootless eruptions. As witnessed rootless eruptions are rare, we rely heavily on evidence from past lava flows to recognize the range of environments where they can form and help identify potentially hazardous areas for future eruptions.

Despite their abundance, rootless cones were probably less of a hazard for the local population than other LWI during the Laki eruption. Most Laki cones are in the highlands near the fissure, and there are no explicit accounts of rootless eruptions causing injury or damage. However, the presence of a cone group (8) in the Fire Districts, ∼47 km from the fissure, is a reminder that they can happen anywhere along a lava flow given the right conditions, i.e. saturated, low permeability sediments.

Tephra from rootless eruptions can be thrown >100 m from the explosion site (Hamilton et al., 2017), and debris from similar littoral rootless eruptions in Hawai'i created jets of steam and lava >60 m high that injured several onlookers (Mattox, 1994). It is unlikely that many people will be this close to an active lava flow, although a group of tourists, film crew and volcanologists were injured by a rootless eruption on Mt Etna in 2016 (Andronico et al., 2018). Their unpredictability makes them a potential hazard for volcanologists and emergency workers during an eruption. Indeed, ballistics are most likely to cause fatalities for field researchers and are of key concern when assessing risk for field work (Brown et al., 2017; Deligne et al., 2018).

3.5.3 Remote sensing for lava flow assessments

Assessing morphologic evidence for lava–water interaction during the Laki eruption using aerial photographs and satellite-derived DTMs allowed us to quickly and cheaply analyze the whole 600 km^2 lava field. All the data are freely available for research purposes and were analyzed through open-source software. We were able to cover a much larger area than would be feasible in a field campaign during the same timeframe, and to map 2979 rootless cones and measure 2831 cones in 12 of the 15 identified groups. For comparison, Hamilton et al.'s (2010a) DGPS study of rootless cone group 1 (2.77 km^2) took place over five successive field seasons.

The whole-field view provided by aerial photographs and DTMs can also reveal large-scale features that are hard to spot on the ground. For example, the ArcticDEM shows the full extent of the group 13 cones, only some of which were previously identified by Bruno et al. (2004) and Guilbaud et al. (2005). The ArcticDEM, in particular, allowed us to identify a

number of eroded cones that are not apparent in satellite images because of their low relief and the low contrast between the cone sides and craters. Similarly, preserved inflation fronts can be mapped in profile using DTMs, as illustrated by the front near cone group 8 (Figure 3.10). GIS software allows measurement of slope and other derived data that can aid feature identification and provide the basis for further geospatial and statistical analyses.

In remote sensing, the size of discernible features depends on the spatial resolution of the data, so there is bias towards identifying larger features. For example, we were able to map and measure 97.8% of the rootless cones in group 1 identified by Hamilton et al., (2010a) but were unable to see multiple explosion sites within individual cones. Another illustrative example is the field of ∼3800 hornitos (<5 m diameter) on the Younger Laxá Lava in northeast Iceland (Boreham et al., 2018). Here we used high resolution (9 cm/pixel) DTMs derived from an unmanned aerial vehicle (UAV) survey to map the detailed (sub-meter) morphology of the hornitos and underlying lava flow, and remove some of the masking effect of vegetation, but individual UAV surveys were limited to a few hundred square meters. However, aerial photographs and the ArcticDEM allowed us to map and accurately count individual hornitos across the whole lava field. Thus, while we appreciate the importance of field studies, we note that increasing use of UAVs and DTMs created using Structure-from-Motion is bridging the gap between field-based and remote-sensing-based surveys, allowing high-resolution surveying of several square km in days rather than months.

An additional advantage of remote sensing is access to all parts of the flow, even the most remote. For example, we suspect that the group 4 rootless cones had been missed by previous studies because they are small (<10 m basal diameter) and lie >2 km from the nearest track. This makes remote sensing an invaluable tool for difficult-to-access field areas, and it is the only option available for planetary volcanologists. In contrast, only field studies allow reconstruction of tephrostratigraphy and observations of fine-scale lava flow morphology have been key in reconstructing the events of the Laki fissure eruption and evolution of the lava flow (e.g. Thordarson and Self, 1993; Guilbaud et al., 2005; Hamilton et al., 2010a). For example, our test of the origin of the group 8 rootless cones in this study required analysis of tephra samples from the cones and candidate parent lava flows. Similarly, determining the exact mechanism of rootless cone formation in different groups would require sediment samples from different locations.

3.5.4 Suggestions for future hazard assessments

LWI hazards are generally overlooked in volcanic risk assessments. Ignoring LWI makes sense in volcanic environments that lack (near-)surface water, which is common in frequently active regions such as Hawai'i. However, there are many volcanically active regions with considerable surface water where LWI is a significant potential hazard. Of particular concern are regions with distributed vents, as are common in volcanic fields and rift zones, in proximity to large river systems. For example, the Oregon Cascades in northwest USA have a long history of basaltic volcanism near large rivers that are close to or upstream of population centers (O'Connor et al., 2009; Deligne, 2012; Deligne et al., 2016; Deligne et al., 2017). Similarly, Iceland has frequent rift-related basaltic eruptions, and receives abundant precipitation that, along with the many glaciers, feeds numerous active river systems. Indeed, the abundance of rootless cones across Iceland is testament to the frequency of LWI during Icelandic eruptions. Other vulnerable areas include the East African Rift System, which has numerous lakes. Probable rootless cone deposits have been identified in Laki Kivu (Ross et al., 2014). Similarly, both the Jingbo and Wudalianchi volcanic fields in China have produced basaltic lava flows within the last 3 ka that created lava-dammed lakes, which are now popular tourist attractions (Gao et al., 2013a; Global Volcanism Program, `http://volcano.si.edu/`). A lava flow that encroached into one of these lakes created thousands of hornitos as steam escaped through the lava (Gao et al., 2013b), like those on the Younger Laxá Lava in NE Iceland (Boreham et al., 2018).

In addition to recognizing past deposits of LWI, such as rootless cones, DTMs are useful for assessing at-risk areas. For a given vent location, DTMs are key to identifying likely lava paths (e.g. Dietterich et al., 2017) and areas where lava flows may be channeled, increasing the distance lava travels (e.g. Dietterich and Cashman, 2014), as happened for both the Laki eruption (Thordarson and Self, 1993; Guilbaud et al., 2007) and the Younger Laxá Lava (Boreham et al., 2018). Topographic analysis can also be used to identify where lava is likely to interact with rivers, and whether rivers will be impounded or diverted around a lava flow. Some lava flow models, such as LavaSIM, can model water-cooling of a lava flow and assess whether the path of a given lava flow is likely to be affected by water-cooling (Fujita et al., 2008).

Identifying the likely path of a lava flow and where it will interact with surface water can be used for LWI risk assessments. Communities likely to be impacted by impounded water can be identified using flood models. In addition, assessments of infrastructure networks (e.g. water, power, fuel, telecommunications) in areas with high LWI hazard could highlight

key vulnerabilities, identify roads and bridges susceptible to eruption-induced flooding, and identify communities that could be cut off from vital services, similar to the DEVORA project for Auckland Volcanic Field (Hayes et al., 2018). Maps of possible flooding can also be combined with sediment maps to highlight areas where rootless eruptions are more likely, i.e. low permeability sediments close to lakes or impounded water.

Depending on the spatial and remote sensing data available (DTMs, aerial photographs, hydrologic maps, soil maps, infrastructure maps), simple hazard assessments can be made in a matter of hours. Therefore, this approach could be used during an eruption to predict LWI as a lava flow develops. Lava flow models (e.g. DOWNFLOW; Favalli et al., 2005) are already used to predict lava flow paths during active eruptions, alongside overflights and UAV surveys to monitor flow development (Dietterich et al., 2019). These flights can also be used to visually inspect the expected flow path and identify areas of standing water or waterlogged ground where LWI could occur. Where overflights are not possible, a visual check of satellite images can be used instead. Lava flow modelling would provide timescales for lava reaching these regions and, depending on the model, may incorporate water-cooling to update lava flow paths (e.g. LavaSIM; Fujita et al., 2008). Where lava is expected to enter or block a river, flood models can be used to predict the likely extent and impact of any upstream flooding on homes or infrastructure. In the event of flooding or predicted flooding, soil maps could help identify whether rootless eruptions are likely. For example, during the 2018 Holuhraun eruption, rootless eruptions were assessed to be a low risk because of the high permeability of the Jökulsá á Fjöllum river sediments.

3.6 Concluding remarks

The Laki fissure eruption demonstrates what can happen when lava flows and rivers interact and can be used to guide volcanic risk and hazard assessments. While lava–river interaction deposits have been studied elsewhere, the addition of eyewitness accounts of these interactions makes Laki unique and provides valuable information about the range of different LWI hazards and the circumstances under which they occur. The lava flows dammed at least 10 rivers, impounding water, flooding farms, hindering travel across the region, and polluting water supplies. LWI created at least 2979 rootless cones across 15 distinct groups. Some of these groups formed near impounded water, suggesting that the lava–river interactions created the conditions necessary for rootless eruptions. The eyewitness accounts at Laki are particularly important because short-term hazards such as floods and water pollution may not leave geological deposits that indicate the scale of damage caused. Combining these

accounts with study of the geological deposits improves our understanding of these hazards and the deposits they leave behind, helps us look for evidence of LWI at past unobserved lava flows, and recognize the potential risks for future similar eruptions.

Our study shows that remote sensing can provide flow-field-wide evidence of LWI and improve our understanding of potential future hazards. The combination of aerial photographs and satellite-derived DTMs enables efficient analysis of lava flow morphologies and rootless cones over large and difficult-to-access lava flows, and provides a reliable tool for mapping rootless cones and large-scale lava flow morphologies. This kind of analysis allows comparison between multiple sites and can strip away the masking effects of vegetation. Although remote sensing cannot replace the detail and nuance obtained from field studies, it can help direct fieldwork by identifying features of interest and allows quantitative assessment of flow-field morphology. In cases where field sites are truly inaccessible, such as planetary lava flows, comparison with similar features that have been studied in the field provides a useful reality check.

This study also raises further questions about lava–river interactions and their associated hazards. To our knowledge, Laki is the only eruption where there are eyewitness accounts of lava–river interaction, from rapid damming of a river by a high-flux lava flow in a narrow gorge, to rivers diverting around or being displaced by lava on a broad plain. These accounts also suggest that the impounded water affected the emplacement of the lava flow. To accurately assess future hazard, we need to know more about the tipping points in the battle between lava and rivers. For example, what balance of lava flux and river discharge is required for a river to divert, stall or stop a lava flow? How does the confining topography affect the formation of lava dams for varying lava flux and river discharge? How do the local conditions affect the longevity of lava dams and impounded lakes, and can we predict when they might fail?

Chapter 4

Numerical modelling of pore fluid evolution in wet sediments heated by lava

Author contributions and declaration: This chapter is a draft manuscript in preparation for publication. The numerical modelling, post-processing and interpretation of the results were done by Frances Boreham. Alison Rust and Kathy Cashman provided guidance on modelling strategy and interpreting the results. Frances Boreham prepared the manuscript, incorporating comments from Alison Rust and Kathy Cashman. We thank Andrey Afanasyev for his help in the initial setup of the model and troubleshooting with MUFITS.

Abstract

Previous studies have developed two different conceptual models for triggering rootless eruptions and building rootless cones. The static model suggests that conduction from a lava flow to an underlying sediment heats pore water to create steam and drive repeated steam explosions (Greeley and Fagents, 2001). The dynamic model is based around the molten fuel-coolant (MFCI) heat transfer mechanism and requires intimate and rapid mixing between lava and wateror wet sediment prior to an explosion (Fagents and Thordarson, 2007). However, neither of these models explains the full range of deposits seen in the field.

While the static heat transfer model has been largely disregarded in favour of the dynamic model it has been shown to be a feasible trigger mechanism for rootless eruptions on Mars (Dundas and Keszthelyi, 2013), but has not been tested for terrestrial lava flows. We ran a series of numerical models to assess the potential for steam generation and pressure build-up in a sediment heated by an overlying lava flow, using the MUFITS software package. The rates of steam generation and pressure build-up depend heavily on the sediment properties. By systematically varying the sediment permeability and porosity, we show that conduction could generate sufficient pore pressure to cause steam explosions and break through the overlying lava flow. In low and very low permeability sediments (e.g. clays, oozes) these explosions would happen at the lava flow front as it advances. However, in moderate and high permeability sediments (e.g. peat, silt and sand) the lava flow can advance tens of metres before sufficient pressure builds up, driving steam explosions behind the active lava front. In this case, the initial steam explosion may promote mingling between the wet sediment and hot, fluid lava in the flow interior, creating the conditions necessary for a more energetic molten fuel-coolant interaction.

4.1 Introduction

The presence of sediment in rootless cones, both in layers (e.g. Hamilton et al., 2017) and incorporated into vesicles in scoria (Einarsson, 1982), suggests that it plays an important role in rootless eruptions (Fagents and Thordarson, 2007). Rootless cones form on a wide range of sediment types in lake, river and wetland environments. However, there has been no systematic study of how the sediment properties affect rootless eruptions, or whether some sediments are more conducive to triggering eruptions than others. This knowledge is important for assessing the risk of explosive LWI in future volcanic eruptions. Similarly, little attention has been paid to the effect of sediment properties on the type of rootless

cones formed, from large scoriaceous cones with internal layers to hornitos built exclusively from welded spatter.

As discussed in Section 1.2.2, two different end-member conceptual models for cone formation have been proposed: the 'static' model based on conduction from a lava flow into a wet underlying sediment, and the 'dynamic' model based on pre-explosion mingling of lava and wet sediment triggering a molten fuel-coolant interaction (MFCI). In recent years, the dynamic model has been favoured because it explains the presence of very fine ash in rootless cones. However, there are a number of problems with the dynamic model. Lava and water have very different densities and viscosities, so they do not readily mingle. The addition of sediment to create a water-sediment slurry could aid mingling but also makes heat transfer between lava and water less efficient (White, 1996). Even with the addition of slurry, relative flow rates >10 m/s are still required to produce hydrodynamic mingling, and mingling rates of >1 $m^2/m^3/s$ of lava and water are required to trigger a MFCI. These thresholds are unlikely to be achieved in the gravity-driven mingling proposed by previous studies.

The recent focus on MFCI means that the static heat transfer model has been discounted. However, conduction has been shown to be a feasible mechanism for triggering rootless eruptions on Mars, where pre-explosion mingling between lava and wet sediment is not possible because water is trapped several metres below the surface as ice (Dundas and Keszthelyi, 2013). However, conditions under which static heat transfer might generate explosions have not been tested for terrestrial environments, where liquid water exists at the surface. Additionally, hornitos and rootless spatter cones contain no fine ash, suggesting that MFCI does not contribute to their formation and another trigger mechanism is at work. Despite their physical differences, scoriaceous rootless cones, spatter cones and hornitos can all form on the same lava flow, sometimes in close proximity to one another (Boreham et al., 2018). Static heating may provide a better explanation for these features, and may also provide a feasible trigger mechanism for initiating a rootless eruption and creating the mixture of lava and wet sediment needed to start a MFCI.

To assess whether the static heat transfer model could feasibly apply to terrestrial rootless cones and to understand the role of sediment properties in triggering rootless eruptions, we modelled the heat transfer from a lava flow into a range of fully-saturated sediments. To assess the effect on steam generation and subsequent pressure changes, we used 2D rectangular domains of homogeneous sediment, systematically varying permeability and porosity. We used four different model scenarios:

1. A lava flow 35 m long 'instantaneously emplaced' over homogeneous sediment.

2. A higher resolution model to assess degassing at the lava flow front in the opening minutes of emplacement.

3. Sediment with an initial thermal gradient under a 35 m long lava flow.

4. A permeable break in the solidified lava flow base 15 m behind the flow front, to simulate an active rootless vent.

Our aim is to understand conditions that could produce sufficient pressure build up to break through the overlying lava flow and initiate a rootless eruption.

4.2 Modelling heat transfer under lava

Modelling of heat transfer beneath lava flows has evolved considerably over the last century, from analytical solutions of the Fourier conduction equation (Lovering, 1935) to complex numerical simulations that account for temperature-dependent properties, sediment water content, and the effects of convection (e.g. Delaney, 1987; Hort, 1997). The scarcity of temperature data collected from under active lava flows and the growing concern from infrastructure providers about potential impacts of lava flows on buried cables, pipes etc. (Tsang et al., 2019) makes numerical modelling a vital tool for assessing hazards.

Numerical modelling has been applied to a range of different lava flow and dyke intrusion scenarios. These models show that magma intrusions into water-bearing sediments create natural convective cells, increasing cooling rates compared to lava flows for both the intrusions and their surrounding sediments (Wilson, 1962; Baker et al., 2015). Convection also plays an important role in thermal erosion, increasing the heat transfer from an established lava flow to the underling sediment (Fagents and Greeley, 2001).

The predicted substrate temperature in numerical models depend heavily on the physical and thermal properties used. Sediments with a high heat capacity or thermal conductivity will increase the rate of heat transfer through the sediment and cooling at the base of the lava flow, leading to a lower interface temperature. These properties vary between different sediments and may change over time in a single sediment, as the temperature and water saturation change. Similarly, the chemical composition, temperature and vesicularity of the lava affect its heat capacity and thermal conductivity (e.g. Lange et al., 1994; Bouhifd et al., 2007; Eppelbaum et al., 2014); higher lava heat capacity and conductivity increase heat transfer and resulting sediment temperatures (Fagents and Greeley, 2001). Numerical

models may be calibrated using analogue experiments (e.g., lava poured on soil), where the substrate temperature is monitored through time with embedded thermocouples, and results compared to temperature profiles inferred from soil samples underneath long-lived lava flows (Tsang et al., 2019).

Numerical modelling has been used to assess pressure build-up and rootless eruptions under Martian lava flows, to test whether the conduction-only model of triggering rootless eruptions is feasible where water is trapped in subsurface ice (Dundas and Keszthelyi, 2013). Here a fully explicit 1D finite difference model was used to solve the heat equation:

$$\rho c_p \frac{\partial T}{\partial t} = \frac{\partial}{\partial z}\left(\kappa \frac{\partial T}{\partial z}\right) \tag{4.1}$$

Model assumptions were based on analogues of Martian soils and include a sediment with 40% porosity (ϕ), ice saturated below the ice table (0.1 – 1.2 m depth), and permeability (κ) of 10^{-11}–10^{-13} m^2 (approx. 10–1000 mD). MUFITS specifies permeability in milli Darcys (mD), named after Henry Dacry. This relates to the SI units of permeability of m^2 by the following relationship:

$$1 \text{ mD} = 9.869233 \times 10^{-16} \text{ m}^2 \tag{4.2}$$

A pressure (P) of 1 MPa was deemed to be the maximum pressure needed to overcome the weight and strength of the overlying lava flow (Greeley and Fagents, 2001). Assuming adiabatic expansion to (Martian) atmospheric pressure, the potential work (W) that could be done by the contained steam is:

$$P = (P_0 V_0{}^{\gamma}) V^{\gamma - 1} \tag{4.3}$$

$$W = \int \text{PdV} \tag{4.4}$$

such that

$$W = \frac{1}{1-\gamma} P_0 V_0 \left(\left(\frac{P_0}{P_{\text{atm}}} \right)^{\frac{1-\gamma}{\gamma}} - 1 \right) \tag{4.5}$$

where the initial volume of steam, V_0, is given by

$$V_0 = \phi Z_S \tag{4.6}$$

and Z_S is the thickness of the sediment layer. The energy (e) per m^2 needed to excavate the total lava thickness is

$$e = \rho g Z_L \left(\frac{Z_L}{2} \right) \tag{4.7}$$

where Z_L is the thickness of the lava flow. Limiting conditions of thick lava flows or thin layers of sediment may prevent the steam from breaking all the way through the lava flow. Note that this method neglects any steam condensation, which would reduce the total work done.

The extent to which conduction is a feasible trigger mechanism for rootless eruptions on Earth has not been explored. Similarly, no studies have addressed the phase change, pressure gradients and resulting flow of water and steam underneath a lava flow, as previous studies either neglected phase changes (Tsang et al., 2019) or did not track the location and properties of the steam (Dundas and Keszthelyi, 2013).

More generally, modelling of vapour transport through heated porous media is an important problem in assessing hazards caused by concrete in fires. Explosive spalling, the high energy loss of chunks or flakes of material from a solid, is an important failure case for structural concrete members, particularly in high strength concrete (HSC; Hertz, 1984; Comeau and Wolf, 1996; Winney, 1996, Hertz, 2003; Kalifa et al., 2000). Here failure is caused by a combination of high pore pressure and thermal stresses induced by sharp temperature gradients (Harmathy, 1965; Anderberg, 1997; Hertz, 2003; Kalifa et al., 2000; Zhang and Davie, 2013; Toropovs et al., 2015). High pressures are produced when water vapour migrates away from a heated surface, moving deeper into the concrete block and condensing in the cool interior. This increases the liquid saturation in the pores, reducing the relative permeability of the vapour phase, a phenomenon known as 'moisture clogging'. As vapour is prevented from moving through the block, the pore pressure on the wet side of the vapour front increases until it exceeds the tensile strength of the concrete and causes spalling. Sophisticated numerical models to predict concrete spalling have been developed (e.g. Gawin et al., 2003, Gawin et al., 2004; Gawin et al., 2006; Dwaikat and Kodur, 2009; Dwaikat and Kodur, 2010) and calibrated against experimental studies (e.g. Kalifa et al., 1998; Kalifa et al. 2000; Toropovs et al., 2015). Although there are notable differences between concrete spalling and rootless eruptions, e.g. the lower permeability, lower saturation, and higher strength of HSC than unconsolidated sediments, it is a useful analogue, as much of the governing physics is the same in both cases.

4.3 Numerical modelling in MUFITS

4.3.1 How MUFITS works

MUFITS (Multiphase Filtration Transport Simulator) models multiphase and multi-component mixtures of fluids in porous rocks over a wide range of pressures and temperatures, including sub- and super-critical conditions (`www.mufits.imec.msu.ru`). It was initially developed for modelling the transport of water and CO_2 mixtures in geothermal settings (Afanasyev, 2012), but has since been extended and applied to modelling CO_2 storage (Afanasyev, 2013), oil reservoirs (Afanasyev, 2015; Afanasyev, 2017), volcanic hydrothermal systems (Afanasyev et al., 2014; Afanasyev et al., 2015; Zarin et al., 2016), and the formation of brine lenses above magma chambers (Melnik et al., 2016; Afanasyev and Melnik, 2017; Afanasyev et al., 2018). MUFITS has been validated against CO_2 storage benchmark models and historical data (Afanasyev et al., 2016). We selected this package because of its ability to model both sub-critical mixtures of water and steam and steam at super-critical temperatures and pressures. It is also free to use for research purposes.

MUFITS solves the properties of multiphase and multicomponent mixtures by defining a polynomial equation of state in terms of molar entropy, s:

$$s(Phx) \tag{4.8}$$

Different equation of state modules are available depending on both the working fluids being modelled and the range of conditions. We use the BINMIXT equation of state developed for describing multiphase mixtures of water and CO_2 at sub- and supercritical conditions (Afansyev, 2019). The equation of state is used to find the mixture properties at the point of thermodynamic equilibrium, i.e. maximum total entropy, s_t:

$$\sum_{i=1}^{3} s_i V_i = s_t \rightarrow max, \qquad s_i = s\,(Ph_i\chi_i) \tag{4.9}$$

$$\sum_{i=1}^{3} h_i \upsilon_i = h_t, \qquad \sum_{i=1}^{3} \chi_i \upsilon_i = \chi_t, \qquad \sum_{i=1}^{3} \upsilon_i = 1 \tag{4.10}$$

$$0 \leq \upsilon_i \leq 1 \tag{4.11}$$

where υ is molar fraction, h is enthalpy, P is pressure, χ is the molar mass fraction, and i denotes the i^{th} phase of the mixture. The full method for solving this scheme is given in

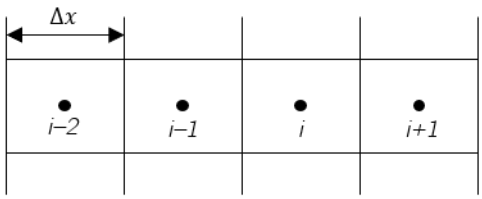

Figure 4.1: Net for 2nd order upwind scheme.

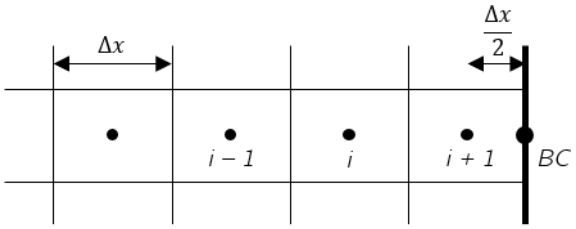

Figure 4.2: Diagram of INFTHIN boundary condition in MUFITS.

Afanasyev (2012). The thermodynamic properties of the mixture are then used to solve the continuity and energy equations and Darcy's law (Afanasyev, 2013):

$$\frac{\partial}{\partial t}\left(\kappa\sum_{i=1}^{3}\rho_i c_{\mathrm{ij}}\phi_i\right)+\nabla.\left(\sum_{i=1}^{3}\rho_i c_{\mathrm{ij}}\mathbf{w}_i\right)=Q_j,\qquad j=1,2 \tag{4.12}$$

$$\frac{\partial}{\partial t}\left(\kappa\sum_{i=1}^{3}\rho_i u_i\phi_i+(1-\kappa)\rho_r u_r\right)+\ \nabla.\left(\sum_{i=1}^{3}\rho_i\widetilde{h}_i\mathbf{w}_i-\lambda\nabla T\right)=Q_u \tag{4.13}$$

$$\mathbf{w}_i=-k\frac{k_{\mathrm{ri}}}{\mu_i}\left(\nabla P-\rho_i g\right) \tag{4.14}$$

MUFITS uses a finite volume approach to discretize and solve these equations across a prescribed grid. Gradients are approximated using a second-order upwind scheme (Figure 4.1):

$$\frac{df_i}{dx}\approx\frac{3f_i-4f_{i-1}+f_{i-2}}{2\Delta x} \tag{4.15}$$

A fully implicit scheme is used to calculate the changes over time, giving the model numerical stability over long timesteps. Other approximations and solver details are given in Afanasyev (2013). We used Dirichlet (constant value) boundary conditions to specify regions of constant pressure and temperature, e.g. under the lava flow or open air (Figure 4.2). Other boundaries were set as impermeable and perfectly insulated, i.e. no mass or energy flux.

MUFITS is designed to run through Message Passing Interface (MPI) software, which allows multiple models to be run in parallel and can be used on high performance computing

networks. Models are described through an input file, which specifies:

- Equation of state module to be used
- Additional modules or schemes, e.g. heat conduction in rock
- Grid extent and cell size
- Rock properties: porosity, permeability, thermal conductivity, density, specific heat capacity
- Relative permeability for liquid and gas phases
- Initial conditions
- Boundary conditions
- Details of any wells or sources in the domain (not used in our models)
- Properties to report for post-processing
- Minimum timestep allowable (in days)
- Reporting interval (in days)

An example input file is given in Appendix C.1. Full details of parameters that can be specified in the input file and the correct syntax are included in the MUFITS reference manual (Afanasyev, 2019). Model outputs are saved at the reporting steps defined in the input file and converted to .pvd files for post-processing in Paraview.

4.3.2 Setting up the model

Grid resolution

The grid resolution was chosen to balance computational cost and capturing sufficient detail in the model. Limits to choosing the grid resolution are outlined below. Fine grid resolutions are computationally expensive, both because of the increase in the total number of cells, and because smaller cells require smaller timesteps to satisfy the Courant-Friedrichs-Lewy (CFL) condition for numerical resolution (i.e. for the solution to be independent of the chosen

timestep). For a linear advection equation, such as Darcy's Law or heat conduction in 1D, this gives a CFL condition of:

$$C = \frac{u\Delta t}{\Delta x} \leq C_{\max} \tag{4.16}$$

MUFITS automatically reduces the timestep used in calculations to meet the CFL condition. To prevent excessive computational expense, we applied a minimum limit to the timestep of 0.001 s. Equation 4.16 shows that the timestep required to meet the Courant condition is also affected by the rate of advection of a property (u) through the system. The rate of heat conduction is relatively slow, so causes no problems. However, in our models high permeabilities (>1000 mD) meant that the Darcy velocity (also known as hydraulic conductivity or Darcy flux) was sufficiently high to violate the CFL condition. Similarly, at very low permeability (<1 mD, 40% porosity), pressure rose too fast to be fully resolved, also violating the CFL condition.

More fundamentally, the choice of grid resolution directly affects the behaviour of the model: since variables are constant throughout a cell, it will take longer for a 10 cm thick cell to heat to a given temperature than a 5 cm cell under the same boundary conditions. Given that steam generation and pressure increase are governed by the cell temperature, and fluid flow is controlled by the pressure gradient, different grid resolutions will create different temperature and pressure fields. Therefore, we must consider the scale over which the processes governing rootless eruptions take place to choose a suitable grid resolution. Observations of exposed rootless cone cross-sections show that explosions can excavate metres down into the underlying sediment, suggesting that the processes of interest happen over the centimetre to decimetre scale rather than the sub-centimetre scale.

We must also consider the scale over which sediment properties, particularly permeability, are applicable. If the cell size approaches the same order of magnitude as the representative elementary volume of the sediment, then the measured properties are no longer valid. This is not a problem for very fine sediments, but modelling high permeability, coarse sediments such as sand and gravel (grain size >1 mm) requires a cell size >1 cm. A coarser lateral grid resolution is permitted because temperature gradients in the x direction are lower than in the z (vertical) direction.

Considering all of the above, we selected a minimum cell depth of 1 cm for our fine-resolution models (Scenarios 0 and 2) and 5 cm for the remaining models (Scenarios 1, 3 and 4; see Section 4.3 for further details of the different scenarios). To reduce computational cost, we made the grid coarser with depth, away from the area most strongly affected by heat transfer. See the descriptions of each model for specific details. The effect of grid resolution

was characterised by running a set of Scenario 2 models on grids with 1 cm, 2.5 cm and 5 cm thick cells, while keeping all other conditions and properties the same. The effect of cell width was tested by running a version of Scenario 1 with cells 10 cm wide rather than 20 cm wide; the results were identical so we kept the coarser grid to minimise computational cost.

Sediment properties

The sediment properties (porosity, permeability, density, thermal conductivity and specific heat capacity) control the heat transfer and transport of steam through the sub-surface. These properties are highly variable across different sediment types and rarely are all of the thermal and mechanical properties determined on the same sample. Table 4.1 shows the range of published values for different sediment types that we used to inform the choice of sediment parameters in our models (further details in supplementary Table C.1 in Appendix C; Manger, 1963; Brooks and Corey, 1964; United States Soil Conservation Service, 1983; Ipekoğlu and Mete, 1990; Inglethorpe, 1993; Revil, 2000 and sources therein; Waples and Tirsgaard, 2002; Hamdhan and Clarke, 2010; Gamage et al., 2011; Brown et al., 2015). Comparison of both wet and dry data for density, thermal conductivity and specific heat capacity show that all are strongly affected by water content. However, MUFITS requires a single set of values for sediment/rock properties, which does not depend on the saturation, temperature or pressure of the cell. Because we are dealing with fully water-saturated sediments, we used the published wet values where available.

Arguably the most important parameter in our models is permeability, as it controls the flow of vapour and therefore the build-up of pore pressure. Scale matters when considering permeability: at large scale (metres to tens of metres), fluid may move along cracks and faults as well as through pore space. This gives a higher permeability than the centimetre-scale samples of sediment typically used to measure permeability. Since we are interested in heat

	Porosity		ρ (kg/m^3)		k (mD)		K	c_p
	Min	Max	Dry	Wet	Min	Max	(W/mK)	(kJ/kg.K)
Clay		0.5	1500	2000	0.00007	0.136	1.3–2.8	
Sandy clay	0.2	0.58	1500	2200	50	166	1.6–4.2	1100–2700
Silt / loam	0.5	0.55	1730	2080	50	500	*No data*	
Fine sand	0.45	0.5	1610	2010	130	288	2.75	1630
Coarse sand		0.4	1730	2080	130	6800000	3.72	1480
Gravel	0.2	0.25	1890	2390	680	6800000	4.44	1175
Diatom ooze		0.9				0.01		

Table 4.1: Summary table showing the range of published physical properties for different sediment types (see supplementary Table C.1 in Appendix C.2 for more detail)

	Sediment
Density (kg/m^3)	2100
Permeability, k (mD)	0.01 – 1000
Permeability, k (m^2)	10^{-17} – 10^{-12}
Porosity	0.2 – 0.9

Table 4.2: Sediment physical properties used in our numerical models

transfer in the top few centimetres of sediment under a lava flow, we used only permeability data measured on this scale. There are also different methods of measuring permeability, which can yield different results for the same sediment (e.g., Gamage et al., 2011). However, since permeability varies by several orders of magnitude and we are most interested in the range of possible values for use in our model, we have not considered these differences as long as the permeabilities were measured on natural samples at the centimetre scale.

While there are abundant data on the permeability of gravels, sands, silts and clay, there is less published information on the properties of lacustrine diatom ooze of the type found at the Lake Mývatn rootless cones in NE Iceland. Most measured diatomite properties are for industrial uses, where processed diatomaceous earth is used as a food additive or as part of filtration systems (e.g. Ipekoğlu and Mete, 1990). Here the values of density, porosity and permeability are for industrially processed samples rather than natural lake sediment (e.g. Inglethorpe, 1993). Therefore, we have taken values from the marine sediment literature, most of which have come from the International Ocean Drilling Program (Gamage et al., 2011). The porosity and permeability of these samples decreases as the effective stress on the sample increases, equivalent to greater burial depth below the sea floor. Since the sediments involved in rootless eruptions are at the surface and immediate subsurface, the effective stress will be lower than for submarine sediments, meaning that the permeability will probably be at the higher end of the published range.

To allow comparison between scenarios, we kept the same values of sediment thermal conductivity, specific heat capacity and density throughout (Table 4.3). These correspond approximately to the published values for wet, sandy clay (Hamdhan and Clark, 2010) and differ somewhat from those used by previous studies (e.g. Fagents and Greeley, 2001; Tsang et al., 2019; Table 4.3). Fagents and Greeley (2001) found that modelled sediment temperature is heavily dependent on the sediment thermal properties. Therefore, we also ran models to test the effect thermal conductivity and specific heat capacity on the results (Table 4.3).

	Fagents and Greeley (2001)[a]		Tsang et al. (2019)[b]		This study	
	Lava	Sediment	Lava	Sediment	Lava	Sediment
Density	2500	2700	2600	1438	2900[c]	2100
c_p (kJ/kgK)	3.6	1.04	1.1	0.45	1.09[d]	2.5, **2.0**, 1.5
κ, (W/m.K)	1.2	1.5	2.2	1.5	1.69[e]	**3.75**, 2.75, 1.75

Table 4.3: Lava and sediment thermal properties used in this study, compared to values used in other studies of lava–sediment heat conduction. Values for c_p and κ shown in **bold** are the default values used in the majority of models. [a]Values at T_L = 1500 K. [b]Lava properties at 1027 °C, wet sediment properties at 20 °C. [c]Bouhifd et al. (2007). [d]Average value for basalt liquid and glass between 900–1700 K, Boufihd et al. (2007). [e]Sharma et al. (2002)

Relative permeability

The range of conditions covered by our models includes liquid water, steam and supercritical fluid, meaning that we have to define the relative permeabilities of the different phases. MUFITS allows the user to specify relative permeability values for the rock. The Corey relative permeability model can be applied to describe the relative flows of liquid water and steam in porous rocks (Horne et al., 2000; Figure 4.3), with the relative permeabilities of water (kr_{liq}) and steam (kr_{gas}) described as a function of liquid saturation (ϑ_{liq}):

$$\mathrm{kr_{liq}} = {\vartheta_{\mathrm{liq}}}^4 \tag{4.17}$$

$$\mathrm{kr_{gas}} = \frac{\left(1-\vartheta_{\mathrm{liq}}\right)^2}{1-{\vartheta_{\mathrm{liq}}}^2} \tag{4.18}$$

As the fluids approach the critical point they become indistinguishable, meaning that the relative permeabilities for the liquid and gas phases become equal. To accommodate this behaviour, MUFITS includes an algorithm that automatically alters the relative permeabilities curves to straight lines near the critical point.

Setting an explosion threshold

To assess whether any of the scenarios modelled in MUFITS could create a rootless eruption, we need to set a pressure threshold at which we assume a steam explosion occurs (P_{max}). This pressure will be a combination of the confining forces acting on the sediment, including the atmospheric pressure (P_{atm}), the weight of the lava flow (P_L), and the failure stress of the lava flow (σ_L):

$$P_{\mathrm{max}} = P_{\mathrm{atm}} + P_L + \sigma_L \tag{4.19}$$

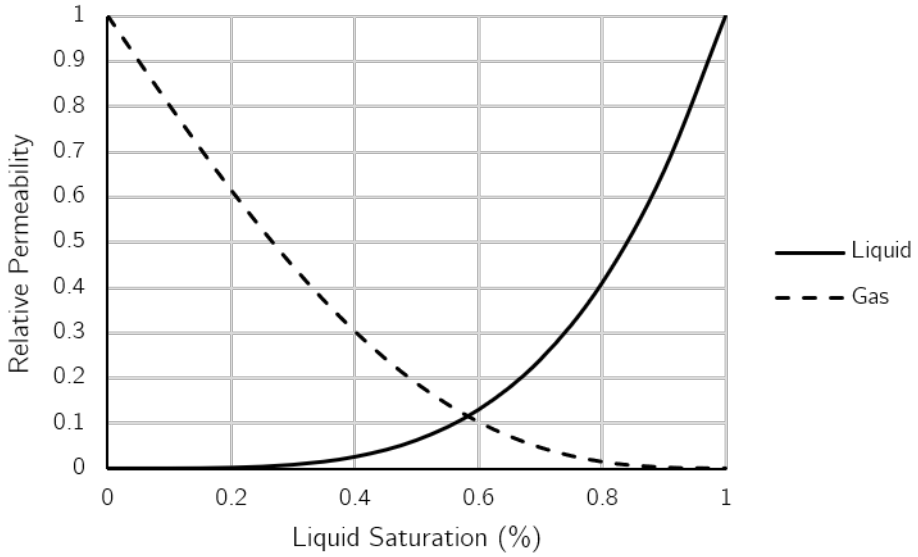

Figure 4.3: Corey relative permeability curves for liquid and gas.

Greeley and Fagents (2001) estimated P_{max} to range from 0.125–1.86 MPa, based on lava flow thicknesses of 1–15 m, lava yield stress of 0–8 kPa, and crust failure stress of 0–1 MPa.

In our calculations, we assume that the fluid lava in the core of the flow has negligible yield strength. We do not consider the strength of the top crust as, once the basal crust has failed, the hot fluid lava will be directly exposed to the wet sediments and heat transfer rates will increase. Since we are dealing with unconsolidated sediments, we assume that the sediment cohesive strength is negligible.

Field observations of inflating lava flows (e.g. Hon et al., 1994) allow us to estimate the increase in flow thickness, $Z_{L,}$ through time. From this, we calculate the confining pressure from the weight of the overlying lava flow as

$$P_L = \rho g Z_L \tag{4.20}$$

Hon et al. (1994) observed that the brittle outer crust of inflating pāhoehoe lava flows often contains numerous cracks and inferred that most of the crustal strength confining the hot, fluid core of the flow must be in the viscoelastic part of the crust. Therefore, we have neglected the strength of the brittle crust in our calculations and focus on the viscoelastic crust. Cooling within the crust causes crystallisation, which increases the viscosity of the lava and, at moderate crystal fractions, creates load-bearing crystal networks (e.g. Dingwell et al., 1993; Philpotts and Carroll, 1996; Cashman et al., 1999). Load-bearing networks of plagioclase and pyroxene crystals in basalt form around at ∼35% crystallisation, allowing

Time (mins)	1	20	30	60	90	120	180
Z_L *[m]*	0.20	0.40	0.55	0.70	0.80	0.90	1.10
P_L *[MPa]*	0.006	0.011	0.016	0.020	0.023	0.026	0.031
P_{atm} *[MPa]*	--- 0.101 ---						
σ_L *[MPa]*	--- 0.4 ---						
P_{max} (MPa abs)	**0.507**	**0.512**	**0.517**	**0.521**	**0.524**	**0.527**	**0.532**

Table 4.4: Estimated failure threshold, P_{max}, through time.

cubes of partially molten basalt keep their shape up to 70% melt (Philpotts and Carroll, 1996).

The approximate strength of the viscoelastic portion of the lava flow crust can be obtained by estimating the overpressure (ΔP) within an inflating lava flow. All published estimates suggest $\Delta P = 0.2$–1 MPa (Hon et al., 1994; Rossi and Gudmundsson, 1996; Cashman and Kauahikaua, 1997; Hoblitt et al., 2011). These values are similar to the stress criteria for propagation of dikes (1 MPa; Rubin, 1995). We chose $\Delta P = 0.4$ MPa for our models.

Putting these values into equation 4.19, we calculate a failure threshold $P_{max} = 0.51$–0.53 MPa (Table 4.4), within the range calculated by Greeley and Fagents (2001). It is a minimum estimate, as we do not account for the strength of the sediment and there is considerable uncertainty about the true strength of the viscoelastic crust and the contribution of the brittle crust, so it should be taken as an order of magnitude approximation of the true failure threshold.

Setting the thermal boundary conditions (Scenario 0)

Scenarios 1–4 only model the extent of the sediment, and do not include the overlying lava flow or atmosphere. The atmospheric temperature and pressure and the lava flow temperature are represented by boundary conditions imposed at the top of the sediment (i.e. $z = 0$ m). To determine an appropriate temperature for the boundary condition, we used MUFITS to model 1D unsteady heat conduction between a 1 m thick lava flow, initially at eruption temperature $T_L = 1170$ °C and an underlying sediment initially at ambient temperature $T_s = 15$ °C (Scenario 0; Figure 4.4). The temperatures at the top boundary of the lava ($z = 1$ m) and bottom boundary of the sediment ($z = -5$ m) are fixed:

$$T_{z=1} = 1170^{o}C \tag{4.21}$$

$$T_{z=-5} = 15^{0}C \tag{4.22}$$

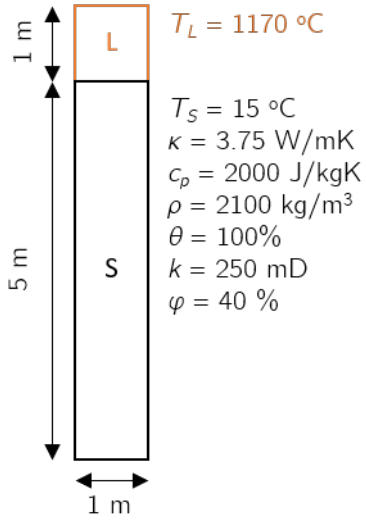

Figure 4.4: Sketch of scenario 0 model setup.

We used 1-cm-thick grid cells and reported results every 30 seconds for one hour. Since this scenario does not include fluid transport, we did not vary the permeability or porosity of the sediment.

In the early stages of contact between lava and sediment, the lava cools and sediment heats rapidly (Figure 4.5). The rate of temperature change decreases over time as the thermal gradient across the interface decreases. After the first hour of contact, only the bottom 17 cm of the lava flow and top 20 cm of sediment had cooled or heated >5 °C from their initial temperature.

The interface temperature at the boundary between the lava and sediment cells, equivalent to the bottom of the lava crust (indicated by the dashed black line in Figure 4.5), decreases rapidly in the opening minutes before stabilising. This decrease, along with the asymmetry of the cooling curves in Figure 4.5, reflects the difference in thermal conductivity between the lava (1.69 W/mK) and sediment (3.75 W/mK) such that heat transfer is more rapid from the lava into the sediment than from the hotter part of the lava flow to the interface.

We used the average interface temperature over the first 30 minutes of contact in Scenario 0, $T_{z=0} = 477$ °C, as the top boundary condition for scenarios 1, 3 and 4. For scenario 2, we were interested in the behaviour in the first 5 minutes so we used the average temperature over the first 5 minutes, $T_{z=0} = 533$ °C. While conduction models tend to underestimate the heat transfer from lava to sediment over long times because they neglect the influence of forced convection from the flowing lava (Fagents and Greeley, 2001), this simplification is appropriate given the other assumptions and simplifications in our models.

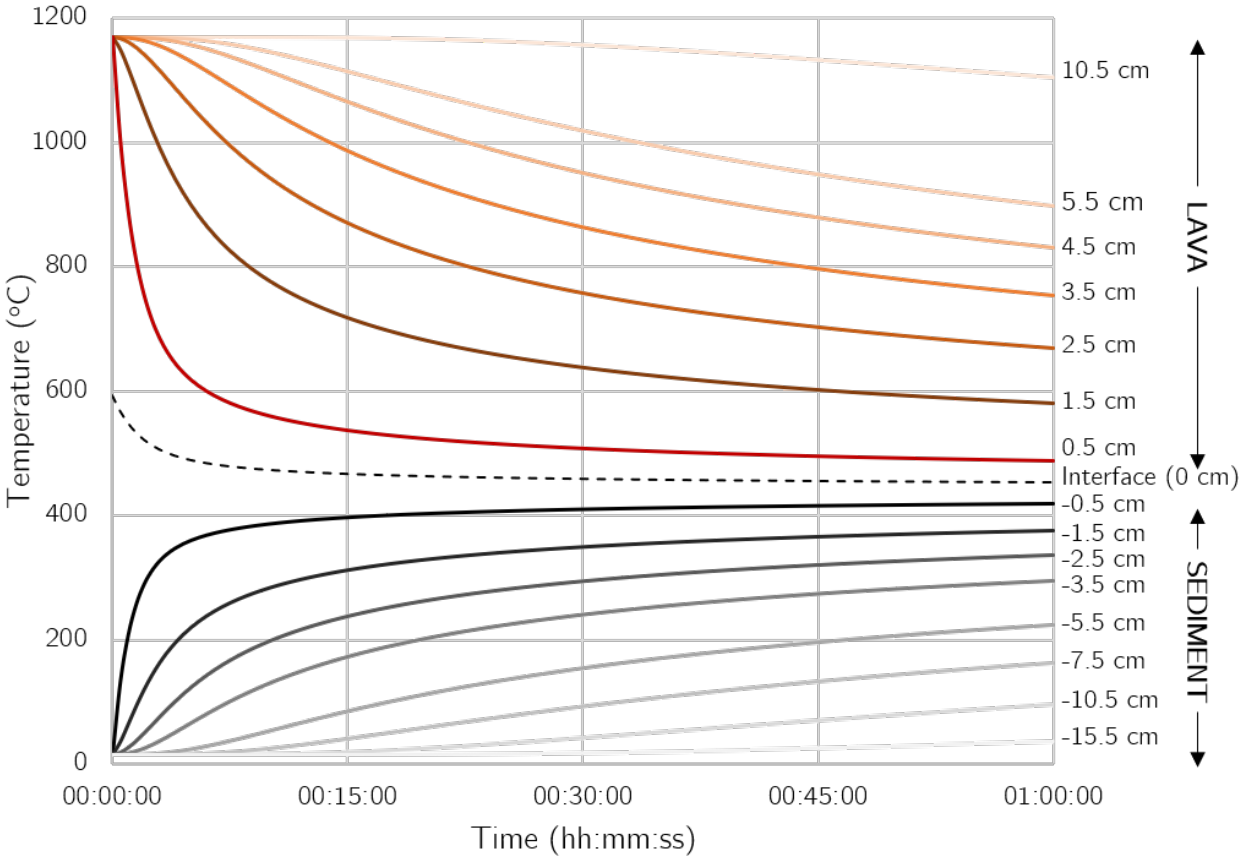

Figure 4.5: Results of Ssenario 0 from MUFITS. Solid lines show the change in temperature with time for different depths of lava (positive depths, shown in red/orange) in contact with sediment (negative depths, black/grey). The dashed grey line shows the interface temperature between the lava and sediment.

Time elapsed (mins)	Interface temperature (°C)
0	592.5
5	533.5
10	502.1
15	491.4
30	476.8
60	466.1

Table 4.5: Time-averaged interface temperature between lava and sediment from scenario 0.

4.3.3 Modelling strategy and scenarios

Since the dynamics of the rootless eruptions are complex, we initially focussed on the time between lava flow emplacement and the onset of an explosion, assuming no mixing between sediment and lava. This matches the opening stages of Greely et al.'s (2001) conceptual model of rootless cone formation (Figure 1.11). We use five scenarios that capture different aspects of lava–sediment heat transfer (Figure 4.6). A brief description of each scenario is provided below, together with the boundary conditions applied and the properties varied.

Scenario 1: 2D instantaneously emplaced lava flow

Here a lava flow is emplaced instantaneously on a fully water-saturated, homogeneous sediment (Figure 4.7). We looked at the effect of the permeability and depth of the underlying sediment on the development of temperature, pressure and boiling in the sediment. The sediment thermal properties are the same as in Scenario 0, but the sediment permeability varies from 1–1000 mD, with an additional diatomite case that assumes 90% porosity and a permeability of 0.01 mD. Values beyond this range generated timesteps below the minimum limit to fulfil the CFL condition.

The modelled domain is 50 m long, with varying depths of 3 m, 4 m and 5 m. The sediment has a uniform starting temperature of 15 ^{o}C and a hydrostatic pressure gradient. The cells in the top 1.5 m of the sediment domain are 5 cm thick, increasing to 10 cm for the remaining depth. The first 15 m of the horizontal domain has a permeable constant pressure and temperature top boundary, representing the open air (T_{atm} = 15 ^{o}C, P_{atm} = 0.1 MPa). The remaining 35 m of the top boundary is impermeable and held at a constant temperature, equivalent to the average lava-sediment interface temperature from Scenario 0 over the first 30 minutes (T_L = 477 ^{o}C). The bottom boundary is impermeable and thermally insulated. The x = 50 m boundary condition (behind the lava front) is also impermeable and insulated. We considered a constant pressure and temperature bottom boundary condition as an alternative, but this would require a highly permeable layer connected to an instantly equilibrating aquifer, which is unrealistic for rootless-cone-forming sites. The x = 0 boundary condition (away from the lava flow) is permeable and held at constant temperature and pressure (15 ^{o}C, hydrostatic pressure), representing a larger sediment body. The dimensions, boundary conditions and grid resolution of Scenario 1 provide the basis for later, more complex scenarios.

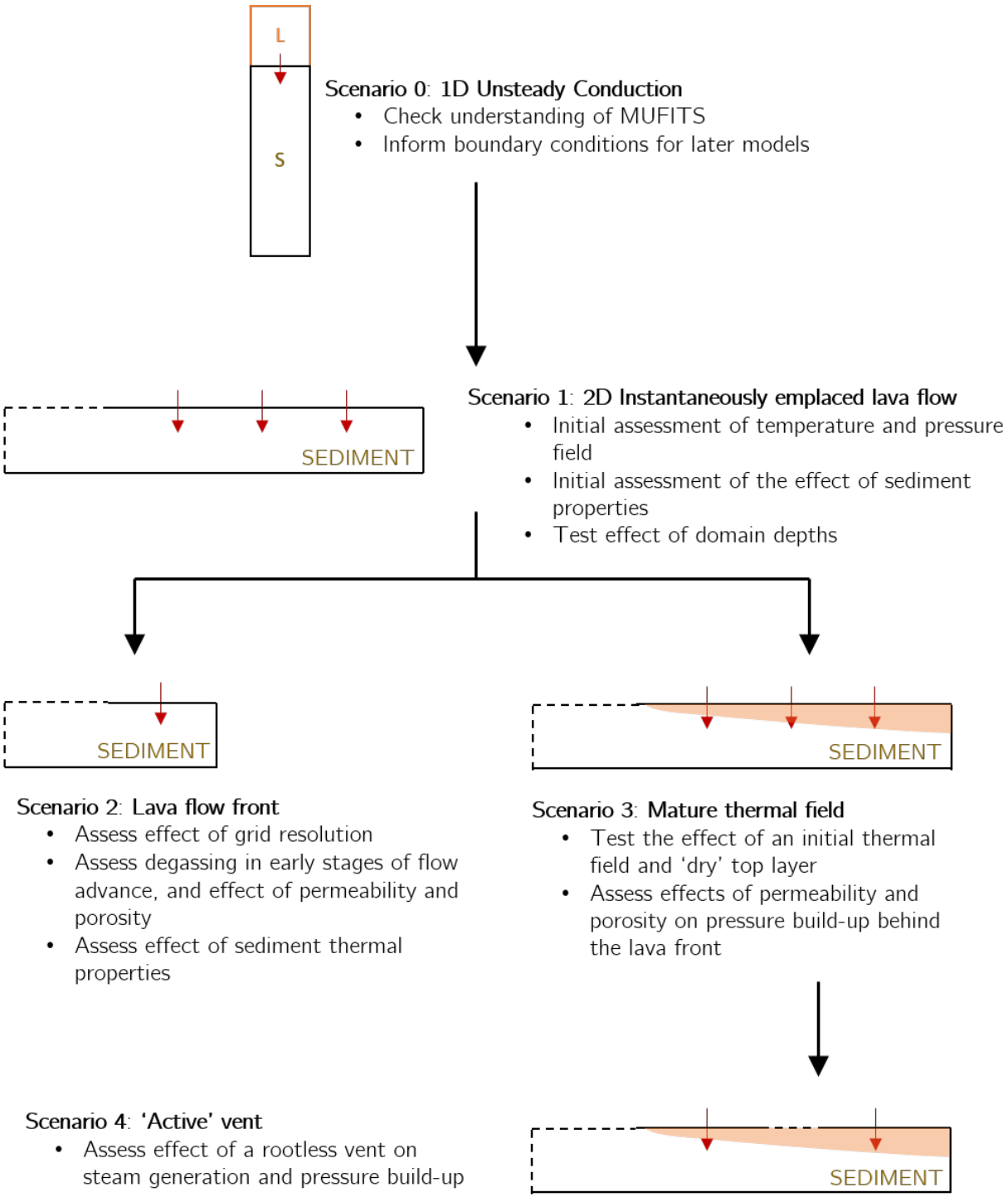

Figure 4.6: Flow diagram of model scenarios and modelling strategy. Red arrows indicate heat flux from overlying lava. Orange shaded areas indicate initial sediment temperatures higher that 15 °C. Dashed lines represent permeable grid boundaries, and solid lines represent impermeable boundaries, More detail on the dimensions, boundary conditions, initial conditions and grid resolution for each model are given in the following sections.

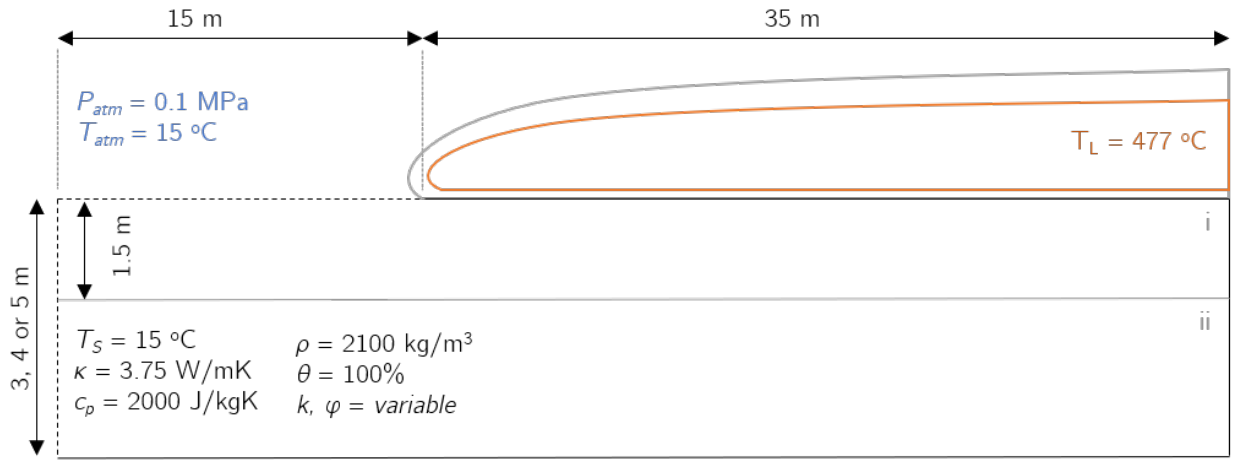

Figure 4.7: Sketch of scenario 1 model set up. Solid black lines represent impermeable, insulated boundaries. Dashed black lines represent permeable, fixed condition boundaries. A sketch of the overlying lava flow is shown here but is not part of the model domain in MUFITS. We used domain depths of 3, 4 and 5 m to explore the effect on pressure build up. Subdomains i and ii , separated by a grey line, show the areas of the domain with different cell sizes. Cells in subdomain i are 20 cm wide x 5 cm deep; cells in ii are 20 cm x 10 cm.

Scenario 2: Lava flow front

Field observations of lava flows advancing over wet sediments show steam and other gases escaping around the flow front, meaning that the top layer of the underlying sediment is no longer fully saturated. To understand how quickly this initial degassing takes place and how sediment properties affect the generation and flow of steam, we created a higher resolution model focussing on the flow front by limiting the computational domain to the first 4 m of the lava front and documenting the opening minutes of the simulation (Figure 4.8). A typical advance rate for a sheet pāhoehoe lava flow over dry ground is 100 m/hr (Hon et al., 1994). We use 1 cm thick grid cells, the minimum over which the permeability data is applicable, to capture the behaviour in the top layers of sediment. Because the simulation focuses on the opening minutes of a lava flow advance, the temperature of the top boundary condition is increased to 533 °C (the temperature after 5 minutes in Scenario 0) to reflect the fact that the basal crust is very thin. All other boundary conditions and sediment properties (permeability and porosity) were kept as per Scenario 1. The permeability and porosity of the sediment are then varied to determine their effect on steam generation and escape and the rate at which the top layers of sediment dry out as the lava flow advances. The goal of this scenario is to determine whether a dry conduit for steam escape is established as the lava flow advances, which is important for interpreting later models.

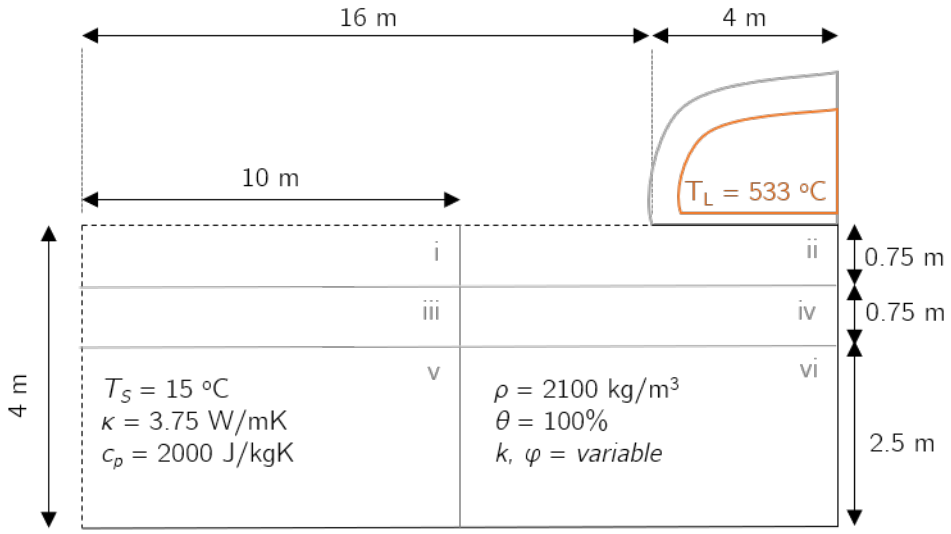

Figure 4.8: Sketch of scenario 2 model setup. Solid black lines represent impermeable, insulated boundaries. Dashed black lines represent permeable, fixed condition boundaries. A sketch of the overlying lava flow is shown here but is not part of the model domain in MUFITS. Subdomains i–vi , separated by grey lines, show the areas of the domain with different cell sizes. Cells in subdomain i are 1 m wide x 1 cm deep; cells in ii are 10 cm x 1 cm; cells in iii are 1 m x 5 cm; cells in iv are 10 cm x 5 cm; cells in v ar e 1 m x 10 cm; and cells in vi are 10 cm x 10 cm.

A slight variation on this grid was used to test the effect of grid resolution on model results. To save computational time, we reduced the grid to 10 m wide and varied the cell thickness in the top 0.75 m of the grid (domain **i** in Figure 4.9). We tested cell thicknesses of 2.5 cm and 5 cm and permeabilities of 50 mD, 250 mD and 1000 mD; all other sediment properties, initial and boundary conditions are identical to Scenario 2.

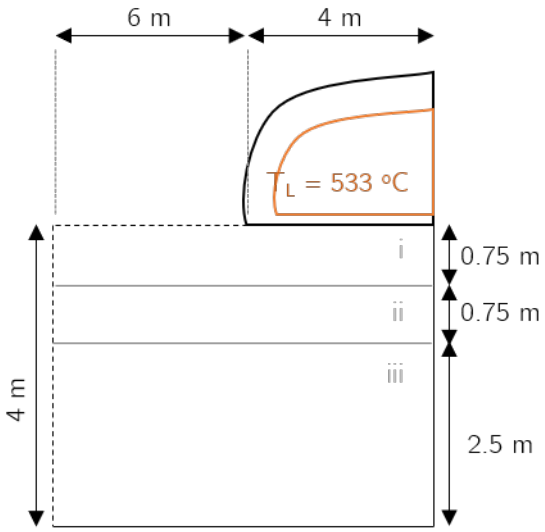

Figure 4.9: Sketch of modified Scenario 2 model used to test effect of grid resolution. Subdomains i–iii, separated by grey lines, show the areas of the domain with different cell sizes. Cells in subdomain i are 1 cm, 2.5 cm or 5 cm thick, cells in ii are 5 cm thick and cells in iii are 10 cm thick. All cells are 10 cm wide.

Scenario 3: Mature Thermal Field

As a lava flow advances, sediment further behind the flow front will be hotter than that near the flow front because it has been heated for longer. To capture this, we modified the initial temperature field in the sediment so that cells further behind the flow front start at a higher temperature than those nearer the flow front (Figure 4.10). To do this the domain under the lava flow was divided into sections 5 m wide. Heating times were calculated using a flow advance rate of 100 m/hr (5 m in 3 mins) and compared with the results of Scenario 0 to assign a temperature. To account for the different spatial resolutions, the temperature was averaged over multiple cells from Scenario 0 to obtain the initial condition for Scenario 3. For example, as the block of cells at 0–5 cm depth and 10–15 m behind the lava front will have been heated for 6–9 minutes, the temperature of the top five cells in Scenario 0 was averaged over this time. The temperature used for each block is shown in Figure 4.10.

For simplicity, a uniform cell width of 20 cm was used across the whole domain. We kept a cell thickness of 5 cm in the top 1.5 m of the domain, and 10 cm in the rest of the domain and used the same range of sediment permeability and porosity values as Scenarios 1 and 2.

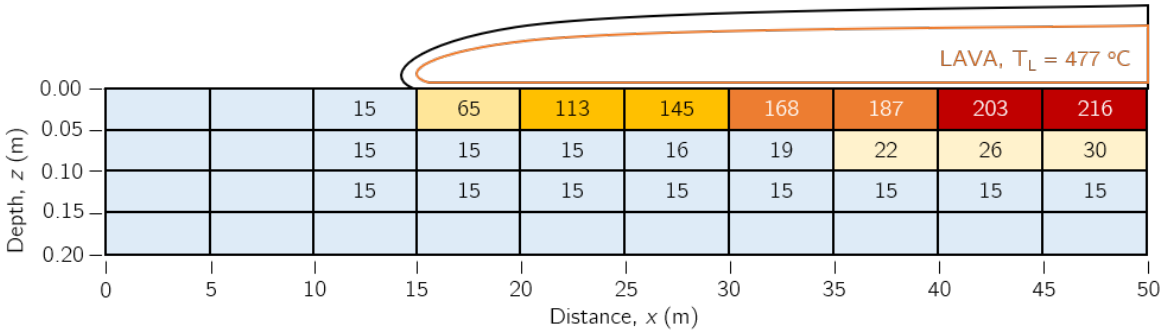

Figure 4.10: Initial thermal field applied to scenario 3 models. The number in each box shows the initial temperature (°C) applied to the cells in that region; cells without a number are at 15 °C. Note that only the top 20 cm of the model domain are shown in this diagram. Boundary conditions and sediment properties are the same as scenarios 1 and 2.

Scenario 4: Active vent

Finally, to determine the effect of an active rootless vent on the pressure and fluid flow through the sediment (Scenario 4; Figure 4.11) we added a 2 m wide permeable 'vent' in the upper boundary of Scenario 0, 14 m behind the lava front, giving an additional steam escape pathway. We tested sediment permeabilities of 50 mD, 250 mD and 500 mD, all at 40% porosity, and a 'diatomite' case with 90% porosity and a permeability of 0.01 mD. This scenario used the same initial thermal field and grid resolution as Scenario 3.

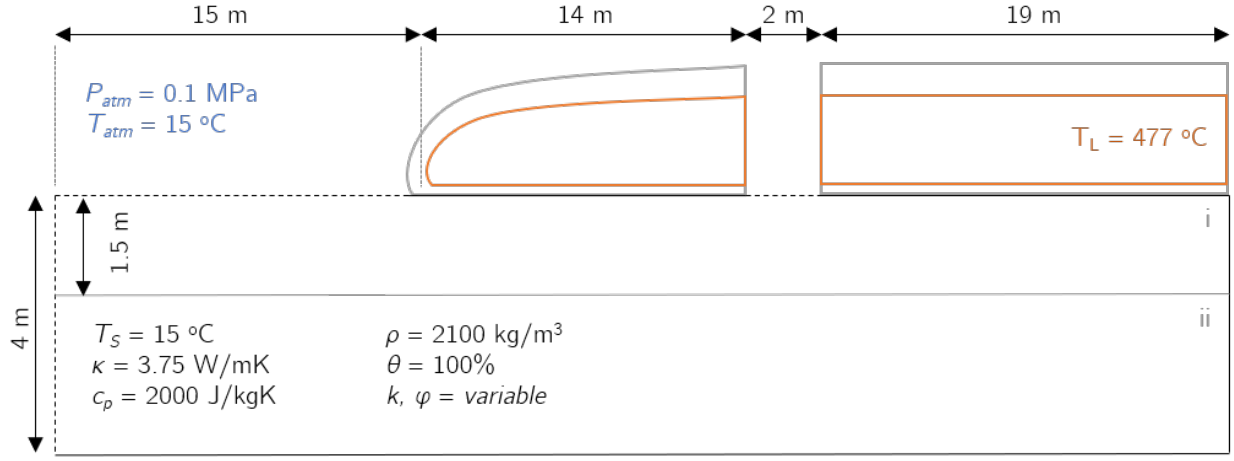

Figure 4.11: Sketch of scenario 4 model setup. Solid black lines represent impermeable, insulated boundaries. Dashed black lines represent permeable, fixed boundaries. Subdomains i and ii, separated by a grey line, show the areas of the domain with different cell sizes. Cells in subdomain i are 20 cm wide x 5 cm deep; cells in ii are 20 cm x 10 cm.

4.4 Results and analysis

The general effects of sediment properties and grid resolution on the numerical results of scenarios 1–4 are described in Section 4.4.1. This is followed by the results from specific scenarios and what they tell us about the situation under a real lava flow.

4.4.1 General results

The shapes of the pressure, temperature and density curves in the models are driven by two factors:

- Heating liquid water confined in sediment pores ($T < T_{boil}$), and
- Rate of steam generation and escape ($T > T_{boil}$).

The relative importance of these two factors depends on the sediment permeability and the model domain extent (length of sediment modelled behind lava flow). The two end-member cases of high and low permeability are used to describe and explain the influence of these factors on the pressure, temperature and density curves.

In all cases in all scenarios, there is an initial pressure rise as the sediment is heated but the temperature remains below $T_{boil.}$ This is caused by the liquid water in the top 'wet' (liquid-saturated) layer of cells warming and trying to expand. As the sediment inhibits fluid expansion and flow, the pressure rises (Figure 4.12i). The cell with the highest pressure is in the top wet layer of the grid, furthest from the lava front. This creates a pressure gradient in the sediment, driving fluid flow towards the lava front. What happens next depends on the sediment permeability and porosity.

In our high permeability cases ($\geq$50 mD), the pressure fluctuates in a series of peaks and troughs that reflect steam generation and escape:

1. As heat transfer continues, the top layer of cells reaches T_{boil} and steam generation begins. Boiling starts close to the lava front, where the pressure is lowest. While there is a mix of liquid water and vapour in a cell, the relative permeability (k_r), and therefore the rate of steam escape, is governed by the proportion of the two phases (Figure 4.3). If the proportion of vapour is low, k_{rgas} is also low and flow is inhibited. This is the same effect as 'moisture clogging' in concrete fires (e.g. Kalifa et al., 2000).

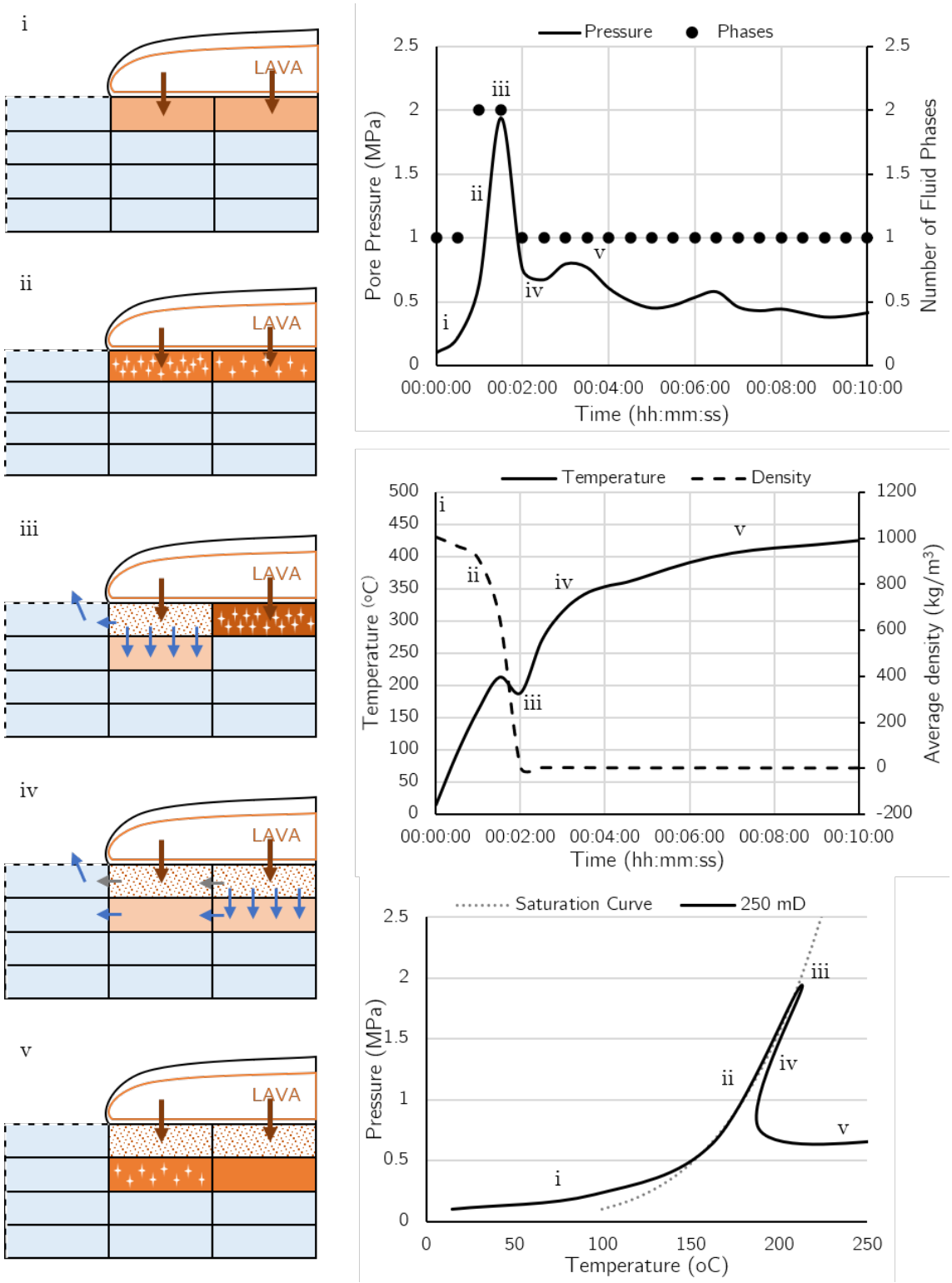

Figure 4.12: Cartoon of the general steps of model behaviour. The numbers match the descriptions given in bullet points in the main text. Blue arrows indicate the flow of liquid water, grey arrows indicate the flow of vapour. Red arrows indicate heat transfer from lava to sediment. Cell colour is indicative of temperature. Pressure, temperature, density and phase curves are taken from the top cell (0.5 cm depth, 4 m behind the lava front) of scenario 2, with a permeability of 250 mD and a porosity of 40%.

Pressure rises along the saturation curve (Figure 4.12ii), and is highest in the 'mixed' cells, i.e. those containing both liquid water and vapour, where k_{rgas} is at a minimum. The average density of fluid in the cell drops as the proportion of vapour increases and the latent heat of vaporisation buffers the temperature.

2. As the vapour phase becomes dominant in the mixed cells, k_{rgas} dramatically increases and the cell begins to degas, reducing the pressure, and the boiling front propagates away from the lava front (Figure 4.12iii). The peak pressure continues to rise along the saturation curve until the whole layer of cells has dried out.

3. When the whole top layer is dry, pressure across the model domain drops (Figure 4.12iv).

4. The pressure begins to rise again as the next cell down reaches T_{boil} and steam is generated. This time, steam is able to expand vertically into the top (now dry) cell. This reduces the pressure build-up in the cell, so the maximum pressure reached is lower than the initial peak (Figure 4.12v).

5. This pattern of pressure peaks and troughs is repeated as each successive layer of cells heats up and boils, with each peak and trough lower in magnitude than the one before.

For moderate-to-high permeabilities (≥50 mD), increasing permeability decreases the maximum pressure reached, as degassing starts earlier (Figure 4.13a).

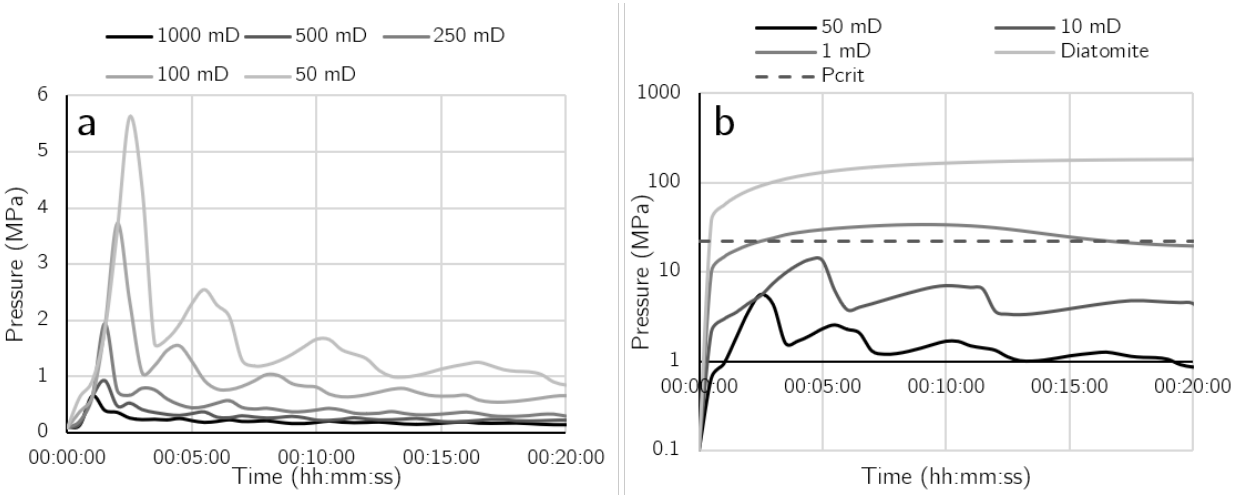

Figure 4.13: Variation of pore pressure with time for different sediment permeabilities (scenario 2). Pressure is measured 4 m behind the lava front in the top cell layer (av. depth 0.5 cm). All models have porosity of 40%, except for the diatomite case, which has a porosity of 90% and a permeability of 0.01 mD. Note the logarithmic axes on plot (b).

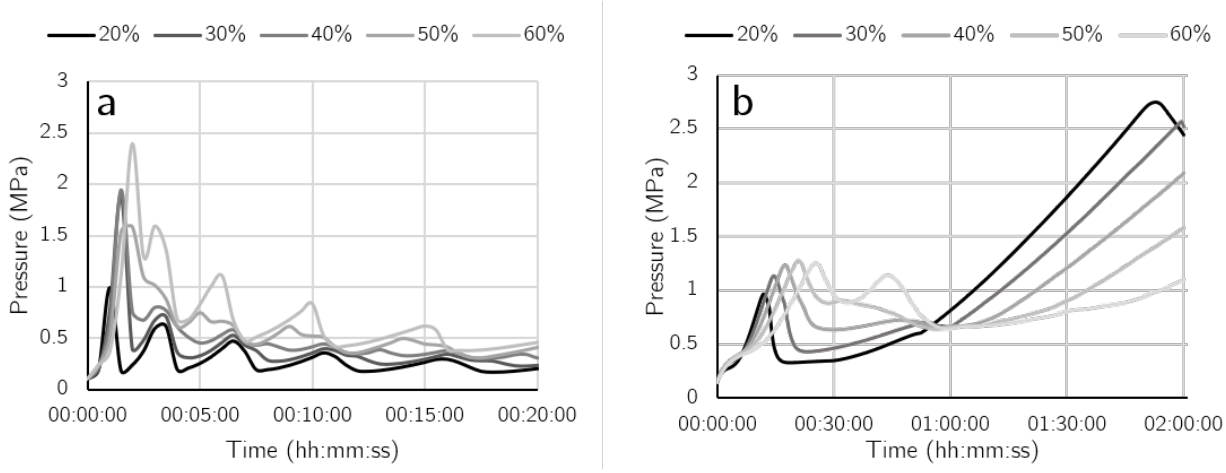

Figure 4.14: Variation of pore pressure for different sediment porosities. (a) Scenario 2, 1 cm grid: Pressure variation through time in the top cell, 4 m behind the lava front, for different porosities. (b) Scenario 3, 5 cm grid: Variation of pore pressure with time for different sediment porosities, measured 35 m behind the lava front in the top cell layer (av. depth 2.5 cm). All models have 250 mD permeability.

When permeability is low ($\leq$10 mD), flow through the pores is low except at very high pressure gradients. In this case, the water in the sediment is heated at, or near, constant volume, raising the pressure (Figure 4.13b). The pressure rise increases the saturation temperature, suppressing boiling and phase change. The pressure rises steadily through time, remaining on the liquid side of the saturation curve. In the lowest permeability cases tested, cells with the highest pressure reached supercritical pressure before they reached T_{boil}. The cell with the highest pressure remains in the top layer of the grid, farthest from the lava front.

The effect of porosity varies across the range tested (Figure 4.14). For 20–50% porosity, increasing porosity delays the phase change and causes increased peak pressure for both the high resolution and coarse grids. This is because water has higher c_p than sediment so more water mass in each cell causes a slower temperature rise and delays steam generation.

Effect of thermal conductivity and heat capacity

The thermal properties of the sediment have a significant effect on the rate of heat transfer (Fagents and Greeley, 2001), and therefore on the resulting temperature and pressure fields. Both the thermal conductivity and the specific heat capacity of the sediment are directly related to the heat flux via the conduction equation (equation 4.1). Increasing the thermal conductivity of the sediment increases the rate of heat transfer, causing earlier boiling and increased peak pressure (Figure 4.15). The effect is the same if the specific heat capacity

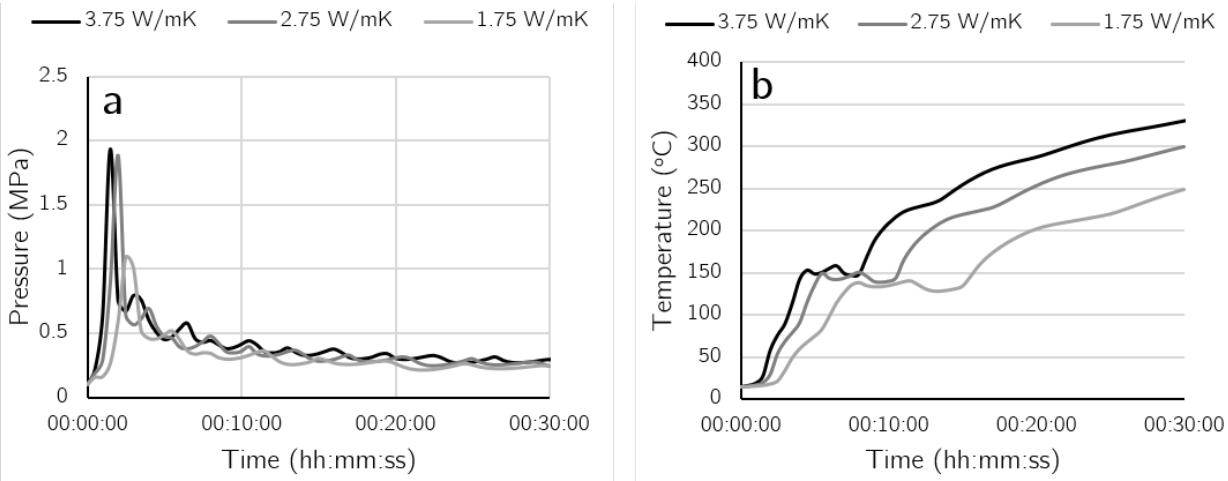

Figure 4.15: Pressure and temperature curves for different sediment thermal conductivities (scenario 2). Values are measured 4 m behind the lava front at a depth of 2.5 cm on a 1 cm grid. Sediment permeability is 250 mD and porosity is 40%. All other properties are unchanged.

is lower (Figure 4.16). In the simple conduction problem described by equation 4.1, these effects would be linear. However, the phase change and fluid flow in this problem also affect heat transfer and temperature throughout the sediment such that changes in temperature for a given cell are no longer directly proportional to changes in the conductivity or heat capacity.

In Scenario 0, the sediment conductivity is higher than the lava conductivity (Table 4.3) and the interface temperature decreases over time. Although the values we use are well within the reported range of sediment and lava properties, previous studies have assumed lower sediment conductivity, resulting in interface temperatures that increase over time (Fagents and Greeley, 2001; Tsang et al., 2019). Increasing the interface temperature would cause higher rates of heat transfer and temperature rise in the sediment, leading to faster steam generation. Additionally, the thermal conductivity and specific heat capacity in natural sediment will vary depending on the amount of liquid water in the pores, as demonstrated by the different published values for wet and dry sediments (Table C.1 in Appendix C.2). The thermal conductivity of liquid water is an order of magnitude higher than that of water vapour. This means that as the top layers of sediment become vapour-dominated, their conductivity will decrease, partially insulating the sediment below and reducing the rate of heat transfer, temperature rise, and steam generation.

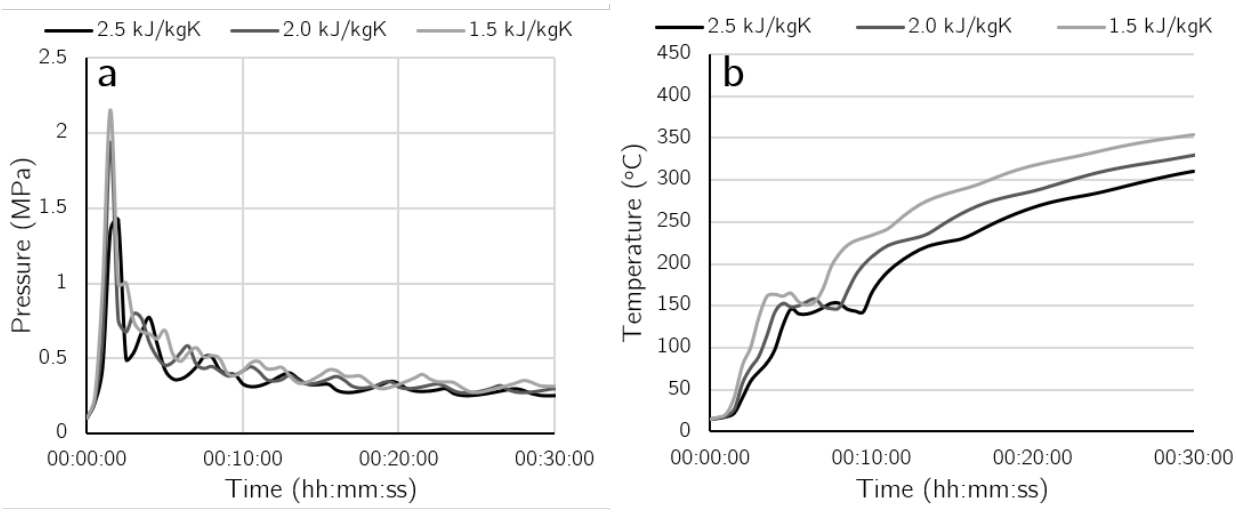

Figure 4.16: Pressure and temperature curves for different heat capacities (scenario 2). Values are measured 4 m behind the lava front at a depth of 2.5 cm on a 1 cm grid. Sediment permeability is 250 mD and porosity is 40%. All other properties are unchanged.

Effect of grid resolution

A coarse grid resolution decreases the thermal gradient ($\frac{\Delta T}{\Delta x}$) between the top cell and the upper boundary and increases the total mass in each cell. Compared to a finer grid, this means that

a) the temperature in the cell rises more slowly,

b) the cell takes longer to reach T_{boil}, and

c) the pressure rise begins later and is slower.

As a result, in the coarse grid scenario it takes longer to build up a sufficient vapour fraction to initiate degassing. However, the slower rate of heating gives the steam longer to dissipate, reducing the maximum pressure for a given permeability and spacing out the pressure peaks (Figure 4.17, top; Table 4.6).

As permeability is decreased, the effect of grid resolution on the peak pressure increases. For example, the initial pressure peak is 1.6 times higher in a 1 cm grid compared with a 5 cm grid at 50 mD, but only 1.2 times higher at 1000 mD (Table 4.6). However, after 2 hours, the grid resolution had little effect on the pressure (Table 4.6).

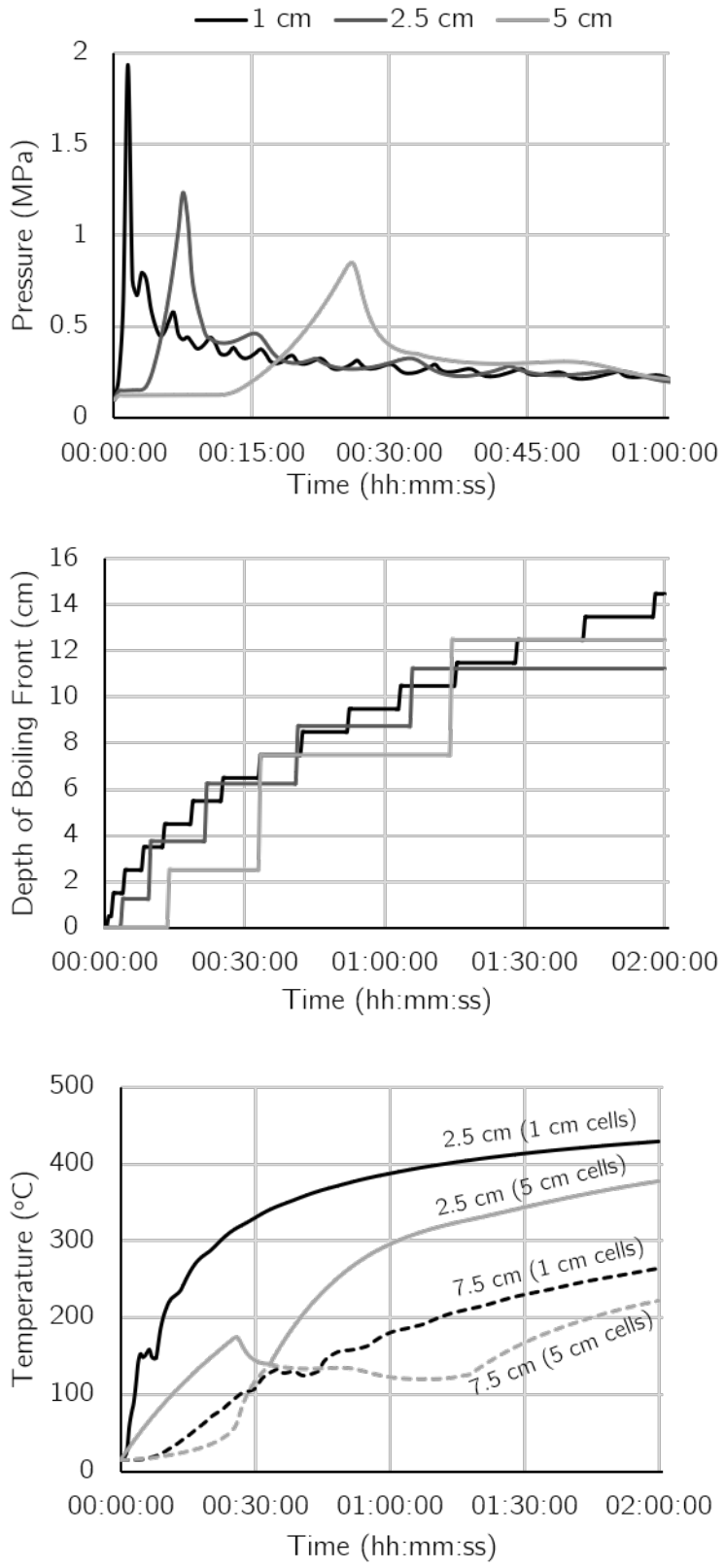

Figure 4.17: Variation in pressure, depth of vapour front, and temperature for different grid resolutions. All results are for 250 mD permeability. Pressures are measured at a depth of 2.5 cm.

Permeability (mD)	Cell thickness (cm)	Initial pressure peak (MPa)	...at time (hh:mm:ss)	Pressure (MPa) at t = 02:00:00
50	1	5.49	00:02:30	0.49
50	2.5	3.37	00:12:00	0.53
0	5	2.20	00:39:00	0.42
250	1	1.93	00:01:30	0.19
250	2.5	1.23	00:07:30	0.20
250	5	0.85	00:26:00	0.20
1000	1	0.66	00:01:00	0.12
1000	2.5	0.56	00:05:30	0.11
1000	5	0.41	00:19:30	0.12

Table 4.6: Effect of grid resolution and permeability on the initial pressure peak and pressure after two hours

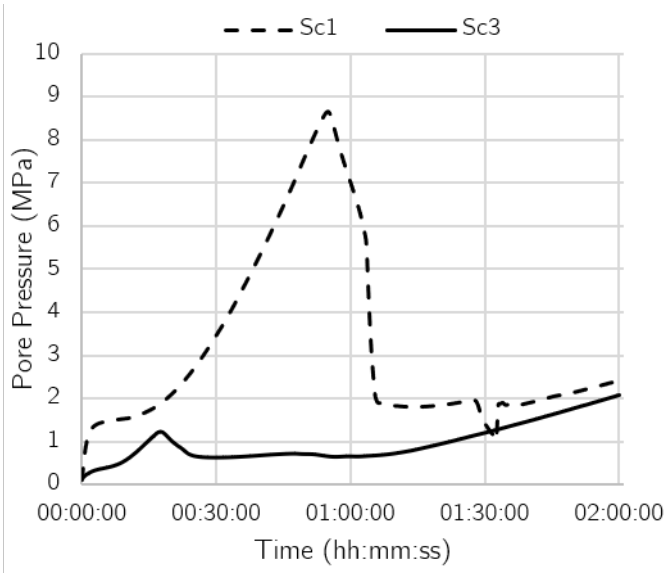

Figure 4.18: Comparison of pressure curves with and without a dry top layer of sediment. Values are measure 35 m behind the flow front at a depth of 2.5 cm (top cell). Sediment permeability is 250 mD and porosity is 40%. All other physical properties are the same.

4.4.2 Specific Scenarios

Rapid degassing of moderate-to-high permeability sediments at the lava front creates a continuous dry layer of sediment as the lava flow advances. This acts as a degassing pathway for steam generated behind the lava front and reduces the pressure build-up. Without this degassing pathway, the pressure under an instantaneously emplaced lava flow rises until the whole top layer of cells has degassed (Scenario 1; Figure 4.18). This situation is unrealistic, as it would imply lava emplacement rates many times higher than seen in natural basalt flows. Instead, we use Scenarios 2–4 to look at specific aspects of pressure build-up and degassing under a lava flow.

	Fluid phase in top cell after...		
Permeability (mD)	1 min	2 mins	3 mins
1000	Liquid + gas	Gas	Gas
500	Liquid + gas	Gas	Gas
250	Liquid + gas	Gas	Gas
100	Liquid	Liquid + gas	Gas
50	Liquid	Liquid + gas	Gas
10	Liquid	Liquid	Liquid + gas
1	Liquid	Liquid	Supercritical

Table 4.7: Fluid phases in top cell (1 cm thick) over time, for varying sediment permeability

	Fluid phase in top cell after...		
Porosity (%)	1 min	2 mins	3 mins
0.2	Liquid + gas	Gas	Gas
0.3	Liquid + gas	Gas	Gas
0.4	Liquid + gas	Gas	Gas
0.5	Liquid + gas	Liquid + gas	Gas
0.6	Liquid + gas	Liquid + gas	Gas

Table 4.8: Fluid phases in top cell (1 cm thick) over time, for varying sediment porosity

Scenario 2: Steam generation and degassing at a lava flow front

The opening minutes of Scenario 2 demonstrate how quickly the top few centimetres of sediment dry out under an advancing lava flow, and therefore whether a dry stream-escape pathway forms. Assuming an advance rate of 100 m/hr ($\sim$ 5 m in 3 mins), the criteria for establishing a dry pathway is that the top layer of cells should be free of water in the first 3 minutes of the model.

In sediment with permeability $\geq$50 mD (equivalent to fine sand, silt, loam, or sandy clay), a dry layer of sediment at least 1 cm thick forms in less than 3 mins, which suggests that these sediments will dry out approximately as fast as a lava flow advances. Thus, a dry top layer of sediment is established as the lava flow advances; as the lava flow creeps forward, water in the sediment immediately underneath the front will rapidly boil and the steam will escape to the air without significant pressure build-up.

A sediment permeability of 10 mD, in contrast, yields a mix of liquid water and gas in the top cell after 3 minutes and does not fully dry until 5:30 minutes. The lowest permeability model (1 mD) went straight from liquid water to supercritical steam at 3 mins, as the pressure rose beyond 22 MPa. This shows that the top layer of low permeability sediments will not degas but instead will build pressure at, and immediately behind, the lava front. This would likely drive small steam explosions, disrupting the advancing lava flow.

Higher porosity slows the rate of drying and decreases the thickness of the dry layer for a given permeability (Table 4.8). Higher porosity also increases the peak pressure in the sediment (Figure 4.14).

Scenario 3: Pressure build-up behind the flow front

Even with an established dry top layer of sediment acting as a steam escape pathway, pressure can build up behind a lava front. In Scenario 3, the top layer of cells from 5–35 m behind the lava front starts above T_{boil} and is therefore vapour-saturated, simulating a dry degassing pathway. The top layer of cells immediately behind the lava front (0–5 m) undergo an initial rise in pressure, which then decays as the cells degas. But after this initial peak and decay, the pressure in the sediment starts to rise again as lower cell layers reach T_{boil}. Boiling starts near the lava front, where the pressure, and therefore T_{boil}, are lowest. The pressure in the model continues to rise until the whole layer of cells degasses. Under these conditions, cells farther from the lava front reach a higher the peak pressure.

The pressure may also rise by heating liquid water confined in pores. Increasing the distance between the heated water and the lava front increases the pressure needed to drive a fast enough flow to allow water expansion. In lower permeability sediments, this may be the main cause of pressure rise in the sediment behind the lava front. For example, even with a pre-existing dry top layer, the maximum pore pressure in our 10 mD and 1 mD models reached 10.8 MPa and 19.5 MPa respectively.

Scenario 4: Active 'Vent' Behind the Flow Front

The break in the top impermeable boundary condition in scenario 4, representing an open rootless 'vent', reduces the distance that steam has to travel to escape. This has two effects on the shape of the pressure curve (compared to scenario 3). Firstly, the vent isolates the cells near the lava front that degas first and cause the initial pressure rise, from those further behind the front. This means that the early pressure peak occurs only between the lava front and the vent and is not seen further behind the front (compare the grey and black lines in Figure 4.19). Secondly, the presence of a vent reduces the pressure build-up behind the lava front before it drops due to degassing (compare the solid and dashed black lines in Figure 4.19). For models with identical thermal fields and sediment properties, the pressure rise after the initial peak follows the same path with and without a vent. However, in the model with a vent (scenario 4) the pressure starts to drop after 1 hour 54 minutes, whereas in the

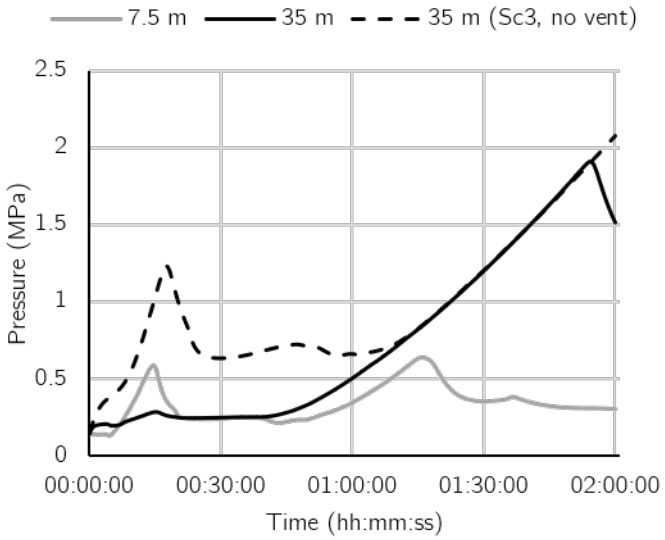

Figure 4.19: Pressure in the top layer of cells (2.5 cm average depth) at different distances behind the lava front. Solid lines show the pressure with an 'active vent' (scenario 4), with pressure measured between the lava front and vent (grey line, 7.5 m) and 35 m behind the lava front (black line). The dashed line shows the pressure 35 m behind the lava front without an 'active vent' (scenario 3).

model without a vent (scenario 3) the pressure continues to rise until the end of the modelled time (2 hours). This neatly demonstrates the effect of the length of the degassing pathway on the pressure field: the greater the distance from the furthest cell to the lava front, the longer pressure will continue to rise for and the higher the resulting peak pressure.

4.5 Discussion

4.5.1 Relating our model results to real life

To understand what happens as a lava flow advances over wet sediment, we must translate the results of our discretized models to a continuous sediment. A simple extrapolation of results from the grid resolution tests (section 5.1.3) would suggest that peak pressure rises asymptotically as cell size decreases to approach a continuous soil. However, there are several problems with this approach. Firstly, simple extrapolation to ever smaller grid sizes is prevented by the permeability and porosity values used in our models, which aren't applicable when we reach a cell size smaller than the representative elementary volume of the sediment. Secondly, a real sediment would have a smooth, continuously moving boiling front instead of discrete cells that change phase and then degas. The result would be to

smooth out the pressure curve, removing the peaks and troughs of the high permeability model results. Finally, the dynamics of an advancing lava flow are not adequately captured by simulating lava emplaced instantaneously upon blocks of sediment (from 4–35 m long) but instead requires that the position of the boiling front relative to the lava flow front be considered.

In a continuous sediment, a boiling front should move deeper into the sediment as the distance to the flow front increases. Instead of peaks and troughs in pressure as discrete blocks of sediment boil and degas (as in our model), there would be continuous steam generation and dissipation, with pressure increasing if steam is generated faster than it dissipates. In this scenario, build-up of sufficient steam pressure to trigger a rootless eruption is enhanced by low permeability and long distances to the lava front, such that sediment with higher permeability will have a lower horizontal pressure gradient than lower permeability sediment. This relationship between sediment permeability and pressure build-up has implications for the spacing of rootless vents, discussed later.

With these factors in mind, we now consider the implications of our results on rootless eruptions. Because sediment properties vary from site to site, and the numerical model results are heavily dependent on the starting parameters, we discuss our results in relation to different sediment types (e.g. gravel, sand, silt, clay), as opposed to specific permeability and porosity values.

4.5.2 Triggering a rootless eruption

In all permeabilities and grid resolutions tested, the pressure in the sediment 35 m behind the lava front exceeded 1 MPa and was generally much higher (Figure 4.13). This implies that for saturated sandy, silty or finer-grained sediments, there is likely to be sufficient pressure build-up behind the lava front to trigger a rootless eruption without the need for pre-explosive mingling of lava and sediment triggering a MFCI.

The upper and lower failure thresholds can be used with Dundas and Keszthelyi's (2013) method to calculate the energy per unit area, and equivalent volume of steam, required to fully excavate different thicknesses of lava (Figure 4.20; Equations 4.5–4.7). We assume a heat capacity ratio of $\gamma = 1.31$ (steam at 200 ^{o}C), a lava density of 2900 kg/m^3, and sediment porosity of 40%, in line with the values used in our numerical models. The line of $\frac{W}{e} = 1$ in Figure 4.20 shows the maximum thickness of lava flow that a given initial volume of steam can excavate.

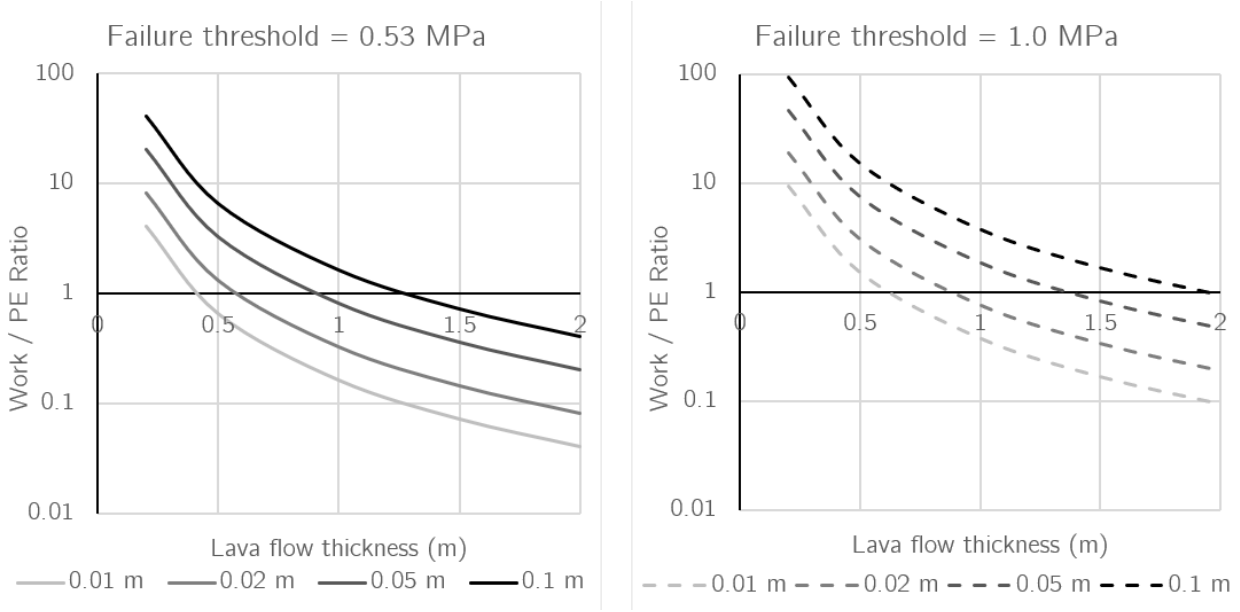

Figure 4.20: Excavation potential for different thicknesses of steam layer. The work/potential energy ratio shows whether sufficient work could be done by adiabatically expanding a volume of steam to fully excavate an overlying lava flow. Ratios >1 show successful excavation, where as ratios <1 would result in partial or no excaation of the overlying flow. The two graphs show the ratios assuming the lower (left, P_{max} = 0.53 MPa) and upper (right, P_{max} = 1.0 MPa) failure thresholds.

The thicker the lava flow, the greater volume of steam is required to break through and fully excavate it. Thin pockets of steam can fully excavate only relatively thin lava flows. For example, if we take $P_{max} = 0.53$ MPa, a 5 cm thick pocket of steam would only have enough energy to break through a lava flow <0.88 m thick. However, over the two hours covered by our numerical models the boiling front rarely progresses below 10 cm deep, except near the lava front where the pressure is low. Boiling fronts progress deeper for higher permeability sediments. Therefore, in moderate and low permeability sediments, where steam is limited to shallow depths, the energy released by a steam explosion may not be sufficient to excavate the entire thickness of the lava flow. Instead, it would inject steam and wet sediment into the fluid centre of the lava flow, without breaking the top crust. Higher permeability sediments, where thicker steam pockets form before the pore pressure reaches P_{max}, will be able to break through thicker lava flows. In the case of inflating lava flows, the initial steam explosion may break through a relatively thin, young flow lobe and then remain an active vent as the lava flow continues to advance and inflate around it.

4.5.3 Effect of sediment saturation

All of our models consider fully water-saturated sediments because MUFITS does not currently have an equation of state for an air-water-steam mixture. As sediments are only fully-saturated at or below the water-table, it is important to consider the effect of lower saturation on steam generation and pore pressure.

Our results show that even a thin layer of gas-dominated sediment in a model can significantly reduce the pressure from steam generation in deeper sediment layers. This is because gas is much more compressible than liquid, with large changes in specific volume as pressure changes. Therefore, we expect that pockets of air in the sediment pores would reduce the pressure rise caused by boiling and steam generation. A lower saturation also means that there is less water in the sediment that can boil, reducing the volume of steam generated and, again, reducing the expected pressure spike.

Sediments that are not fully saturated may also experience moisture clog that may trap steam and build up pressure, similar to observations and numerical model results in wet concrete heated by fire (e.g. Kalifa et al., 2000). The presence of air in the pore space would reduce the relative permeabilities of liquid through the sediment, inhibiting fluid flow and potentially increasing pressure build-up where there is an air-water or air-water-steam mixture in the pores.

Overall, we expect that partially saturated sediments would significantly reduce the magnitude of pressure build-up by steam generation compared to a fully saturated sediment. This means that lower permeability, partially-saturated sediments, e.g. fine silt or clay, may not trigger rootless eruptions, where their fully-saturated counterparts would. Lower water-saturation would allow a lava flow to advance further before building up sufficient pressure to trigger an explosion, leading to rootless eruptions farther behind the lava front than in saturated sediments.

4.5.4 Sustaining a rootless eruption

Our numerical model results apply only to *triggering* a rootless eruption. Once a lava flow and the underlying sediment has been excavated, or partially excavated, by the initial steam explosion, the situation is dramatically altered. Then the question is: how is a rootless eruption sustained? One of the open questions about the dynamic heat transfer model of rootless cone formation is how to intimately mix the fluid lava and water-sediment slurry so

that there is sufficient contact surface between the two fluids.

An initial steam explosion, even if it does not break through the whole lava flow, will inject water-sediment slurry into the lava flow and allow hot, fluid lava to pour into the excavated hole (Greeley and Fagents, 2001; Fagents et al., 2002; Dundas and Keszthelyi, 2013). If it does break through, the explosion will also create a local vertical pressure gradient under the vent, which would send a flow of liquid water and steam upwards, potentially fluidising the sediment (depending on sediment structure; see Appendix C.3). Any fluidisation would aid further mingling between the lava and sediment (Dundas and Keszthelyi, 2013). All of these factors could contribute to creating a suitable pre-mix for MFCI and rootless cone construction. Alternatively, insufficient heat transfer and mingling to initiate an MFCI could still allow peperites to form at the base of the flow (e.g. Skilling et al., 2002). For example, peperites are found where lava flowed over lacustrine sediments in the Paraná Continental Flood Basalt in Brazil (Waichel et al., 2007). Preserved textures show that lava tongues intruded into the wet sediments and broke up, with possible small steam explosions and quench fragmentation, but there was no evidence of MFCI.

A hybrid conceptual model for triggering and building rootless cones is illustrated in Figure 4.21. Here, pressure build up triggers an initial steam explosion that mixes the lava and wet sediment, facilitating a MFCI. MCFI explains the presence of very fine ash and surge deposits (indicating high energy explosions) found in some rootless cones, while the initial trigger creates the required pre-mix of lava and wet sediment. The energy released by MFCI depends on the ratio of interacting lava and melt (e.g. Büttner and Zimanowski, 1998; Wohletz et al., 2013). Therefore as the supply of either lava or wet sediment in the mixture diminishes, so does the explosive energy, resulting in coarser grain sizes and the inverse grading seen in some rootless cones. If MFCI ceases but there is still a steady supply of lava to the rootless eruption site, it will fill in the excavated crater, heating water deeper in the sediment and increasing the pore pressure. This could trigger further steam explosions, injecting wet sediment into the body of the lava flow and triggering another wave of MFCI. The presence of sediment-rich layers at the base of and interspersed throughout the lower layers of exposed rootless cone deposits (Hamilton et al., 2017) supports this. Repeated cycles of pressure build-up, steam explosion, mixing and MFCI could create the layers seen in many large rootless cones.

Critically, however, a hybrid model applies only to moderate–high permeability saturated sediments, e.g. sand, silt, peat, where the lava flow can advance a significant distance before sufficient pressure builds up behind the flow front to cause an explosion. It does not apply to some key rootless cone forming environments, for example the low permeability

diatomite ooze at Lake Mývatn. In these low permeability sediments, rapid pore pressure increase would cause small explosions, disrupting the lava flow advance. This could create hyaloclastite deposits like those seen in foreset beds of lava deltas (e.g. Skilling, 2002; Umino et al., 2006). These newly created layers could then provide a higher permeability, lower saturation layer for subsequent advancing flows. The low yield stress of oozes increases the potential of hydrodynamical mingling with fluid lava and increasing the chances of MFCI. However, the high water content will also increase cooling and quenching of the fluid lava.

Our findings have interesting implications for the formation of hornitos and rootless spatter cones. These features are built entirely of welded spatter, without any fine ash or scoria, implying that they are formed through low energy events rather than MFCI. The examples in Aðaldalur, NE Iceland, are thought to have formed in a wetland environment with peaty sediments (Boreham et al., 2018). Peat permeabilities range from ∼800 mD – 1500 D (Rezanezhad et al., 2016, and sources therin), which overlaps with the range where we expect heat conduction to trigger steam explosions. The energy release from the steam explosions is likely to be very low (Section 6.2), too low to cause brittle fragmentation, but perhaps sufficient to form hot, fluidal spatter. In this way, repeated low energy explosions caused by conduction and steam accumulation in the sediment could be responsible for building hornitos and rootless spatter cones.

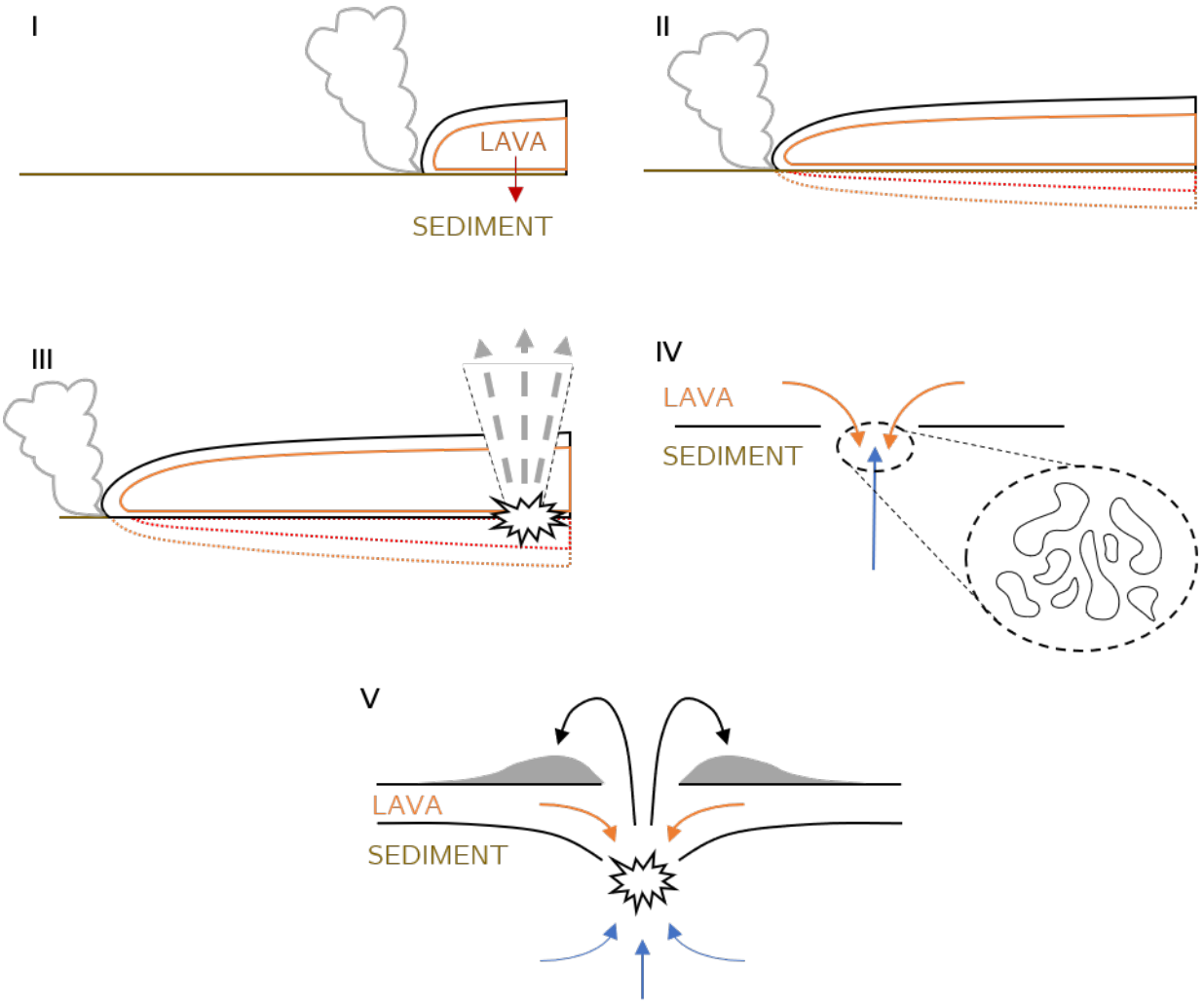

Figure 4.21: Proposed hybrid model for rootless cone formation. I) Lava advances over a medium high permeability sediment (e.g. fine sand, sandy clay, loam, peat) with high liquid water saturation. The top few centimetres of sediment dry out as the lava advances, causing steaming along the lava front. II) As the flow advances, heat transfers deeper into the sediment behind the flow front, heating water in the pore space and generating more steam. III) Steam escape is inhibited by the sediment permeability and the distance to the lava front, causing pressure to rise. Local factors, such as heterogeneities in the sediment structure, and overlying lava tubes, can contributed to the increase in pore pressure. Eventually the pressure exceeds the combined weight of the lava flow and strength of the basal crust, causing a steam explosion. IV) The explosion injects wet sediment into the centre of the lava flow, increasing the contact surface area and rate of heat transfer. Once the initial explosion has occurred, the wet sediment will rapidly depressurise, creating a vertical pressure gradient that drives water towards the rootless vent, potentially fluidising the sediment. At the same time, hot, fluid lava will pour into the excavated explosion site. Hydrodynamic mingling between the two fluids is possible, depending on density and viscosity ratios. The two mixing mechanisms create the pre mix necessary for a molten fuel coolant interaction (MFCI). V) The rootless eruption is sustained by MFCI as long as there are sufficient supplies of water and lava to the eruption site. Debris collects up on the lava flow surface, building a rootless cone. Repeated cycles of explosion and infilling of the rootless vent result in layered cones (e.g. Hamilton et al. 2017).

4.5.5 Cone spacing and distribution

Sediments are not perfectly homogeneous and are likely to have local variations in physical properties (over the scale of decimetres to metres). These local variations will affect the flow of liquid water and steam through the sediment, potentially leading to high local pressure gradients. For example, a low-permeability pocket may act as a focus for pressure build-up and trigger a rootless eruption.

The results from Scenario 4 show that an active rootless vent will lower the pressure in the surrounding sediment, thereby inhibiting further rootless eruptions due to pore pressure build-up. This suggests that, for rootless eruptions triggered by high pore pressure, there would be a minimum separation between rootless cones. This fits with observations of rootless cone groups that exhibit 'self-organisation' (Bruno et al., 2004; Hamilton et al., 2010b), where neighbouring cones compete for water to drive and sustain the rootless eruptions. If the sediment permeability has a strong influence on where rootless eruptions are triggered and the spacing between active vents, we would expect to see a correlation between the nearest neighbour distances of rootless cones and the type of sediments they formed on. Unfortunately, there is currently insufficient data on the sediment properties at different rootless cone types to test this hypothesis, but it would be an interesting area for future investigations.

4.6 Summary and suggested further work

Our numerical models show that heat conduction from a lava flow to a saturated sediment can build up sufficient pore pressure to overcome the confining weight and strength of the lava flow, triggering a rootless eruption. How quickly steam is generated and how quickly pressure builds up are heavily dependent on the sediment properties. Higher permeability and specific heat capacity will tend to reduce pressure build-up. Conversely, higher porosity, thermal conductivity, and saturation will all act to increase the pressure build-up. Greater lateral distance between the heated sediment and the lava front, or an active rootless vent, will also promote pressure build-up.

Based on these findings, we can begin to draw up a framework for where we would expect, or not expect, rootless eruptions to be triggered by this mechanism, based on the balance between heating, steam generation, and steam escape.

Very high permeability sediments (e.g. gravel) allow steam to easily escape, preventing

pressure build-up. Therefore, we would expect to see lots of degassing at the lava front but not enough pressure to break through lava and initiate rootless eruptions. An example of this is the Holuhraun lava flow advancing into the Jökulsá á Fjöllum river with abundant steaming and a few one-off steam explosions, but no sustained explosive activity or rootless cone building (Pedersen et al., 2017).

At the other extreme, in low and very low permeability sediments (e.g. clays, oozes) pressure builds up quickly, likely causing small repeated explosions at the advancing flow front and potentially disrupting the lava flow but not driving sustained rootless cone formation.

It is therefore the high to moderate permeability sediments (e.g. fine sand, loam, sandy clay) where our suggested hybrid mechanism is most likely. Here the top few centimetres of these soils would dry out as the lava flow advances, but pressure can build behind the lava front as water deeper in the sediment is heated but unable to escape to the atmosphere. In this situation, sufficient pressure can build to break through, or partially break through, the overlying lava flow and initiate a rootless eruption.

While this mechanism is unlikely to sustain a rootless eruption, or release enough energy to build a rootless cone, it would lead to intimate mingling between the wet sediment and hot fluid interior of the lava flow. This could potentially create the pre-mix necessary for a sustained MFCI, which would then build a rootless cone.

The numerical modelling in this study is limited to a narrow range of simplified cases and does not cover the full range of environments where rootless cones are found. There are a few key areas of further investigation that would be very interesting. The first, and probably easiest, would be to look at blocks of different sediments in the same model, both stacked in layers and laid adjacent to one another. This would tell us more about the effect of sediment heterogeneity on heat transport, fluid flow and pressure build-up. Further fieldwork to collect sediment samples from in/under/around rootless cones at different sites would allow a more quantitative comparison of sediment properties to cone size, spacing and morphology, and would help link the numerical models to real life. It would also be interesting to look at the case of steam explosions from underneath pyroclastic density current (PDC) deposits, like those that occurred after the 1980 eruption of Mount Saint Helens (e.g. Moyer and Swanson, 1987; Brand et al., 2014). Steam explosions were recorded where PDCs buried pre-existing riverbeds, up to a year after the original deposition. An open question for these explosions is whether they are driven by steam generation and pressure build-up, and to what extent bed fluidisation and deposit grain size matters. A useful extension to the numerical modelling would be the addition of an equation of state module for MUFITS that includes liquid water,

water vapour and air. Additional extensions to include methane and CO, for example from burning peat, would also be interesting.

Chapter 5

Conclusion

5.1 Research Aims

In this thesis, I set out to better understand the factors affecting lava–water interactions (LWI) and the hazards that they pose in future eruptions by addressing three key questions:

1. What is the range of hazardous LWI that should be considered for future eruptions, and under what circumstances are they most likely to occur?
2. How does local environment (sediment type, topography, hydrology) affect the likelihood and dynamics of rootless eruptions?
3. What is the role of lava flow emplacement style and local lava flux in triggering rootless eruptions and controlling the eruption style?

I used case studies of Icelandic rootless cone groups to establish the range of possible rootless eruption deposits and the environments in which they form, identifying systematic relationships between rootless cone morphology, environment and local lava flux (Chapter 2). My review of eyewitness accounts of LWI during the 1783–1784 Laki eruption and comparison with the accompanying deposits shows the wide range of possible LWI hazards and the dynamic interplay between lava and rivers during an eruption (Chapter 3). My review of the Laki cones also highlighted that rootless cones don't always form during LWI, and the relationship between environment and cone size is not straightforward and depends heavily on local conditions. To further investigate the effect of local environment and sediment properties on triggering rootless eruptions, I used numerical models to show

how heat transfer from a lava flow can raise pore pressure in an underlying saturated sediment and trigger a rootless eruption, depending on the sediment permeability (Chapter 4).

In this chapter, I bring all of these findings together to answer the original questions. I discuss how rootless eruptions could be triggered and sustained in a range of environments (lakes, rivers, wetlands, coasts), illustrated with examples from some Icelandic rootless cone groups and previously published cases. Finally, I recommend how to incorporate my findings into hazard assessments and suggest future research to address open questions.

5.2 What is the range of hazardous lava–water interactions?

Hazardous LWI can be split into two groups: passive and explosive. Explosive LWI are driven by flashing water to steam, with dramatic but localised effects, whereas passive LWI can have much larger footprints and durations but without explosions. The main hazard from passive LWI is the formation of lava dams, which cause flooding upstream and disrupt and pollute water supplies downstream. Impounded flood water can damage property and infrastructure, hinder travel, and threaten lives and livelihoods (Chapter 3). During the 1783–1784 Laki eruption, the main impact of disrupted and polluted water supply was on local agriculture and the health of livestock, which then impacted human health. With increased urbanisation and industrialisation, there is potential for much more widespread impact, depending on how many people and businesses rely on the affected river(s). For example, Deligne (2012) showed that disruption to the upper reaches of the McKenzie river in the Oregon Cascades, USA, which sits near Three Sisters volcano and has a history of being dammed by lava flows, would affect supplies for drinking water and industry for 2.7 million people.

The impacts of explosive LWI are much more localised, being limited to the region directly affected by tephra and ballistics. However, they are nonetheless dangerous, as demonstrated by recent incidents of tourists being injured in steam explosions from lava flows (e.g. Mattox, 1993; Andronico, 2018). Explosions may be one-off events, such as littoral tephra blasts (Mattox and Mangan, 1997), repeated low-energy bubble bursts that build hornitos, or repeated energetic explosions that build scoriaceous rootless cones. The deposits from these LWI are all part of the rootless cone 'family', including littoral cones formed along coastlines. The variety of rootless cone types and sizes, and the range of environments in which they form, can't be captured with a single conceptual model. Instead, my work shows

that different mechanisms are at work, depending on the sediment properties (Chapter 4), available water and local lava flux (Chapter 2). To assess the risk of explosive LWI in future volcanic eruptions, we need to understand these different mechanisms and the factors that affect them.

5.3 How are rootless eruptions triggered?

Previous studies provide two conceptual models for triggering rootless eruptions inland (i.e. excluding littoral cones): dynamic and static heat transfer (Fagents and Thordarson, 2007). While the dynamic heat transfer model has been the most popular in recent years, there are a few practical problems with it. Firstly, the model assumes that subsidence of the underlying sediment bends and cracks the basal lava crust, initiating contact and gravity-driven mingling between lava and wet sediment. However, observations of lava flows in the field show that the brittle outer crust is generally full of cracks and that the majority of the strength is in the viscoelastic portion of the crust (Hon et al., 1994). Below a threshold deformation rate, this region can stretch and deform plastically, without cracking. Therefore, if the underlying sediment does subside, we could expect the viscoelastic crust to deform with it, rather than failing entirely. Secondly, the relative flow rates between lava and wet sediment required to hydrodynamically mix the two fluids (>10 m/s; Zimanowski et al., 1997; Büttner and Zimanowkis, 1998; Zimanowski and Büttner, 2002) are higher than would be expected for gravity-driven mingling of fluids with similar densities. Thirdly, the rapid build-up of pressure in very low permeability environments, e.g. the diatomaceous ooze of Lake Mývatn, means that steam explosions would disturb the advancing lava flow, as demonstrated in Chapter 4. This makes it unlikely that the coherent tube- or sheet-fed pāhoehoe lava flow required for the dynamic model could form directly on top of these sediments. For these reasons, it is unlikely that subsidence, basal crust failure and gravity-driven mingling are the trigger for the majority of rootless eruptions, especially in low permeability environments.

In contrast, my numerical modelling in Chapter 4 shows that the conceptual model of static heat transfer from a lava flow to a wet underlying sediment is a feasible mechanism for triggering rootless eruptions in a range of sediment types. The rate of steam generation and pore pressure rise is strongly affected by the sediment properties, meaning that the type of sediment, in addition to the local topography and hydrology will affect whether a rootless eruption is triggered. With this in mind, I have developed a flow diagram that highlights some of the key factors affecting whether a rootless eruption is triggered and whether rootless cones form (Figure 5.1). I will now discuss a number of different paths through the flow diagram,

corresponding to different scenarios, conceptual models, and some key rootless cone sites.

Preserved rootless cones on pāhoehoe lava flows all sit on top of a solid upper crust. Therefore, the first condition for rootless cone formation is that the lava flow remains coherent. This will depend on the slope of the underlying surface and any external factors that could disturb the flow. Wetlands are generally flat or have very shallow slopes (e.g. Aðaldalur has 2^{o} slope) so lava is likely to progress as coherent inflating lobes or sheets. The transition from subaerial flow into a lake may provide greater slope, depending on the bathymetry. Observations of subaqueous lava flows show that for slopes $>25^{o}$ pāhoehoe lava breaks up, creating a flow with a rubbly surface texture (Tribble, 1991). On shallower slopes, flows can progress as intact lobes (Umino et al., 2000). Other factors, such as water waves and quench fragmentation, may also break up the advancing lava flow.

While it's possible for rootless eruptions to happen without a stable top crust, the resulting deposits aren't preserved as they fall back into the lava flow and are carried away. For example, eyewitnesses described steam explosions as the Laki lava progressed down the Skaftá river gorge, but there are no visible cones in this area now (Chapter 3). For hazard assessment purposes, it is the explosion rather than cone building that is of concern. However, without preserved deposits or eyewitness accounts, we do not know how often rootless eruptions occur without building cones. That said, there are practical reasons why rootless eruptions would be less likely on rubbly lava flows. Since rubbly lava flows have a greater surface area, they cool faster than those that remain as insulated tube or sheet flows. Therefore, rubbly flows are more likely to quench before generating sufficiently high pressure steam to drive an explosion. Zimanowski et al. (1995) showed that centimetre-scale domains of melt in water quench in less than a second, so are unable to drive steam explosions. Additionally, broken up lava flows will be more permeable, and therefore less able to build up pressure to drive rootless eruptions.

Assuming the lava flow remains coherent, the next important factor is whether the lava sits on top of the wet sediment or sinks into it. If the lava flow sits on top of the sediment, we get a case similar to the numerical models in Chapter 4. Therefore, what happens next will depend primarily on the sediment physical and thermal properties and the advance rate of the lava flow.

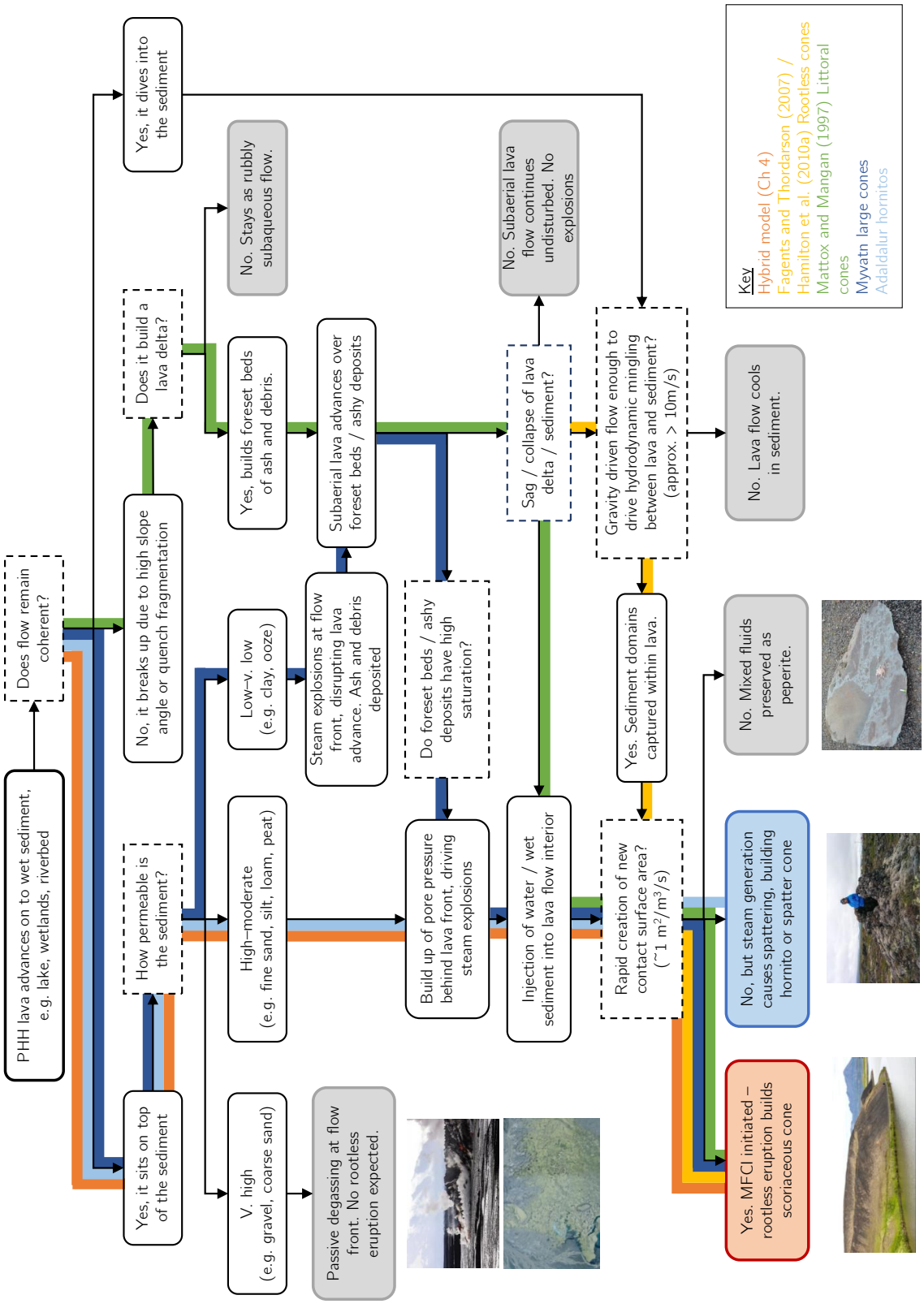

Figure 5.1: Flow diagram showing different scenarios for triggering rootless eruptions

For coarse, very high permeability sediments (e.g. gravel), steam will be able to move through the sediment as fast as it is generated, causing passive degassing at the flow front. Pore pressure remains low so we do not expect rootless eruptions. An example of this is the abundant steaming when the 2016 Holuhraun lava entered the Jökulsá á Fjollum river (Pedersen et al., 2017). Although a few isolated steam explosions were heard, there was no sustained explosive activity and no rootless cone building. This section of the river flows over a flat plain of old lava flows, topped with igneous tephra deposits, ranging from sand and pumice to metre-scale boulders (Wells, 2016). As well as these relatively high permeability sediments, the river was displaced away from the lava front, further reducing LWI (Pedersen et al., 2017).

For high to moderate permeability sediments (e.g. fine sand, silt, peat, loam), the top layer of sediment is likely to dry out as the lava flow advances and the hybrid conceptual model proposed in Chapter 4 applies (orange path in 5.1). Pore pressure will build up tens of metres behind the lava front, triggering steam explosions that inject wet sediment into the hot, fluid interior of the lava flow. If the rate of induced mixing is high enough (≥ 1 $m^2/m^3/s$; Austin-Erickson et al., 2008), plus potential mingling of lava and fluidised sediment in the explosion crater, then this may trigger a MFCI, leading to a more energetic explosion and the start of scoriaceous rootless building. If the mixing rate is insufficient for a MFCI, repeated small steam explosions caused by cycles of pore pressure build-up and steam explosions could build spatter cones and hornitos through low-energy bubble bursts (pale blue path in Figure 5.1). Similar bubble bursts building spatter cones were observed in littoral settings (Mattox and Mangan, 1997).

However, in low permeability environments (e.g. clay or ooze), such as Lake Mývatn, rapid pore pressure rises would cause steam explosions along the lava front, disrupting the flow (dark blue path in 5.1). Diatom remains in vesicles from rootless cone scoria around Mývatn show that the sediment was predominantly diatomaceous ooze, which holds up to 92 wt% water (Einarsson, 1988). Proto-Mývatn was created by a depression in an underlying lava flow (Thorarinsson, 1953) so is likely to have had shallow slopes around lake shores. Despite this, the combination of steam explosions from low permeability sediment and possible lake water wave action would probably have broken up the flow as it advanced into the lake, depositing a mixed layer of sediment and hyaloclastite debris, similar to a coastal lava delta. Cores from Lake Mývatn reveal layers of tephra from the Younger Laxá Lava mixed with layers and lenses of diatomaceous sediment (Einarsson, 1982), and the beaches around the shores of Mývatn are all made up of ash. Ash is orders of magnitude more permeable than diatomaceous sediment, so these ash layers may have provided a more permeable substrate

for the lava to flow over without immediate disruption from steam explosions. Rootless eruptions could then be triggered by pore pressure build-up in the debris layer, assuming that there is a high enough saturation. Alternatively, Mattox and Mangan (1997) observed littoral explosions and cone building associated with lava delta collapse and proposed that steam generation was driven by ocean water entering a lava tube partially-severed by bench collapse (green path in 5.1). This mechanism is also plausible in lacustrine environments if lava flows build up unstable deltas which then collapse under the weight of an inflating subaerial flow. Since bench collapse happens suddenly, the viscoelastic lava crust may not have time to deform plastically and may fail. Sudden exposure of fresh lava to lake water and wet sediment, confined in a lava tube, could generate high pressure steam and trigger a rootless eruption.

Though there are no documented examples, it is possible that a lava flow diving into wet sediment could produce rootless eruptions. Basalt lava is generally denser than sediment (see 4.3 in Chapter 4) and has been known to intrude downwards into soft sediments. For example, Rev. Jón Steingrímsson described the 1783—1784 Laki lava flow burrowing into and lifting up pre-existing peat sediments (Kunz, 1998). Similarly, a lava flow from Cinder Cone in California, USA, disrupted diatomite sediment when it entered Snag Lake (USGS, 2000). Preserved peperitic textures show that there is often mingling between wet sediment and an intruding melt. If this mingling reaches the mixing threshold for a MFCI then it could trigger an energetic rootless eruption. Similarly, vesiculated sediments in peperite formations show that conduction from the intruding lava can boil water in the surrounding sediment (e.g. Waichel et al., 2007). It is therefore possible that the pore pressure could rise enough to trigger a steam explosion, potentially leading to further mixing and explosions. This is another alternative for the formation of the Mývatn rootless cones, and the layers of disturbed ash and sediment mentioned above could perhaps be the result of the lava diving into the sediment in places. There are no excavations or core samples that identify an intact pāhoehoe lava flow in or near the shores of the lake, so we do not know the extent to which this happened. However, the cooling rate of an intruded melt will be much higher than for a tube-fed pahoehoe, which is insulated by the top crust. The addition of wet sediment on all sides will increase the rate of heat lost by conduction and may set up natural convection cells above the lava flow, further increasing heat loss. Therefore, rootless cones from intruded lava flows seem less likely than from subaerial flows.

5.3.1 Rootless eruptions in different environments

Rootless cones are not evenly distributed across all water-rich environments. For example, there are many more Icelandic cones in lake and wetland environments than in river valleys and there are no known intact rootless cones that formed on ice. Similarly, the number of surviving inland rootless cones is orders of magnitude higher than littoral cones. A lack of rootless cones in any particular setting does not necessarily reflect a lack of rootless eruptions: there may have been rootless eruptions that did not last long enough to form cones, or cones could have formed and since been eroded or buried. Littoral cones are rapidly eroded by wave action (Moore and Ault, 1965). Similarly, rootless cones that form on snow or ice may be destroyed if the ice melts. However, the type and amount of sediment associated with different environments also plays an important role in cone distribution.

Sediment-rich environments: Lakes, rivers and wetlands

Lakes and wetlands tend to have finer sediments than rivers and coastal regions. Rivers and coastal waves can carry away the finest sediment, depositing it in regions with lower flow velocity, such as river deltas and lakes. There is no such transport in lakes, especially shallow ones, where the biogenic and wind-blow sedimentation, and input from rivers increases the sediment thickness over time. These biogenic sediments, e.g. diatomaceous oozes, can have very high porosity and water content, but low permeability (e.g. Einarsson, 1982). Given that lower permeability sediment is more conducive to building up pore pressure than high permeability sediment when heated (Chapter 4), rootless eruptions are more likely to be triggered in depositional environments with fine sediments.

In river settings, this means rootless eruptions are more likely if lava encroaches into a delta or other area where fine sediment is being deposited, rather than in steeper, faster flowing regions. Riverbeds with very high permeability sediments are unlikely settings for rootless eruptions unless there is a significant external force driving mixing between the lava and water. For example, rootless cone groups in Laxárdalur are limited to areas where tributaries joined the valley, depositing wet sediments (see Chapter 2). While the underlying bedrock may have low permeability, if the sediment is coarse then steam will be able to escape readily.

The distribution of rootless cone groups from the Laki fissure eruption (Chapter 3) demonstrate how impounded water from dammed rivers can increase potential for rootless eruptions by saturating surrounding land. For example, there are rootless cones in the upper reaches of Skaftá, upstream of a large lava damn, and on the bed of the Hellisá river

where it was dammed by lava (Thordarson et al., 1998). Similarly, rootless cones near the Ásar farm probably formed on the edge of a 10 km^2 temporary lake created when the lava dammed the Tungufljót and Hólmsá rivers. There are also cones in Reykjadalur where the Younger Laxá Lava dammed the Reykjadalsá river on a broad, flat plain, creating an area of wetlands and lakes that still persists. This dynamic interplay between lava and water has implications for future hazard assessments. Accounting for areas of possible flooding and updating potential hazards around impounded water will help assess the risk of explosive LWI in future eruptions.

Coastal settings and low sediment lakes

The contrast between inland rootless cones and littoral cones highlights the importance of sediment in triggering and sustaining rootless eruptions. In the case of littoral cones, the main source of water is the ocean, rather than water-sediment slurry. The extreme viscosity and density contrasts between lava and liquid water make their mixing much harder than with a water-sediment slurry (White, 1996). This makes it less likely that rootless eruptions will be triggered by water-lava mixing and explains why many lava flows enter the ocean without forming rootless or littoral cones. An analogous inland example would be the pair of rootless cones formed when the Nesjahraun lava flow entered Lake Thingvallavatn (Stevenston et al., 2012). Thingvallavatn sits in Iceland's Western Volcanic Zone, on the plate boundary between the European and North American plates, in a deep, fault-bounded depression (Stevenson et al., 2012). The lake covers 84 km^2, averages 40–80 m deep throughout (114 m max) and has very little sediment in regions shallower than 30 m (Bull et al., 2003). The lava flow entered the lake as a mixture of pāhoehoe and 'a'ā flows. While the total volume of water was not a limiting factor in rootless cone formation, the lack of sediment means that lava had to mix with liquid water, rather than water–sediment slurry, to drive rootless eruptions. Lapilli-sized spatter deposits are found along the shoreline of the pāhoehoe part of the lava flow, created by littoral fire fountains as water infiltrated the lava tubes (Stevenson et al., 2012), but with insufficient mixing to initiate a MFCI. Later lobes of shelly pāhoehoe are interbedded with this rootless spatter. A single rootless cone, Eldborg, sits on the pāhoehoe part of the flow, and has a central pond of water that is hydrologically connected to the main lake. This shows that the cone sits on top of a permeable, saturated layer in the lava flow, likely a lava delta made of hyaloclastite and spatter debris. When contrasted with the thousands of rootless cones around the relatively shallow, sediment-laden Lake Mývatn, this demonstrates the importance of sediment as a vector for water in triggering rootless eruptions.

5.3.2 Rootless eruptions on 'a'ā lava

The previous discussion, and the flow diagram in Figure 5.1, relate to pāhoehoe lava flows, since this is where the majority of rootless cones form. However, rootless eruptions can occur on 'a'ā lava flows. The lack of solid top crust in 'a'ā flows means that any debris falling on the flow surface is rafted away, leaving a characteristic pair of half-cones, which sit on either side of the main flow.

The largest littoral cones in Hawai'i are found on basaltic 'a'ā lava flows (Moore and Ault, 1965; Jurado-Chichay et al., 1996). The only inland example is a pair of half-cones formed where the 'a'ā part of the Nesjahraun lava flow entered Lake Thingvallavatn in Iceland (Stevenson et al., 2012). The relative lack of rootless cones on inland 'a'ā flows compared to coastal settings suggests their formation is controlled by mixing with liquid water rather than water-sediment slurry. This pattern, and its contrast with rootles cones associated with pāhoehoe, can be explained by 'a'ā lava flows being cooler, more crystalline and slower moving than pāheohoe lavas (Kilburn, 2000). Lower temperatures mean slower heat transfer from the lava to the sediment, and that the lava will quench more easily in contact with cold wet sediment or water. The lack of solid basal crust makes the flow more permeable, perhaps allowing steam to escape more readily than under a pāhoehoe lava. Most importantly, the high crystallinity of 'a'ā lava increases its viscosity, so that flows advance as a tumbling, blocky avalanche. This higher viscosity hinders hydrodynamic mingling of lava and sediment. However, the tumbling motion at the flow front does promote mixing with liquid water, enhanced by the break-up of the flow on steep slopes, e.g. at coastlines or the edge of large lakes. The lava can trap pockets of water within the bulk of the flow, which can then drive steam explosions and build rootless cones. The lack of sediment also means that all of the energy transferred from the lava goes to heating the steam rather that sediment, which increases the explosive efficiency (White et al., 1996). This may, in part, explain why 'a'ā rootless cones are larger than those on pāhoehoe flows.

5.3.3 Non-explosive and 'failed' rootless eruptions

There are innumerable instances of lava flows covering wet sediments or entering lakes or rivers that do not result in rootless eruptions. For example, lava from the 2018 Lower Eastern Rift Zone eruption of Kilauea, HI, inundated Green Lake without any reported explosions. Examples from the Pacific northwest of the USA include lava flows from the Sand Mountain Volcanic Field damming the McKenzie River (e.g. Deligne, 2012), and lava

from Cinder Cone, CA that entered Butte Lake and Snag Lake, ploughing up the sediment without creating rootless cones. Similarly, during the 1783–1784 Laki eruption, there were many instances of lava damming tributaries without any rootless eruptions (see Chapter 3). In all of these cases, the conditions necessary for triggering a rootless eruption were not met.

Some possible pathways to 'failed' rootless eruptions are included in Figure 5.1, ending in grey boxes. For instance, where there is insufficient mixing between lava and wet-sediments to trigger a MFCI, the contact between the two may be preserved as peperites. Examples of these include peperites at the base of lava flowing over wet sediment in the Paraná Continental Flood Basalts in Brazil (Waichel et al., 2007), and in the Columbia River Flood Basalts (e.g. Ebinghaus et al., 2014). Vesiculation of sediments around the contact shows that the lava did boil pore water, but that pressure was insufficient to trigger steam explosions (Waichel et al., 2007). Another possible reasons for a lack of rootless eruptions is a lava flow moving too slowly to build up sediment pressure, instead allowing passive steaming at the lava front. Conditions favouring the formation of pillow basalts, which were found at lava dams in both the Owyhee and Colorado rivers (Crow et al., 2008; Ely et al., 2012) would also not favour rootless eruptions.

5.4 Sustaining rootless eruptions

5.4.1 The role of lava volume flux

Higher local volume fluxes of lava build larger rootless cones. For example, littoral cones on 'a'ā flows range from 400–1000 m diameter, compared to a maximum diameter of 450 m for pāhoehoe examples (Jurado-Chichay et al., 1996), due to the difference in volume flux of the parent lava flows (Moore and Ault, 1965). This trend also applies to inland rootless cones. On the Nesjahruan, the 'a'ā half-cone pair Gramelur is ∼720 m wide and 40 m tall, compared to its pāhoehoe twin Eldborg, which is ∼160 m wide.

Of the littoral cone building events observed by Mattox and Mangan (1997) on pāhoehoe lavas, volume flow rates were estimated at >4 m^3/s, producing cones up to 10 m high. In contrast, the largest pāhoehoe littoral cones, up to 450m diameter, are estimated to have been created by flows with bulk volume fluxes >80 m^3/s, an order of magnitude higher and possibly as high as 900 m^3/s (Jurado-Chichay et al., 1996). While this flow was distributed over several flow lobes, it would still deliver significantly higher local volume flux than the flows that built smaller cones. The volume flux of lava that inundated Mývatn was estimated

at 0.7–7 m^3/s, based on the slope and dimensions of the main feeder channel (Skelton et al., 2012). At Mývatn, the largest cone is 400 m in basal diameter, and the majority of cones are much smaller.

Large rootless cones contain a greater total mass of tephra, requiring a sustained supply of lava to the eruption site and/or a high lava flux. In MFCI, energy release is controlled by the ratio of interacting melt and water. Assuming that the interacting ratio is favourable, greater volumes of lava and water interacting will lead to larger total energy release. In the Younger Laxá Lava case study, rootless cones formed along flow margins, where local lava flux is low, were consistently smaller than those in the middle of a sheet flow (see Chapter 2). The internal layers seen in exposed cross-sections of scoriaceous cones show that they are formed by repeated explosive episodes, which require a sustained lava supply (e.g. Fagents and Thordarson, 2007). This relationship between cone size and lava supply is illustrated by the x axis of Figure 5.2.

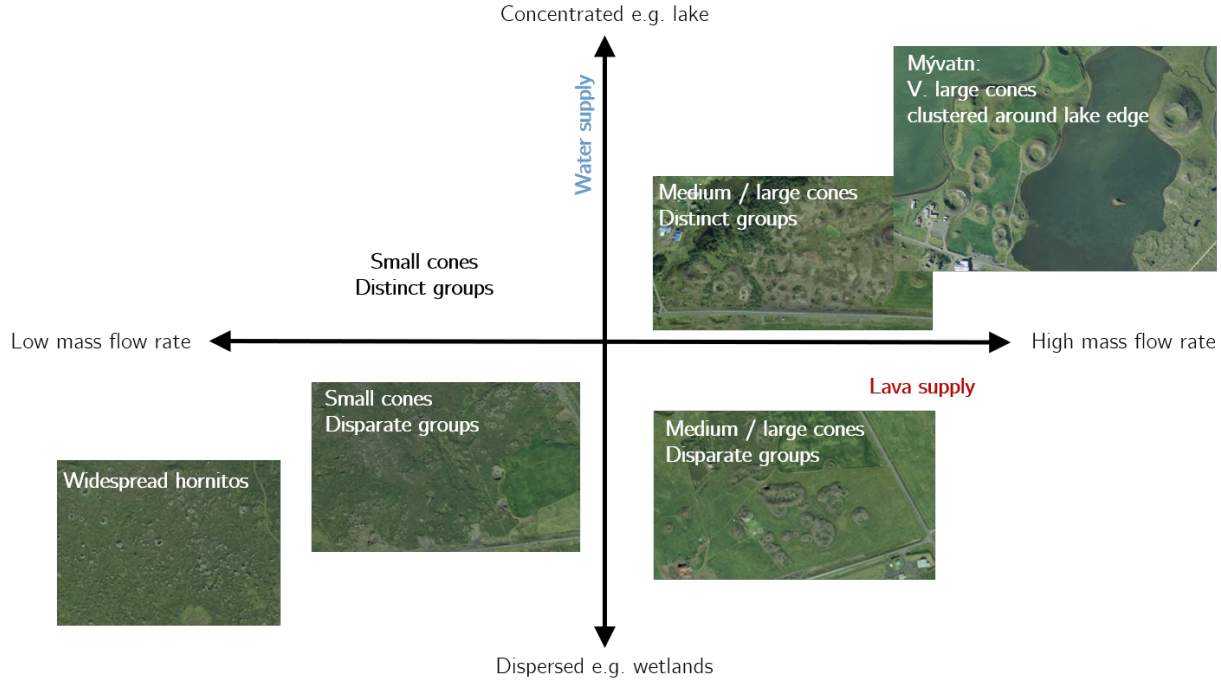

Figure 5.2: Schematic illustrating the effects of local lava supply and water distribution on the size and spacing of rootless eruptions.

5.4.2 The role of sediment and water distribution

The distribution of water in an environment controls the locations and types of rootless eruptions. This is demonstrated by the distribution of cones on the Younger Laxá Lava

(see Chapter 2). For example, the outline of the proto-Lake Mývatn is revealed by the extent of the rootless cones visible today, and the grouping of cones across Aðaldalur reflects where water was collected in ponds or distributed in wetland sediments. Similarly, the large, contiguous group of rootless cones at Landbrosthólar in southern Iceland formed on a broad Sandur plain, a relatively homogeneous environment of sandy sediment deposited by glacial outwash floods (Thorarinsson, 1953).

The water availability in the environment is also a controlling factor in the size of rootless cones that form. Large cones are built by long-lived explosive activity, which requires a large, sustained, or periodically replenished supply of water. For example, the size of the Mývatn rootless cones reflects their proximity to the edge of proto-Laki Mývatn: larger cones formed inside the boundary of the lake where there was abundant water and water-saturated sediment; smaller cones formed around the edges where sediment was thinner and there was less water (see Chapter 2). There is also a greater proportion of multi-cratered cones at Mývatn, which may have been formed by secondary phases of explosive activity, driven by a replenishment of water supply to the eruption site (Noguchi et al., 2016). Competition for water supply between neighbouring cones explains the self-organisation seen in some rootless cone groups (Bruno et al., 2004; Hamilton et al., 2010b) and is supported by my modelling results (Chapter 4).

The general relationship between cone size and spatial distribution is illustrated along the y axis of Figure 5.2. Large, overlapping cones, sometimes with multiple craters, form in high-water environments e.g. Lake Mývatn. Distinct, clustered groups may reflect the outline of old lakes e.g. Grp 1 of the Laki rootless cones (Chapter 3). Disparate groups or widespread cones could reflect more distributed water supplies, such as wetlands e.g. hornitos in Aðaldalur, cones in upper reaches of Skaftá with widespread flooding, and Landbrotshólar.

5.5 Implications for future hazard assessments

This thesis highlights the variety of secondary hazards caused by LWI and the broad range of environments in which they can occur. These hazards, both explosive and passive, could present a significant threat to life, private property and infrastructure for future eruptions in wet environments. Low viscosity basaltic lavas are often erupted from volcanic fields and rift zones, which may have abundant surface water. However, the distributed nature of these eruptive vents makes it hard to predict in advance where lava will erupt and flow, complicating the analysis for hazard maps.

Instead of traditional hazard maps, a more practical approach would be to follow the model of the DEVORA hazard assessment exercise (Hayes et al., 2018). This involves identifying vital infrastructure (e.g. roads, pipelines, electricity etc.) and how it would be affected by an eruption, including LWI. Raising awareness of secondary LWI hazards is important to ensure that they are considered, where appropriate. Analysis of topography may identify likely lava flow paths and highlight areas where lava could inundate lakes or dam rivers and cause flooding. During eruptions, monitoring of active lava flows and projecting likely flow paths (largely based on topography) will allow real-time hazard assessments/forecasts of LWI in the following hours/days. This will give advanced warning of floods and disruptions to water supplies. Sediment maps should be used to identify areas whether/where rootless eruptions are most likely.

5.6 Suggestions for futher research

The work presented in this thesis advances our understanding of how rootless eruptions are triggered, and the roles of sediment and lava in building rootless cones. It also highlights the broad range of hazards associated with LWI, and the importance of including them in future eruption hazard assessments in wet environments. However, there are still numerous gaps in our knowledge, open questions and research opportunities that could improve our understanding of these hazards further.

When assessing hazards from non-explosive LWI, e.g. flooding or disruption to water supplies, it would help to know the balance of lava flux to river discharge needed to dam a river or divert a lava flow. How do the lava flow properties (e.g. temperature, viscosity, mass flux, emplacement style) affect whether or not a river is dammed? What effect does the local topography have on lava dam formation? And what affects lava dam stability, i.e. can we predict when and how a dam might fail? For example, some lava dams can persist for thousands of years (e.g. Orem, 2010; Deligne, 2012; Deligne et al. 2017) while some of the Laki lava dams lasted only days or months (Chapter 3). Depending on the size of the dam, failure may lead to catastrophic flooding downstream (e.g. Fenton et al., 2006).

To help understand the risk of future rootless eruptions, it would be interesting to collect and characterise sediment samples from different rootless cone sites, and sediment trapped within vesicles in rootless cone scoria, to look for systematic relationships between sediment properties (porosity, permeability, thermal conductivity) and their associated rootless cones (size, shape, spacing). This would help test the hypotheses from numerical models on the

effect of sediment properties on cone formation. Another interesting option would be to conduct lava-pour experiments on different saturated sediments and observe the degassing, for example at the Syracuse Lava Project (`http://lavaproject.syr.edu/`; e.g. Tsang et al., 2020). Similar experiments on lava over ice and snow were conducted by Edwards et al. (2013).

More sophisticated numerical models would also help us understand rootless eruption triggers better. For example, extending the equation of state modules in MUFITS to include a liquid water-steam-air system would help understand the effect of sediment saturation. Including other gas species, such as CO and methane, would show the impact of burning peat or vegetation in an environment. Similarly, investigating the effects of heat transfer by radiation and forced convection would give a more complete picture of lava-sediment heat transfer, steam generation and rootless eruption triggers. Modelling lava over melting snow would be a very interesting challenge, as the permeability would vary across the modelled domain and change through time as melt-water percolates through the snow.

Chapter 6

References

Aebischer, J., 2018. *Syneruptive Crystallisation and Degassing in the Laxárhraun Lava Flow, Northern Iceland*, MSc thesis, ETH Zurich.

Afanasyev, A.A., 2012. Simulation of the Properties of a Binary Carbon Dioxide–Water Mixture under Sub- and Supercritical Conditions*, High Temperature*, 50, pp.340–347.

Afanasyev, A.A., 2013. Application of the reservoir simulator MUFITS for 3D modelling of CO_2 storage in geological formations, *Energy Procedia*, 40, pp.365–374.

Afanasyev, A.A., 2015. Hydrodynamic modelling of petroleum reservoirs using simulator MUFITS, *Energy Procedia*, 86, pp.427–435.

Afanasyev, A.A., 2017. Reservoir simulation with the MUFITS code: extension for horizontal wells and fractured reservoirs, *Energy Procedia*, 125, pp.596–603.

Afanasyev, A.A., 2019. *MUFITS Reservoir Simulation Software version 2019.B Reference Manual* [pdf]. Available at: `http://www.mufits.imec.msu.ru/documentation.html#Documents_1`, [Accessed February 2020].

Afanasyev, A.A., Melnik, O., Porritt, L., Schumacher, J.C. and Sparks, S., 2014. Hydrothermal alteration of kimberlite by convective flows of external water, *Contributions to Mineralogy and Petrology*, 168, p.1038.

Afanasyev, A.A., Costa, A. and Chiondini, G., 2015. Investigation of hydrothermal activity and Campi Flegrei caldera using 3D numerical simulations: Extension to high temperature processes, *Journal of Volcanology and Geothermal Research*, 299, pp.68–77.

Afanasyev, A.A., Kempka, T., Kühn, M. and Melnik, O., 2016. Validation of the MUFITS

reservoir simulator against standard CO_2 storage benchmarks and history-matched models of the Ketzin pilot site, *Energy Procedia*, 97, pp.395–402.

Afanasyev, A.A., Blundy, J., Melnik, O. and Sparks, S., 2018. Formation of magmatic brine lenses via focussed fluid-flow beneath volcanoes, *Earth and Planetary Science Letters*, 486, pp.119-128.

Afanasyev, A.A. and Melnik, O.E., 2017. Numerical simulation of formation of a concentrated brine lens subject to magma chamber degassing, *Fluid Dynamics*, 52, pp.416–423.

Agustín-Flores, J., Németh, K., Cronin, S.J., Lindsay, J.M. and Kereszutri, G., 2015, Shallow-seated explosions in the construction of the Motukorea tuff ring (Aukland, New Zealand): Evidence from lithic and sedimentary characteristics, *Journal of Volcanology and Geothermal Research*, 304, pp.272–286.

Anderberg, Y., 1997. Spalling phenomena of HPC and OC. In: *NIST Workshop on Fire Performance of High-Strength Concrete*, National Institute of Standards and Technology: USA.

Andronico, D., Cappelli, L., Ciancitto, F., Cioni, R., Cristaldi, A. and Corsaro, R.A., 2018. *The 16 March 2017 phreatomagmatic explosion at Mt Etna, Italy.* Cities on Volcanoes 10, Naples.

Austin-Erickson, A., Büttner, R., Dellino, P., Ort, M.H. and Zimanowski, B., 2008. Phreatomagmatic explosions of rhyolotic magma: Experimental and field evidence, *Journal of Geophysical Research*, 113, doi: 10.1029/2008JB005731.

Baker, L.L., Bernard, A., Rember, W.C., Milazzo, M., Dundas, C., Abramov, O. and Keszthelyi, L, 2015. Temperature profile around basaltic sill intruded into wet sediments, *Journal of Volcanology and Geothermal Research*, 302, pp.81–86.

Belousov, A., Behncke, B. and Belousova, M., 2011. Generation of pyroclastic flows by explosive interaction of lava flows with ice/water-saturated substrate, *Journal of Volcanology and Geothermal Research,* 202, pp. 60–72.

Björnsson, E., 1783. Relation eins prests sem ár 1783 ferðaðist um sumarið á Suðurland frá Múlasýslu yfir Skaftafells bæði áfram og heimleiðis (Relation by one pastor, who travelled in the summer 1783 in Southern Iceland from Múlashire through Skaftafellshire back and forth). In Einarsson, T., Gudbergsson, G.M., Gunnlaugsson, G.Á., Rafnsson, S., and Thorarinsson, S., eds., 1984, *Skaftáreldar 1783–1784, Ritgerðir og Heimildir*, Reykjavík: Mal og Menning,

p. 295–297.

Boreham, F., Cashman, K.V., Rust, A. and Höskuldsson, Á., 2018. Linking lava flow morphology, water availability and rootless cone formation on the Younger Laxá Lava, NE Iceland, *Journal of Volcanology and Geothermal Research*, 364, pp.1–19, doi:10.1016/j.jvolgeores.2018.08.019.

Boreham, F., Cashman, K.V. and Rust, A., 2020. Hazards from lava–river interactions during the 1783–1784 Laki fissure eruption, *Geological Society of America Bulletin*, 132 (11–12), pp.2651–2668.

Bouhidf, M.A., Besson, P., Courtial, P, Gérardin, C., Navrotski, A. and Richet, P., 2007. Thermochemistry and melting properties of basalt, *Contributions to Mineral Petrology*, 153, pp.689–698.

Brand, B.D., Mackaman-Lofland, C., Pollock, N.M., Bendaña, S., Dawson, B. and Wichgers, P., 2014. Dynamics of pyroclastic density currents: Conditions that promote substrate erosion and self-channelization – Mount St Helens, Washington (USA), *Journal of Volcanology and Geothermal Research*, 276, pp.189–214.

Brooks, R.H. and Corey, A.T., 1964. Hydraulic Properties of Porous Media, *Hydrology Papers*, Colorado State University.

Brown, M., Perez, J., and Miles, A., eds., 2015. *Soil and Soil Properties in: Teaching Organic Farming and Gardening: Resources for Instructors, The Center for Agroecology and Sustainable Food Systems*, University of California Santa Cruz: Santa Cruz.

Brown, S., Jenkins, S.F., Sparks, R.S.J., Odbert, H. and Auker, M.R, 2017. Volcanic fatalities database: analysis of volcanic threat with distance and victim classification, *Journal of Applied Volcanology*, 6, doi:10.1186/s13617-017-0067-4.

Bruno, B.C., Fagents, S.A., Thordarson, Th., Baloga, S.M. and Pilger, E., 2004. Clustering within rootless cone groups on Iceland and Mars: Effect of non-random processes, *Journal of Geophysical Research*, 109.

Bull, J.M., Minshull, T.A., Mitchell, N.C., Thors, K., Dix J.K. and Best, A.I., 2003. Fault and magmatic interaction within Iceland's western rift over the last 9 kyr, *Geophysical Journal International*, 154, pp. F1–F8.

Büttner, R. and Zimanowski, B., 1998. Physics of thermohydraulic explosions, *Physical Review E*, 57(5), p.5726.

Bütter, R., Dellino, P. and Zimanowksi, B., 1999. Identifying magma–water interaction from

the surface features of ash particles, *Nature*, 401, pp.688–690.

Büttner, R., Dellino, P., La Volpe, L., Lorenz, V. and Zimaonwski, B., 2002. Thermohydraulic explosions in phreatomagmatic eruptions as evidence by the comparison between pyroclasts and products from Molten Fuel Coolant Interaction experiments, *Journal of Geophysical Research*, 107, p.2277.

Büttner, R., Dellino, P., Raue, H., Sonder, I. and Zimaonowski, B., 2006. Stress-induced brittle fragmentation of magamatic melts: Theory and experiments, *Journal of Geophysical Research*, 111(B8).

Carpenter, P.K., and Vicenzi, E.P., 2012. Mineral reference standards and quantitative electro-probe microanalysis, *Microscopy and Microanalysis*, 18, pp.1734–1735.

Cashman, K.V. and Kauahikaua, J.P., 1997. Reevaluation of vesicle distributions in basaltic lava flows, *Geology*, 25, pp.419–422.

Cashman, K.V., Thornber, C. and Kauahikaua, J.P., 1999. Cooling and crystallization of lava in open channels, and the transition from Pāhoehoe Lava to ‘A’ā, *Bulletin of Volcanology*, 61, pp.306–323.

Cashman, K.V. and Mangan, M.T., 2014. A Century of Studying Effusive Eruptions in Hawai’i. In: Poland, M.P., Takahashi, T.J. and Landowski, C.M., ed., *Characteristics of Hawaiian Volcanoes,* USGS Professional Paper 1801.

Crow, R., Karlstrom, K.E., McIntosh, W., Peters, L. and Dunbar, N., 2008. History of Quaternary volcanism and lava dams in western Grand Canyon based on lidar analysis, $^{40}Ar/^{39}Ar$ dating, and field studies: Implications for flow stratigraphy, timing of volcanic events, and lava dams, *Geosphere*, 4, pp.183–206, doi: 10.1130/GES00133.1.

Comeau, E. and Wolf, A., 1996. Fire in the chunnel, *National Fire Protection Association Journal*, 91, pp.58–64.

Cummins, A., 2017. BBC crew makes dramatic escape as Mount Etna volcano erupts, *CNN*, [online] 17 March 2017. Available at: <`https://edition.cnn.com/2017/03/17/europe/bbc-crew-volcano-mount-etna-eruption/index.html`> [Accessed 1 August 2018]

Delaney, P.T., 1987. Heat transfer during emplacement and cooling of mafic dykes. I*n:* Halls, H.C. and Fahrin, W.F., ed., *Geological Association of Canada Special Paper 34*, Geological Association of Canada: St John’s, Newfoundland, pp.31–46.

Deligne, N.I., 2012, *After the flow: landscape response to the emplacement of Holocene lava flows, Central Oregon Cascades, USA,* PhD thesis: University of Oregon, 217 p.

Deligne, N.I., Conrey, R.M., Cashman, K.V., Champion, D.E. and Amidon, W.H., 2016. Holocene volcanism of the upper McKenzie River catchment, central Oregon Cascades, USA, *Geological Society of America Bulletin*, 218, pp.1618–1635, doi:10.1130/B31405.1.

Deligne, N.I., Mckay, D., Conrey, R., Grant, G.E., Johnson, E.R., O'Connor, J. and Sweeney, K., 2017. *A Field-trip guide to mafic volcanism of the Cascade Range in central Oregon – A volcanic, tectonic, hydrologic, and geomorphic journey: U.S. Geological Survey Scientific Investigations Report 2017–5022–H*, 94 p., `https://doi.org/sir20175022H`.

Deligne, N.I., Jolly, G.E., Taig, T. and Webb, T.H., 2018. Evaluating life-safety risk for fieldwork on active volcanoes: the volcano life risk estimator (VoLREst), a volcano observatory's decision-support tool, *Journal of Applied Volcanology*, 7, doi:10.1186/s13617-018-0076-y.

Dietterich, H.R. and Cashman, K.V., 2014. Channel networks within lava flows: Formation, evolution, and implications for flow behavior, *Journal of Geophysical Research: Earth Surface*, 119, pp.1704–1724.

Dietterich, H.R., Lev, E., Chen, J., Richardson, J.A., and Cashman, K.V., 2017. Benchmarking computational fluid dynamics models of lava flow simulation for hazard assessment, forecasting, and risk management, *Journal of Applied Volcanology*, 6.

Dietterich, H.R., Patrick, M.R., Diefenback, A.K., Parcheta, C., Lev, E. and Folks, N.L., 2018. Lava flow hazard modeling and the assessment of effusion rates and topographic change with UAS and lidar during the 2018 Kilauea lower East Rift Zone eruption, *AGU Fall Meeting Abstracts*.

Dundas, C.M. and Keszthelyi, L.P., 2013. Modeling steam pressure under martian lava flows, *Icarus*, 266, pp.1058–1067.

Dwaikat, M.B. and Kodur, V.K.R., 2009. Hydrothermal model for predicting fire-induced spalling in concrete structural systems, *Fire Safety Journal*, 44, pp.425–434.

Dwaikat, M.B. and Kodur, V.K.R., 2010. Fire induced spalling in high strength concrete beams, *Fire Technology*, 46, pp.251–274.

Ebinghaus, A., Hartley, A.J., Ebinghaus, A., Hartley, A.J., Jolley, D.W., Hole, M. and Millett, J., 2014. Lava–Sediment Interaction and Drainage-System Development In A Large Igneous Province: Columbia River Flood Basalt Province, Washington State, US, *Journal of Sedimentary Research*, 84(11), pp.1041-1063.

Edwards, B., Magnússon, E., Thordarson, T., Guðmundsson, M., Höskuldsson, A.,

Oddson, B. and Haklar, J., 2012. Interactions between lava and snow/ice during the 2010 Fimmvörðuháls eruption, south-central Iceland, *Journal of Geophysical Research*, 117, B04302, doi:10.1029/2011JB008985.

Edwards, B.R., Karson, J., Wysocki, R., Lev, E., Bindeman, I. and Keuppers, U., 2013. Insight on lava–ice/snow interactions from large-scale basaltic melt experiments, *Geology*, 41(8), pp. 851–854.

Edwards, B.R., Belousov, A., Belousova, M. and Melnikov, D., 2015. Observations on lava, snowpack and their interactions during the 2012–13 Tolbachik eruption, Klyuchevskoy Group, Kamchatka, Russia, *Journal of Volcanology and Geothermal Research*, 307, pp. 107–119.

Einarsson, Á., 1982. The palaeolimnology of Lake Mývatn, northern Iceland: plant and animal microfossils in the sediment, *Freshwater Biology*, 12:63-82

Einarsson, T., Guðbergsson, G.M., Gunnlaugsson, G.Á., Rafnsson, S., and Thórarinsson, S., ed., 1984. *Skaftáreldar 1783–1784, Ritgerðir og Heimildir,* Reykjavík: Mal og Menning.

Einarsson, Á., Halfliðalson, H. and Óskarsson, H., 1988. *Mývatn: Saga lífríkis og gjóskutímatal í Syðriflóa, Rannsóknastöð við Mývatn*, Skýrsla 4: Reykjavik.

Einarsson, Á., Stefánsdóttir, G., Jóhannesson, H., Ólafsson, J., Gíslason, G., Wakana, I., Gudbersson, G. and Gardarsson, A., 2004. The ecology of Lake Mývatn and the River Laxá: Variation in space and time, *Aquatic Ecology,* 38: 317-348.

Ely, L.L., Brossy, C.C., House, P.K., Safran, E.B., O'Connor, J.E., Champion, D.E., Fenton, C.R., Bondre, N., Orem, C.A., Grant, G.E., Henry, C.D. and Turrin, B.D., 2012. Owyhee River intracanyon lava flows: Does the river give a dam?, *Geological Society of America Bulletin*, 124, pp.1667–1687, doi:10.1130/B30574.1.

Eppelbaum, L., Kutasov, I. and Pilchin, A., 2014. *Applied geothermics*, Springer: Berlin, Heidelberg.

Fagents, S.A. and Greeley, R., 2001. Factors influencing lava–substrate heat transfer and implications for thermomechanical erosion, *Bulletin of Volcanology*, 62, pp.519–523.

Fagents, S., Lanagan, P. and Greeley, R., 2002. Rootless cones on Mars: a consequence of lava-ground ice interaction. In: Smellie, J.L. and Chapman, M.G., ed., *Volcano-Ice Interaction on Earth and Mars,* Geological Society Special Publication: London, 202, pp.295–317.

Fagents, S. and Thordarson, Th., 2007. Rootless volcanic cones in Iceland and on Mars. In

Chapman, M.G., ed, *The Geology of Mars: Evidence from Earth-Based Analogs,* Cambridge University Press: Cambridge, pp. 151–177.

Favalli, M., Pareschi, M.T., Neri, A. and Isola, I., 2005. Forecasting lava flow paths by a stochastic approach, *Geophysical Research Letters*, 32.

Fell, M., 2002. *A very present help in trouble: the autobiography of the fire-priest by Rev. Jón Steingrímsson,* P. Lang: New York.

Fenton, C.R., Poreda, R.J., Nash, B.P., Webb, R.H. and Cerling, T.E., 2004. Geochemical discrimination of the five Pleistocene lava-dam outburst-flood deposits, western Grand Canyon, Arizona, *The Journal of Geology*, 112, pp.91–110.

Fenton, C.R., Webb, R.H. and Cerling, T.E., 2006. Peak discharge of a Pleistocene lava-dam outburst flood in Grand Canyon, Arizona, USA, *Quaternary Research*, 26, pp.324–335.

Fink, J.H. and Griffiths, R.W., 1992. A laboratory analog study of the surface morphology of lava flows extruded from point and line sources, Journal of Volcanology and Geothermal Research, 54, pp.19-32.

Fisher, R.V., 1968. Pu'u Hou littoral cones, Hawaii, Geol. Rundschau. 57, pp.837-864.

Fitch, E.P., Fagents, S.A., Thordarson, T. and Hamilton, C.W., 2017. Fragmentation mechanisms associated with explosive lava–water interactions in a lacustrine environment, *Bulletin of Volcanology*, 79, p. 12.

Fujita, E., Hidaka, M. and Goto, A., 2009. Simulations of measures to control lava flows, *Bulletin of Volcanology*, 71, pp.401–408.

Gamage, K., Screaton, E., Bekins, B. and Aiello, I., 2011. Permeability–porosity relationships of subduction zone sediments, *Marine Geology*, 29, pp.19–36.

Gao, W., Li, J., Mao, X. and Li, H., 2013a. Geologic and Geomorphological Value of the Monogenetic Volcanoes in Wudalianchi National Park, NE China, *Geoheritage*, 5, pp.73–85.

Gao, W., Li, J., Mao, X. and Zhang, T., 2013b. Discussion on genetic mechanism of hornitos in Wudalianchi volcanic province, *Acta Petrologica Sinica*, 26, pp.309–317.

Gawin, D., Pesavento, F and Schrefler, B.A., 2003. Modelling of hygro-thermal behaviour of concrete and high temperature with thermo-chemical and mechanical material degradation, *Computer Methods in Applied Mechanics and Engineering*, 192, pp.1731–1771.

Gawin, D., Pesavento, F and Schrefler, B.A., 2004. Modelling of deformations of high strength concrete at elevated temperature, Materials and Structures, *Concrete Science and*

Engineering, 37, pp.218–236.

Gawin, D., Pesavento, F. and Schrefler, B.A., 2006. Towards prediction of the thermal spalling risk through a multi-phase porous media model of concrete, *Computer Methods in Applied Mechanics and Engineering*, 195, pp.5707–5729.

Graettinger, A.H., Skilling, I., McGarvie, D., and Höskuldsson, Á., 2013, Journal of Volcanology and Geothermal Research, 264, pp.17–35.

Grattan, J., Durand, M. and Taylor, S., 2003. Illness and elevated human mortality in Europe coincidence with the Laki Fissure eruption. In Oppenheimer, C., Pyle, D.M. and Barclay, J., ed., *Volcanic Degassing,* Geological Society Special Publications 213, The Geological Society: London, pp.401–414.

Greeley, R. and Fagents, S.A., 2001. Icelandic pseudocraters as analogs to some volcanic cones on Mars, *Journal of Geophysical Research*, 106, pp.20,527–20,546.

Gregg, T.K.P. and Chadwick, W.W. Jr., 1996. Submarine lava-flow inflation: A model for the formation of lava pillars, *Geology*, 24, pp.981–984.

Gregg T.P.K., Fornari, D.J., Perfitt, M.R., Ridley, W.I. and Kurz, M.D., 2000. Using submarine lava pillars to record mid-ocean ridge eruption dynamics, *Earth and Planetary Science Letters,* 178, pp.195–214, doi:10.1016/S0012-821X(00)00085-6.

Gregg, T.K.P. and Smith, D.K., 2003. Volcanic investigations of the Puna Ridge, Hawai'i: relations of lava flow morphologies and underlying slopes, *Journal of Volcanology and Geothermal Research*, 126, pp.63–77.

Gregg, T.K.P. and Christle, K.W., 2013. Non-explosive lava–water interaction in Skaelingar, Iceland and the formation of subaerial lava pillars, *Journal of Volcanology and Geothermal Research*, 246, pp.36–48.

Guilbaud, M-N., Thordarson, T. and Blake, S., 2005. Morphology, surface structures, and emplacement of lavas produced by Laki, A.D. 1783-1784. In: Manga, M. and Ventura, G., ed., *Kinematics and dynamics of lava flows,* Geological Society of America Special Paper 396, pp.81–102, doi:10.1130/2005.2396(7).

Guilbaud, M-N., Blake, S., Thordarson, Th. and Self, F., 2007. Role of Syn-eruptive Cooling and Degassing on Textures of Lavas from the AD 1783-1784 Laki Eruption, South Iceland, *Journal of Petrology*, 48, pp.1265–1294.

Hamdhan, I.N. and Clarke, B.G., 2010. Determination of thermal conductivity of coarse and fine sand soils, *Proceedings World Geothermal Congress.*

Hamilton, C.W., Thordarson, Th. and Fagents, S.A., 2010a. Explosive lava-water interactions I: architecture and emplacement chronology of volcanic rootless cone groups in the 1783-1784 Laki lava flow, Iceland, *Bulletin of Volcanology*, 72, pp.449–467.

Hamilton, C.W., Fagents, S.A. and Thordarson, Th., 2010b. Explosive lava–water interactions II: self-organization processes among volcanic rootless eruption sites in the 1783-1784 Laki lava flow, Iceland, *Bulletin of Volcanology*, 72, pp.469–485.

Hamilton, C.W., Fagents, S.A. and Thordarson, Th., 2011. Lava-ground ice interaction in Elysium Planitia, Mars: Geomorphological and geospatial analysis of the Tartarus Colles cone groups, *Journal of Geophysical Research*, 116, E03004.

Hamilton C.W., Fitch E.P., Fagents S.A. and Thordarson Th., 2017. Rootless tephra stratigraphy and emplacement processes, *Bulletin of Volcanology*, 79.

Harmathy, T.Z., 1965. Effect of moisture on the fire endurance of building element, *Research paper No. 270 of the Division of Building Research*, National Research Council: Ottawa.

Hauptfleisch, U. and Einarsson, Á. 2012. Age of the Younger Laxá Lava and Lake Mývatn, Northern Iceland, Determined by AMS Radiocarbon Dating, *Radiocarbon,* 54, pp. 155-164.

Hayes, J.L., Tsang, S.W., Fitzgerald, R.G., Blake, D.M., Deligne, N.I., Doherty, A., Hopkins, J.L., Hurst, A.W., Le Corvec, N., Leonard, G.S., Lindsay, J.M., Miller, C.A., Németh, K., Smid, E., White, J.D.L. and Wilson, T.M., 2018. *The DEVORA scenarios: multi-hazard eruption scenarios for the Aukland Volcanic Field, GNS Science Report 2018/29*, 138 p., doi: 10.21420/G20652.

Hertz, K.D., 1984. Explosion of silica-fume concrete, *Fire Safety Journal*, 85, pp.8–77.

Hertz, K.D., 2003. Limits of spalling of fire-exposed concrete, *Fire Safety Journal*, 38, pp.103–116

Hoblitt, R.P., Orr, T.R., Denlinger, R.P., Hon, K. and Cervelli, P.F., 2011. Inflation rates, rifts, and bands in pāhoehoe sheet flow, *Geosphere*, 8, pp.179–195.

Hon, K., Kauahikaua, J., Denlinger, R. and MacKay, K., 1994, Emplacement and inflation of pāhoehoe sheet flows: Observations and measurements of active lava flows on Kilauea Volcano, Hawaii, Geological Society of America Bulletin, 106, pp.351-370, doi: 10.1130/0016-7606(1994)106<0351:EAIOPS>2.3.CO;2.

Horne., R.N., Cengiz, S., Mahiya, G., Li, M., Ambusso, W., Tovar, R., Wang, C. and Nassori, H., 2000. Steam–water relative permeability, *Proceedings World Geothermal Conference*

Hort, M., 1997. Cooling and crystallization in sheet-like magma bodies revisited, *Journal of Volcanology and Geothermal Research*, 76, pp.297–317.

Höskuldsson, Á., Dyrh, C., Dolvik, T., 2010. *Grænavatnsbruni og Laxárhraun yngra*, Fall Meeting JFI, Ágrip erinda Jaðfræðafélag Íslands, 65 bls.

Inglethorpe, S.D.J., 1993. *Industrial minerals laboratory manual: Diatomite, British Geological Survey Technical Report WG/92/39*, British Geological Survey: Nottingham.

Ipekoğlu, U. and Mete, Z., 1990. Determination of the properties of various diatomite deposits within Aegean Region of Turkey, *Geologija*, 33., pp.447–459.

Jaeger, W.L., Keszthelyi, L.P., Skinner, J.A., Milazzo, M.P., McEwen, A.S., Titus, T.N., Rosiek, M.R., Galuszka, D.M., Howington-Kraus, E., Kirk, R.L. and HiRISE Team, 2010. Emplacement of the youngest flood lava on Mars: A short, turbulent story, *Icarus,* 2015, pp.230–243

Jakobsson, T., 1963, *Myndun Aðaldals*, Árbók Thingeyinga, pp.112-122.

Jakobsson, S.P., 1979. Petrology of recent basalts of the Eastern Volcanic Zone, Iceland, *Acta Naturalia Islandica*, 26.

Jensen, R.A. and Donnelly-Nolan, J.M., 2017. *Field-trip guide to the geologic highlights of Newberry Volcano, Oregon*, U.S. Geological Survey Scientific Investigations Report 2017–5022–J2.

Jónsson, J., 1784. A letter from Síra Jón Jónsson of Mýrar regarding the flight from Hólmasel during the Laki eruption of 178. In: Fell, M., translator., 2002, *A very present help in trouble: the autobiography of the fire-priest by Rev. Jón Steingrímsson.* P. Lang, New York.

Jurado-Chichay, Z., Rowland, S. and Walker, G.P.L., 1996. The formation of circular littoral cones from tube-fed pāhoehoe: Mauna Loa, Hawai'i, *Bulletin of Volcanology*, 57, pp.471-482, doi:10.1007/BF00304433.

Kalifa, P., Tsimbrovska, M. and Barghel-Bouny, V., 1998. High performance concrete at elevated temperatures – an extensive experimental investigation on thermal, hygral and microsctucture properties. In: Aïtcin, P.C. and Delgrave, Y., ed., *Proceedings of the International Symposium on High-Performance and Reactive Powder Concretes*, Sherbrooke, Canada, pp. 259–279.

Kalifa, P., Menneteau, F.-D. and Quenard, D., 2000. Spalling and pore pressure in HPC at high temperatures, *Cement and Concrete Research*, 30, pp.1915–1927.

Kauahikaua, J., Denlinger, R., Foster, J. and Keszthelyi, L., 1993. Lava delta instability: Is it mass-wasting or is it triggered by lava flowing through tubes?, *Eos, Transactions of the American Geophysical Union*, 74, p. 616.

Kauahikaua, J., Sherrod, D.R., Cashman, K.V., Heliker, C., Hon, K., Mattox, T. and Johnson, J., 2003. Hawaiian Lava-Flow Dynamics During the Pu'u 'Ō'ō-Kūpaianaha Eruption: A Tale of Two Decades, *US Geological Survey Professional Paper 1676,* pp.63-87.

Keszthelyi, L.P., Jaeger, W.L., Dundas, C.M., Martínez-Alonso, S., McEwen, A.S. and Milazzo, M.P., 2010. Hydrovolcanic features on Mars: Preliminary observations from the first Mars year of HiRISE imaging, *Icarus*, 205, pp.211–229.

Kerr, R.C., Griffiths, R.W. and Cashman, K.V., 2006. Formation of channelized lava flows on an unconfined slope, *Journal of Geophysical Research: Solid Earth*, 111(B10), doi: `https://doi.org/10.1029/2005JB004225`.

Kilburn, C.R.J., 2000. Lava flows and lava fields, *Encyclopedia of volcanoes*, pp. 291–305.

Kunz, K., translator, 1998, *Fires of the Earth: The Laki Eruption 1783-1784 by the Rev. Jón Steingrímsson,* University of Iceland Press: Reykjavík.

Lange, R.A., Cashman, K.V. and Navrotski, A., 1994. Direct measurements of latent heat during crystallization and melting of a ugandite and an olivine basalt, *Contributions to Mineralogy and Petrology*, 188, pp.169–181.

Lewis, M.A., Chesney, C.S. and ÓDochartaigh, B.E., 2006. Guide to Permeability Indices: *British Geological Survey Open Report CR/06/160N*, British Geological Survey: Keyworth, Nottingham.

Liu, E.J., Cashman, K.V., Rust, A.C. and Gislason, S.R. 2015. The role of bubbles in generating fine ash during hyromagmatic eruptions, *Geology,* 43, pp.239-242, doi: 10.1130'G36336.1.

Liu, E.J., Cashman, K.V., Rust, A.C. and Höskuldsson, Á., 2017. Contrasting mechanisms of magma fragmentation during coeval magmatic and hydromagmatic activity: the Hverfjall Fires fissure eruption, Iceland, Bulletin of Volcanology, 79, p.68, doi: 10.1007/s00445-017-1150-8.

Lorenz, V. and Kurszlaukis, S., 2007, Root zone processes in the phreatomagmatic pipe emplacement model and consequences for the evolution of maar-diatreme volcanoes, *Journal of Volcanology and Geothermal Research*, 159, pp.4–32.

Lovering, T.S., 1935. Theory of heat conduction applied to geological problems, *Geological*

Society of America Bulletin, 46, pp.69–94.

Manger, G.E., 1963. Porosity and Bulk Density of Sedimentary Rocks, Contributions to Geochemistry, *Geological Survey Bulletin 1144–E*, US Atomic Energy Commission, United States Government Printing Office: Washington.

Mattox, T.N., 1993. Where Lava Meets the Sea: Kilauea Volcano, Hawai'i, *Earthquakes and Volcanoes*, 24, pp.160–177.

Mattox, T.N. and Mangan, M.T., 1997. Littoral hydrovolcanic explosions: a case study of lava-seawater interaction at Kīlauea Volcano, *Journal of Volcanology and Geothermal Research*, 75, pp.1-17, doi:10.1016/S0377-0273(96)00048-0.

Mattsson, H.B. and Höskuldsson, Á., 2011. Contemporaneous phreatomagmatic and effusive activity along the Hverfjall eruptive fissure, north Iceland: Eruption chronology and resulting deposits, Journal of Volcanology and Geothermal Research, 201 pp.241-252.

Melnik, O.E., Afanasyev, A.A. and Zarin, G.A., 2016. Magma degassing during eruption through water-saturated porous rocks, *Doklady Physics*, 61, pp.235-238.

Moore, J.G. and Ault, W.U., 1965, Historic littoral cones in Hawaii, Pacific Science, 19, pp.3-11.

Moore, J.G., Phillips, R.L., Peterson, D.W. and Swanson, D.A., 1973. Flow of Lava into the Sea, 1969-1971, Kīlauea Volcano, Hawaii, *Geological Society of America Bulletin*, 84, pp.537–546.

Moore, J.G., 1975. Mechanism of Formation of Pillow Lava, *American Scientist*, 63, pp. 269–277.

Moreland, W.M., Thordarson, Th., Houghton, B.F. and Larsen, G., 2019. Driving mechanisms of subaerial ad subglacial explosive episodes during the 10^{th} century Eldgjá fissure eruption, southern Iceland, *Volcanica*, 2, pp.129–150, doi:10.20909/vol.02.02.129150.

Morgan, A.V., 2000. The Eldfell Eruption, Heimaey, Iceland: A 25-Year Retrospective: *Geoscience Canada*, 27(1).

Moyer, T.C. and Swanson, D.A, 1987. Secondary hydroeruptions in pyroclastic-flow deposits: examples from Mount St. Helens, *Journal of Volcanology and Geothermal Research*, 32, pp.299–319.

Noguchi, R. and Kurita, K., .2015. Unique characteristics of cones in Central Elysium Planitia, Mars, *Planetary and Space Science*, 111, pp.44-54.

Noguchi, R., Höskuldsson, Á. and Kurita, K., 2016. Detailed topographical, distributional, and material analyses of rootless cones in Mývatn, Iceland, *Journal of Volcanology and Geothermal Research*, 318, pp.89-102.

Noh, M.-J. and Howat, I.M., 2015. Automated stereo-photogrammetric DEM generation at high latitudes: Surface Extraction with TIN-based Search-space Minimization (SETSM) validation and demonstration over glaciated regions, *GIScience & Remote Sensing,* 52, pp.198–217, doi: 10.1080/15481603.2015.1008621.

Nygard, I., 1959. *Jardvegskort af Islandi (soil map of Iceland)*, University Research Institute: Reykjavík, scale 1:750 000, 1 sheet.

O'Connor, J.E. and Burns, S.F., 2009. Cataclysms and Controversy – Aspects of the geomorphology of the Columbia River Gorge, *Geological Society of America*, Field Guide 15, pp.237–251.

Óladóttir, B.A., Sigmarsson, O., Larsen, G. and Thordarson, Th., 2008. Katla volcano, Iceland: magma composition, dynamics and eruption frequency as recorded by Holocene tephra layers, *Bulletin of Volcanology*, 70, pp.475–493.

Orem, C.A., 2010. *Lacustrine sediment record of multiple Quaternary lava dams on the Owyhee River, Southeastern Oregon,* MSc thesis, Central Washington University, 137 p.

Pálsson, S., 1784. Historia ignis in oriente Islandiæ erumpentis Anno 1783, qvoad innotuit in tractu Skagafjördensi, complectitur in se et effectus varios (The story of the earth fire which broke out in Eastern Iceland in the year 1783, as long as it was observed in Skagafjörður; concerning the progress of the eruption and its various effects). In Einarsson, T., Gudbergsson, G.M., Gunnlaugsson, G.Á., Rafnsson, S., and Thorarinsson, S., ed., 1984. *Skaftáreldar 1783–1784, Ritgerðir og Heimildir*, Mal og Mennig: Reykjavík, pp.419–422.

Pedersen, G.B.M., Höskuldsson, Á., Dürig, T., Thordarson, T., Jónsdóttir, I., Riishuss, M.S., Óskarsson, B.V., Dumont, S., Magnusson, E., Gudmundsson, M.T., Sigmundsson, F., Drouin, V.J.P.B., Gallagher, C., Askew, R., Gudnason, J., Moreland, W.M., Nikkola, P., Reynolds, H.I., Schmith, J. and the IES eruption team, 2017. Lava field evolution and emplacement dynamics of the 2014–2015 basaltic fissure eruption at Holuhraun, Iceland, *Journal of Volcanology and Geothermal Research*, 340, pp.155–169, doi:10.1016/j.volgeores.2017.02.027.

Pétursson M (1784; trans. Thordarson et al., 2003) Höskuldsstaðarannáll 1730–1784, Annálar 1400–1800, (Annales Islandici) IV. Hið Íslenska Bókmenntafélag, Reykjavík 1940–1948, 463–603

Philpotts, A.R. and Carroll, M, 1996. Physical properties of partly melted tholeiitic basalt, *Geology*, 24, pp.1029–1032.

Putirka, K., 2008. Thermometers and Barometers for Volcanic Systems, Reviews in Mineralogy and Geochemistry, v.69 pp.61-120, doi: 10.2138/rmg.2008.69.3.

Revil, A., 2000. Thermal conductivity of unconsolidated sediments with geophysical applications, Journal of Geophysical Research, 105, pp.16,749–16,768.

Reynolds, P., Brown, R.J., Thordarson, Th., Llewellin, E.W. and Fielding, K., 2015. Rootless cone eruption processes informed by dissected tephra deposits and conduits, *Bulletin of Volcanology*, 77, pp.72.

Rezanezhad, F., Price, J.S., Quinton, W.L., Lennartz, B., Milojevic, T. and Van Cappellen, P., 2016. Structure of peat soils and implications for water storage, flow and solute transport: A review update for geochemists, *Chemical Geology*, 429, pp.75–84.

Ross, K.A., Smets, B., De Batist, M., Hilbe, M., Schmid, M. and Anselmetti, F.S., 2014. Lake-level rise in the late Pleistocene and active subaquatic volcanism since the Holocene in Laki Kivu, East African Rift, *Geomorphology*, 221, pp.274–285.

Rossi, M.J. and Gudmundsson, A., 1996. The morphology and formation of flow-lobe tumuli on Icelandic shield volcanoes, *Journal of Volcanology and Geothermal Research*, 72, pp.291–308.

Rubin, A.M., 1995. Propagation of magma-filled cracks, *Annual Review of Earth and Planetary Sciences*, 23, pp.287–336.

Sæmundsson, K., Hjartarson, Á., Kadal, I., Sigurgeirsson, M.Á., Kristinsson, S.G. and Víkingsson, S., 2012. *Geological Map of the Northern Volcanic Zone, Iceland. Norther Part* 1:100 000, Iceland GeoSurvey and Landsvirkjun: Reykjavik

Schmidt, A., Ostro, B., Carslaw, K.S., Wilson, M., Thordarson, Th., Mann, G.W. and Simmons, A.J., 2011. Excess mortality in Europe following a future Laki-style Icelandic eruption, *Proceedings of the National Academy of Sciences*, 108(38), p.15715.

Schmidt, A., Thordarson, Th., Oman, L., Robock, A. and Self, S., 2012. Climactic impact of the long-lasting 1783 Laki eruption: Inapplicability of mass-independent sulfur isotopic composition measurement. *Journal of Geophysical Research*, 117, doi:10.1029/2012JD018414.

Scott, W.E., Iverson, R.M., Schilling, S.P. and Fisher, B.J., 1999. *Volcano hazards in the Three Sisters Region, Oregon, U.S. Geological Survey Open-File Report 99-437.*

Self, S., Keszthelyi, L. and Thordarson, Th., 1998. The Importance of Pāhoehoe, Annual Review of Earth and Planetary Science, 26, pp.81-110.

Sharma, P.V., 2002. *Environmental and engineering geophysics*, Cambridge University Press: Cambridge.

Sheridan, M.F. and Wohletz, K.H., 1983. Hydrovolcanism: Basic Considerations and Review, Journal of Volcanology and Geothermal Research, 17, pp.1-29.

Skelton, A., Sturkell, E., Jokobsson, M., Einarsson, D., Tollefsen, E. and Orr, T., 2016. Dimmuborgir: a rootless shield complex in northern Iceland, Bulletin of Volcanology, 78, p.40, doi:10.1007/s00445-016-1032-5

Skilling, I.P., 2002, Basaltic pāhoehoe lava–fed deltas: large-scale characteristics, clast generation, emplacement processes and environmental discrimination. I*n:* Smellie, J.L. and Chapman, M.G., ed., *Volcano–Ice Interaction on Earth and Mars*, Geological Society, London, Special Publications: London, 202, pp.91–113.

Skilling, I.P., White, J.D.L. and McPhie, J., 2002, Peperite: a review of magma–sediment mingling, *Journal of Volcanology and Geothermal Research*, 114, pp.1–17.

Sigmarsson O., Condomines, M., Grönvold, K. and Thordarson, Th., 1991. Extreme magma homogeneity in the 1783–84 Lakagigar Eruption: Origin of a large volume of evolved basalt in Iceland, *Geophysical Research Letters*, 18(12), pp.2229–2232.

Steingrímsson, J., 1783a. Lítið ágrip um nýja eldsuppkomu í vestariparti Skaftafellssýslu og thess verkanir sem framkommar eru (A short compendium of the recent volcanic outburst in western part of Skaftafellshire). In: Einarsson, T., Gudbergsson, G.M., Gunnlaugsson, G.Á., Rafnsson, S. and Thorarinsson, S., ed., 1984. *Skaftáreldar 1783–1784, Ritgerðir og Heimildir*, Mal og Menning: Reykjavík, pp.272–274.

Steingrímsson, J., 1783b, Póstur úr bréfi prófasts síra Jóns Steingrímssonar (Abstract from a letter to Rev. Bjarni Jónsson). In: *Safn til Sögu Íslands IV*, Copenhagen 1907–1915, pp.69–71.

Steingrímsson, J., Ólafsson, S., 1783, Einfold og sönn frásaga um jarðeldshlaupið í Skaftafellssýslu árið 1783 (A simple but true narrative of the eruption in Skaftafellshire in the year 1783. In: *Safn til Sögu Íslands IV*, Copenhagen 1907–1915, pp.58-69.

Stephensen, O., 1785, Abstract from prefect Stephensen's letter to Erichsen, the deputy of the treasury, dated 15 August 1783. In Einarsson, T., Gudbergsson, G.M., Gunnlaugsson, G.Á., Rafnsson, S., and Thorarinsson, S., ed., 1984. *Skaftáreldar 1783–1784, Ritgerðir og*

Heimildir, Mal og Menning, Reykjavík, p. 279.

Stevenson, J.A., Mitchell, N.C., Mochrie, F., Cassidy, M. and Pinkerton, H., 2012. Lava penetrating water: the different behaviours of pāhoehoe and 'a'ā at the Nesjahraun, Thingvellir, Iceland, *Bulletin of Volcanology,* 74, pp.33-46.

Sumner, J.M., Black, S., Matela, R.J. and Wolff, J.A., 2005, Spatter, Journal of Volcanology and Geothermal Research, 142, pp.49-65.

Thorarinsson, S., 1951. Laxárgljúfur and Laxárhraun: A Tephrochonological Study, *Geografiska Annaler*, 33, pp.1-89.

Thorarinsson, S., 1953. The Crater Groups in Iceland, *Bulletin of Volcanology*, 14, pp.3-44.

Thorarinsson, S., 1968, The Lakagigar eruption of 1783 and the Lakagigar crater row, *Natturufraedhingurinn*, 37, pp.27-57.

Thorarinsson, S., 1979. The Postglacial History of the Mývatn Area, *Oikos,* 32, pp.17-28.

Thordarson, Th. and Self, S., 1993, The Laki (Skaftár Fires) and Grímsvötn eruptions in 1783-1785, *Bulletin of Volcanology*, 55, pp.233–263.

Thordarson, Th., Self, S., Óskarsson, N. and Hulsebosch, T., 1996. Sulfur, chlorine, and fluorine degassing and atmospheric loading by the 1783–1784 AD Laki (Skaftár Fires) eruption in Iceland, *Bulletin of Volcanology*, 58, pp.205–255.

Thordarson, Th., Miller, D.J. and Larsen, G., 1998. New data on the age and origin of the Leiðólfsfell Cone Group in south Iceland, *Jökull*, 46.

Thordarson, Th., Miller, D.J., Larsen, G., Self, S. and Sigurdsson, H., 2001. New estimates of sulfur degassing and atmospheric mass-loading by the 934 AD Eldgjá eruption, *Journal of Volcanology and Geothermal Research*, 108, pp. 33–54.

Thordarson, Th., 2003, The 1783–1785 A.D. Laki-Grímsvötn eruptions I: A critical look at the contemporary chronicles, *Jökull*, 53, pp.1—10.

Thordarson, Th., Larsen, G., Steinthórsson, S. and Self, S., 2003. The 1783-1785 A.D. Laki-Grímsvötn eruptions II: Appraisal based on contemporary accounts, *Jökull*, 53, pp.11–48.

Thordarson, Th. and Larsen, G., 2007. Volcanism in Iceland in historical time: Volcano types, eruption styles and eruptive history, *Journal of Geodynamics*, 43, pp.118-152.

Thordarson, Th. and Höskuldsson, Á., 2008. Postglacial volcanism in Iceland, *Jökull*, 58.

Tribble, G.W., 1991. Underwater observations of active lava flows from Kīlauea volcano,

Hawaii, *Geology*, 19, pp.633–636.

Tsang, S.W.R., Lindsay, J.M., Coco, G., Wysocki, R., Lemer, G., Rader, E., Turner, G.M. and Kennedy, B., 2019. The heating of substrates beneath basaltic lava flows, *Bulletin of Volcanology*, 81.

Toropovs, N., Lo Monte, F., Wyrzykowski, M., Weber, B., Sahmenko, G., Vontobel, P., Felicetti, R. and Lure, P, 2015. *Cement and Concrete Research*, 68, pp.166–173.

Umino, S., Nonaka, M., and Kauahikaua, J., 2006. Emplacement of subaerial pahoehoe lava sheet flows into water: 1990 Kupaianaha flow of Kilauea volcano at Kaimu Bay, Hawai'i, *Bulletin of Volcanology*, 69, pp.125–139.

United States Geological Survey, 2000. *How Old is "Cinder Cone"? – Solving a Mystery in Lassen Volcanic National Park, California*, USGS Fact Sheet-023-00, U.S. Department of the Interior, U.S. Geological Survey.

United States Soil Conservation Service, 1983. *National Engineering Handbook Section 3, Sedimentation*, US Deparment of Agriculture, Soil Conservation Service: Washington DC.

Valentine, G.A. and White, J.D.L., 2012, Revised conceptual model for maar-diatremes: Subsurface processes, energetics and eruptive products, *Geology*, 40(12), pp. 1111–1114.

Valentine, G.A., Graettinger, A.H., and Sonder, I., 2014, Explosion depths for phreatomagmatic eruptions, *Geophysical Research Letters*, 41(9), pp.3045–3051.

Waichel, B.L., de Lima, E.F., Sommer, C.A. and Lunchesky, R., 2006. Peperite formed by lava flows over sediments: An example from the central Paraná Continental Flood Basalts, Brazil, *Journal of Volcanology and Geothermal Research,* 159, pp.343–354.

Walker, G.P.L., 1971. Compound and simple lava flows and flood basalts, *Bulletin of Volcanology*, 35, pp.579-590.

Walker, G.P.L. and Croasdale, R., 1971. Characteristics of some basaltic pyroclasts, *Bulletin of Volcanology,* 35, pp.303–317.

Waples, D.W. and Tirsgaard, H., 2002. Changes in matrix thermal conductivity of clays and claystones as a function of compaction, *Petroleum Geoscience*, 8, pp.365–370.

Wells, G.H., 2017. *Timeline Reconstruction of Holocene Jökulhlaups along the Jökulsá á Fjöllum Channel, Iceland*, MA Thesis, University of Texas at Austin, p. 71.

White, J.D.L., 1996. Impure coolants and interaction dynamics of phreatomagmatic eruptions, *Journal of Volcanology and Geothermal Research*, 74, pp.155–170.

White, J.D.L. and Ross, P.-S., 2011, Maar-diatreme volcanoes: A review, *Journal of Volcanology and Geothermal Research*, 201, pp. 1–29.

White, J.D.L. and Valentine, G.A., 2016. Magmatic versus phreatomagmatic fragmentation: Absence of evidence is not evidence of absence, *Geosphere,* 12(5), pp.1478-1488, doi: `https://doi.org/10.1130/GES01337.1`.

Williams, R.S. and Moore, J.G., 1983. *Man against volcano: the eruption on Heimaey, Vestmannaeyjar, Iceland*, US Department of the Interior, Geological Survey.

Williams, R.S., 1997. *Lava-cooling operations during the 1973 eruption of Eldfell volcano, Heimaey, Vestmannaeyjar, Iceland*, U.S. Geological Survey Open-File Report 97-724.

Wilson, R.L., 1962. The palaeomagnetism of baked contact rocks and reversals of the Earth's magnetic field, *Geophysical Journal of the Royal Astronomical Society*, 7, pp.194–202.

Winney, M., 1996. Arches brace chunnel for six month repair schedule, *New Civil Engineer*, p. 28.

Witham, C.S. and Oppenheimer, C., 2004. Mortality in England during the 1783–4 Laki Craters eruption, *Bulletin of Volcanology*, 67, pp.15-26.

Wohletz, K., Zimanowksi, B., and Büttner, R., 2013, Magma–water interactions *in:* Fagetns, S.A., Gregg, T.P., and Lopes, R.M.C., ed., *Modeling volcanic processes: The physics and mathematics of volcanism*, Cambridge University Press: Cambridge.

Zarin, G.A., Melnik, O.E., Tsvtkova, Y.D. and Afanasyev, A.A., 2016. On the influence of a geothermal system on ground deformation during a volcanic eruption, *Journal of Applied Mechanics and Technical Physics*, 57, pp.1151–1158.

Zhang, H.L. and Davie, C.T., 2013. A numerical investigation of the influence of pore pressures and thermally induced stresses for spalling of concrete exposed to elevated temperatures, *Fire Safety Journal*, 59, pp.102–110.

Zimanowksi, B., Frölich, G. and Lorenz, V., 1995. Experiments on steam explosion by interaction of water with silicate melts, *Nuclear Engineering and Design*, 155(1–2), pp. 335–343.

Zimanowski, B., Büttner, R., Lorenz, V. and Häfele, H.-G., 1997a. Fragmentation of basaltic melt in the course of explosive volcanism, Journal of Geophysical Research, 102, pp.803-814

Zimanowski, B., Büttner, R. and Lorenz, V., 1997b, Premixing of magma and water in MFCI experiments, *Bulletin of Volcanology,* 58, pp.491-495.

Zimanowski, B., and Büttner, R., 2002. Dynamic mingling of magma and liquified sediments, *Journal of Volcanology and Geothermal Research*, 144, pp.37–44.

Appendices

Appendix A

Supplementary Material for Chapter 2

A.1 Supplementary Figures

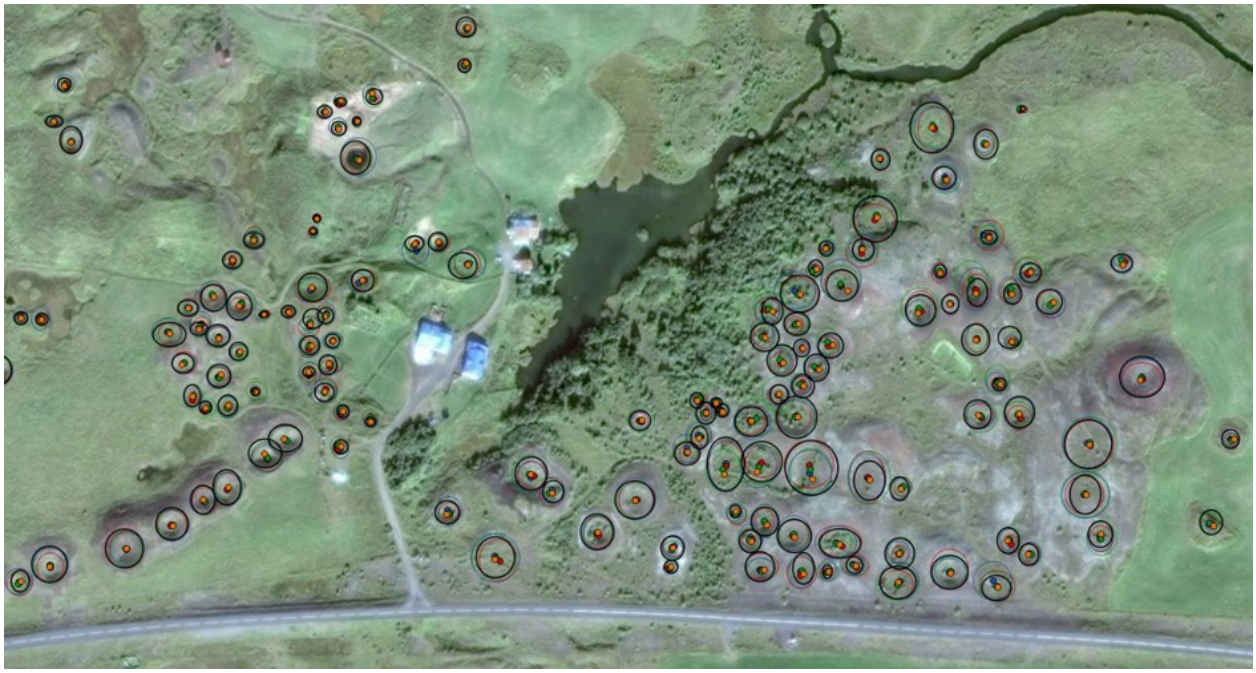

Figure A.1: View of a subset of the rootless cones used for error assessment. The location and area of each cone were independently digitised four times (shown by green, blue, orange and black dots and cirlces) and then the results compared.

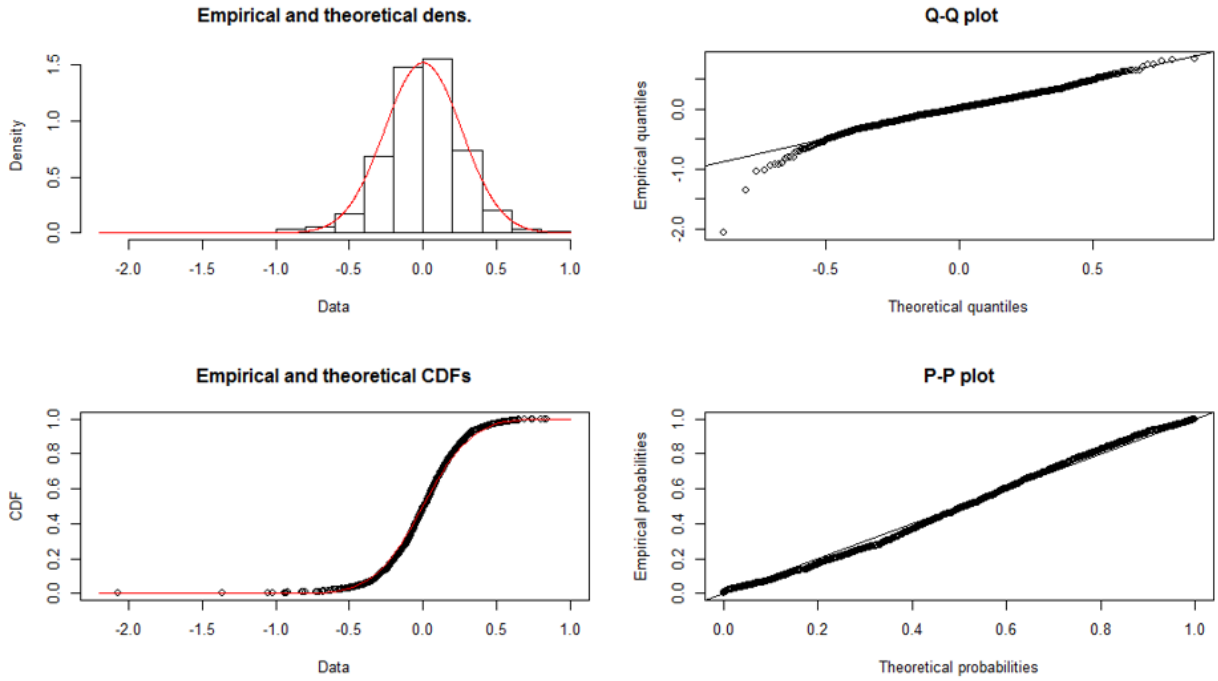

Figure A.2: Relative (%) error distribution for rootless cone area for set of cones shown in Figure A.1. Q-Q and P-P plots show the comparison between the theoretical and empirical quantiles (Q) and probabilities (P) for the model, respectively. CFD means 'Cumulative Distribution Function. Black points and bars show the measured error distribution and red lines show the function used to model the distribution.

A.2 Supplementary Tables

Location	Capture Satellite	Capture Date [yyyy-mm-dd]	Image ID	Max Ground Sample Distance [m]
Mývatn	WorldView-2	2016-07-15	1030050051F92D00	0.58
Laxárdalur	WorldView-2	2015-06-26	1030010044AE0100	0.49
Aðaldalur (south and east)	WorldView-3	2015-09-06	104001001029F700	0.35
Aðaldalur (north and west)	GeoEye-1	2010-09-02	1050410002286800	0.47

Table A.1: Details of DigitalGlobe images used for digitising rootless cones across the YLL (from https://discover.digitalglobe.com).

Location	Date	Flight Time [mm:ss]	Altitude (above ground) [m]	Grid spacing spacing [m]	Spatial resolution of captured images [m/pix]	RMS error for georeferences DTM [m]
Aðaldalur – inflation front	27/7/2016	13:45	70	35	10.4	1.27
Aðaldalur – scoriaceous cones	27/7/2016	14.52	70	35	10.4	0.29
Aðaldalur – hornitos	27/7/2016	10:13	40	20	6.0	0.46

Table A.2: Flight details for UAS surveys

Appendix B

Supplementary Material for Chapter 3

B.1 Selected passages from contemporary sources

This appendix includes selected from contemporary accounts of the 1783—1784 Laki fissure eruption, describing the area before the eruption (A), the lava flow progress, lava–river interactions and flooding (B), explosive lava-–water interactions (C) and weather during the eruption (D).

B.1.1 Sources

1) Kunz, K., translator, 1998. *Fires of the Earth: The Laki Eruption 1783-1784 by the Rev. Jón Steingrímsson*, University of Iceland Press: Reykjavík.

2) Pálsson, S., 1784. Historia ignis in oriente Islandiæ erumpentis Anno 1783, qvoad innotuit in tractu Skagafjördensi, complectitur in se et effectus varios (The story of the earth fire which broke out in Eastern Iceland in the year 1783, as long as it was observed in Skagafjörður; concerning the progress of the eruption and its various effects). In Einarsson, T., Gudbergsson, G.M., Gunnlaugsson, G.Á., Rafnsson, S., and Thorarinsson, S., ed., 1984. *Skaftáreldar 1783–1784, Ritgerðir og Heimildir*, Mal og Mennig: Reykjavík, pp.419–422.

3) Fell, M., 2002. *A very present help in trouble: the autobiography of the fire-priest by Rev. Jón Steingrímsson* P. Lang: New York.

4) Steingrímsson, J., 1783a. Lítið ágrip um nýja eldsuppkomu í vestariparti Skaftafellssýslu og thess verkanir sem framkommar eru (A short compendium of the recent volcanic outburst in western part of Skaftafellshire). In: Einarsson, T., Gudbergsson, G.M., Gunnlaugsson, G.Á., Rafnsson, S. and Thorarinsson, S., ed., 1984. *Skaftáreldar 1783–1784*, Ritgerðir og Heimildir, Mal og Menning: Reykjavík, pp.272–274.

5) Steingrímsson, J., Ólafsson, S., 1783, Einfold og sönn frásaga um jarðeldshlaupið í Skaftafellssýslu árið 1783 (A simple but true narrative of the eruption in Skaftafellshire in the year 1783. In: *Safn til Sögu Íslands IV*, Copenhagen 1907–1915, pp.58-69.

6) Steingrímsson, J., 1783b, Póstur úr bréfi prófasts síra Jóns Steingrímssonar (Abstract from a letter to Rev. Bjarni Jónsson). In: *Safn til Sögu Íslands IV*, Copenhagen 1907–1915, pp.69–71.

7) Stephensen, O., 1785, Abstract from prefect Stephensen's letter to Erichsen, the deputy of the treasury, dated 15 August 1783. In Einarsson, T., Gudbergsson, G.M., Gunnlaugsson, G.Á., Rafnsson, S., and Thorarinsson, S., ed., 1984. *Skaftáreldar 1783–1784, Ritgerðir og Heimildir*, Mal og Menning, Reykjavík, p. 279.

8) Pétursson, M., 1784 (trans. Thordarson et al., 2003). *Höskuldsstaðarannáll 1730–1784, Annálar 1400–1800, (Annales Islandici) IV*. Hið Íslenska Bókmenntafélag: Reykjavík 1940–1948, pp.463–603.

9) Björnsson, E., 1783. Relation eins prests sem ár 1783 ferðaðist um sumarið á Suðurland frá Múlasýslu yfir Skaftafells bæði áfram og heimleiðis (Relation by one pastor, who travelled in the summer 1783 in Southern Iceland from Múlashire through Skaftafellshire back and forth). In Einarsson, T., Gudbergsson, G.M., Gunnlaugsson, G.Á., Rafnsson, S., and Thorarinsson, S., eds., 1984, *Skaftáreldar 1783–1784, Ritgerðir og Heimildir*, Reykjavík: Mal og Menning, p. 295–297.

Table A - Conditions before the eruption

Ref	Source	Date	Details	Passage
A1	7	Spring 1783	High river levels before eruption	*The water level was unusually high in the Skaftá River and the water dirty and ill-smelling*
A2	6	June 1783	Description of area around Laki fissuers	*The lava from comes from one of the boggiest dells here in the Síða highlands, to the north of us*
A3	3	1778–1783	Description of the Fire districts before the eruption	*In this district there was a great abundance of livestock and sheep – so much so that some of the farmers hardly knew how much they owned*
A4	1	Pre-1783		*For a number of years preceding this volcanic fire and scourge of the land, this country had experienced high fertility and great bounty*
A6	1	15th June	Laki lava destroys the older Eldgjá lava	*In addition the surge of this fire laid waste and covered all the older lava between the Síða and Skaftártunga areas, which was covered with extensive dwarf birch and willow shrub and one of the most serviceable stretches of grazing land*
A7	1	15th June		*A second surge headed south towards the Meðalland area where there were already two large fields of older lava, Botnahraun and Steinsmýrarhraun*
A8	1	15th June		*In the path of the stream was a stretch of old lava, under and through which the flood of fire was eating its way [. . .]. The outermost layer, or crust, of the older lava that remained behind could be swept off like dross.*

Ref	Source	Date	Details	Passage
A9	1	19th June	Description of hydrology in Meðalland before the lava flow	*In a great shower of sparks the fire now set its course southeast towards the Meðalland area, following primarily the course of the stream Melkvísl, which previously had flower from the river Skaftá into a spring-fed river. Near its source, the river was called the Botnar stream, for the farm on that name which stood to the west of it a short distance from its source. This stream flower eastward above Meðalland, To the south, under the edge of the former lava, the farm Hólmar stood on an islet of land, with the church at Hólmasel on a leve bank south of it. The farm Efri-Steins'yri lay to the north, where the river turned to the southeast toward the sea and away from the lava, with the former farmsite there to the east-southeast somewhat farther away and the farm Syðri-Steinsmýri on the other side of the stream. A stream called Feðgakvísl, which megan in Meðalland to the east and south of Hólmasel, flowed eastwards to join the Steinmýri stream to the south of Steinsmýri. The farm Efri-Fljótar stood on the north side of this stream and Syðri-Fljótar on the bacnk to the south of it.*
A10	1	19th–24th June	Lava destroys rich farmlands in Meðalland	*The great flood of fire which poured forth that same day [...] laid waste and destroyed Hólmar, a farm worth 12 hundreds, both of the Fljótar farms, worth 24 hundreds, Hólmasel, 12 hundreds, Botnar, 12 hundreds and forced so much water towards the farm Hnausar that it was uninhabitable for four years afterwards. It came very close to destroying both the Steinsmýri farms [...]. The fire did destroy much of their meadows and lyme grass lands.*
A11	1	30th June	Lava destroys pastures at Austari-Ásar and Ytri-Ásar	*This flood of fire then spread itself out over the land of the farms of Austari-Ásar and Ytri-Ásar, approaching the high land upon which these farms stand. There it laid waste and covered with lava hay meadows, pastures and lyme grass lands belonging to the farms*

Table B.1: Table A - Conditions before the eruption

Table B - Lava–river interactions and flooding

Ref	Source	Date	Details	Passage
B1	1	9th June	Lava begins to dam the Skaftá	*The flow of the river Skaftá, a stream so great that at the ferry site here horses had to swim some seventy fathoms to cross it, and which ran eastward along the Síða area, now began to decrease substantially*
B2	1	10th June	Skaftá river dries up	*By now the river Skaftá had dried up entirely, except for the water emptying into it from local streams*
B3	5			*It became apparent that the Skaftá was beginning to decline and was the same day dry in front of the monastery, except for small streams that flowed from the mountains*
B4	7			*To everybody's surprise the Skaftá River dried up and disappeared on this day*
B5	5			*. . . it was noticed that the Skaftá River had dwindled considerably apart from the tributaries, which flowed into it from the mountains bordering the Síða district*
B6	2	11th June	Cloud of steam seen over the Skaftá gorge	*We noticed that the great Skaftá River had dried up. . . North of us further up the gorge we saw a high smoke or steam cloud [. . .] the whole gorge was filled with lava and its sides were glowing like iron. The rocks, both the glowing and unburned ones collided in the air causing loud cracking sounds*
B7	2	12th June	Progress of the lava slowed down by a fishing lake	*But the threat of fire which now occurred did not in hurry inevitably fall here on the people and animals in most countries. Due to God's wise counsel, one apparent obstacle stood in the way and altered and reduced the progression of the fire, a single whirlpool in one of the fishing lakes*
B8	1		Lava exists the Skaftá gorge into the Fire Districts	*Now the flood of lava spilled out of the canyon of the River Skaftá and poured forth with frightening speed, crashing, roaring and thundering*
B9	1		Lava preferentially follows the course of the Skaftá	*At first this fiery flood followed the course of the river, and then spread over the banks and out over the older lava fields*
B10	2			*[the lava] first processed to follow the main path of the river*

Ref	Source	Date	Details	Passage
B11	1	18th June	Lava dams tributaries and causes flooding in Skaftá gorge	*On both sides the water of rivers and streams, whose paths were blocked, collected to the west and below Hæll and the farm Hvammur, which was soon devastated by floodwaters. Both these waters, and any others which the fire did not dry up or set alight and were dammed up here and there along the edges of the fire, were turned into a boiling lake of or hot springs. From these pools, and the flood of fire itself, rose thick steam and vapours, which were especially foul smelling.*
B12	1	19th June	Lava occupies course of the Melkvísl river	*The great flood of fire which poured forth that same day (on the 19th) quickly filled up the course of the river and during the course of these same five days laid waste and destroyed Hólmar*
B13	5			*. . . the flow split up, one branch advanced eastward along the mountain [Skálarheiði], but another due south along the channel of the river Melkvísl*
B14	9	20th June	Lava flows along the plain of the Hellisá river	*. . . an exploratory party went as far north into the highlands as possible to investigate the status here. Those who knew the highlands recognised that the fires emerged from three small lava streams in the northern part of the pasture (almost a [day's journey on horse] to the west from the glaciers), located on a flat fluvial plain north of the Hellisá river. The valley [Varmárdalur] where the inhabitants of Síða picked roots was east of the lava streams. Activity increased with loud cracking, ejecta, ashy cloud, yes a storm emerging from the earth. The lava streams grew steadily and covered more ground as they moved away from the source until they merged into one main stream, which flowed like molten copper, first into the above mentioned valley, and when it was filled, the lava threw itself westwards off the mountains above the southwestern part of the Síða district, into the Skaftá River gorge.*
B15	5		Lava crossed the Melkvísl and Steinsmýrarfljót rivers	*This Saturday when the lava passed over the Melkvísl rapids, it ran very rapidly across the Steinsmýrarfljót River and onto the Stekkjatún grass fields north of the farm Hólmasel*
B16	1		Lava causes flooding at Hnausar	*[the lava] forced so much water towards the farm Hnausar [on the southern edge of the lava flow] that it was uninhabitable for years afterwards.*

Ref	Source	Date	Details	Passage
B17	1	22nd June	Lava flow rips up turf and floods farm of Skál	*There came a fiery surge up near the mountain Skálarfjall and the slopes and bluffs east of the farm Skál, which stood amongst them in a fair and sheltered valley facing south. A brook flowed down the valley on each side of the farm and the church stood in front of the row of farm buildings. This surge pressed so close against the lower, front extremes of the ridges, that the sod was uprooted and twisted like a ribbon. [...] This dammed up the streams and the situation was made worse by unceasing rain. The inhabitants of the farm deserted the house and fled higher up the slopes behind it, sleeping in outbuildings and tents. They took anything that was of value with them [...] so that they should not meet the same fate as Hólmasel. Because of the downpour, however, they kept their cows in the cowshed, which proved to be of little help because the waters rose more quickly than they had expected and flooded church, house and cowshed alike. [...] The water which flooded the farm bubbled and boiled in the heat.*
B18	1		Lava crosses river near Hólmskirkja and destroys the church	*The newly constructed church Hólmskirkja [...] was destroyed by fire. All the ornaments in the church, its books and burial implements burned as well, as did the beautiful bell from Thykkvabæjarklaustur weighing 240 pounds, which had been loaned to the church with the bishop's consent until an appropriate bell had been obtained. This had been done and an order had been given for the bell to be returned to Thykkvabæjarklaustur, but it had not yet been carried out, with the result that the church ornaments and other possessions, which might easily have been removed, burned there and were destroyed. Some people have placed the blame with the minister there who, upon having removed his own belongings and those of others from the church, locked it and left the key in another building before he left on Friday. [...] The fact that, compared to the others, he was so slow to waken to the danger and remove his property was probably due to a delusion – he had expected the fire to come to a halt and be extinguished in the river which ran above the farm. Both he and others were mistaken here, as it was only natural that the greater force should subdue the lesser, as proved to be true here. But in this case it went even farther: as the fire poured and tumbled into the water it was turned into fuel and began itself to combust as if it were the purest of oils, and to this I myself and others are living witnesses.*

Ref	Source	Date	Details	Passage
B19	1		Lava crosses river at Botnar and farmer loses flock	*Another noteworthy example: the farmer who lived at Botnar, [...] was preparing to leave the farm he collected together on an island in the river a great number of his sheep, which he intended to have herded away. The fire, however, spread over the river and the island more quickly than he expected, so that after only a brief time there was neither hide nor hair of them to be seen.*
B20	1	24th June	Lava observed coming from the Hellisá river channel	*... men from Skaftártunga went to explore what was happening to the north of the settlement; they saw that the lava had emerged from the channel of the Hellisá River, here in the pasture. [Note that the lava must have been flowing through this area a week previously, based on the accounts of rootless cone formation at Leiðólfsfell (Thordarson et al., 1998)]*
B21	1	29th June	Lava and floodwaters inundate Hvammur again	*The same fiery lava entered the farm Hvammur [...] so much water had flooded the farm site that it was never again located in the same place*
B22	1	30th June	Lava flow splits into three branches to follow the rivers	*The flood of fire streaming from the canyon now split into three separate branches: one flowest west into the stream Landá, which had left the river Skaftá at Skaftártunga and emptied into the river Kúðafljót between Hraun and Leiðvöllur. The other two branches went east, the more southerly of them headed towards the Landbrot region and the bore northerly east along the settlements of the Síða mountains.*
B23	1	30th June and following days	Lava dams Tungufljót, Hólmsá and Kúðafljot rivers	*The most westerly of the streams of fire, which followed the course of the Landá, now laid waste to the farm of Botnar. [...] This flood of fire then spread itself out over the land of the farms of Austari-Ásar and Ytri-Ásar, approaching the high land upon which these farms stand. There it laid waste and covered with lava hay meadows, pastures and lyme grass lands belonging to the farms, especially Austari-Ásar. This flood of fire continued on to the river Kúðafljót, filling up much of its course, and then flowing a good way along it until it stopped down distance about Leiðvöllur. In doing so, it dammed up the Tungufljót and the river Hólmsá at Hrífunes. The whole area, up to the gravelling knolls of the gorge Fauskalækjargljúfur, was turned into a fjord, covering the meadows of Flöguengjar as far as the ford Hemruvað*

Ref	Source	Date	Details	Passage
B24	1	1st July	North branch of lava follows the Skaftá	*The most northern branch ran into the old course of the river Skaftá, where much of the first surge was now cooling and hardening, and then out of the channel again in several directions.*
B25	1	2nd July	North branch of lava flow dams the Holtsá and Fjaðará rivers	*The liquid fire poured forth over the land so that everything became mixed together. It dammed up the river Holtsá, so that the valley filled with water, after which it crossed the river bed to burn down the Holt farmstead and continued east along the slopes and dammed up the river Fjaðará, which is now called Fjaðará. This flooded the meadows Heiðarengjar, at the foot of the slopes, with water and sand.*
B26	5	13th July		*. . . the lava swelled up and flowed east towards Dælur and Fjaðará River, blocked the river in its gorge, then followed its channel advancing beyond the promontory.*
B27	1	14th July	Lava causes flooding at Hunkubakkar	*Although the fire did not burn down Hunkubakkar, which stood on the bank north of the river, the water which subsequently streamed north from the lava so eroded the home field there that most of it will be given up and the buildings moved to a less-threatened site*
B28	1		Floods damage Hólmur farm	*The farm Hólmur in the Landbrot region [. . .] suffered considerably where the streams which formerly ran to both sides of the farm were dammed up, along with other waters higher up. As a result the farm can now only be reached from one direction, and not at all when the rivers are high*
B29	1			*To the north of the river, across from Hólmur, was a croft belonging to Kirkjubæjarklaustur called Laxárness. It was only occasionally inhabited and was so flooded by water that it will never be inhabited again*

Ref	Source	Date	Details	Passage
B30	1	20th July	Fire Sermon	*I was filled with sorrow at the thought that this might well be the last service to be held in the church, as the terror which now threatened and approached ever nearer appeared likely to destroy it as it had the other two. [...] After the service concluded and men went out to see how the fire had advanced, it turned out that it had come not a foot nearer than before. During the time which have elapsed, it had collected and piled up in the same place, layer upon layer, in a downward sloping channel some 70 fathoms wide and 20 deep, and will rest there in plain sight until the end of the world, unless transformed once again. The rivers Holtsá and Fjaðará poured over the dams which the new lava had made them, and with great torrents and splashing smothered the fire, which was churning and rumbling in the channel, then poured forwards and off the front of the aforementioned pile, streaming and splashing. There was so much water that horses should not cross the river at all by the cloister all that day.*
B31	3			*The molten lava now began to flow down the [Skaftá] riverbed; and it seemed inevitable that it would destroy the church. It was in full course down the slope of the riverbed, heading for the monastic farm and the church. [...] We called fervently and earnestly upon God, who so ordained it that the lava did not advance a single foot beyond where it had been before the service. Instead, it piled itself up in a heap, layer upon layer. In addition, all the local lakes and rivers came flooding down upon the heaped-up lava, and violently quenched it.*
B32	1	31st Ju;y	Lava begins to interaction with Hverfisfljót river	*The cloud of smoke and steam moved along the gorge of the river Hverfisfljót, which was almost as wide and deep as that of the river Skaftá, and contained almost as much water. In some of the channels the water seethed with the heat*
B33	1	1st August	Flow starts to drop in the Hverfisfljót	*The same shrieking continued on the 1st, 2nd and 3rd of August, accompanied by quaking, thundering and lightning, with a flow of fire behind the mountains which dried up the river Hverfisfljót*
B34	2	3rd August	Hverfisfljót dries up	*...people noticed that the water in the Hverfisfljót River was getting warmer. The temperature increased steadily until it finally dried up.*
B35	1	7th August	Lava exits Hverfisfljót gorge	*On August 7th the first visible stream of fire poured from the Hverfisfljót gorge. On the 8th and 9th, it continued to follow the course of the river*

Ref	Source	Date	Details	Passage
B36	1	14th August	Flooding observed along eastern edge of lava flow from Hverfisfljót gorge	I went up to Hörgsland, eastward up on the hearth, to see whether there was a possibility of crossing over in front of the point where the lava flow had advanced. There I saw a huge flood of water churning seaward to the east of the lava which was simply impossible to cross.
B37	1	17th–23rd August	Flood waters begin to subside but contnue to damage farmland	*The waters previously mentioned now began to subside, as the farmer at Thverá clearly noticed, and he began preparations to leave for good when the fire and water began to damage his home field and hay meadow.*
B38	1	20th August	Floods make travel difficult in the area	*I decided to make an attempt to journey eastwards... When I reached the river Brunná at Hvoll I first sank into quicksand and then had to swim the horse from one bank to the other... [We] returned by the common route which was further inland, thinking the water would be shallower there than at Hvoll, which proved to be the case. But so much glacial silt and floodwater had collected on those alluvial flats that it took the boy and I from six o'clock one evening until around nine the next morning to cross there... After that no one crossed there.*
B39	1	1st September	2nd surge of lava exits Hverfisfljót gorge and damns the river Brunná	*[The lava] dammed up the river Brunná just above and across from Núpar, then followed its course along the older lava as far as Hvoll, where it stopped short of destroying the route used by travellers. [...] The river Brunná later found a new course following the old lava, much of which it eroded and thus damaged the lamb-pen field near Núpar.*
B40	1	7th September	All of the local mountain rivers dry up	*There was such a mass of fire beyond the mountains that it dried up and combusted all the lakes and streams which had previously coursed the gravel flats*
B41	1	21st September	Skaftá and Hverfisfljót flow again	*From that day on no one suffered ant severe damage from any flooding. Both the rivers Skaftá and Hverfisfljót and all the streams of the mountains about the settlements have now found themselves a path once more and have not yet caused any great damage*
B42	1	29th September	Hverfisfljót dries up again as fissure 9 opens	*They were followed by the same outbursts of great fire beyond the mountains which dried up a great portion of the rivers and streams which had made their way through the lava*

Ref	Source	Date	Details	Passage
B43	1	Throughout July, August and September	Lava flow keeps rivers dry	*All that month along with August and September the lava flow continued to flow out of the Skaftá River gorge, but in late September the flow dwindled and stopped. At this time, sheep and other goods were taken over the lava flow west of Skaftárdalur because the lava that was still flowing further up in the pasture kept the rivers to the north of the Skaftárdalur farm dry.*
B44	3	Throughout eruption	Eruption contaminated water supply, causing sickness	*The flesh of the livestock that we ate was thoroughly contaminated, and so was the water that we had to drink. My physical strength now began for the first time to be undermined, since I had to drink so much of the water and was constantly harassed with problems during that entire period*
B45	3			*We became so used to drinking water that it tasted to us like sweet whey. But it was polluted and brought in its train more disorders than I care to mention.*

Table B.2: Table B - Lava–river interactions and flooding

Ref	Source	Date	Details	Passage
C1	1	12th June	Rootless eruptions on the bed of the Skaftá	*When the molten lava ran into wet-lands or streams of water, the explosions were as loud as if many cannon had fired*
C2	1	17th June	Formation of the Leiðólfsfell rootless cones (6) (Thordarson et al., 1998)	*The flames of fire then rose so high that from the afore-mentioned canyon Úlfardalsgjá to the northwest, from which a steady rushing and boiling sound could be heard [. . .] The volcanic fires reached over the Geirland heath, where the Geirland property had a shieling*
C3	1			*The fire column was seen from Prestbakki farm above the Geirlandsheiði moor.*
C4	5	18th June	Rootless eruptions from lava flow in Skaftá gorge	*. . . more had come on around the Skaftá River gorge and nearby areas, was clearly visible on the ground as later observations revealed; it was ripped apart and had been thrown around and had undergone amazing transformation. There were found here and there fire-blobs, which had fallen down from the air and burned the grass around them as they chilled and lithified. Some of these blobs were half buried in the ground and shaped like a cow-dung. Others were shaped like twisted bundles and had pierced into the ground and broken up on impact. These fire-blobs appeared to weigh around ten pounds or more. [Note: attributed by Thordarson et al. (2003) to rootless eruptions within the Skaftá gorge. No known surviving rootless cones associated with this description]*
C5	1		Spatter from rootless eruptions	*Near the farm Skaftárdalur on the eastern side of the Skaftá River gorge lava bombs, which had fallen out of the air, could still be seen, some were elongated and twisted together like cow-dung. Some were still in one piece; others had broken up on impact.*

Table B.3: Table C - Explosive lava–water interactions

Ref	Source	Date	Details	Passage
D1	4	8th June	Eruption cloud brings heavy rain	*The heavy rain which fell from the eruption from the fire and smoke columns that rose from the fissure [...] contained salty and sulphur smelling water which caused smarting in the eyes and on the skin*
D2	6			*For the next three days the ash-fall was accompanied by heavy rainfall*
D3	1	9th June		*That night heavy rainfall came down from it*
D4	5			*...torrential rain from the plume that now continuously rose higher and higher by the day. The rain was loaded with before mentioned sandy ash and hairs, light blue in colour and smelled like a mixture of nitrate and sulphur.*
D5	1		Snowfall	*Snowfall and snowdrift in the easterly wind, that was derived from the plume*
D6	5	14th June	Heavy rainfall	*...in the early evening a heavy rainfall occurred from the plume*
D7	1	Mid-June	Floods exacerbated by rainfall	*[The lava] has risen so high there that it is almost on a level with the ridges. This dammed up the streams and the situation was made worse by unceasing rain. [...] the waters rose more quickly than they had expected and flooded church, house and cowshed alike. [...] The water which flooded the farm bubbled and boiled in the heat.*
D8	5	21st June	Snowfall, rain and foggy weather	*... large amount of ash fell here in the Síða district, followed by sleet and snowfall so that the mountains became white*
D9	8			*...followed by rainy and foggy weather. The face of the earth became white.*
D10	1			*...wind from the east with rain [in Síða district]...*
D11	1	27th June	Torrential rain	*...wind was from the west and bringing with it a torrential rainfall.*
D12	1	11th–12th July	Heavy rain	*Heavy rain and wind so the volcanic ash was washed down in the ground or was blown off such that the ground was visible again*
D13	5	22nd July		*...occasional heavy rainfall, and during this time columns of fire and smoke with intermittent thunder and rumbling were observed in the pasture.*
D14	1	1st–7th September		*Rain and acrid rain, fog and mist, thunder and lightning occurred frequently that week.*

Table B.4: able D - Weather conditions during the eruption

B.2 Supplementary Table

Location	Capture Satellite	Capture Date [yyyy-mm-dd]	Image ID	Max Ground Sample Distance [m]
Skaftá river gorge, Kúðafljót area, Hraun valley, Úlfarsdalur, fissure segment 1	WorldView-2	2011-08-09	103001000D08B700	0.50
Kirjubæjarklaustur, Holtsá and Fjaðará rivers	WorldView-2	2015-05-22	1030010043049700	0.47
Hverfisfljót river gorge	WorldView-2	2014-09-05	10300100365CB500	0.60
Highlands and remainder of fissure	*No metadata available through Google Earth*			

Table B.5: Details of DigitalGlobe images used for digitising rootless cones across the Laki lava field (from https://discover.digitalglobe.com).

Appendix C

Supplementary Material for Chapter 4

C.1 Example MUFITS input file

```
-------------------------------------------------------------------------------

   Note:
   We type all comments in lowercase letters while all keywords and mnemonics
   must be in uppercase letters.

-------------------------------------------------------------------------------

   Note:
-- any line beginning with '!' or '--' is a comment line;
   any line not beginning with an uppercase letter outside keyword
!  instruction is also a comment line.

-------------------------------------------------------------------------------

   Note:
   Any data line must be terminated by the slash '/' sign.

-------------------------------------------------------------------------------

   Note:
   We denote by the repeated symbols the following structural elements of this
      RUN-file:
      '###############' - delimits the sections of the RUN-file.
      '<<<<<<<<<<<<<<' - designates an opening bracket.
      '>>>>>>>>>>>>>>' - designates a closing bracket.
      '^^^^^^^^^^^^^^' - designates the keyword, which affects the order of the
                         data input for all the following keywords (both in the
                         current and in the following sections).
      '==============' - merge the keywords and the comments in paragraphs.

-------------------------------------------------------------------------------

   Note:
   This input file corresponds to SCENARIO 2 in this chapter,
   Permeability is set to 250 mD, porosity is 40 %

-------------------------------------------------------------------------------


RUNSPEC   ################### RUNSPEC section begins here ######################

BINMIXT                  We select BINMIXT equation of state module.

HCROCK                   We enable heat conduction in rock

SATCRT                   Enable relative saturation to go linear at critical point

CFLCTRL
   ON   1 /              Enable control of timestep based on CFL condition.
                         max courant no = 1
```

Figure C.1: Example MUFITS input file (p. 1)

```
GRID      ###################### GRID section begins here ######################

          The grid is specified within brackets MAKE-ENDMAKE
MAKE      <<<<<<<<<<<<<<<<<<<<<<<<<<<<<<<<<<<<<<<<<<<<<<<<<<<<<<<<<<<<<<<<<<<<<<<
-- cartesian                                    We select Cartesian gridding
--    grid   nx    ny  nz                       option and specify the number of
      CART   110   1    115    /               grid blocks along every axis.
                                                There are 12,650 grid blocks in the domain

XYZBOUND
-- xmin-xmax   ymin-ymax   zmin-zmax            we specify the domain extent in meters.
    0   20     0    1      0    4   /           20 m long * 1 m wide * 4 m deep

DZV
   75*0.01 15*0.05 25*0.1   /                   Grid gets coarser with depth
                                                top 75 rows are 0.01 m thick,
                                                next 15 are 0.05 m
                                                remainder are 0.1 m

DXV
   10*1 100*0.1 /                               Grid is finer near lava front
/                                               first 10 columns are 1m wide
                                                remainder are 0.1 m wide


-- we specify the extent of the four different boundary conditions
BOUNDARY
-- fluxnum imin-imax jmin-jmax kmin-kmax di...type...actnum
   110   1   70  1   1   1   1   K- 5*  INFTHIN   4*  1  2  / Top boundary, sed/air,
   120   71  110 1   1   1   1   K- 5*  SAMESIZE  4*  2  2  / Top boundary, sed/lava,
   200   1   110 1   1   115 115 K+ 5*  INFTHIN   4*  2  2  / Bottom boundary,
   300   1   1   1   1   1   115 I- 5*  INFTHIN   4*  1  2  / Side boundary at x=0,
/

ENDMAKE   >>>>>>>>>>>>>>>>>>>>>>>>>>>>>>>>>>>>>>>>>>>>>>>>>>>>>>>>>>>>>>>>>>>>>>>

-- Specify rock data for SEDIMENT layers

EQUALS
   PORO       0.4 /                  Porosity = 40 %
   ROCKNUM    1 /                    Rocknum (a lable) = 1
   PERMX      250 /                  Permeability in x direction = 250 mD
   PERMZ      250 /                  Permeability in z direction = 250 mD
   HCONDCFX   3.75 /                 Thermal conductivity in x direction = 3.75 W/mK
   HCONDCFZ   3.75 /                 Thermal conductivity in z direction = 3.75 W/mK
/

================================================================================

RPTGRID
-- We define which properties to output from the GRID section.
   PORO PERMZ HCONDCFZ ROCKNUM CELLID /
```

Figure C.2: Example MUFITS input file (p. 2)

```
PROPS     ######################## PROPS section begins here ####################

          Rock properties are specified within brackets ROCK-ENDROCK
ROCK      <<<<<<<<<<<<<<<<<<<<<<<<<<<<<<<<<<<<<<<<<<<<<<<<<<<<<<<<<<<<<<<<<<<<<<<
   1 /      Properties for ROCKNUM=1 region (SEDIMENT)

ROCKDH                                          We specify that
  2100  2.0 /                                   rock density is 2100 kg/m3
                                                rock heat capacity is 2.0 kJ/kg/K

ENDROCK  >>>>>>>>>>>>>>>>>>>>>>>>>>>>>>>>>>>>>>>>>>>>>>>>>>>>>>>>>>>>>>>>>>>>

          The relative permeabilities are specified within brackets SAT-ENDSAT
SAT       <<<<<<<<<<<<<<<<<<<<<<<<<<<<<<<<<<<<<<<<<<<<<<<<<<<<<<<<<<<<<<<<<<<<<<<
   /

SATTAB                                      We specify that
-- sliq    krliq    krgas                  liquid phase relative permeability is
    0.0     0.0      1.0     /             krliq=sliq^4
    0.1     0.0001   0.8019  /             gas phase relative permeability is
    0.2     0.0016   0.6144  /             krgas=((1-sliq)^2)/(1-sliq^2)
    0.3     0.0081   0.4459  /             (Corey relative permeability model)
    0.4     0.0256   0.3024  /             The relative permeability curves
    0.5     0.0625   0.1875  /             are specified in tabular form.
    0.6     0.1296   0.1024  /
    0.7     0.2401   0.0459  /
    0.8     0.4096   0.0144  /
    0.9     0.6561   0.0019  /
    1.0     1.0      0.0
/

ENDSAT    >>>>>>>>>>>>>>>>>>>>>>>>>>>>>>>>>>>>>>>>>>>>>>>>>>>>>>>>>>>>>>>>>>>>>>

-- We load EOS-file, located in the INCLUDE folder.
LOADEOS
   '../../../INCLUDE/CO2H2O_V3.0.EOS' /


INIT      ######################## INIT section begins here ####################
-- set the initial conditions in the model

EQUALS
  TEMPC    15   /                           We set T = 15 C in all cells
  COMP2T   1.0  /                           H2O mol fraction = 1 in all cells
  PRES     0.1  /                           pressure = 0.1MPa in all cells
/

OPERATE
  PRES  DEPTH  MULTA 0.1  0.01 /            Pressure = 0.1 + (0.01*z)MPa (=hydrostatic)
/


REGALL
-- set the properties for the boundary conditions

--Set upper boundary (air) T=15C, P=atmos, SATCO2=0
```

Figure C.3: Example MUFITS input file (p. 3)

```
EQUALREG
   PRES 0.1 FLUXNUM 110  /
   TEMPC 15 /
   COMP1T 0 /
/

--Set upper boundary (lava) conditions T = 533C
EQUALREG
   TEMPC 533 FLUXNUM 120 /
/

--Set lower boundary conditions T = 15C
EQUALREG
   TEMPC 15  FLUXNUM 200 /
/

--Set the x=0 boundary (sediment) T = 15C, P=0.12MPa, SATCO2=0
EQUALREG
   PRES 0.12  FLUXNUM 300 /
   TEMPC 15 /
   COMP1T 0 /
/

-- We specify the properties which are saved at every report time step

RPTSUM
   PRES TEMPC PHST FLUX2I FLUX2K DENT VRAC$1 VFRAC$2 /
-- pressure (PRES), no. of phases (PHST), temperature (TEMPC) and water flux (FLUX2I and
FLUX2K)

SCHEDULE   ##################### SCHEDULE section begins here ####################

-- report model progress
REPORTS
  CHOPSREP /

TUNING
  3* 0.00000001 /                              minimum time step set to 0.000001 days

TSTEP
  60*0.0003472222 /                            report every 30sec for 30mins


POST      ######################## POST section begins here ######################

-- Save consolidated time series report for time, pressure, temperature and phases,
-- mass fluxes, cell density, volume fraction of different phases
RPTPOST
   TIMESEC PRES TEMPC PHST FLUX2I FLUX2K DENT VRAC$1 VFRAC$2 /


CONVERT                                        We enable the MUFITS output files
                                               conversion to ParaView compatible
                                               formats (the .vtu and .pvd files output
                                               is initiated by this keyword).
   END       ###########################################################################
```

Figure C.4: Example MUFITS input file (p. 4)

C.2 Table of published sediment properties

Sediment	Density [kg/m^3] Dry	Wet	Porosity [%]	Permeability [mD] Min	Max	Conductivity [W/m.K]	Bulk c_p [kJ/kg.K]	Source
Clay (unspecified)				0.00068	1.36			Lewis et al. (2006)
Upper Clay Member, Mojave River, CA	1550	1980	43.1					Manger (1963)
Lower Clay Member, Mojave River, CA	1730	2090	35.7					Manger (1963)
Clay loam, sandy clay loam, silty clay loam				166	499			Brown et al. (2015)
Sandy clay, silty clay, clay ¡60 %				49.9	166			Brown et al. (2015)
Clay (unspecified)						1.3–1.45		Revil (2000)
Mixed clay layer						1.85		Revil (2000)
Smectite						1.88		Revil (2000)
Kaolinite						2.64–2.77		Revil (2000)
Illite						1.85		Revil (2000)
Chlorite						3.26–4.9		Revil (2000)
China clay (saturated)	1183	1730	55			15.2	2362	Hamdhan and Clark (2010)
Sandy clay	1494	1890	40			1.61	2696	Hamdhan and Clark (2010)
Sandy clay	1757	2100	34			2.45	2459	Hamdhan and Clark (2010)
Soft dark grey sandy gravelly clay	1488	1912	42			3.57	2764	Hamdhan and Clark (2010)
Soft grey fine sandy gravelly clay	10.67	1650	58			4.20	2646	Hamdhan and Clark (2010)
Soft grey fine sandy gravelly clay	1231	1741	51			3.03	2200	Hamdhan and Clark (2010)
Stiff dark grey sandy gravelly clay	2088	2299	21			3.69	1141	Hamdhan and Clark (2010)
Stiff dark grey sandy gravelly clay	2161	2369	21			3.28	1125	Hamdhan and Clark (2010)
Stiff grey brown sandy gravelly clay	2158	2352	19			3.20	1104	Hamdhan and Clark (2010)
Very soft grey fine sandy clay	1170	1711	54			3.51	2362	Hamdhan and Clark (2010)
Silty gravelly clay	1916	2182	27			5.03	1270	Hamdhan and Clark (2010)
Sand, silt and clay (subaqueous)		1440	75					Manger (1963)
Loess soil, ID	1000	1600	53–69	13.6	1364			Manger (1963)
Silt				1.36	136			Lewis et al. (2006)
Silt (subaqueous, Hudson River, 50 ft)			55					Manger (1963)

Sediment	Density [kg/m^3] Dry	Wet	Porosity [%]	Permeability [mD] Min	Max	Conductivity [W/m.K]	Bulk c_p [kJ/kg.K]	Source
Silt loam			47		505			Brooks and Corey (1964)
Fine sandy loam, San Diego, CA			50–54					Manger (1963)
Gravelly loam, ID	1190	1730	54					Manger (1963)
Sandy loam, Hamburg	2000	2080						Manger (1963)
Loamy sand				499	1660			Brown et al. (2015)
Coarse sandy loam, sandy loam, fine sandy loam				166	499			Brown et al. (2015)
Very fine sandy loam, loam				49.9	166			Brown et al. (2015)
Silt loam, silt				49.9	166			Brown et al. (2015)
Sandy coarse silt (subaqueous)		1860	51					Manger (1963)
Silty very fine sand (subaqueous)		1680	61					Manger (1963)
Medium silt (subaqueous)		1690	61					Manger (1963)
Clayey fine silt (subaqueous)		1600	67					Manger (1963)
Sand				136	682000			Lewis et al. (2006)
Fine sand			36		2880			Brooks and Corey (1964)
Volcanic sand			37		11100			Brooks and Corey (1964)
Beach sand, well sorted			39					Manger, (1963)
Cape May sand, Pleasentville, NJ	1740	2020	26–40					Manger, (1963)
Cape May sand, Abescon, NJ	1630	2000	31–40					Manger (1963)
Coarse sand, San Diego, CA			39–41					Manger (1963)
Medium sand, San Diego, CA			41–48					Manger (1963)
Fine sand, San Diego, CA			44–49					Manger (1963)
Sand				4990	16600			Brown et al. (2015)
Coarse sand (saturated)	1730	2080	35			3.72	1438	Hamdhan and Clark (2010)
Dark grey clayey fine sand/silt	1444	1848	40			4.26	1747	Hamdhan and Clark (2010)
Fine sand (saturated)	1613	2010	40			2.75	1632	Hamdhan and Clark (2010)
Medium sand (saturated)	1730	2080	35			3.34	1438	Hamdhan and Clark (2010)
Coarse sand (subaqueous)		2080	39					Manger (1963)
Medium sand (subaqueous)		2000	41					Manger (1963)
Fine sand (subaqueous)		1930	46					Manger (1963)

Sediment	Density [kg/m^3] Dry	Wet	Porosity [%]	Permeability [mD] Min	Max	Conductivity [W/m.K]	Bulk c_p [kJ/kg.K]	Source
Very fine sand (subaqueous)		1920	48					Manger (1963)
Gravel				6280	6820000			Lewis et al. (2006)
Gravel, Yellowstone River	2190	2390	20					Manger (1963)
Gravel, Fergus Co., MT	1890	2140	25					Manger (1963)
Grey slightly sandy silty gravel	1785	1983	20			4.44	1175	Hamdhan and Clark (2010)
Sand and gravel				6820	136000			Lewis et al. (2006)
Peat	20	254	71–95	825	1530000			Rezanezhad et al. (2016)
Diatom-rich clay (17.1 m depth)			89		0.03			Gamage et al. (2011)
Diatom-rich nanofossil ooze (24.7 m depth)			78		0.32			Gamage et al. (2011)

Table C.1: Published sediment properties from various sources.

C.3 Sediment fluidisation example

Fluidisation occurs when the drag force on a bed of particles from an upwards flowing fluid is greater or equal to the bed weight (Holiduch, 2002). The point at which a bed of particles goes from being static to fluidised is defined by the minimum fluidising velocity, u_{mf}, given by:

$$u_{\mathrm{mf}} = \frac{kg(1-\varphi)}{\mu}\left(\rho_S - \rho_{\mathrm{liq}}\right) \tag{C.1}$$

If we assume our sediments are made up of separate uniform particles resting on one another, we can then use their physical properties to estimate a minimum fluidisation velocity. This assumption is a significant simplification, as we know that soils are not made up of uniform particles, and often have internal cohesion. However, it's a good starting point. To calculate the pressure gradient necessary to achieve this flow, we can apply Darcy's Law:

$$\frac{\mathrm{dP}}{\mathrm{dz}} = \frac{\mu u_{\mathrm{mf}}}{k} \tag{C.2}$$

Combining equations (C.1) and (C.2) gives an expression for the pressure gradient necessary for fluidisation:

$$\frac{\mathrm{dP}}{\mathrm{dz}} = g\left(\rho_s - \rho_l\right)(1-\varphi) \tag{C.3}$$

Let us take fine sand as an example, as it is the closest sediment to our simplified particle bed. Sand has a dry density of ∼1500 kg/m^3 (Hamdhan and Clark, 2010), porosity of ∼40 %. If we assume that the water flowing through the sediment is at ambient temperature (since the majority of the sediment is unaffected by heat transfer from the lava), this gives us a density of 1000 kg/m^3. If we take a sediment depth of 4 m (in line with our numerical models), we obtain a bed pressure of 0.113 MPa (abs), well below even our estimated minimum threshold pressure for causing a steam explosion (0.55 MPa abs, 0.45 MPa gauge). Therefore, when an initial steam explosion at the surface of the sediment occurs, and an instantaneous vertical pressure gradient exists, we expect the resulting flow of water towards the explosion site to be sufficient to fluidise the sediment.